Large eddy simulation of nanoparticle synthesis from spray flames

Von der Fakulät für Ingenieurwissenschaften, Abteilung Maschinenbau und Verfahrenstechnik

der

Universität Duisburg-Essen

zur Erlangung des akademischen Grades

eines

Doktors der Ingenieurwissenschaften

Dr.-Ing.

genehmigte Dissertation

von

Andreas Rittler
aus
Heidelberg

Gutachter: Univ.-Prof. Dr.-Ing. Andreas M. Kempf
Univ.-Prof. Dr.-Ing. Andreas Kronenburg

Tag der mündlichen Prüfung: 24.10.2017

Abstract

The presented work focuses on the development of a multiscale and multiphysics simulation approach for the prediction of nanoparticle synthesis from turbulent flames and spray flames. The models proposed and applied for the description of the flow-, spray-, combustion- and particle dynamics are formulated for the large eddy simulation methodology. The presented global simulation approach is independent of the material system and has been used to investigate the synthesis of silica (SiO_2) and iron-oxide (Fe_2O_3) particles from spray flame pyrolysis processes with hexamethyldisiloxane and ironpenthacarbonyl as precursors.

An Eulerian-Lagrangian-Eulerian approach has been used to model the gas-, spray- and particle phases respectively. To describe combustion, an existing flamelet generated manifold approach (FGM) combined with the artificially thickened flame method (ATF) was modified to account for (a) spray combustion and (b) to account for spray combustion of three feed systems − due to the fact that most spray pyrolysis reactors feature such a set-up. Two mixture fractions and one joint reaction progress variable are used as control variables in the combustion model. In contrast to the standard FGM approach, which is based on one Bilger mixture fraction, two element mass fractions are used as control variables to describe the mixture composition. During the flamelet calculations, the chemistry of the precursor was considered in the determination of the thermo-chemical quantities, which were stored in multidimensional look-up tables as functions of the control variables. The general dynamics equation in continuous form, a population balance equation that describes the evolution of particle from gas phase synthesis, is approximated by (a) a simple monodisperse model, (b) a more advanced bimodal model and (c) a detailed sectional model. While the sectional model considers the formation of particles by nucleation and their growth by coagulation, the monodisperse and bimodal models consider additionally the coalescence of particles. The formation of particles from the gas phase was determined during the flamelet calculations and stored as a nucleation source term in the look-up tables.

In the first part of the study, the suitability and validity of the flamelet generated manifold approach combined with the artificially thickened flame method was examined and demonstrated for a well investigated lab-scale spray flame burner operated with ethanol and air. Secondly, the well-known monodisperse population balance equation model was applied to study the formation of silica particles from a spray flame pyrolysis reactor operated with ethanol, hexamethyldisiloxane, methane and oxygen. The findings of this study raised the question how well the monodisperse model is suited to describe simultaneously nucleation, coagulation, sintering and mixing as these processes occur simultaneously in turbulent flames. Therefore, the suitability, performance and validity of the three particle models has been demonstrated for a case with simultaneous nucleation, coagulation, coalescence and mixing of particle populations with different histories. Due to the lack of time resolved measurements of particle properties and particle size distributions, a generic test case was used and modified for the aforementioned studies. In the final part of this thesis, the global simulation approach has been used to investigate the formation of silica particles from spray flame pyrolysis in a lab-scale reactor and for the synthesis of iron-oxide particles from a pilot-scale reactor. The simulation results were (a) shown to be in reasonable agreement with the experiments, (b) to help to improve the understanding of the underlying processes and (c) to improve the processes in the investigated reactors.

Zusammenfassung

Die präsentierte Arbeit befasst sich mit der Entwicklung eines Multiskalen und Multiphysik Simulationsansatzes zur Beschreibung der Nanopartikelsynthese aus turbulenten Flammen und Sprayflammen. Die vorgeschlagenen und angewandten Modelle zur Beschreibung der Gasphasenprozesse, der Sprayprozesse, sowie der Verbrennung und der Partikeldynamik sind für das Large Eddy Simulation Verfahren ausgedrückt. Der vorgestellte globale Simulationsansatz ist unabhängig vom Materialsystem und wurde genutzt, um die Siliziumoxid (SiO_2) und Eisenoxid (Fe_2O_3) Synthese aus Sprayflammen mit Hexamethyldisiloxan und Eisenpentacarbonyl als Präkursoren zu Untersuchen.

Zur Modellierung der Gasphase, Sprayphase und der Partikelphase wurde ein Euler-Lagrange-Euler Ansatz gewählt. Zur Beschreibung der Gasphasenverbrennung wurde ein existierender "Flamelet Generated Manifold" Ansatz (FGM) kombiniert mit einem "Artificial Thickened Flame" Model (ATF) modifiziert um (a) Sprayflammen und (b) Systeme mit mehreren Strömen beschreiben zu können − da die meisten Spraysynthese Reaktoren auf den zuvor genannten Mehrstromsystemen basieren. Zwei Mischungsbrüche und eine Verbrennungsvortschrittsvariable wurden in dem entwickelten Verbrennungsmodell als Kontrollparameter genutzt. Im Gegensatz zum Standard FGM Model, in dem der Mischungsbruch nach Bilger zum Einsatz kommt, wurden in dieser Arbeit zwei Elementarmassenbrüche zur Beschreibung der Gemischzusammensetzung eingesetzt. Der Einfluss der Präkursorchemie auf die thermochemischen Größen wurde während der Tabellengenerierung berücksichtigt. Die thermochemischen Größen wurden in einer mehrdimensionalen Tabelle als Funktionen der Kontrollparameter gespeichert. Die "General Dynamics Equation" in kontinuierlicher Form, eine Populationsbilanzgleichung zur Beschreibung der Partikelsynthese aus der Gasphase, wurde mit (a) einem simplen monodispersen Modell, (b) einem weiterentwickelten bimodalen Modell und (c) einem detaillierten sektionalen Modell approximiert. Während das sektionale Modell die Partikelerzeugung durch Nukleation und das Partikelwachstum durch Koagulation berücksichtigt, ist im monodispersen und bimodalen Modell zusätzlich Koaleszenz berücksichtigt. Die Partikelerzeugung aus der Gasphase wurde während den Flamelet Berechnungen ermittelt und als Nukleationsquellterm in den Tabellen gespeichert.

Im ersten Teil der Arbeit wurde die Eignung und die Validität des Flamelet Generated Manifold Ansatz's gekoppelt mit dem Artificial Thickened Flame Modell anhand einer gut untersuchten Ethanol-Luft Sprayflamme im Labormaßstab untersucht und nachgewiesen. Danach, wurde das namhafte monodisperse Populationsbilanzgleichung-Modell genutzt um die Siliziumoxid-Synthese aus einem Spraypyrolyse-Reaktor betrieben mit Ethanol, Hexamethyldisiloxan Methan und Sauerstoff zu untersuchen. Die Ergebnisse dieser Studie führten zu der Frage, wie gut das monodisperse Modell geeignet ist, die gleichzeitig stattfindenden Prozesse Nukleation, Koagulation, Koaleszenz und Mischen in turbulenten Flammen zu Beschreiben. Daher wurden die Tauglichkeit und Validität von drei Populationsbilanzmodellen für Fallstudien mit parallel ablaufender Nukleation, Koagulation, Koaleszenz und Mischung von Partikelpopulationen mit unterschiedlichen Historien untersucht und demonstriert. Auf Grund fehlender zeitaufgelöster Messungen von Partikeleigenschaften und Partikelgrößenverteilungen wurde ein generischer Testfall basierend auf einem veröffentlichen Referenzfall erzeugt und genutzt, um die zuvor genannte Studie durchzuführen. Im finalen Abschnitt der Arbeit wurde der globale Simulationsansatz zur Beschreibung und Untersuchung der Siliziumoxid-Synthese aus einem Reaktor im Labormaßstab sowie der Eisenoxid-Synthese aus einem Reaktor im Versuchsmaßstab angewandt.

Preface

This thesis was written during my tenure as a research assistant at the department for fluid dynamics at the University of Duisburg-Essen. I would like to take the opportunity to express my gratitude to Prof. Dr.-Ing. Andreas Kempf for giving me the possibility to work quite autonomously in his research group, for his ongoing support and motivation − not only in the working environment. I am glad that I had the possibility to attend national and international conferences not only to present my research work but also to meet very inspirational scientists.

I am thankful to my colleagues at the Chair for Fluid Dynamics Fabian Proch, Claudia Weise, Miriam Rabacal, Thuong Nguyen and Sylvia Helwig who started together with me and who contributed to a nice working environment with many fruitful discussions and also a nice time after work. I also would like to thank my colleagues I met during my time as doctoral candidate Eray, Johannes, Hossein, Khadijeh, Lei, Luis, Martin, Nejra, Olaf, Pascal, Patrick, Peter, Timo and Vahid for the nice time and working atmosphere we had together.

Also to Irenäus Wlokas I am very thankful for his ongoing scientific support, his motivation and the nice time we spent together in the office, at many conferences and awesome BBQ's.

Finally I would like to thank my parents Rosemarie and Siegfried who raised me to who I am today and my brother Daniel for his inspiration and motivation and for always believing in me.

To my wife Lisa, I am deeply thankful for your love and patience

"You can't climb the ladder of success with your hands in the pocket"
Arnold Schwarzenegger

Contents

List of Figures

List of Tables

Nomenclature

Lower case latin symbols

a	surface area	m^2
$a_{d,i}$	components of the droplet acceleration vector	m/s^2
a_m	surface area of monomer particles	m^2
c	molar concentration	mol/m^3
c	speed of sound	m/s
c_p	heat capacity at constant pressure	$J/(kg \cdot K)$
c_v	heat capacity at constant volume	$J/(kg \cdot K)$
d	particle/droplet diameter	m
d_a	aggregate particle diameter	m
d_c	collision particle diameter	m
d_m	volume averaged particle diameter	m
d_p	primary particle diameter	m
e_i	face normal vector	-
g_i	gravitational acceleration	m/s^2
g_i	particle transition parameter	m
h	enthalpy	J/kg
h_c	heat of formation	J/kg
h_s	sensible enthalpy	J/kg
k	turbulent kinetic energy	m^2/s^2
k	wave number	1/m
m	mass	kg
n	particle number concentration in the PBE	-
p	pressure	Pa
q	enthalpy flux	J/kg
r	reaction rate	$mol/(m^3s)$
r_b	backward reaction rate	$mol/(m^3s)$
r_f	forward reaction rate	$mol/(m^3s)$
t	time	s
u_i	(components) of the velocity vector	m/s
v_m	volume of monomer particles	m^3
x_i	(components) of the spatial coordinate vector	m

Upper case latin symbols

A	area concentration of aggregate particles, monodisperse model	m^2/m^3
A	pre exponential coefficient	-
A_1	area concentration of monomer particles, bimodal model	m^2/m^3
A_2	area concentration of aggregate particles, bimodal model	m^2/m^3
B_h	Spalding number for heat transfer	-
B_m	Spalding number for mass transfer	-
C	molar concentration	$kmol/m^3$
C	normalized reaction progress variable	-
C_k	Kolmogorov constant in the efficinecy function	-
C_S	constant in the Smagorinsky/Sigma turbulence model	-
D	binary diffusion coefficient	m^2/s

E	activation energy in the Arrhenius equation	J/mol
E	efficiency function in the ATF approach	-
E	energy	J
F_t	thickening factor in the ATF approach	-
I	monomer particles source term	$1/(m^3s)$
J_i	components of diffusive flux vector	$m^2/(s \cdot m)$
L	length	m
L_t	turbulent length scale	m
L_v	latent heat of vaporization	J/kg
L_{ij}	Germano identity/Leonard stress tensor	-
N	number concentration of aggregate particles, monodisperse model	$1/m^3$
N	number	-
N_1	number concentration of aggregate particles, bimodal model	$1/m^3$
N_2	number concentration of monomer particles, bimodal model	$1/m^3$
N_r	number of reactions	-
N_s	number of sections	-
N_s	number of species	-
Q	volume source term in energy equation	J/kg
Q_k	number concentration of section k, sectional model	$1/m^3$
R	gas constant	J/(kgK)
S_0	fitting constant in Sutherland law	-
S_A	area source term in momentum	$kg/(m^2 \cdot s^2)$
S_{ij}	strain rate	1/s
S_l^0	laminar flame speed	m/s
S_V	volume source term in momentum	$kg/(m^2 \cdot s^2)$
T	temperature	K
T_0	reference temperature in Sutherland law	K
V	volume concentration of aggregate particles, monodisperse model	m^3/m^3
V_1	volume concentration of monomer particles, bimodal model	m^3/m^3
V_2	volume concentration of aggregate particles, bimodal model	m^3/m^3
W	molecular weights	kg/kmol
X	molar fraction	-
Y_α	mass fraction of species alpha	-
Z	Bilger mixture fraction	-
Z_α	element mass fraction	-

Lower case greek symbols

β	coagulation kernel / frequency	m^3/s
γ	ratio of specific heats	-
δ_{ij}	Kronecker delta	-
δ_l^0	thermal flame thickness	m
ϵ	rate of dissipation	m^2/s^3
η	Kolmogorov length scale	m
θ	flux limiter function in the TVD scheme	-
χ_{ijk}	interpolation term in the sectional particle model	-
λ	thermal conductivity	W/(mK)
μ	dynamic viscosity	$Pa \cdot s$
μ_0	reference viscosity in Sutherland law	$Pa \cdot s$
ν	kinematic viscosity	m/s^2
ρ	density	kg/m^3
σ_i	singular values	-

τ_{ij}	viscous stress tensor	$\mathrm{N/m^2}$
τ_d	droplet/particle relaxation time	s
τ_s	characteristic sintering time	s
ϕ	scalar quantity	-
χ	chemical species	-
$\dot{\omega}$	source term for species/progress variable	$\mathrm{kg/(m^3 \cdot s)}$
$\dot{\omega}_\alpha$	chemical source term for species α	$\mathrm{kg/(m^3 \cdot s)}$
$\dot{\omega}_E$	evaporation source term for species α	$\mathrm{kg/(m^3 \cdot s)}$
$\dot{\omega}_{Z_\alpha}$	evaporation source term for the element mass fraction Z_α	$\mathrm{kg/(m^3 \cdot s)}$
$\dot{\omega}_k^Q$	coagulation surce term in the sectional model	$\mathrm{1/(m^3 s)}$

Upper case greek symbols

$\dot{\Gamma}_\rho$	mass source term due to evaporation	$\mathrm{kg/(m^3 \cdot s)}$
Δ	cell size	m
Δ	difference	$\star$
T	stress tensor	$\mathrm{N/m^2}$
Ω	flame sensor	-

Subscripts to an arbitrary quantity ϕ

ϕ_0	initial
ϕ_α	species
ϕ_A	area
ϕ_c	chemical
ϕ_d	droplet
ϕ_{ij}	two dimensional tensor in index notation, $k = 1, 2, 3$
ϕ_i	vector in index notation, $i = 1, 2, 3$
ϕ_j	vector in index notation, $j = 1, 2, 3$
ϕ_k	vector in index notation, $k = 1, 2, 3$
ϕ_{max}	maximum of ϕ
ϕ_{min}	minimum of ϕ
ϕ_M	momentum
ϕ_m	monomer
ϕ_{NP}	nano particle
ϕ_p	at constant pressure
ϕ_r	reaction
ϕ_s	sensible
ϕ_s	sintered
ϕ_t	turbulent
ϕ_V	volume
ϕ_v	at constant volume

Superscripts to an arbitrary quantity ϕ

$\dot{\phi}$	time derivative
ϕ°	reference point
ϕ'	fluctuation
ϕ^{sgs}	sub-grid scale
ϕ^S	surface

Operators to an arbitrary quantity ϕ

d	total derivative
$\overline{\phi}$	mean part of scalar quantity ϕ

∂	partial derivative
$\widetilde{\phi}$	Favre filtered part of scalar quantity ϕ
ϕ''	sub-filter part of fluctuating quantity ϕ

Dimensionsless numbers

B_h	Spalding number for heat transfer
B_m	Spalding number for mass transfer
CFL	Courant-Friedrichs-Lewy number: ratio of physical to numerical velocity
Kn	Knudsen number: ratio of mean free path of the gas phase to particle diameter
Le	Lewis number: ratio of thermal diffusivity to mass diffusivity
Ma	Mach number: ratio of velocity to speed of sound
Nu	Nusselt number: ratio of total to conductive heat transfer
Pr	Prandtl number: ratio of viscous to thermal diffusion
Re	Reynolds number: ratio of inertial to viscous forces
Re_d	Reynolds number of droplets/particles
Re_t	Reynolds number of turbulence
Sc	Schmidt number: ratio of momentum to mass diffusivity
Sh	Sherwood number: ratio convective mass transfer to diffusion rate

Physico-chemical constants

k_b	Boltzmann constant	$1.38064852 \cdot 10^{23}$ J/K
N_A	Avogadro constant	$6.022 \cdot 10^{26}$ 1/kmol
R_m	ideal gas constant	$8.314459 \cdot$ J/(molK)

Acronyms

1D	one dimensional
3D	three dimensional
ATF	artificial thickened flame method
CCSS	Center for Computational Sciences and Simulation
CDS	central differencing scheme
CENIDE	Center for Nanointegration Duisburg-Essen
CFD	computational fluid dynamics
CMC	conditional moment closure
CV	control volume
CVS	chemical vapor synthesis
DNS	direct numerical simulation
EBU	eddy break-up combustion model
EDM	eddy dissipation combustion model
FGM	flamelet generated manifolds approach
FSP	flame spray pyrolysis
FVM	finite volume method
GDE	general dynamics equation for particle dynamics
GRI	gas research institute
HMDSO	hexamethyldisiloxane
ICE	internal combustion engines
IPC	iron-penthacarbonyl
LDA	laser Doppler anemometry
LES	large eddy simulation
LHS	left hand side
MPI	message passing interface
PBE	population balance equation

PDE	partial differential equation
PDF	probability density function
PFGM	premixed flamelet generated manifolds approach
PIV	particle image velocimetry
PSD	partical size distribution
QUICK	quadratic upstream interpolation for convective kinematics
RANS	Reynolds averaged Navier-Stokes
RHS	right hand side
rms	root mean square
RST	Reynolds stress tensor
SD	size distribution
SGS	sub-grid scale
TNF	turbulent non-premixed flame workshop
TVD	total variation diminishing
UDS	upwind differencing scheme
URANS	unsteady Reynolds averaged Navier-Stokes
UV	ultra violet

Chapter 1
Introduction

Particles with a diameter of less than 100 nm are known as nanoparticles. These nanoparticles are found almost everywhere, in the environment or in our every day life, for example in the atmosphere as soot particles from the smoke of combustion processes, as dust from volcanic ash or soil, in haze [49], as color pigment in paint or in cosmetic products. Nanoparticles are also used in a wide range of applications in many fields of research and science. In biomedicine and healthcare, for example, nanoparticles are utilized for cancer therapy, drug delivery, imaging or ultra violet (UV) protection [140, 168]. In the field of food agriculture, nanoparticles are applied for food packaging or food processing catalysts. In industrial applications, nanoparticles are used for example as carbon blacks in tires, as metal nanoparticles in catalysts to speed up the chemical reactions [12], in fuel cells [22, 104, 125] or in electronic devices [94] and many more, an overview is given by e.g. Kruis [94].

The popularity of nanoparticles is explained by their size dependent properties. In contrast to the corresponding bulk materials, particles on the nanoscale feature a different chemical [30], mechanical [62], optical [80] or physical behaviour. The change of the properties compared to the corresponding bulk material result from the increased surface area to volume ratio of the nanoparticles and therewith the atoms and molecules on the surface of the material become significant. Influenced properties of the nanoparticles are for example the color, a reduced melting temperature, a different crystal structure, an increased chemical reactivity, an increased electrical conductivity, a different magnetic behaviour or an increased mechanical strength.

To utilize nanoparticles in any application requires specific and controllable particle properties. A common way to control the properties of the particles and therefore of the related applications, is to control the shape, the particle size and the particle size distribution already during the production process. The production or synthesis of nanoparticles may be characterized by two methods, i.e. the top-down method and the bottom-up method. In the top-down method the particles are created from a bulk material by nano-structuring via, for example, laser-beam lithography [182], electro-beam-lithography [182] or photo-lithography [153]. The synthesis of nanoparticles according to the bottom up method, formation of particles from precursor molecules, plays a more important role in industrial production processes, is part of the studies presented in this thesis and is explained in more detail below. Different processes have been developed to produce particles with specific properties from the bottom up method, for example the synthesis with the sol-gel method where the particles are created from precursors solved in a solution [24] or the creation of particles from the vapor phase [189]. Prior to the synthesis from the vapor phase, molecules are released from a precursor that is supplied into an environment which provides the conditions needed for the particles to nucleate and grow. The synthesis of nanoparticles from the vapor phase may be furthermore separated, depending on the state of the precursor [189] i.e. solid, liquid or gaseous. Synthesis processes for nanoparticles from solid precursors are e.g. inert gas condensation [142], pulsed laser ablation [34], spark discharge generation [190] or ion sputtering [200], which are not part of the present study and the interested reader is referred to the literature [34, 142, 190, 200].

The precursors of interest in the scope of this work are in liquid and gaseous form, where again multiple ways exist of providing the energy to decompose the precursor and induce supersatu-

ration, leading to nucleation of the particles - (not only supersaturation may lead to nucleation of particles). In the chemical vapor synthesis (CVS) process the precursor is injected in gaseous form into a hot wall reactor, where the nucleation occurs within the vapor phase and the required energy is provided by the hot walls of the reactor. The CVS-process is used diversely, e.g. to produce silicon particles coated with oxide in a two stage reactor [138], for the generation of multi-component nanoparticles from different precursors [170] or for the synthesis of composite particles where one species is encapsulated from another [38]. Furthermore, the synthesis of nanoparticles may be achieved by spraying a liquid precursor into a hot wall reactor as demonstrated by Ahonen for the synthesis of titanium dioxide nanoparticles [3]. Two more techniques are mentioned here, where an external energy source is used to provide the conditions for the precursor that is needed for supersaturation and hence a condensation and particle growth, namely the laser pyrolysis [103] and a thermal plasma source [107].

1.1 Flame-made nanoparticles

The production processes investigated in the scope of this thesis are the nanoparticle synthesis from turbulent flames and spray flames. (The particle synthesis from spray flames is sometimes also referred to as "flame spray pyrolysis", abbreviated as FSP). These two aforementioned techniques showed a high commercial efficiency in the synthesis of carbon black and metal-oxide nanoparticles at a high process complexity which is difficult to control [189]. In the flame synthesis of nanoparticles, the conditions needed for nucleation and growth of the particles is provided by the heat released from the exothermic chemical reactions in the flame. The general processes involved in the synthesis of nanoparticles are discussed in detail by Janzen et al. [70], Roth [167], Knipping et al. [89], Kammler et al. [76] and Wegner et al. [212], amongst others. The processes in the synthesis of nanoparticles from spray flames are discussed in detail by Mädler et al. [113], Mueller et al. [129], Strobel and Pratsinis [183], Mädler et al. [191], and others. The major advantages of the spray flame synthesis are a simple precursor handling and supply and that it overcomes the limits of different partial pressures of the precursors. The focus of this thesis is on the nanoparticle synthesis from spray flames and hence this process is discussed in more detail below.

The spray flame pyrolysis process may be separated into three main zones [165, 214], as outlined in Fig. (1.1). A liquid precursor/solvent mixture is injected into a combustion chamber, dispersed and atomized by an oxidizer coflow and evaporated by a secondary heat source in zone A. The secondary heat source is usually provided by a pilot flame, which ignites the precursor/solvent vapor and subsequently stabilizes the main flame in zone B. Furthermore in zone B, the precursor is decomposed and the nanoparticle monomers are released, which nucleate, coagulate and coalesce in zone C. The processes in zones A to C are instantaneous, depend highly non-linearly on the process parameters such as temperature or pressure and happen simultaneously [165, 214]. More details on the involved processes and their modelling is presented in the following chapters.

To optimize the production processes for the synthesis of nanoparticles, a detailed understanding of the physical and chemical phenomena is crucial. Experiments and numerical simulations are the basis to improve the understanding of the aforementioned processes. In contrast to experiments, simulations are often cheaper and enable a detailed spatial and temporal insight into the processes involved in the flow dynamics, the spray formation, the combustion processes and the particle dynamics simultaneously.

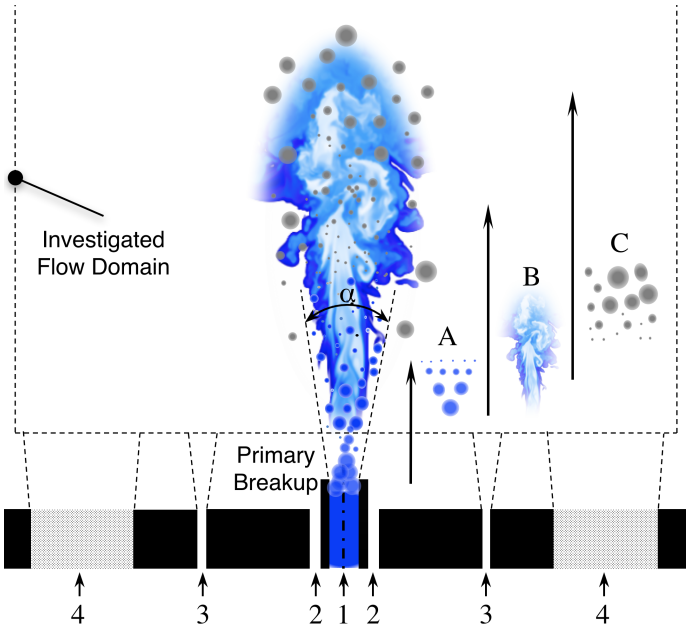

Figure 1.1: Sketch of a spray flame burner with zone A for the spray formation, zone B for turbulent combustion and zone C for the particle synthesis.

1.2 Aim of the thesis

The aim of this work is to improve the understanding of the particle synthesis from spray flames by numerical investigations in the context of large eddy simulations (LES). The major advantage of the LES methodology is the fact that it resolves the unsteady gas phase velocity, the thermochemical properties of the mixture (e.g. species mass fractions or temperature) and the resulting nanoparticle fields, which again depend highly non-linearly on the aforementioned processes. In contrast to the Reynolds Averaged Navier-Stokes (RANS) simulation approach, the probability density functions (PDF) of the gas phase properties, thermochemical properties and nanoparticle properties result directly from solving the Favre filtered conservation equations instead of the temporally averaged equations (except the sub-filter distribution, which need further modelling). In the RANS approach, the PDF of the gas-, chemical- and particle properties must be modelled. In the presented work, the evolution of the particle properties and the corresponding particle size distributions are discussed based on spatially and temporally resolved results.

Therefore, the LES methodology that resolves the unsteady flow field and the major turbulence effects is combined with the flamelet generated manifold approach (FGM or PFGM for premixed flamelet generated manifold approach) and the artificially thickened flame method (ATF) and three population balance equation models (PBE) and has been used for the first time to investigate numerically the nanoparticle synthesis from spray flames. Important steps during this thesis were a modification of the PFGM/ATF approach to account for spray combustion and three feed systems and to formulate and implement the PBE models for the LES methodology. The suitability, validity and correctness of implementation of the modified PFGM/ATF approach for spray combustion is shown for a well investigated lab-scale burner, the Sydney piloted diluted spray flame reactor [57]. The validity and suitability of the PBE models for cases with simultaneous nucleation, coagulation, coalescence and mixing is shown for a well investigated generic test case, the synthesis of titania particles from the gas phase synthesis [180]. Subsequently the developed methods have been applied to investigate the particle synthesis in different spray reactors.

1.3 Structure of the thesis

This thesis consists of ten chapters which are briefly summarized below.

In the subsequent chapter 2, the theoretical background, relevant for the presented work, is discussed. The balance equations for mass, momentum, energy and species together with the state equations are outlined first, followed by the fundamentals of turbulence, combustion and spray processes. The last section of chapter 2 gives a detailed overview about the population balance equations describing the particle synthesis from the gas phase.

Chapter 3 gives an overview on the available models and focuses on the models used to simplify the fundamentals introduced before. Firstly, the turbulence models are discussed. Secondly, models describing combustion and the modifications proposed to the standard combustion model are outlined. The approximation of the population balance equation for the particle synthesis from the gas phase is finally outlined for the applied models.

The numerical solution methods for the convective, diffusive, and temporal terms are discussed in chapter 4. The application of the developed and implemented models is presented in chapters 5-9, which have been submitted and published in international journals and presented on conferences.

Chapter 5 is the numerical study of the Sydney piloted spray burner, to which the developed combustion model was applied as a first but thorough test in spray combustion. Chapter 6 is about the application of the developed models to describe the synthesis of silica particles from a hexamethyl/ethanol spray flame with the simple monodisperse PBE model and to our knowledge the first such LES ever conducted. The findings of the studies performed in chapter 6 triggered detailed investigations about the validity and performance of the monodisperse, bimodal and sectional model for the gas phase synthesis of nanoparticles based on a numerical reference case. A mixing case was designed and investigated as discussed in chapter 7. The developed and implemented combustion and PBE models, i.e. the modified flamelet generated manifold model and the sectional- and monodisperse particle models have been applied to study numerically the formation and evolution of iron-oxide and silica particles, which is discussed in chapter 8 and chapter 9.

Chapter 2
Theoretical Background

The physics of the investigated fluid flow, spray, combustion and nanoparticle synthesis phenomena are explained in chapter 2 − based on their basic equations. The flow of a reactive multiphase system may be described by different approaches, in the present work an Eulerian-Lagrangian-Eulerian approach has been used to describe the gas phase, liquid phase and nanoparticle phase, respectively.

2.1 Fluid flow

The motion of gases and liquids, the fluid flow, is of great importance in nature, science and applications such as internal combustion engines, gas or steam turbines, synthesis reactors and many more. The theoretical description of the fluid flow relevant in the scope of this thesis is based on the assumption that the fluid can be treated as continuum or as continuous and Newtonian, i.e. the viscous stresses of the fluid are linearly proportional to the local strain rate. Based on the continuum assumption the properties of the gas phase (e.g. density, temperature or velocity) at one point are assumed to be continuous, neglecting the molecular structure of the gas phase. The fluid flow of a reacting gas, here treated by an Eulerian framework, is then adequately described by a set of coupled partial differential equations (PDE) for mass, momentum, energy and species.

2.1.1 Conservation equations

2.1.1.1 Conservation of mass

Assuming that atoms can neither be destroyed nor created, the change of mass is described by the conservation equation for mass, Eq. (2.1), which is also known as continuity equation (in this work of the gas phase):

$$\frac{\partial \rho}{\partial t} + \frac{\partial \rho u_j}{\partial x_j} = \dot{\Gamma}_\rho. \tag{2.1}$$

The change of density ρ in Eq. (2.1) is governed through convective transport by the velocity field, where u_j is the velocity vector in index notation with $j =\in \{1, 3\}$. The spatial location is described by the spatial position vector x_j also in index notation. Furthermore, the source term $\dot{\Gamma}_\rho$ in Eq. (2.1) accounts for the exchange of mass from the spray to the gas phase, due to evaporating spray droplets.

2.1.1.2 Conservation of momentum

The change of the velocity and hence of the location of a fluid continuum, can only be achieved in response to forces acting upon the fluid. The conservation of the momentum as outlined in Eq. (2.2), results from applying Newton's second law of motion to a fluid.

$$\frac{\partial \rho u_i}{\partial t} + \frac{\partial \rho u_i u_j}{\partial x_j} = +\frac{\partial \mathrm{T}_{ij}}{\partial x_j} + S_V + S_A \tag{2.2}$$

In the previous equation, the two terms on the left hand side (LHS) are the accumulation of the momentum (ρu_i) and its convection, respectively. The terms on the right hand side (RHS) of Eq. (2.2) are the stress tensor T_{ij}, the term S_V summarizes the volume forces (e.g. gravitational force

$S_V = \rho g_i$) and S_A are additional forces, for example a source term due to momentum exchange between different phases. The stress tensor T_{ij} depends on the fluid properties and is, in the scope of this work, given for a Newtonian fluid. T_{ij} is the sum of the pressure and the viscous stress tensor τ_{ij} as outlined in Eq. (2.3).

$$\mathrm{T}_{ij} = -\delta_{ij} p + \tau_{ij} \tag{2.3}$$

The Kronecker delta δ_{ij} equals 1 for $i = j$ and 0 for $i \neq j$. The viscous stresses τ_{ij} are determined from the dynamic viscosity μ and the strain rate of the fluid as described by Eq. (2.4), (for Newtonian fluids, the viscous stresses are proportional to the strain rate of the flow).

$$\tau_{ij} = \mu \left(\frac{\partial u_i}{\partial x_j} + \frac{\partial u_j}{\partial x_i} \right) - \mu \frac{2}{3} \frac{\partial u_k}{\partial x_k} \delta_{ij} \tag{2.4}$$

Substituting Eq. (2.4) and (2.3) into Eq. (2.2) yields the final transport equation for momentum of a Newtonian fluid as outlined in Eq. (2.5). This is the well known Navier-Stokes equation, which contains the information on all scales of the (continuous) fluid motion.

$$\frac{\partial \rho u_i}{\partial t} + \frac{\partial \rho u_i u_j}{\partial x_j} = -\frac{\partial p}{\partial x_i} + \frac{\partial}{\partial x_j} \left(\mu \left(\frac{\partial u_i}{\partial x_j} + \frac{\partial u_j}{\partial x_i} \right) - \mu \frac{2}{3} \frac{\partial u_k}{\partial x_k} \delta_{ij} \right) + \rho g_i + \dot{S}_M \tag{2.5}$$

The last term on the RHS of Eq. (2.5) $\dot{S}_M$ expresses the exchange of momentum between the gas and liquid phase. Equation (2.5) is used in laminar flows directly and as basic equation for further turbulence modelling, which is discussed in chapter 3.

2.1.1.3 Conservation of species

The composition of a gas can be described by the mass fractions Y_α of all constituent species α in the gas. This mass fraction is defined as the ratio of the mass m_α of species α, with respect to the total mass of all species m_t as outlined in Eq. (2.6).

$$Y_\alpha = \frac{m_\alpha}{m_t} = \frac{m_\alpha}{\sum_{i=1}^{N_S} m_i} \tag{2.6}$$

In the previous equation, N_S indicates the number of species. For cases where mixing occurs but also for reacting cases, which are of more interest in the present work, the evolution of the gas composition is of major importance to accurately describe the thermochemical properties of the system. The evolution of the mass fractions Y_α is described by their transport equations:

$$\frac{\partial \rho Y_\alpha}{\partial t} + \frac{\partial \rho Y_\alpha u_j}{\partial x_j} = \frac{\partial}{\partial x_j} \left(\rho D_{\alpha,\beta} \frac{\partial Y_\alpha}{\partial x_j} \right) + \dot{\omega}_\alpha + \dot{\omega}_E. \tag{2.7}$$

The two terms on the LHS of Eq. (2.8) represent the accumulation of Y_α and its convection by the gas phase velocity. The first term on the RHS is the change of Y_α by diffusion, where the diffusivity of species α into the surrounding fluid species β is described by the binary diffusion coefficient $D_{\alpha,\beta}$, applying Fick's law for the diffusive flux $J_\alpha = -D_{\alpha,\beta} \frac{\partial \phi}{\partial x_i}$. A common approach is to describe the diffusivity $D_{\alpha,\beta}$ by the non-dimensional Schmidt number Sc, which relates the individual diffusivity of species α to the viscosity of the mixture $\mathrm{Sc}_\alpha = \frac{\mu}{\rho D_{\alpha,\beta}}$. Substituting Sc into Eq. (2.6) yields the equation below.

$$\frac{\partial \rho Y_\alpha}{\partial t} + \frac{\partial \rho Y_\alpha u_j}{\partial x_j} = \frac{\partial}{\partial x_j} \left(\frac{\mu}{\mathrm{Sc}_\alpha} \frac{\partial Y_\alpha}{\partial x_j} \right) + \dot{\omega}_\alpha + \dot{\omega}_E \tag{2.8}$$

The source terms $\dot{\omega}_\alpha$ and $\dot{\omega}_E$ in Eq. (2.8) account for the change of Y_α due to chemical reactions and due to evaporation. (Further source terms for Y_α could arise due to nucleation or condensation, which are neglected at this point of the work). The description of the aforementioned source terms is discussed in sections 2.3 and 2.4, respectively. The transport equation (2.8) as previously discussed is the basis for the modelling of the combustion progress variable as discussed in chapter 3.

2.1.1.4 Conservation of energy

Additionally to the aforementioned transport equations for mass, momentum and species, a further transport equation is needed to describe the energy in the system. In this work the energy equation is not solved explicitly, assuming adiabatic conditions. However, in this subsection the conservation equation for the mean enthalpy of the mixture, the sum of the sensible enthalpy h_s and the heat of formation h_c, is discussed:

$$h = h_s + h_c \tag{2.9}$$

$$h_s = \sum_{\alpha=1}^{N_s} \int_{T_0}^{T} Y_\alpha c_{p,\alpha} dT \tag{2.10}$$

$$h_c = \sum_{\alpha=1}^{N_s} Y_\alpha \Delta h_{f,\alpha}^\circ. \tag{2.11}$$

In Eq. (2.10), the sensible enthalpy h_s is calculated as the sum of the individual sensible enthalpies of each species α, where $c_{p,\alpha}$ is the specific heat capacity of species α at constant pressure. The heat of formation of the mixture h_c is determined according to Eq. (2.11) as the sum of the enthalpy change of formation Δh_f° for each species. The conservation equation for the mean enthalpy is outlined in Eq. (2.12).

$$\frac{\partial \rho h}{\partial t} + \frac{\partial \rho h u_j}{\partial x_j} = \frac{\mathrm{Dp}}{\mathrm{Dt}} - \frac{\partial q_j}{\partial x_j} + \tau_{ij} \frac{\partial u_i}{\partial x_j} + \dot{Q} + \rho \sum_{\alpha=1}^{N_s} Y_{\alpha,j} f_{\alpha,j} J_{\alpha,j} \tag{2.12}$$

The first two terms on the LHS of Eq. (2.12) are the accumulation and convection of the enthalpy. The term $\frac{\partial q_j}{\partial x_j}$ represents the heat or enthalpy flux, the pressure term (Dp/Dt) is set to zero for assuming a constant pressure within the flame, which is a good approximation for flames in open devices at low Mach numbers. Furthermore, the change of enthalpy due to viscous heating ($\tau_{ij} \frac{\partial u_j}{\partial x_j}$) in Eq. (2.12), is small compared to the other terms especially in low Mach number cases, and hence it may be neglected. The volume sources, such as radiation are also neglected in the present work. Simplifying Eq. (2.12) with the aforementioned assumptions yields the transport equation for the mean enthalpy:

$$\frac{\partial \rho h}{\partial t} + \frac{\partial \rho h u_j}{\partial x_j} = -\frac{\partial q_j}{\partial x_j} + \dot{Q} + \rho \sum_{\alpha=1}^{N_s} Y_{\alpha,j} f_{\alpha,j} J_{\alpha,j}. \tag{2.13}$$

A good overview of the transport equations for the energy in their different forms is given by Poinsot and Veynante [151].

2.1.2 Equations of state

The pressure p and the viscosity μ appear in the previous equations in an unclosed form. A common way to determine these quantities are the equations of state, which relate the gas properties for given physical conditions. In this work, the assumption of an ideal gas is made, and hence the pressure and the density are correlated based on the temperature T, universal gas constant R_m and the mean molecular weight of the gas W according to the ideal gas law and is outlined below.

$$p = \rho \frac{T R_m}{W} \tag{2.14}$$

The gas mean molecular weight W is computed from the mass fractions Y_α of species α and the corresponding molecular weights W_α:

$$W = \left(\sum_{\alpha=1}^{N_s} \frac{Y_\alpha}{W_\alpha} \right)^{-1}. \tag{2.15}$$

The Mach number Ma relates the gas phase velocity u to the speed of sound c and is the criteria to choose the numerical solution method.

$$\mathrm{Ma} = \frac{u}{c} \tag{2.16}$$

(Usually for $\mathrm{Ma} < 0.3$ an incompressible solution method is sufficient, whereas for $\mathrm{Ma} > 0.3$ a compressible numerical method has to be used.) For an ideal gas, the speed of sound c can be calculated from the heat capacity ratio $\gamma = c_p/c_v$, the universal gas constant R_m, the temperature T and the molecular weight W.

$$c = \sqrt{\gamma \frac{R_m T}{W}} \tag{2.17}$$

The averaged viscosity of the gas may be determined from the molar fraction X and viscosity μ of species α (with $X_\alpha = Y_K W/W_\alpha$) according to Eq. (2.18) as proposed by Wilke [218] and adapted by Bird et al. [14].

$$\begin{aligned} \mu &= \sum_{\alpha=1}^{N_s} \frac{X_\alpha \mu_\alpha}{\sum_{\beta=1}^{N_s} X_\beta \phi_{\alpha\beta}} \qquad \text{with} \\ \phi_{\alpha\beta} &= \frac{1}{\sqrt{8}} + \left(1 + \frac{W_\alpha}{W_\beta}\right)^{-\frac{1}{2}} \left(1 + \left(\frac{\mu_\alpha}{\mu_\beta}\right)^{\frac{1}{2}} \left(\frac{W_\alpha}{W_\beta}\right)^{\frac{1}{4}}\right)^2 \end{aligned} \tag{2.18}$$

Due to the high numerical cost of calculating the viscosity based on Eq. (2.18), it may be sufficient to determine μ based on the polynomial fit as proposed by Sutherland [187] according to

$$\mu = \mu_0 \frac{T_0 + S}{T + S} \left(\frac{T}{T_0}\right)^{\frac{2}{3}}. \tag{2.19}$$

In Eq. (2.19), μ_0 and T_0 are the mixture viscosity and temperature at a reference point and S denotes a fitting constant. In this work, the gas viscosity is determined prior to the CFD simulations by solving a set of 1D flamelets and is stored as a function of two or three control variables in a multidimensional look-up table, as will be discussed later.

2.2 Turbulence

Flows where the fluid parcels follow a structured pattern, where the exchange of momentum between the streams normal to the main flow direction is small and where no eddies occur is called *laminar flow*. In turbulent flows, a fluid parcel exhibits random, three dimensional, chaotic motion with changing velocity from point to point, and changing velocity at one point from time to time. Furthermore in a turbulent flow the exchange of momentum normal to the main flow direction is large as compared to a laminar flow. Reynolds found the relation between the inertial forces and the viscous forces in a fluid flow to be critical and introduced the non-dimensional number, that was later named Reynolds number [160]: the ratio of inertial forces to viscous forces that is used to differentiate laminar from turbulent flows, Eq. (2.20).

$$\mathrm{Re} = \frac{\rho \mathrm{uL}}{\mu} \tag{2.20}$$

In Eq. (2.20), ρ and μ are the material properties of the fluid, i.e. density and viscosity respectively, u and L are a characteristic flow velocity and length, e.g. the diameter of a pipe or length of a plate. Most of the flow problems in real applications are found to be turbulent for different reasons, either high velocities cannot be avoided or the devices are large. In combustion processes,

turbulence is desired to increase mixing and hence the global rate of chemical conversion and heat release and to reduce the size of the combustion chamber. The fluid flow with all flow regimes (laminar, transitional and turbulent) is completely described by the equations introduced in this chapter so far. However, no algebraic solutions have been found for the Navier-Stokes equations (except for very simple problems). Therefore, numerical solutions are necessary to solve the flow problems, the related difficulties are discussed in chapter 3.1.
A common approach to describe turbulence are statistical methods. Even though the local flow velocities change in time due to turbulence, many flows are assumed to be statistically stationary, i.e. the probability density function (PDF) at one point does not change with respect to time. Osborne Reynolds proposed to decompose the velocity into its mean and fluctuating part, $\overline{u}_i$ and u_i' respectively, which is known as the Reynolds decomposition [161].

$$u_i(t) = \overline{u}_i + u_i'(t) \tag{2.21}$$

More general for an arbitrary quantity ϕ it can be written:

$$\phi(t) = \overline{\phi} + \phi'(t). \tag{2.22}$$

The mean value $\overline{\phi}$ of an arbitrary quantity ϕ is defined via the integral within the time interval t_0 to $t_0 + T$ in the limit of T approaching infinity:

$$\overline{\phi} = \lim_{T\to\infty} \frac{1}{T} \int_{t_0}^{t_0+T} \phi dt \tag{2.23}$$

Besides the mean values, also the root mean square (rms) or standard deviation, is commonly used to describe the extent of turbulence. The rms of ϕ is defined according to Eq. (2.24).

$$\phi_{rms}^2 = \overline{\phi'^2} = \lim_{T\to\infty} \frac{1}{T} \int_{t_0}^{t_0+T} \left(\phi - \overline{\phi}\right)^2 dt \tag{2.24}$$

In fluid flows, a portion of the energy contained in the flow is converted into heat due to the molecular viscosity of the fluid. In turbulent flows the amount of energy dissipated into heat is increased, compared to laminar flows due to the impact of the increased viscous shear stresses. The energy contained in the velocity fluctuations is the turbulent kinetic energy k, which is defined according to Eq. (2.25).

$$k = \frac{1}{2}\overline{u_i' u_i'} \tag{2.25}$$

The dissipation of the energy occurs on the smallest scales, the Kolmogorov scales η, where the viscosity of the fluid is dominant as assumed by Kolmogorov [90]. In his theory, Kolmogorov relates the length scale of the smallest turbulent eddies η to the viscosity of the fluid and to the average rate of dissipation ϵ.

$$\eta = \left(\frac{\nu^3}{\epsilon}\right)^{\frac{1}{4}} \tag{2.26}$$

The smallest scales η depend on the fluid viscosity ν (here given as kinematic viscosity) and on the energy introduced to the system. The size of η has an important impact on the amount of the un-resolved (by a simulation) velocity fluctuations as it will be discussed in chapter 3.

A classical approach to outline the energy contained in the velocity fluctuations is the energy spectrum of turbulence. Figure (2.1) illustrates the energy spectrum of a turbulent flow, which shows the energy E contained in the velocity fluctuations as a function of the wavenumber k. The wavenumber represents the inverse length scale of a turbulent flow. The energy is introduced to the „energy containing eddies“, i.e. on the largest scales and is transfered from the energy

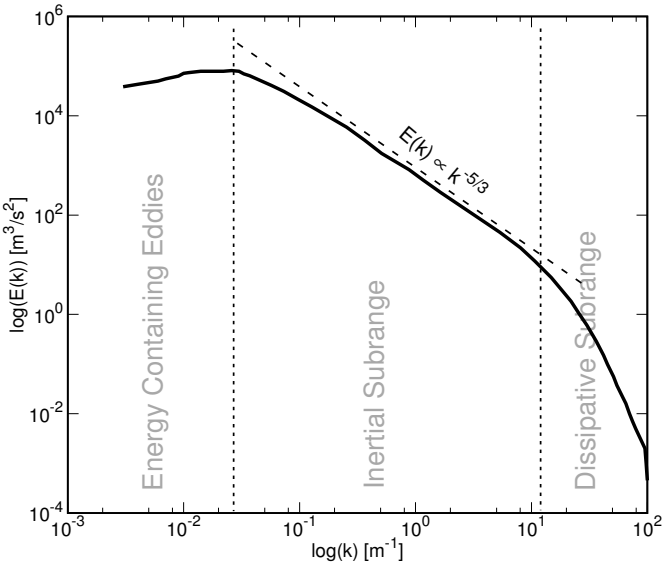

Figure 2.1: Classical illustration of the energy spectrum of turbulence.

of the main flow. Hence, a constant energy supply must be provided to the main flow. In the inertial subrange the energy is transfered down the energy cascade from the larger eddies to the smaller eddies, and a power law is found, where the energy is proportional to the wavenumber $E \propto k^{-5/3}$, the famous five-third-law. Finally the energy is dissipated on the smallest scales in the dissipative subrange.

2.3 Combustion

Combustion refers to a high temperature exothermic chemical reaction between fuel and oxidizer and is used to convert the chemically bound energy of a fuel into heat. This chemical reaction of fuel and oxidizer may be described by a one step global reaction as shown below for methane CH_4 and oxygen O_2.

$$CH_4 + 2O_2 \rightarrow CO_2 + 2H_2O \tag{2.27}$$

In reality the formation of combustion products, water H_2O and carbon dioxide CO_2, follows a complex and random formation path with many intermediate species and elementary reactions. The number of intermediate species and reactions depends strongly on the fuel.
In the present work, methane and ethanol have been used as fuel and carrier for the precursors hexamethyldisiloxane (HMDSO) or iron-penthacarbonyl (IPC). The corresponding reaction mechanism GRI-3.0 [177] for methane and the mechanism proposed by Marinov [118] for ethanol consider 53 and 56 species with 325 and 351 elementary reactions (for methane/ethanol). Additionally to the standard reaction mechanism for methane and ethanol, further reactions have been added to the reaction mechanisms to describe the oxidation of $C_6H_{18}OSi_2$ (HMDSO) and the formation of silica particles SiO_2 [42, 165] or iron-oxide Fe_2O_3.

2.3.1 Reaction kinetics

Considering that the reaction can be forward and backward, two arbitrary species A and B form the new species AB and vice versa as indicated by the reaction below.

$$A + B \rightleftharpoons AB \tag{2.28}$$

Commonly, the elementary bidirectional reactions for a large number of species N_s and reactions N_r may be written for reaction k as

$$\sum_{\alpha=1}^{N_s} \nu'_{\alpha,k}\chi\alpha \rightleftharpoons \sum_{\alpha=1}^{N_s} \nu''_{\alpha,k}\chi\alpha, \tag{2.29}$$

where χ_α is the symbol for the chemical species α and $\nu'_{\alpha,k}$ and $\nu''_{\alpha,k}$ indicate the stoichiometric coefficients of the forward and backward reactions, respectively. The reaction rate r of reaction k indicates the speed at which reaction k progresses. As forward and backward reactions are considered, the resulting reaction rate is the difference between the forward and backward reaction rates as outlined below.

$$r_k = r_{k,f} - r_{k,b} = q_{k,f} \prod_{\alpha=1}^{N_s} c_\alpha^{\nu'_{\alpha,k}} - q_{k,b} \prod_{\alpha=1}^{N_s} c_\alpha^{\nu''_{\alpha,k}} \tag{2.30}$$

In Eq. (2.30), $c_\alpha = \rho Y_\alpha / W_\alpha$ and q indicate the molar concentration of species α and the reaction rate constant, respectively. Furthermore the reaction rate constants are calculated based on an Arrhenius equation as outlined in Eq. (2.31).

$$q = AT^n \exp\left(-\frac{E}{TR_m}\right) \tag{2.31}$$

In the previous equation A, T, E and R_m indicate the pre-exponential constant, the temperature, the activation energy and the universal gas constant, respectively. (More complex formulations are used for pressure dependent and fall of reactions.)
The chemical source term in the transport equation for species α, Eqs. (2.7, 2.8), is then calculated from the reaction rate r, the molar mass W and the stoichiometric coefficients $\nu'_{\alpha,k}$ and $\nu''_{\alpha,k}$ as outlined by Eq. (2.32).

$$\dot{\omega}_\alpha = W_\alpha \sum_{k=1}^{N_r} \left(\nu''_{\alpha,k} - \nu'_{\alpha,k}\right) r_k \tag{2.32}$$

The chemically reacting flow system can now be described with the chemical equations, the introduced transport equations for mass, momentum, species and energy Eqs. (2.1, 2.5, 2.8, 2.13), and the equations of state.

2.3.2 Modes of combustion

In many combustion applications fuel and oxidizer are first "premixed" and then fed into the combustion chamber, or they are supplied separately and "non-premixed" into the combustor. Both modes permit different modelling assumptions, that must be relaxed for partially premixed combustion.

2.3.3 Non-premixed combustion

In non-premixed or diffusion flames, oxidizer and fuel enter the flame region separately and reactant molecules have to diffuse into the reaction zone first before they can react to products. Due to the fact that the time scale of the reaction is much smaller than the time scale of the molecular diffusion, combustion is assumed to be mixing controlled in the non-premixed combustion regime. In the majority of applications based on non-premixed configurations, the flame cannot propagate against the main flow direction and is therefore easier to control and safer as premixed configurations, and as a consequence, non-premixed configurations are used in many applications. However, the disadvantage of non-premixed combustion is a higher emission of pollutants and a

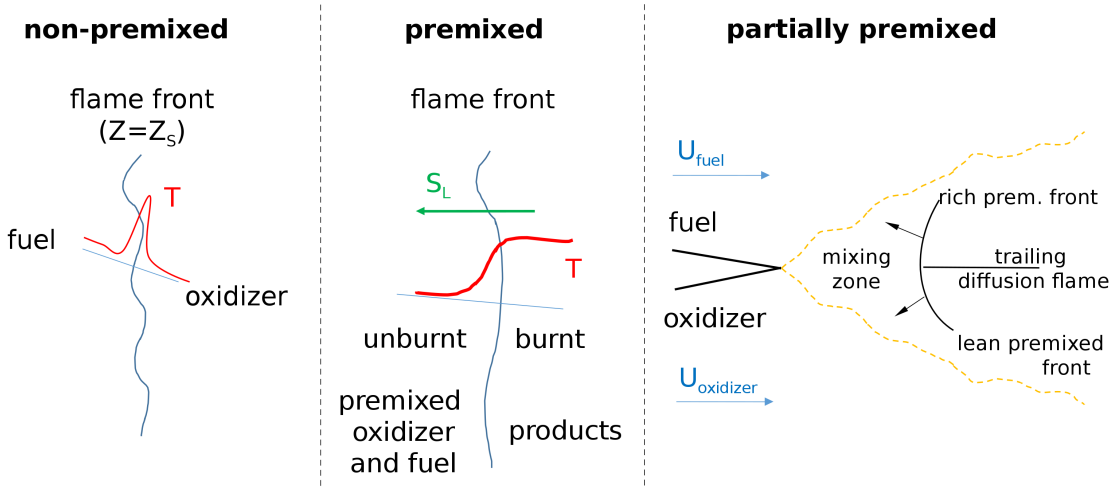

Figure 2.2: Illustration of the flame fronts in non-premixed-, premixed- and partially premixed modes of combustion (from left to right).

reduced efficiency in comparison to premixed flames.

The mixture fraction is a measure for the mixture between fuel and oxidizer. Different definitions of the mixture fraction have been proposed, e.g. based on the different mass fluxes ($\dot{m}_1$ and $\dot{m}_2$) in a two feed system [151] as given in the equation below.

$$Z = \frac{\dot{m}_1}{\dot{m}_1 + \dot{m}_2} \tag{2.33}$$

As the mass of a chemical species changes in a reaction, a more general way to describe the mixture is the element mass fraction Z_α, which is related to the mass of chemical species α and is conserved during combustion [144].

$$Z_\alpha = \frac{m_\alpha}{m} = \sum_{\beta=1}^{N_s} a_{\beta\alpha} \frac{W_\alpha}{W_\beta} Y_\beta \tag{2.34}$$

In Eq. (2.34), the number of atoms α in molecule β is given by $a_{\beta\alpha}$, the atomic and molecular weights by W_α and W_β, and Y_β is the mass fraction of species β, respectively. The spatial and temporal evolution of Z_α is described by its transport equation as outlined in Eq. (2.35).

$$\frac{\partial \rho Z_\alpha}{\partial t} + \frac{\partial \rho Z_\alpha u_j}{\partial x_j} = \frac{\partial}{\partial x_j}\left(\rho D \frac{\partial Z_\alpha}{\partial x_j}\right) + \dot{\omega}_{Z_\alpha} \tag{2.35}$$

A further common (normalized) definition of the mixture fraction for hydro-carbon fuels was proposed by Bilger [13] and is based on the element mass fractions of carbon Z_C, hydrogen Z_H and oxygen Z_O as outlined by Eq. (2.36).

$$Z = \frac{Z_C/(mW_C) + Z_H/(nW_H) + 2(Y_{O_2,u} - Z_O)/(\nu'_{O_2} W_{O_2})}{Z_{C,1}/(mW_C) + Z_{H,1}/(nW_H) + 2Y_{O_2,u}/(\nu'_{O_2} W_{O_2})} \tag{2.36}$$

For this mixture fraction, a transport equation may be solved to describe the mixing in a system, as given by Eq. (2.37).

$$\frac{\partial \rho Z}{\partial t} + \frac{\partial \rho Z u_j}{\partial x_j} = \frac{\partial}{\partial x_j}\left(\rho D \frac{\partial Z}{\partial x_j}\right) + \dot{\omega}_Z \tag{2.37}$$

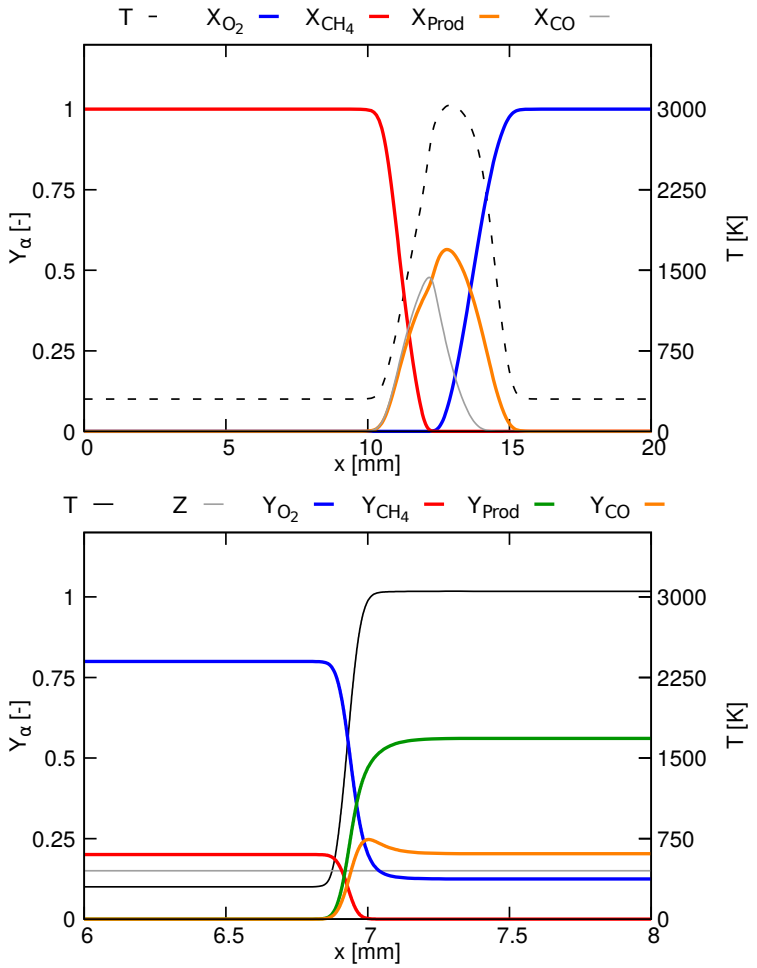

Figure 2.3: Axial profiles of the temperature, methane-, oxygen-, products- and intermediate carbon monoxide mass fractions for a non-premixed (top) and premixed (bottom) methane oxygen flame.

In the transport equations (2.35, 2.37) for Z_α and Z, a unity Lewis number assumption (Le = 1) has been applied and the source terms $\dot{\omega}_{Z_\alpha}$ and $\dot{\omega}_Z$ account for the exchange of mass due to evaporation. In the present work both definitions of the mixture fraction, the element mass fraction and the mixture fraction according to Bilger, have been used. The equivalence ratio is also used to specify the composition of the mixture and is defined according to the equations below.

$$\phi = \frac{(m_{f,u}/m_{o,u})}{(m_{f,u}/m_{o,u})_S} \qquad \text{or} \qquad \phi = \frac{(\mathrm{Y_{f,u}}/\mathrm{Y_{o,u}})}{(\mathrm{Y_{f,u}}/\mathrm{Y_{o,u}})_\mathrm{S}} \tag{2.38}$$

This equivalence ratio relates the fuel to oxidizer ratio to the stoichiometric fuel to oxidizer ratio.

2.3.4 Premixed combustion

In contrast to non-premixed combustion, in premixed combustion fuel and oxidizer are mixed before they enter the combustion zone. One of the most important quantities describing the evolution of a premixed flame is the flame speed, S_L depends on the reaction rate of the chemical species. In a stagnant mixture the flame front propagates with the burning velocity S_L into the unburnt mixture, which depends on the fuel and oxidizer species, the equivalence ratio, the pressure strain, and the temperature of the unburnt mixture, respectively. In one dimensional premixed flame calculations the laminar burning velocity may be defined according to Eq. (2.39)

[144] and can be calculated by solving a detailed or reduced reaction mechanism with a chemistry library, e.g. Cantera [56] as used in this work.

$$\left(\rho S_L^0\right)_u = (\rho u)_{-\infty} \tag{2.39}$$

The laminar thermal flame thickness δ_{th} as used in this work is determined from the burnt and unburnt temperature and the maximum temperature gradient in the 1D flame according to the equation below.

$$\delta_{th} = \frac{T_b - T_u}{\max\left|\frac{\partial T}{\partial x}\right|} \tag{2.40}$$

Due to the fact that reactants are available at the same location in premixed flames, the laminar flame thickness is much smaller in comparison to a non-premixed flame (compare Fig. 2.3 left and right). The progress of combustion may be described and determined by a reaction progress variable Y_P or the normalized reaction progress variable C. The normalized reaction progress variable may be based on the temperature or mass fractions [151] according to Eq. (2.41).

$$C = \frac{Y - Y_u}{Y_b - Y_u} \qquad \text{or} \qquad \mathrm{C} = \frac{\mathrm{T} - \mathrm{T_u}}{\mathrm{T_b} - \mathrm{T_u}} \tag{2.41}$$

The choice of the reaction progress variable Y_P depends on the investigated set-up, in the present work the progress variable is based on the product mass fractions: the sum of the species mass fractions of water, carbon dioxide, carbon monoxide and hydrogen (Eq. (2.42)) has been used for the spray flame simulations and the mass fractions of carbon dioxide and carbon monoxide (Eq. (2.43)) for the nanoparticle cases.

$$Y_P = Y_{H_2O} + Y_{CO_2} + Y_{CO} + Y_{H_2} \tag{2.42}$$

$$Y_P = Y_{CO_2} + Y_{CO} \tag{2.43}$$

Where any monotonic combination of mass-fractions can be used, it should be noted that Ihme proposed a formalism to determine the best suited reaction progress variable for a given constraint of parameters [67]. The transport equation for the progress variable Y_P is outlined by Eq. (2.44).

$$\frac{\partial \rho Y_P}{\partial t} + \frac{\partial \rho Y_P u_j}{\partial x_j} = \frac{\partial}{\partial x_j}\left(\rho D \frac{\partial Y_P}{\partial x_j}\right) + \dot{\omega}_{Y_P} + \dot{\omega}_E \tag{2.44}$$

Besides the accumulation, convection and diffusion term, the source terms $\dot{\omega}_{Y_P}$ and $\dot{\omega}_E$ on the RHS of Eq. (2.44) account for chemical reactions and the influence of evaporation on the reaction progress variable.

2.3.5 Partially premixed combustion

The flames in real applications usually do not follow the classical description for non-premixed or premixed flames. Partially premixed flames occur for instance in regions where non-premixed streams mix before the flame front, due to incomplete mixing in premixed flames, in flames with stratification or in spray flames and may be found in most technical systems, including IC engines, gas turbines and synthesis flames.

2.4 Spray

Generally, sprays are mixtures of liquid droplets dispersed in a surrounding gas and belong to the class of multiphase flows. Sprays are found in natural processes (e.g. sea-sprays, clouds, mist, ...) and in many technical applications, such as household burners, industrial furnaces,

internal combustion engines, gas turbines or chemical reactors. In the aforementioned technical applications, the purpose of the spray is to deliver the chemically bound energy of the fuel to the combustion chamber, with the advantage of a high power density, a simple supply and, for nanoparticle synthesis, of avoiding the limits of the partial pressures of different precursors. In the investigated spray flame reactors, the liquid fuel is also carrier for the liquid nanoparticle precursor, both are mixed first and subsequently fed to the combustion chamber. Different injection methods have been developed to generate sprays of specific properties. The sprays investigated in this work were generated by a) an ultrasonic nebulizer in the Sydney piloted spray burner [57] and by b) a pressurized nozzle in all other cases [113, 165].

2.4.1 Spray formation

The formation of spray droplets is classically described by the primary and secondary breakup. In the primary breakup the liquid core forms large and irregular filaments which break up further into smaller droplets in the secondary breakup. With the ultrasonic nebulizer, high frequency soundwaves are used to generate spray droplets, avoiding the necessity to account for primary and secondary breakup of the droplets in the models and leading to a relatively narrow size distribution of the droplets.
In the spray nozzles used in the investigated synthesis cases, a liquid fuel core is fed into the combustion chamber dispersed by a concentric oxidizer stream. In the atomization region, the liquid core undergoes primary and secondary breakup and forms subsequently more or less spherical droplets. These droplets are transported by the surrounding gas and vapor and are subsequently evaporated due to a heat of the spray flame or a secondary pilot flame. In the present work, the primary and secondary breakup have been neglected in the simulations of the Sydney piloted spray flame series as an ultrasonic nebulizer has been used to generate the spray droplets [57] upstream of the inflow plane of the simulation. Also in the simulations of the spray pyrolysis reactor the breakup has been neglected and only the dispersion and the evaporation of the droplets was considered. Therefore, the initial droplet size distribution in the simulations was taken from experiments [57], determined from a volume of fluid method [214], or estimated based on the median mass droplet diameter from experimental data [113].

2.4.2 Liquid phase dispersion and evaporation

The dispersion and evaporation is described based on simplifying assumptions, namely that a) the density of the gas phase is much smaller than the density of the spray, b) the droplets are spherical and that c) internal vortical flow of droplets is neglected. While the gas phase is described by an Eulerian specification of the flow field, the spray phase is described by a Lagrangian representation of the flow field, i.e. a set of ordinary differential equations for each droplet describes the evolution of the droplet location $x_{d,i}$, velocity $u_{d,i}$, acceleration $a_{d,i}$, mass m_d and temperature T_d, respectively.

The location of the droplets is determined from the droplet velocity $u_{d,i}$ in direction of i as outlined in the equation below.

$$\frac{\mathrm{dx_{d,i}}}{\mathrm{dt}} = u_{d,i} \tag{2.45}$$

The droplet velocity is determined from the droplet acceleration, which again is calculated from the drag, buoyancy and gravitational forces acting on the droplets.

$$\frac{\mathrm{du_{d,i}}}{\mathrm{dt}} = a_{d,i} = \frac{f_1}{\tau_d}\left(u_i - u_{d,i}\right) + \left(1 - \frac{\rho}{\rho_d}\right) g_i \tag{2.46}$$

In Eq. (2.46), τ_d, u_i, $u_{d,i}$, ρ, ρ_d and g_i denote the droplet relaxation time, the gas phase and droplet velocity, the gas phase and liquid density and the gravitational acceleration, respectively.

The droplet relaxation time τ_d for a Stokes flow is determined from the density of the liquid ρ_d, the droplet diameter d_d and the viscosity seen by the droplet μ_m according to Eq. (2.47).

$$\tau_d = \frac{\rho_d d_2^d}{18\mu_m} \tag{2.47}$$

The Schiller-Naumann correlation is used to determine the Stokes drag coefficient f_1 as outlined below [169].

$$f_1 = \begin{cases} 1 + \frac{3}{20}\mathrm{Re_d^{0.687}} & \text{for} \quad \mathrm{Re_d} \leq 1000 \\ 0.44\mathrm{Re_d}4 & \text{for} \quad \mathrm{Re_d} > 1000 \end{cases} \tag{2.48}$$

The droplet Reynolds number $\mathrm{Re_d}$ in Eq. (2.48) is determined according to Eq. (2.49).

$$\mathrm{Re_d} = \frac{\rho\,|\mathrm{u_i} - \mathrm{u_{d,i}}|\,\mathrm{d_d}}{\mu_\mathrm{m}} \tag{2.49}$$

The change of the droplet mass $\dot{m}_p$ is determined from the Schmidt and Sherwood numbers Sc and Sh, respectively, the mass of the droplet m_d and the Spalding number for mass transfer B_m according to Eq. (2.50).

$$\frac{\mathrm{dm_d}}{\mathrm{dt}} = -\frac{\mathrm{Sh}}{3\,\mathrm{Sc}}\frac{m_d}{\tau_d}\ln\left(1 + \mathrm{B_m}\right) \tag{2.50}$$

The Spalding mass transfer number B_m is determined from the fuel mass fraction at the droplet surface Y_F^S and the fuel mass fraction in the far field Y_F^S according to the equation below.

$$B_m = \frac{Y_F^S - Y_F^\infty}{1 - Y_F^\infty} \tag{2.51}$$

The mass fraction of the fuel vapor at the droplet surface is determined from the fuel molar fraction at the droplet surface X_F^S,

$$Y_F^S = \frac{X_F^S}{X_F^S + \left(1 - X_F^S\right)\frac{W_F}{W}}, \tag{2.52}$$

which may be determined with the Clausius-Clapeyron equation according to Eq. (2.53).

$$X_F^S = \exp\left[\frac{L_v}{R_m/W}\left(\frac{1}{T_b} - \frac{1}{T_d}\right)\right] \tag{2.53}$$

In the previous equation, L_v, T_b and T_d denote the latent heat of vaporization, as well as the boiling temperature of the liquid and the temperature of the droplet, respectively. The change of the droplet temperature is determined based on the infinite conductivity model, in which it is assumed that the temperature throughout the droplet is uniform but time-evolving, according to Eq. (2.54).

$$\frac{\mathrm{dT_d}}{\mathrm{dt}} = \frac{\mathrm{Nu\,c_p}}{3\,\mathrm{Pr\,c_{pl}}}\frac{(T_g - T_d)}{\tau_d}\frac{\ln\left(1 + \mathrm{B_h}\right)}{B_h} + \frac{\dot{m}_d L_v}{m_d\,c_{pl}} \tag{2.54}$$

In the previous equation, T_g denotes the temperature of the gas, Nu and Pr denote the Nusselt and Prandtl numbers, c_p and c_{pl} represent the specific heats at constant pressure of the gas and the liquid respectively, B_h is the Spalding number for heat transfer, respectively. The Spalding number for heat transfer is determined as outlined below.

$$B_h = \frac{c_p}{L_v}\left(T_g - T_d\right) \tag{2.55}$$

The Sherwood number, Sh and Nusselt number, Nu in Eqs. (2.50,2.54) account for the influence of the convective flow around the droplets and are calculated with the Ranz-Marshall correlation according to Eq. (2.56) and Eq. (2.57) [159].

$$\mathrm{Sh} = 2 + 0.552\mathrm{Re}^{\frac{1}{2}}\mathrm{Sc}^{\frac{1}{3}} \tag{2.56}$$

$$\mathrm{Nu} = 2 + 0.552\mathrm{Re}^{\frac{1}{2}}\mathrm{Pr}^{\frac{1}{3}} \tag{2.57}$$

The Prandtl number Pr and the Schmidt number Sc are determined from the viscosity μ, the specific heat at constant pressure c_p, the thermal conductivity λ and the diffusivity D a priori to the CFD simulations.

$$\mathrm{Pr} = \frac{\mu c_p}{\lambda} \qquad \text{and} \qquad \mathrm{Sc} = \frac{\mu}{\rho D} \tag{2.58}$$

The one third rule is applied to determine the temperature T_m, the mass fraction Y_m, the specific heat c_{pm} and the viscosity μ_m in the film ϕ_m from the corresponding droplet ϕ_d and far field properties ϕ_∞, according to equation for the arbitrary quantity ϕ_m.

$$\phi_m = \left(1 - \frac{1}{3}\right)\phi_d + \frac{1}{3}\phi_\infty \tag{2.59}$$

2.5 Nanoparticle synthesis

As outlined in the introduction, the production of nanoparticles may be characterized by two methods, namely the top-down method, where the particles are generated from a bulk material, and the bottom-up method, where the particles are generated from precursor molecules. In the top-down method, the particles are created by nano-structuring via e.g. laser-beam lithography [182], electro-beam-lithography [182] or photo-lithography [153]. Within the bottom-up method, there are several different production processes, e.g. the synthesis with the sol-gel method, where the particles are created from precursors solved in a solution [24], or the creation of particles from the vapor phase [189]. The synthesis of particles according to the bottom-up method plays a more important role in industrial production of particles as compared to the top-down method. The synthesis of nanoparticles from the vapor phase may be furthermore separated, depending on the state of the precursor [189], i.e. solid, liquid or gaseous. Processes to create nanoparticles from solid particles are e.g. inert gas condensation, pulsed laser ablation, spark discharge generation or ion sputtering. The precursors of interest in this work are in liquid and gaseous form.

The gaseous precursor is injected into an environment with a secondary heat source, the liquid precursor is usually solved in a combustible liquid fuel and is then also injected into a combustion chamber, evaporated and ignited by the secondary heat source. Subsequently, the first nanoparticles, i.e. monomer particles, are produced. The most dominant aerosol processes in the synthesis of particles from flames after particles have been nucleated, are coagulation (growth due to collisions of particles), sintering of particles, (coalescence or melting of two or more particles), and surface growth or condensation (accumulation of gas phase molecules or smaller particles on the surface of larger particles), as illustrated in Fig. 2.4 (right). The evolution of the particle population from the gas-phase, is described by the general dynamics equation (GDE) in the discrete or continuous form, which is derived and discussed in the following section. The GDE describes the evolution of particles by convective and diffusive transport, due to gas to particle conversion and further particle growth due to coagulation, coalescence, condensation or surface growth as illustrated in Fig. 2.4.

2.5.1 Particle conservation equations

A population of particles inside of a fixed physical domain V may be characterized by the size distribution function of the particle number or number concentration n, which have a certain

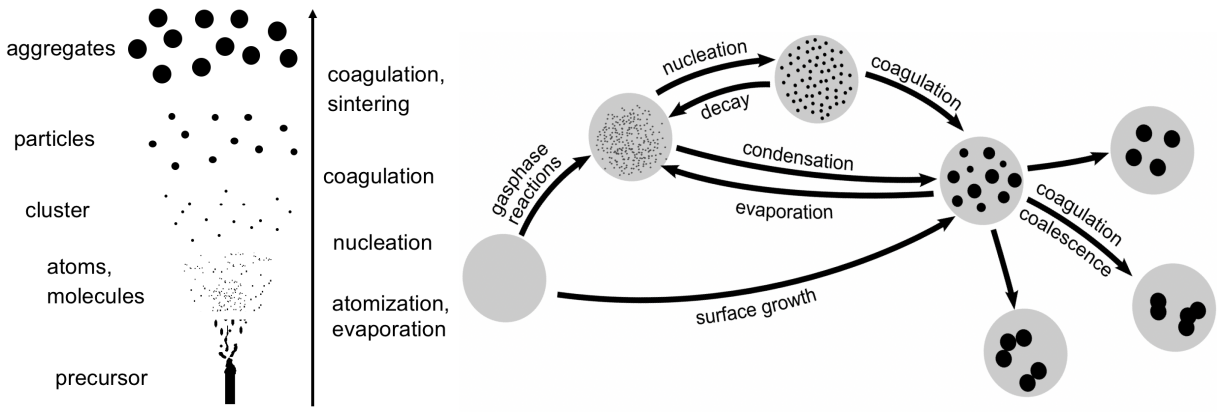

Figure 2.4: Illustration of the internal aerosol dynamical processes, left: the main processes in a spray flame (adapted from Weise [213])− from a liquid precursor to aggregates; right: detailed processes involved in the particle synthesis from the gas-phase − from a gaseous precursor to aggregates.

particle property, (here expressed by the particle volume) $n(v)$. The change of the particle population $n(v)$ inside its physical domain results from internal aerosol processes such as nucleation of new particles from gas phase molecules, condensation, coagulation or coalescence as illustrated in Fig. 2.5 left. In the following, the change of the particle population due to aerosol processes is summarized by the source term $\mathcal{I}$. Besides the aforementioned aerosol processes, the popula-

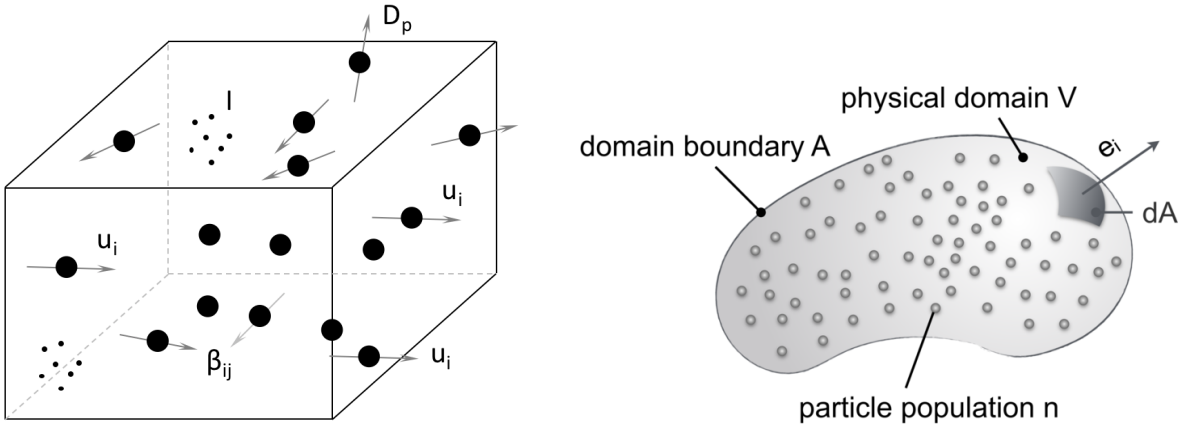

Figure 2.5: Illustration of particles inside a control volume (CV) (right), and an illustration of the aerosol processes inside the CV, (sketch adapted from Friedlander [49]).

tion $n(v)$ changes also due to transport processes, i.e. gas phase convection, particle diffusion, sedimentation or thermophoresis as shown in Fig. 2.5 (left). Considering aerosol and transport processes inside a fixed physical domain dV, the change of the particle size distribution function in time $\frac{\partial n}{\partial t}$ is described by the canonical conservation equation for the particle number concentration. This equation is derived by making a material balance on the fixed volume [49] (compare Fig. 2.5 right) and is outlined by Eq. (2.60).

$$\int_V \frac{\partial n}{\partial t} dV = -\int_A J_i e_i dA + \int_V \mathcal{I} dV. \tag{2.60}$$

The first term on the RHS describes the flux across the CV surface A, where J_i summarises the convective and diffusive flux of n normal to the CV area increment dA, with the normal vector

e_i. Applying Fick's law for diffusion, J_i is determined according to Eq. (2.61).

$$J_i = nu_i + \left(-D\frac{\partial n}{\partial x_i}\right) \tag{2.61}$$

According to Gauss' theorem, the total flux across the control surface is equal to the volume integral of the vectors divergence field.

$$\int_A J_i e_i dA = \int_V \frac{\partial J_i}{\partial x_i} dV \tag{2.62}$$

The second term on the RHS of Eq. (2.60) ($\int_V \mathcal{I} dV$) describes the change of the population n by nucleation, coagulation and coalescence, in this work condensation and surface growth are neglected as their impact is small in the investigated systems. Substituting Eqs. (2.61) and (2.62) into Eq. (2.60) yields the transport equation for the particle number concentration in integral form, as given by Eq. (2.63).

$$\int_V \frac{\partial n}{\partial t} dV + \int_V \frac{\partial n u_j}{\partial x_j} dV = \int_V \frac{\partial}{\partial x_j}\left(D\frac{\partial n}{\partial x_j}\right) dV + \int_V \mathcal{I} dV \tag{2.63}$$

Having only volume integrals in Eq. (2.63) and allowing the CV to get infinitesimally small, the transport equation for n in differential form is derived from the integral form and reads:

$$\frac{\partial n}{\partial t} + \frac{\partial n u_j}{\partial x_j} = \frac{\partial}{\partial x_j}\left(D\frac{\partial n}{\partial x_j}\right) + \mathcal{I}. \tag{2.64}$$

For incompressible flows and divergence free velocity fields ($\frac{\partial u_j}{\partial x_j} = 0$), the previous equation becomes:

$$\frac{\partial n}{\partial t} + u_j\frac{\partial n}{\partial x_j} = \frac{\partial}{\partial x_j}\left(D\frac{\partial n}{\partial x_j}\right) + \mathcal{I}. \tag{2.65}$$

2.5.1.1 Particle conservation equations with the gas phase density

In reactive flows, the gas phase density depends also on the temperature and can vary by one order of magnitude and should be considered in the conservation equations. To include the density in the conservation equation for the particle size distribution function, some mathematical treatments have to be applied to the accumulation, convection and diffusion terms as shown in the following section. Equation (2.65) is first multiplied with the gas phase density ρ what yields Eq. (2.66).

$$\rho\frac{\partial n}{\partial t} + \rho u_j\frac{\partial n}{\partial x_j} = \rho\frac{\partial}{\partial x_j}\left(D\frac{\partial n}{\partial x_j}\right) + \rho\mathcal{I} \tag{2.66}$$

The accumulation term including density Eq. (2.67) is obtained by applying the product rule and substituting the continuity equation ($\frac{\partial \rho}{\partial t} = -\frac{\partial \rho u_j}{\partial x_j}$) to the first term on the LHS of Eq. (2.66) as outlined below.

$$\frac{\partial \rho n}{\partial t} = \rho\frac{\partial n}{\partial t} + n\frac{\partial \rho}{\partial t} = \rho\frac{\partial n}{\partial t} - n\frac{\partial \rho u_j}{\partial x_j} \tag{2.67}$$

The convection term including density is obtained by applying the product rule to the second term on the LHS of Eq. (2.66) as outlined below.

$$\rho u_j\frac{\partial n}{\partial x_j} = \frac{\partial \rho n u_j}{\partial x_j} - n\frac{\partial \rho u_j}{\partial x_j} \tag{2.68}$$

The diffusion term with density is obtained by applying the product rule to the first term on the RHS of Eq. (2.66):

$$\rho\frac{\partial}{\partial x_j}\left(D\frac{\partial n}{\partial x_j}\right) = \frac{\partial}{\partial x_j}\left(\rho D\frac{\partial n}{\partial x_j}\right) - D\frac{\partial n}{\partial x_j}\frac{\partial \rho}{\partial x_j}. \tag{2.69}$$

Substituting Eqs. (2.67-2.69) into Eq. 2.65 yields the transport equation for the particle size distribution function, including density.

$$\frac{\partial \rho n}{\partial t} + \frac{\partial \rho n u_j}{\partial x_j} = \frac{\partial}{\partial x_j}\left(\rho D\frac{\partial n}{\partial x_j}\right) - D\frac{\partial n}{\partial x_j}\frac{\partial \rho}{\partial x_j} + \rho\mathcal{I} \tag{2.70}$$

In the following section the transport equations for the GDE are given without density, as it is standard in the literature [49, 117], first for the discrete distribution function and subsequently for the continuous distribution function.

2.5.2 The GDE for the discrete distribution function

The evolution of a complete particle population is described by the transport equations as introduced and discussed in the previous section. For small particles, i.e. particles consisting of less than a few thousand molecules ($d_p <\approx 50\,\text{nm}$), it is convenient to express the general dynamics equation for the discrete distribution function [49] as outlined in Eq. (2.71).

$$\begin{aligned}\frac{\partial n_k}{\partial t} + (u_j + u_j^e)\frac{\partial n_k}{\partial x_j} = \frac{\partial}{\partial x_j}\left(D_k\frac{\partial n_k}{\partial x_j}\right) + \left[\frac{\partial n_k}{\partial t}\right]_{\text{nucleation}} + \left[\frac{\partial n_k}{\partial t}\right]_{\text{coagulation}} \\ + \left[\frac{\partial n_k}{\partial t}\right]_{\text{coalescence}} + \left[\frac{\partial n_k}{\partial t}\right]_{\text{condensation}} + \left[\frac{\partial n_k}{\partial t}\right]_{\text{growth}}\end{aligned} \tag{2.71}$$

In the discrete form of the GDE, k represents the number of molecules in the particle for which the equation is valid. Besides the convective transport of n_k by the gas phase velocity u_j, also external forces such as gravity, electro potential or temperature gradients are considered by the external velocity u_j^e. The diffusion of the particles with k molecules is described by the diffusion coefficient D_k (its modelling is explained in chapter 3). The coagulation source term may be determined as outlined below, the modelling of the other terms is described in chapter 3, the modelling section.

$$\left[\frac{\partial n_k}{\partial t}\right]_{\text{coagulation}} = \begin{cases} -\sum_{i=1}^{K_{max}} \beta_{ik} n_i n_k & \text{for} \quad k = 1 \\ \frac{1}{2}\sum_{i=1}^{K_{max}}\sum_{j=1}^{K_{max}} \beta_{ij} n_i n_j - \sum_{i=1}^{K_{max}} \beta_{i,k} n_i n_k & \text{for} \quad k > 1 \end{cases} \tag{2.72}$$

It is convenient to pass from the discrete form of the GDE to the continuous form of the GDE if particles with more than a few 1000 molecules (much less in CFD) ($d_p >\approx 50\,\text{nm}$) have to be considered [49].

2.5.3 The GDE for the continuous distribution function

The general dynamics equation for the continuous size distribution function is outlined in Eq. (2.73).

$$\begin{aligned}\frac{\partial n}{\partial t} + (u_j + u_j^e)\frac{\partial n}{\partial x_j} = \frac{\partial}{\partial x_j}\left(D\frac{\partial n}{\partial x_j}\right) + \left[\frac{\partial n}{\partial t}\right]_{\text{nucleation}} + \left[\frac{\partial n}{\partial t}\right]_{\text{coagulation}} \\ + \left[\frac{\partial n}{\partial t}\right]_{\text{coalescence}} + \left[\frac{\partial n}{\partial t}\right]_{\text{condensation}} + \left[\frac{\partial n}{\partial t}\right]_{\text{growth}}\end{aligned} \tag{2.73}$$

Assuming that all other velocities than convection are zero, which is a good approximation for turbulent flows, the external velocity is null, $u_j^e = 0$. As the most important processes in the synthesis of particles from flames are nucleation, coagulation and sintering, the GDE in the continuous form can be written as outlined below [49].

$$\frac{\partial n(v)}{\partial t} + u_j \frac{\partial n(v)}{\partial x_j} = \frac{\partial}{\partial x_j}\left(D \frac{\partial n(v)}{\partial x_j}\right) + I(v)\delta(v - v_0) + \frac{1}{2}\int_0^v \beta(v - v', v')n(v - v')n(v)dv - \int_0^\infty \beta(v, v')n(v')dv' - \left[\frac{\partial n(v)}{\partial t}\right]_{\text{coalescence}} \tag{2.74}$$

2.5.4 Dynamic equations for the total number and volume concentration

The total number concentration of particles N_∞ (or simply N) and the total volume concentration of particles V_∞ (or V) are quantities of special interest and are defined as the integral over all particle sizes $v \in [v_{\min}, \infty]$ which are considered in a reference volume, as outlined below.

$$N = \int_{v_{\min}}^{\infty} n(v)\, dv \tag{2.75}$$

$$V = \int_{v_{\min}}^{\infty} n(v)\, v\, dv \tag{2.76}$$

The minimum volume $v_{\min}$ represents the smallest particles, in this work the volume of monomer particles. Applying the integration to the GDE for the continuous size distribution function, Eq. (2.74), yields the transport equations for the total number- and volume concentration.

$$\begin{aligned}\frac{\partial N}{\partial t} + u_j \frac{\partial N}{\partial x_j} = {} & \frac{\partial}{\partial x_j}\left(D \frac{\partial \int_{v_{\min}}^{v_\infty} n(v)dv}{\partial x_j}\right) + \int_{v_{\min}}^{v_\infty} [I(v)\delta(v - v_0)]\, dv \\ & + \frac{1}{2}\int_{v_{\min}}^{v_\infty} \left[\int_0^v \beta(v - v', v')n(v - v')n(v)dv\right] dv \\ & - \int_{v_{\min}}^{v_\infty} \left[\int_0^\infty \beta(v, v')n(v')dv'\right] dv\end{aligned} \tag{2.77}$$

$$\frac{\partial V}{\partial t} + u_j \frac{\partial V}{\partial x_j} = \frac{\partial}{\partial x_j}\left(D \frac{\partial \int_{v_{\min}}^{v_{\max}} n(v)vdv}{\partial x_j}\right) + \int_{v_{\min}}^{v_{\max}} [I(v)\delta(v - v_0)]\, dv \tag{2.78}$$

There is no coagulation term in Eq. (2.78), as coagulation does not affect the particle volume.

Chapter 3
Modelling of Turbulent Reactive Particle Laden Flows

The set of differential and ordinary differential equations introduced in chapter 2 describes a turbulent reacting spray flame with nanoparticle synthesis. However, there are difficulties in solving the flow field, spray, combustion and particle equations in all details due to the limited computational resources available. In chapter 3.1 the direct numerical simulation (DNS) approach, the Reynolds averaged Navier-Stokes (RANS) approach and the large eddy simulation technique (LES) are discussed first. The applied combustion model and the particle models are discussed in chapters 3.2.2 and 3.3.

3.1 Modelling of turbulence

To solve the equations introduced in chapter 2 for the complete velocity spectrum of a turbulent flow would require a computational grid with a spacing smaller than the smallest scales, the Kolmogorov microscales $\eta = \left(\frac{\nu^3}{\epsilon}\right)^{\frac{1}{4}}$, as introduced in the previous chapter. A further important correlation exists between the velocity fluctuations u', the integral length scale L and the dissipation of the turbulent kinetic energy ϵ as outlined in Eq. (3.1).

$$\epsilon \approx \frac{u'^3}{L} \tag{3.1}$$

Turbulence models may be classified into statistical models, based on the Reynolds averaged Navier-Stokes equations RANS and time resolving models as used in the direct numerical simulation (DNS) or large eddy simulation (LES) approach. Furthermore, turbulence models may be classified by the amount of energy they resolve as it will be discussed in the following subsections.

3.1.1 Direct numerical simulations

The direct numerical simulation (DNS) technique does not use modelling assumptions at all and resolves all scales of the energy spectrum from the energy containing eddies over the inertial subrange to the dissipative subrange (compare Fig. (2.1)). The grid must have a spacing Δ that is smaller than Kolmogorovs microscale, η and the total size of the domain $n_t\Delta$ must be larger than the integral length scale L, with the total number of grid points in one direction being n_t. This leads to the dependency of the number of grid points of the Reynolds number, outlined in Eq. (3.2).

$$n_t \approx \frac{L}{\Delta} \approx \left(\frac{Lu'}{\nu}\right)^{\frac{3}{4}} = \mathrm{Re_t}^{\frac{3}{4}} \tag{3.2}$$

Assuming that the number of grid points is equal in all three dimensions, the total number of required grid points $N_t = n_t^3$ can be estimated from the turbulent Reynolds number.

$$N_t \propto \mathrm{Re_t}^{\frac{9}{4}} \tag{3.3}$$

A further limiting factor of a DNS is the time step width Δt, which is required to advance the solution in time. The Courant-Friedrichs-Lewy (CFL) condition is used to determine the

maximum allowed time step for an explicit time integration method [29] and is defined as outlined below.

$$CFL = \frac{u}{\frac{\Delta}{\Delta t}} \tag{3.4}$$

The time dependency of the three dimensional simulation leads to a cubic correlation between the computational effort and the turbulent Reynolds number ($\propto \mathrm{Re}_t^3$). This high computational cost limits the application of DNS to cases with low Reynolds numbers for the (near) future.

3.1.2 Reynolds averaged simulations

For many industrial, technical and scientific applications the RANS approach is a suitable technique, e.g. for stationary non-reactive flows or for flows with high Reynolds numbers. In contrast to the DNS approach, the RANS approach is a statistical method based on the Reynolds averaged conservation equations. To obtain the time averaged conservation equations, the velocity vector u_i, the pressure p, the species mass fractions Y_α and the enthalpy h in Eqs. (2.1,2.5,2.8,2.13) are first replaced by their Reynolds decomposed counterpart (here shown for an arbitrary quantity ϕ) $\phi(t) = \overline{\phi} + \phi'(t)$. The resulting equations are then averaged over an infinite sampling period for steady problems, which yields the RANS approach, or over a sampling interval that allows to capture some major integral time scales of a unsteady problem, for the unsteady Reynolds averaged Navier-Stokes (URANS) approach. Substituting the Reynolds decomposed quantities and subsequent averaging yields unclosed terms, which do not disappear, as shown for the Reynolds stress tensor (RST) $\overline{u_i' u_j'}$.

$$\overline{u_i u_j} = \overline{\left(\overline{u}_i + u_i'\right)\left(\overline{u}_j + u_j'\right)} = \overline{\overline{u}_i \overline{u}_j} + \cancel{\overline{\overline{u}_i u_j'}} + \cancel{\overline{u_i' \overline{u}_j}} + \overline{u_i' u_j'} = \overline{u}_i \overline{u}_j + \overline{u_i' u_j'} \tag{3.5}$$

Due to the fact that variable density flows have to be considered, Favre averaging is applied to products of ϕ with the density.

$$\widetilde{\phi} = \frac{\int_t \rho(t)\phi(t)\mathrm{dt}}{\int_t \rho(t)\mathrm{dt}} = \frac{\overline{\rho\phi}}{\overline{\rho}} \tag{3.6}$$

The "fluctuating" part ϕ'' for the Favre averaged quantities is defined as outlined below.

$$\phi'' = \phi - \widetilde{\phi} \tag{3.7}$$

The conservation equations for the Favre weighted and Reynolds averaged mass, momentum, species and enthalpy (without source terms for spray evaporation) may be written as outlined below.

$$\frac{\partial \overline{\rho}}{\partial t} + \frac{\partial \overline{\rho}\widetilde{u}_j}{\partial x_j} = 0 \tag{3.8}$$

$$\frac{\partial \overline{\rho}\widetilde{u}_i}{\partial t} + \frac{\partial \overline{\rho}\widetilde{u}_i\widetilde{u}_j}{\partial x_j} = -\frac{\partial \overline{p}}{\partial x_i} + \frac{\partial \widetilde{\tau}_{ij}}{\partial x_j} - \frac{\partial \overline{\rho u_i'' u_j''}}{\partial x_j} \tag{3.9}$$

$$\frac{\partial \overline{\rho}\widetilde{Y}_\alpha}{\partial t} + \frac{\partial \overline{\rho}\widetilde{Y}_\alpha\widetilde{u}_j}{\partial x_j} = \frac{\partial}{\partial x_j}\left(\overline{\rho} D_\alpha \frac{\partial \widetilde{Y}_\alpha}{\partial x_j}\right) + \overline{\dot{\omega}}_\alpha - \frac{\partial \overline{\rho u_j'' Y_\alpha}}{\partial x_j} \tag{3.10}$$

$$\frac{\partial \overline{\rho}\widetilde{h}}{\partial t} + \frac{\partial \overline{\rho}\widetilde{h}\widetilde{u}_j}{\partial x_j} = +\frac{\partial}{\partial x_j}\left(\overline{\frac{\lambda}{c_p}\frac{\partial h}{\partial x_j}}\right) - \frac{\partial \overline{\rho u_j'' h}}{\partial x_j} \tag{3.11}$$

Boussinesq proposed to model the Reynolds stress tensor $\overline{\rho u_i' u_j'}$ (or sometimes $\overline{u_i' u_j'}$) based on a turbulent viscosity (or eddy viscosity), as the Reynolds stress tensor has a similar impact on the flow field as the molecular viscosity [17, 171]. The RST is then modelled based on the turbulent viscosity μ_t, the modelled and known averaged velocity $\overline{u}$ and the turbulent kinetic energy k as outlined below (first for the not density weighted equation).

$$\overline{\rho u_i' u_j'} = -\mu_t \left(\frac{\partial \overline{u}_i}{\partial x_j} + \frac{\partial \overline{u}_j}{\partial x_i} - \frac{2}{3} \frac{\partial \overline{u}_k}{\partial x_k} \delta_{ij} \right) + \frac{2}{3} \rho k \delta_{ij} \tag{3.12}$$

In almost the same manner, the Reynolds stress tensor for the Favre weighted equations may be modelled based on the Favre weighted Reynolds averaged velocity $\widetilde{u}$, the turbulent viscosity μ_t and the turbulent kinetic energy k as outlined below.

$$\overline{\rho u_i'' u_j''} \approx -\mu_t \left(\frac{\partial \widetilde{u}_i}{\partial x_j} + \frac{\partial \widetilde{u}_j}{\partial x_i} - \frac{2}{3} \frac{\partial \widetilde{u}_k}{\partial x_k} \delta_{ij} \right) + \frac{2}{3} \rho k \delta_{ij} \tag{3.13}$$

The turbulent transport of the enthalpy and of the species mass fraction $\overline{\rho u_j'' h}$ and $\overline{\rho u_j'' Y}$ may be approximated with a gradient model according to the equations below.

$$\overline{\rho u_j'' h} \approx \frac{\mu_t}{\mathrm{Pr_t}} \frac{\partial \widetilde{h}}{\partial x_j} \tag{3.14}$$

$$\overline{\rho u_j'' Y} \approx \frac{\mu_t}{\mathrm{Sc_t}} \frac{\partial \widetilde{Y}}{\partial x_j} \tag{3.15}$$

The objective of the turbulence model in the RANS approach is to estimate the RST, which is usually based on an eddy viscosity approach. The turbulent viscosity μ_t in Eqs. (3.12-3.15) is unclosed and is usually modeled by algebraic models, e.g. Prandtl's mixing length model [217], or more commonly based on transport equation models, e.g. the k-equation or Spalart-Allmaras model [178, 217] or a two equation model, e.g. $k-\epsilon$ or SST model [74, 119]. The $k-\epsilon$ model, in which the turbulent viscosity is determined from the turbulent kinetic energy k and its dissipation ϵ is probably the most common turbulence model in the RANS context.

$$\mu_t = \rho C_\mu \frac{k^2}{\epsilon} \tag{3.16}$$

To determine k and ϵ, two additional transport equations are solved:

$$\frac{\partial \rho k}{\partial t} + \frac{\partial \rho k u_j}{\partial x_j} = \frac{\partial}{\partial x_j} \left[\left(\mu + \frac{\mu_t}{\sigma_k} \right) \frac{\partial k}{\partial x_j} \right] + 2\mu_t S_{ij} S_{ij} - \rho \epsilon, \tag{3.17}$$

$$\frac{\partial \rho \epsilon}{\partial t} + \frac{\partial \rho \epsilon u_j}{\partial x_j} = \frac{\partial}{\partial x_j} \left[\left(\mu + \frac{\mu_t}{\sigma_\epsilon} \right) \frac{\partial \epsilon}{\partial x_j} \right] + \frac{\epsilon}{k} \left(C_{1\epsilon} \mu_t S_{ij} S_{ij} - \rho C_{2\epsilon} \right). \tag{3.18}$$

In the two previous equations, S_{ij} is the rate of strain which is defined as

$$S_{ij} = \frac{1}{2} \left(\frac{\partial u_i}{\partial x_j} + \frac{\partial u_j}{\partial x_i} \right) \tag{3.19}$$

The model constants in Eqs. (3.16-3.18) are case dependent, the common set of used values is: $C_\mu = 0.09$, $\sigma_k = 1.00$, $\sigma_\epsilon = 1.30$, $C_{1\epsilon} = 1.44$ and $C_{2\epsilon} = 1.92$. Many modifications for the $k-\epsilon$ model have been proposed e.g. by Yakhot et al. [224], which is known as the $k-\epsilon$ RNG model, or the realizable $k-\epsilon$ model proposed by Shih et al. [175]. As the $k-\epsilon$ models are not well suited to predict flows close to walls, Wilcox et al. [216] proposed the $k-\omega$ model, which solves a transport equation for the specific dissipation rate ω instead for ϵ. Superior to the $k-\epsilon$ close to walls, it is inferior in free stream regions. Menter combined the advantages of the $k-\epsilon$ and $k-\omega$ and proposed the shear stress transport (SST) model [119].

3.1.3 Large eddy simulations

In contrast to the RANS approach where almost the complete energy spectrum has to be modelled based on a statistical method, in the large eddy simulation approach (LES), the large scales are solved directly and only the small scales have to be modelled. The large scales are separated from the small scales by a low pass filter, based on an explicit or implicit spatial filtering operation as shown for an arbitrary quantity ϕ.

$$\overline{\phi}(x_i) = \int_V \phi\left(x_i'\right) \mathcal{G}\left(x_i - x_i'\right) \mathrm{dx_i'} \tag{3.20}$$

The filtering operation applied to ϕ separates the resolved part $\overline{\phi}$ from the sub-filter scale part ϕ'.

$$\phi = \overline{\phi} + \phi' \tag{3.21}$$

If the filtering operation is applied to non-constant density flows, the product of two quantities would lead to additional unclosed terms as outlined below.

$$\overline{\rho\phi} = \overline{\left(\overline{\rho} + \rho'\right)\left(\overline{\phi} + \phi'\right)} = \overline{\rho}\overline{\phi} + \overline{\rho'\phi'} \tag{3.22}$$

To avoid this, the density weighted Favre filtering is applied instead, as shown by the following equation.

$$\widetilde{\phi} = \frac{\overline{\rho\phi}}{\overline{\rho}} \tag{3.23}$$

Therefore, the Favre filtered (density weighted) transport equations [41] are solved.

3.1.3.1 Mass and momentum transport

The Favre filtered conservation equation for mass, including a source term for spray evaporation is outlined in Eq. (3.24).

$$\frac{\partial\overline{\rho}}{\partial t} + \frac{\partial\overline{\rho}\widetilde{u}_j}{\partial x_j} = \overline{\dot{\Gamma}}_{\overline{\rho}} \tag{3.24}$$

The unclosed Favre filtered conservation equation for momentum, including source term for momentum exchange is outlined in Eq. (3.25).

$$\frac{\partial\overline{\rho}\widetilde{u}_i}{\partial t} + \frac{\partial\overline{\rho}\widetilde{u_i u_j}}{\partial x_j} = -\frac{\partial\overline{p}}{\partial x_i} + \frac{\partial}{\partial x_j}\left(\overline{\mu}\left(\frac{\partial\widetilde{u}_i}{\partial x_j} + \frac{\partial\widetilde{u}_j}{\partial x_i}\right) - \frac{2}{3}\overline{\mu}\frac{\partial\widetilde{u}_k}{\partial x_k}\delta_{ij}\right) + \overline{\dot{M}}_S \tag{3.25}$$

The unclosed velocity correlations in the convective part may be further split up into a resolved $\widetilde{u}_i\widetilde{u}_j$ and unresolved τ_{ij}^{sgs} part.

$$\widetilde{u_i u_j} = \widetilde{u}_i\widetilde{u}_j + \tau_{ij}^{sgs} \tag{3.26}$$

It may be assumed that the turbulence on the small scales has a similar effect on the flow field as the molecular viscosity. Hence, the sub-filter term τ_{ij}^{sgs} is closed with the eddy viscosity approach based on an additional viscosity, i.e. the eddy viscosity or turbulent viscosity μ_t (similar as in the RANS approach) (with $\mu_t = \rho\nu_t$).

$$\tau_{ij}^{sgs} - \frac{1}{3}\tau_{kk}^{sgs}\delta_{ij} = -\frac{2}{3}\nu_t\frac{\partial\widetilde{u}_k}{\partial x_k}\delta_{ij} + \nu_t\left(\frac{\partial\widetilde{u}_i}{\partial x_j} + \frac{\partial\widetilde{u}_j}{\partial x_i}\right) \tag{3.27}$$

Note that the isotropic part τ_{kk}^{sgs} has been added to the deviatoric part to avoid the trace of τ_{ij}^{sgs} to become zero. Therefore and instead of the physical pressure p, the modified pressure parameter P including the isotropic part is introduced, which is modelled as outlined below.

$$\overline{P} = \overline{p} + \frac{1}{3}\tau_{kk}^{sgs}\delta_{ij} \tag{3.28}$$

Substituting Eqs. (3.27) and (3.28) into Eq. (3.25) yields finally the Favre filtered conservation equation for momentum.

$$\frac{\partial \overline{\rho}\widetilde{u}_i}{\partial t} + \frac{\partial \overline{\rho}\widetilde{u}_i\widetilde{u}_j}{\partial x_j} = -\frac{\partial \overline{p}}{\partial x_i} + \frac{\partial}{\partial x_j}\left[(\overline{\mu}+\mu_t)\left(\frac{\partial \widetilde{u}_i}{\partial x_j} + \frac{\partial \widetilde{u}_j}{\partial x_i}\right) - \frac{2}{3}(\overline{\mu}+\mu_t)\frac{\partial \widetilde{u}_k}{\partial x_k}\delta_{ij}\right] + \overline{\dot{A}}_M \tag{3.29}$$

The remaining task of the turbulence model is to determine the turbulent viscosity μ_t. Transport equation models exist to calculate μ_t in the LES context, which solve transport equations for the turbulent kinetic energy k. However, and in contrast to the RANS approach, the impact of the turbulence model on momentum transfer is much smaller as only a small amount of the turbulent kinetic energy has to be modelled. Furthermore, turbulence models may be simpler than in RANS context as isotropy on the small scales may be assumed. Subsequently, most LES approaches are based on simple algebraic models such as the Smagorinsky [176] or sigma model [133], which have been applied in the present work.

3.1.3.2 Smagorinsky model

With the model proposed by Smagorinsky [176], the turbulent viscosity is modelled based on the magnitude of the filtered strain rate $\widetilde{S}_{ij}$, the filter size Δ and the Smagorinsky constant C_S as outlined below.

$$\nu_t = (C_S\Delta)^2\,|\boldsymbol{S}| = (C_S\Delta)^2\sqrt{2\widetilde{S_{ij}}\widetilde{S_{ij}}} \tag{3.30}$$

$$\text{with} \qquad |\boldsymbol{S}| = \sqrt{2\widetilde{S_{ij}}\widetilde{S_{ij}}} \qquad \text{and} \qquad \widetilde{S}_{ij} = \frac{1}{2}\left(\frac{\partial \widetilde{u}_i}{\partial x_j} + \frac{\partial \widetilde{u}_j}{\partial x_i}\right)$$

The choice of a value for C_S is strongly related to the investigated case and the Reynolds number and should be chosen between $0.06 \leq C_S < 0.2$. In the present work, either a value of 0.173 has been used for C_S in the simulations performed with the Smagorinsky turbulence model or the dynamic procedure as proposed by Germano [54] has been used to determine C_S dynamically (the dynamic procedure is explained in subsection 3.1.3.4). As the Smagorinsky model is known to predict non-zero viscosity at walls and due to the high computational cost for the dynamic procedure, Nicoud's σ-model [133] has been used as an alternative choice in this work.

3.1.3.3 Nicoud's σ-model

The σ model determines the turbulent viscosity also based on the filter size Δ, a model parameter C_S and based on the singular values of the velocity gradient as outlined below.

$$\nu_t = (C_S\Delta)^2\,D_m \tag{3.31}$$

$$D_m = \frac{\sigma_3(\sigma_1-\sigma_2)(\sigma_2-\sigma_3)}{\sigma_1^2} \tag{3.32}$$

$$G_{ij} = \frac{\partial \widetilde{u}_k}{\partial x_i}\frac{\partial \widetilde{u}_k}{\partial x_j} \tag{3.33}$$

The singular values σ_i in the previous equations are identical to the square roots of the eigenvalues of the tensor G_{ij}. The model constant C_S was set to 1.5 in the present work. The σ model is known to be well suited for combustion applications, as it predicts zero turbulent viscosity for solid body rotations and zero turbulent viscosity for thermal expansions [164]. The dynamic procedure proposed by Germano et al. [54] can also be used to determine C_S for the σ model.

3.1.3.4 Dynamic procedure

The well known shortcomings of a constant model parameter were addressed by Germano who proposed to determine the model parameter C_S dynamically varying in space and time. The algebraic Germano identity is based on two filtering levels, namely grid filtered and test filtered, and the resolved turbulent stresses [54]. The grid filtered τ_{ij}^{sgs} and test filtered τ_{ij}^{test} unresolved fluxes may be written as outlined below (for non-constant density [124])

$$\tau_{ij}^{sgs} = \overline{\rho u_i u_j} - \frac{\overline{\rho u_i}\ \overline{\rho u_j}}{\overline{\rho}} \tag{3.34}$$

$$\tau_{ij}^{test} = \widehat{\overline{\rho u_i u_j}} - \frac{\widehat{\overline{\rho u_i}}\ \widehat{\overline{\rho u_j}}}{\widehat{\overline{\rho}}} \tag{3.35}$$

(It should be noted that in the LES approach the grid filtered term may also be determined with the filter-width and not necessarily with the grid size.) The Germano identity L_{ij}, which is also known as Leonard stress tensor, is defined as the sum of the grid filtered and test filtered unresolved fluxes.

$$L_{ij} = \tau_{ij}^{test} - \widehat{\tau_{ij}^{sgs}} = \widehat{\overline{\rho}\widetilde{u}_i\widetilde{u}_j} - \frac{\widehat{\overline{\rho}\widetilde{u}_i}\widehat{\overline{\rho}\widetilde{u}_j}}{\widehat{\overline{\rho}}} \tag{3.36}$$

Equations (3.34) and (3.35) include the trace parts for the grid filtered and test filtered unresolved fluxes, the model for the traceless part reads:

$$\tau_{ij}^{sgs} - \frac{1}{3}\delta_{ij}\tau_{kk}^{sgs} = \overline{\rho}\Delta^2|\boldsymbol{S}|\widetilde{u}_i\left[\frac{2}{3}\frac{\partial\widetilde{u}_i}{\partial x_k}\delta_{ij} - \left(\frac{\partial\widetilde{u}_i}{\partial x_j} + \frac{\partial\widetilde{u}_j}{\partial x_i}\right)\right] = \frac{\beta_{ij}}{C_s^2} \tag{3.37}$$

$$\tau_{ij}^{test} - \frac{1}{3}\delta_{ij}\tau_{kk}^{test} = \widehat{\overline{\rho}}\widehat{\Delta}^2|\boldsymbol{S}|\widehat{\widetilde{u}}_i\left[\frac{2}{3}\frac{\partial\widehat{\widetilde{u}}_i}{\partial x_k}\delta_{ij} - \left(\frac{\partial\widehat{\widetilde{u}}_i}{\partial x_j} + \frac{\partial\widehat{\widetilde{u}}_j}{\partial x_i}\right)\right] = \frac{\alpha_{ij}}{C_s^2} \tag{3.38}$$

Replacing the traceless part in Eq. (3.36) with the before given equations yields M_{ij} as outlined below.

$$M_{ij} = L_{ij} - \frac{1}{3}\delta_{ij}L_{kk} = \widehat{C_s^2\beta_{ij}} - C_s^2\alpha_{ij} \tag{3.39}$$

Lilly [106] proposed to determine C_s^2 based on a least square error estimation and to assume that C_s is independent of the filtering. The resulting expression for C_s^2 is written below.

$$C_s^2 = \frac{M_{ij}\left(L_{ij} - \frac{1}{3}\delta_{ij}L_{kk}\right)}{M_{mn}M_{mn}} \tag{3.40}$$

Alternatively, Piomelli and Liu [149] proposed to determine C_s^2 based on the constant of the last iteration as given in the equation below.

$$C_s^2 = \frac{-\left(L_{ij} - \frac{1}{3}\delta_{ij}L_{kk} - \widehat{C_s^{\star 2}\beta_{ij}}\right)\alpha_{ij}}{\alpha_{mn}\alpha_{mn}} \tag{3.41}$$

3.1.3.5 Scalar transport equations

Further unclosed terms arise from filtering in the transport equations for the scalar quantities ϕ, i.e. the species mass fractions Y_α, the enthalpy h and the mixture fractions Z and Z_α. Generally,

the Favre filtered conservation equation for a scalar quantity ϕ can be written as shown by Eq. (3.42):

$$\frac{\partial \overline{\rho}\widetilde{\phi}}{\partial t} + \frac{\partial \overline{\rho}\widetilde{\phi}\widetilde{u}_j}{\partial x_j} = \frac{\partial}{\partial x_j}\left(\overline{\rho} D_\phi \frac{\partial \widetilde{\phi}}{\partial x_j} - \overline{\rho}\tau_\phi^{sgs}\right) + \overline{\dot{\omega}}_\phi. \tag{3.42}$$

The unclosed term τ_ϕ^{sgs} refers to the turbulent fluxes and consists of a closed and unclosed term. The eddy diffusivity approach [151] is used here to model τ_ϕ^{sgs}.

$$\overline{\rho}\tau_\phi^{sgs} = \overline{\rho}\left(\widetilde{\phi u_j} - \widetilde{\phi}\widetilde{u}_j\right) = \overline{\rho} D_t \frac{\partial \widetilde{\phi}}{\partial x_j} \tag{3.43}$$

The turbulent diffusivity D_t in the previous equation is modelled based on the turbulent viscosity μ_t and the turbulent Schmidt $\mathrm{Sc_t}$ or turbulent Prandtl $\mathrm{Pr_t}$ number – depending on the transported scalar.

$$D_t = \frac{\nu}{\mathrm{Sc_t}} \qquad \text{or} \qquad D_t = \frac{\nu}{\mathrm{Pr_t}} \tag{3.44}$$

The molecular (D) and turbulent ($/D_t$) diffusivities may be summed up to an effective diffusivity $D_s = D + D_t$. Applying the eddy diffusivity approach to the conservation equations of the species mass fractions, the enthalpy and the mixture fraction, yields the closed transport equations as outlined in Eqs. (3.45), (3.46), (3.47) and (3.48), respectively.

$$\frac{\partial \overline{\rho}\widetilde{Y}_\alpha}{\partial t} + \frac{\partial \overline{\rho}\widetilde{Y}_\alpha \widetilde{u}_j}{\partial x_j} = \frac{\partial}{\partial x_j}\left(\overline{\rho}\left(\frac{\mu}{\mathrm{Sc}} + \frac{\mu_t}{\mathrm{Sc_t}}\right)\frac{\partial \widetilde{Y}_\alpha}{\partial x_j}\right) + \overline{\dot{\omega}}_{C,\alpha} \tag{3.45}$$

$$\frac{\partial \overline{\rho}\widetilde{h}}{\partial t} + \frac{\partial \overline{\rho}\widetilde{h}\widetilde{u}_j}{\partial x_j} = \frac{\partial}{\partial x_j}\left(\overline{\rho}\left(\frac{\mu}{\mathrm{Pr}} + \frac{\mu_t}{\mathrm{Pr_t}}\right)\frac{\partial \widetilde{h}}{\partial x_j}\right) \tag{3.46}$$

$$\frac{\partial \overline{\rho}\widetilde{Z}}{\partial t} + \frac{\partial \overline{\rho}\widetilde{Z}\widetilde{u}_j}{\partial x_j} = \frac{\partial}{\partial x_j}\left(\overline{\rho}\left(\frac{\mu}{\mathrm{Sc}} + \frac{\mu_t}{\mathrm{Sc_t}}\right)\frac{\partial \widetilde{Z}}{\partial x_j}\right) \tag{3.47}$$

$$\frac{\partial \overline{\rho}\widetilde{Z}_\alpha}{\partial t} + \frac{\partial \overline{\rho}\widetilde{Z}_\alpha \widetilde{u}_j}{\partial x_j} = \frac{\partial}{\partial x_j}\left(\overline{\rho}\left(\frac{\mu}{\mathrm{Sc}} + \frac{\mu_t}{\mathrm{Sc_t}}\right)\frac{\partial \widetilde{Z}_\alpha}{\partial x_j}\right) \tag{3.48}$$

The source terms arising in the equations above necessitate an individual description. Additional to the equations needed to describe the state of the gas phase, the population balance equations for the nanoparticles must be derived in a Favre filtered expression, which will be shown below.

3.2 Turbulent combustion modelling

3.2.1 Combustion model overview

Combustion models which have been successfully applied for the prediction of laminar and turbulent flames have often been extended to account for spray combustion. An overview on the modelling of turbulent dilute spray combustion is for example given by Jenny et al. [71]. Some well known combustion models which have been applied for the simulation of dilute spray flames in the recent years are presented in the next section. Subsequently, a detailed discussion of the applied standard flamelet generated manifold approach for gas phase combustion is presented,

followed by the descriptions of the extensions made to the FGM approach for spray combustion and two fuels.

Detailed chemistry
In detailed chemistry models, the conservation equations as introduced in chapter 2 for mass, momentum, species and energy including source terms for the spray phase are solved directly in the DNS of spray flames. In the RANS or LES approach, the Reynolds averaged or Favre filtered conservation equations are solved. These models are computationally expensive due to the fact that for each species a separate conservation equation has to be solved. Furthermore, the calculation of the reaction rates and the transport coefficients leads to an increased numerical stiffness of the simulations and an increased demand for computational resources. Commonly, this method is based on an Eulerian/Lagrangian representation of the flow field equations for the gas and liquid phase, respectively.
This method has been used by e.g. Gutheil and Sirignano [63] to study counterflow spray combustion with detailed transport and chemistry for a n-heptane/O_2 flame. Kong and Reitz [91] applied a detailed chemistry model for the simulation of a direct-injection homogeneous charge compression ignition (HCCI) engine with emissions. Despite this, Kong et al. [92] applied a detailed chemistry model together with a phenomenological model for the soot evolution in a combined simulation approach to a diesel spray. Due to the high numerical expenses and stiffness of the simulations, combustion is usually not modelled with detailed chemistry but rather with tabulated chemistry approaches based on control variables that describe the mixture composition and progress of combustion.

Flamelet models
Flamelet models have been originally proposed to model non-premixed turbulent flames [143]. In non-premixed turbulent flames, the chemical time scale and the mixing time scale may be of the same order. Hence it is important to account for finite chemistry effects in the combustion model. The general idea of the flamelet model is that a three dimensional turbulent flame may be represented by an ensemble of one dimensional flames, the flamelets, which are stretched and wrinkled in space. In the model, the 1D flamelets are aligned with the flame normal direction. A coordinate transformation from physical space x_i to the mixture fraction space Z and some further manipulations applied to Eq. (2.8) yields the so called flamelet equation in an unsteady representation [143, 144] and is outlined below.

$$\rho\frac{\partial Y_\alpha}{\partial t} = \rho D\left(\frac{\partial Z}{\partial x_i}\right)^2\frac{\partial^2 Y_\alpha}{\partial Z^2} + \dot{\omega}_\alpha \tag{3.49}$$

While the gradients tangential to the flame normal direction are neglected, only the gradients normal to the flame affect chemistry [144]. For steady state problems, the flamelet equation may be expressed without accumulation term and the previous equation becomes:

$$\rho D\left(\frac{\partial Z}{\partial x_i}\right)^2\frac{\partial^2 Y_\alpha}{\partial Z^2} = -\dot{\omega}_\alpha. \tag{3.50}$$

In Eqs. (3.49) and (3.50), the scalar dissipation rate χ is commonly introduced, which correlates the strain of the fluid with the species diffusivity.

$$\chi = 2D\left(\frac{\partial Z}{\partial x_i}\right)^2 \tag{3.51}$$

The scalar dissipation rate may be used to account for effects like flame quenching.
In the flamelet approach, the thermochemical properties are commonly determined a priori to the simulations by solving detailed or reduced reaction mechanisms with a chemical library such

as Chemkin [79] or Cantera [56], amongst others. The thermochemical data is stored in multidimensional look-up tables as functions of control parameters such as the mixture fraction Z and the scalar dissipation rate χ. In the LES methodology, the transport equation for Favre filtered mixture fraction is solved as described in Eq. (3.47). As only the spatially filtered values of the mixture fraction $\widetilde{Z}$ are known, the PDF or FDF must be determined (e.g. by an assumed shape function), so that the variance of the mixture fraction $\widetilde{Z''^2}$ must be modelled and a sub-filter distribution must be assumed. The mixture fraction variance is commonly determined from an algebraic equation or a transport equation as outlined below.

$$\widetilde{Z''^2} = C_m \Delta^2 \left(\frac{\partial \widetilde{Z}}{\partial x_i} \right)^2 \tag{3.52}$$

$$\frac{\partial \overline{\rho} \widetilde{Z''^2}}{\partial t} + \frac{\partial \overline{\rho} \widetilde{u}_i \widetilde{Z''^2}}{\partial x_i} = \frac{\partial}{\partial x_i} \left(\overline{\rho}(D + D_t) \frac{\partial \widetilde{Z''^2}}{\partial x_i} \right) + 2\overline{\rho} D_t \left(\frac{\partial \widetilde{Z}}{\partial x_i} \right)^2 - 2\overline{\rho} \chi_{\widetilde{Z}} \tag{3.53}$$

For more information on the modelling of the variance and sub-filter distribution, the interested reader is referred to chapter 5 or the original work by Rittler et al. [164]. The scalar dissipation rate χ may be determined from the gradient of the mixture fraction.

$$\chi = 2\left(D + D_t\right) \left(\frac{\partial \widetilde{Z}}{\partial x_i} \right)^2 \tag{3.54}$$

Conditional moment closure

In the conditional moment closure (CMC) method [88], the evolution of the mixture composition is described by transport equations for the mixture fraction and the conditional moments of the reacting species. The transport of the reacting species is modelled by the CMC, by assuming that the fluctuations of the reacting species correlate with the fluctuations of the mixture fraction. The unconditioned quantities (mass fractions Y_α) are then determined based on the conditional quantity (mixture fraction Z) and the sampling space (η) with a certain probability $P(\eta)$. Ukai et al. [196–198] adapted CMC to account for spray combustion by extending the transport equations for the mixture fraction and the conditional moments of the enthalpy and species by source terms for mass and heat transfer.

Flame surface density models

The flame surface density models (FSD) are finite-rate models which are commonly applied to premixed combustion. In premixed flames the fuel and oxidizer species are premixed a priori to combustion and the flame front propagates from the burnt products into the unburnt reactants. Hence, the progress of combustion is commonly described by the reaction progress variable C which was introduced in Eq. (2.41). The temporal and spatial evolution of the combustion progress are described by a transport equation for the progress variable C:

$$\frac{\partial \rho C}{\partial t} + \frac{\partial \rho C u_i}{\partial x_i} = \frac{\partial}{\partial x_i} \left(\rho D_C \frac{\partial C}{\partial x_i} \right) + \dot{\omega}_C. \tag{3.55}$$

Filtering of the previous equation yields

$$\frac{\partial \overline{\rho} \widetilde{C}}{\partial t} + \frac{\partial \overline{\rho} \widetilde{C} \widetilde{u}_i}{\partial x_i} = \overline{\frac{\partial}{\partial x_i} \left(\rho D_C \frac{\partial C}{\partial x_i} \right)} + \overline{\dot{\omega}}_C - \frac{\partial}{\partial x_i} \left[\overline{\rho u_i C} - \overline{\rho} \widetilde{u}_i \widetilde{C} \right]. \tag{3.56}$$

The three terms on the RHS of the previous equation, the filtered molecular diffusion of C, the filtered chemical reaction rate and the sub-filter turbulent flux of the reaction progress variable are unclosed and need to be modelled. In many studies it was shown that a common eddy

diffusivity approach is not suitable to model the unresolved turbulent flux of the progress variable $\left(\overline{\rho u_i C} - \overline{\rho}\widetilde{u}_i\widetilde{C}\right)$, as nicely summarized by Ma et al. [111], amongst others. It was shown that the impact of counter gradient transport (CGT) is not negligible [101, 111]. Furthermore Lecoq [101] showed that the model for the sub-filter scalar flux proposed by Weller et al. [215],

$$\left(\overline{\rho u_i C} - \overline{\rho}\widetilde{u}_i\widetilde{C}\right) = -\overline{\rho} D_t \frac{\partial \widetilde{C}}{\partial x_i} - \Xi \rho_0 S_L \left(\overline{C} - \widetilde{C}\right) M_i \tag{3.57}$$

with the resolved flame normal vector $M_i = -\left(\partial\overline{C}/\partial x_i\right) / \left|\partial\overline{C}/\partial x_i\right|$ leads to the Favre filtered transport equation for the progress variable [111] as outlined below.

$$\frac{\partial \overline{\rho}\widetilde{C}}{\partial t} + \frac{\partial \overline{\rho}\widetilde{C}\widetilde{u}_i}{\partial x_i} = \frac{\partial}{\partial x_i}\left(\rho(D_C + D_t)\frac{\partial \widetilde{C}}{\partial x_i}\right) + \rho_0 S_L \Xi \frac{\partial \widetilde{C}}{\partial x_i} \tag{3.58}$$

In the FSD approach, the filtered reaction rate source term and the filtered diffusion of C are modelled together based on the displacement speed S_d and the flame surface density Σ according to the following equation.

$$\overline{\frac{\partial}{\partial x_i}\left(\rho D_C \frac{\partial C}{\partial x_i}\right)} + \overline{\dot{\omega}}_C = \overline{\rho S_d}\Sigma_{\mathrm{Gen}} \tag{3.59}$$

For flames in which a unity Lewis number may be assumed, the filtered local displacement speed is commonly approximated as the laminar flame speed as illustrated below.

$$\overline{\rho S_d} \approx \rho S_L \tag{3.60}$$

Several models have been proposed to determine the flame surface density Σ, for example the algebraic models proposed by Fureby [51] or Mupalla et al. [131] in which the flame surface density Σ may be modelled by the wrinkling factor Ξ and the gradient of the filtered progress variable $\overline{C}$.

$$\Sigma \approx \Xi \left|\frac{\partial \overline{C}}{\partial x_i}\right| \tag{3.61}$$

More information on FSD models and their implementation in the LES inhouse code PsiPhi may be found in the work of Ma et al. [111]. Furthermore, transport equation models have been proposed to determine the evolution of the flame surface density [181].

Eddy break-up and eddy dissipation model

The eddy break-up model (EBM) was originally proposed by Spalding [179] and extended by Magnussen and Hjertager [115] to the eddy dissipation model (EDM) and assumes that the chemical reaction is controlled by turbulent mixing. This assumption holds for fast chemical processes. In the EBU model, the chemical reaction rate is determined from a global one step reaction with the model constant C_{EBU}, the turbulent time scale τ_t, i.e. the ratio of turbulent kinetic energy and its dissipation $\tau_t = k/\epsilon$ and the variance of the product mass fraction $\widetilde{Y_P''^2}$, as outlined below.

$$\widetilde{\dot{\omega}}_P = -\overline{\rho}\frac{\epsilon}{k} C_{EBU}\left(\widetilde{Y_P''^2}\right)^{0.5} \tag{3.62}$$

In the LES methodology, the turbulent time scale is often determined from the grid size Δ and the velocity fluctuation $u_{sgs}^{'}$ and the chemical reaction rate may be determined as outlined below.

$$\widetilde{\dot{\omega}}_P = -\overline{\rho}\frac{u_{sgs}^{'}}{\Delta} C_{EBU}\left(\widetilde{Y_P''^2}\right)^{0.5} \tag{3.63}$$

In the EDM model, the fuel consumption rate $\tilde{\dot{\omega}}_f$ is determined from the local fuel, oxidizer and product mass fractions (Y_f, Y_O and Y_P), the turbulent time scale and the two model parameters A and B as outlined below.

$$\widetilde{\dot{\omega}}_f = -\overline{\rho}\frac{\epsilon}{k}\min\left[A\widetilde{Y}_f, A\frac{\widetilde{Y}_o}{s}, A\cdot B\frac{\widetilde{Y}_p}{1+s}\right] \tag{3.64}$$

Flamelet progress variable
The flamelet progress variable (FPV) approach was proposed by Pierce and Moin in a large eddy simulation formulation and solves two transport equations to describe the evolution of the mixture composition and the progress of combustion, i.e. the mixture fraction and the reaction progress variable [146, 148]. Moin and Apte adapted the flamelet progress variable approach to account for a spray phase, by adding source terms for the transport equations of the mixture fraction, momentum equation and density [123].

3.2.2 The flamelet generated manifold approach

In the present work, combustion is modelled based on the Flamelet Generated Manifold (FGM) approach, which was originally proposed by van Oijen and de Goey [201] for premixed flames. It was, however, successfully applied to the prediction of partially premixed spray flames in the works of Bekdemir et al. [11], Chrigui et al. [25, 26], De et al. [32] or Rittler et al. [164]. Vreman et al. [207] applied the FGM model, in which the tables where produced based on premixed and non-premixed flamelets, to their studies of Sandia flame D [1].
The basic idea of the FGM approach is to combine the flamelet assumption that a three dimensional flame can be represented by a set of one dimensional flamelets [143, 144], with the manifold approach, in which the thermochemical properties of the gas phase are determined a-priori and are stored in low dimensional manifolds [112] as a function of control variables. In the present work, the thermochemical properties are determined from solving a set of one dimensional, premixed, freely propagating flames with the open source chemical library Cantera [56]. The thermochemical quantities such as ρ, μ, T or Y_α are subsequently stored in a two- or multi-dimensional look-up table as a function of the control variables − in this work the mixture fraction Z (or Z_α) and the normalized reaction progress variable C are used for the table look-up. Within the flammability limits, the initial and boundary conditions in the 1D simulations are varied in equidistant steps ΔZ (or ΔZ_α) from a minimum to maximum value to ensure a simple table look-up. Outside of the flammability limits ideal mixing is assumed. (2D effets are neglected in the presented work).

To resolve the flame on the numerical grid, Kuenne et al. [95, 96] combined the FGM approach with the artificial flame thickening (ATF) method [27]. The idea of the artificial flame thickening is to avoid numerical instabilities and errors, by increasing the diffusion coefficient D and reducing the chemical source term $\dot{\omega}$. This artificial flame thickening was also used in this work [164, 165]. The modified and applied FGM/ATF approach for spray flames and flames with three streams is discussed in the following section.

3.2.2.1 The FGM approach for spray flames

The standard FGM approach was first modified to account for spray combustion. This was achieved by adding an evaporation source term $\dot{\Gamma}_Z$ to the transport equation of the mixture fraction [25, 32, 164], as outlined in the equation below.

$$\frac{\partial\overline{\rho}\widetilde{Z}}{\partial t} + \frac{\partial\overline{\rho}\widetilde{Z}\widetilde{u}_j}{\partial x_j} = \frac{\partial}{\partial x_j}\left(\overline{\rho}\left(\frac{\mu}{\mathrm{Sc}} + \frac{\mu_t}{\mathrm{Sc_t}}\right)\frac{\partial\widetilde{Z}}{\partial x_j}\right) + \overline{\dot{\Gamma}}_Z \tag{3.65}$$

While the mixture composition is described by the mixture fraction $\widetilde{Z}$, the progress of combustion is described by the reaction progress variable $\widetilde{Y}_P$. For the standard case of the spray flames (without liquid precursor), the progress variable is the sum of the mass fractions of carbon dioxide, water, carbon monoxide and hydrogen as given by Eq. (3.66).

$$Y_p = Y_{CO_2} + Y_{H_2O} + Y_{CO} + Y_{H_2} \tag{3.66}$$

The diffusion coefficient D_P and the chemical reaction source term $\dot{\omega}_C$ in the transport equation for Y_P are modified by the thickening factor F_t and the efficiency function E to account for artificial thickening as outlined below.

$$\frac{\partial \overline{\rho}\widetilde{Y}_P}{\partial t} + \frac{\partial \overline{\rho}\widetilde{Y}_P\widetilde{u}_j}{\partial x_j} = \frac{\partial}{\partial x_j}\left[\overline{\rho}\left(F_t E D_P + (1-\Omega)D_t\right)\frac{\partial \widetilde{Y}_P}{\partial x_j}\right] + \frac{E}{F_t}\overline{\dot{\omega}}_C \tag{3.67}$$

The thickening factor F_t in Eq. (3.45) is determined from the flame sensor Ω and the maximum value of F_t.

$$F_t = 1 + \Omega\left(F_{t,max} - 1\right) \tag{3.68}$$

The maximum value of the thickening factor is calculated from the grid spacing Δ, the laminar flame thickness δ_l^0 and the number of grid points n, on which the flame front is resolved.

$$F_{t,max} = \max\left(\frac{\Delta n}{\delta_l^0}, 1\right) \tag{3.69}$$

The laminar flame thickness δ_l^0 and the flame sensor Ω, which is used to indicate the location of the flame front, are calculated as proposed by Proch and Kempf [157] and is outlined below.

$$\Omega = \frac{\frac{\mathrm{dY_p}}{\mathrm{dx}}}{\max\left(\frac{\mathrm{dY_p}}{\mathrm{dx}}\right)} \tag{3.70}$$

The flame thickness δ_l^0 and sensor Ω are determined a-priori in the flamelet calculations, and are stored as functions of the control variables Z and C in the 2 dimensional look-up tables. The normalized reaction progress variable C is computed from the progress variable Y_P and the minimum and maximum progress variables, which both depend on the mixture fraction $Y_{P,min}(Z)$ and $Y_{P,max}(Z)$.

$$C = \frac{Y_{p,max}(Z) - Y_P}{Y_{p,max}(Z) - Y_{P,min}(Z)} \tag{3.71}$$

In the used definition of the progress variable the minimum value of Y_p is zero, and only the maximum value $Y_{p,max}$ is stored as a function of the mixture fraction in the look up table. The efficiency function E accounts for the loss of the flame speed or flame wrinkling due to thickening and is calculated as proposed by Charlette et al. [23] and modified by Wang et al. [209] from the maximum value of the thickening factor $F_{t,max}$, the laminar flame speed s_l^0, the velocity fluctuation u'_Δ, the turbulent Reynolds number on the sub grid scales Re_δ, the fitted efficiency function Γ_δ and the model parameter $\beta = 0.5$. The Charlette model was implemented in the PsiPhi code by Proch and Kempf [157].

$$E = \left[1 + \min\left(F_{t,max} - 1, \Gamma_\Delta\left(F_{t,max}, \frac{u'_\Delta}{s_l^0}, \mathrm{Re}_\Delta\right)\frac{u'_\Delta}{s_l^0}\right)\right]^\beta \tag{3.72}$$

The turbulent Reynolds number is determined from the maximum thickening factor, the velocity fluctuations and the laminar flame thickness,

$$\mathrm{Re}_\Delta = 4\mathrm{F_{t,max}}\frac{\mathrm{u'_\Delta}}{\mathrm{s_l^0}}, \tag{3.73}$$

the fitted efficiency function from

$$\Gamma_\Delta\left(F_{t,max}, \frac{u'_\Delta}{s_l^0}, \mathrm{Re}_\Delta\right) = \left\{\left[\left(f_u^{-a} + f_\Delta^{-a}\right)^{-\frac{1}{a}}\right]^{-b} + f_{\mathrm{Re}}^{-b}\right\}^{-\frac{1}{b}}, \tag{3.74}$$

and the functions f_u, f_Δ and f_{Re} from:

$$f_u = 4\left(\frac{27C_k}{110}\right)^{0.5}\left(\frac{18C_k}{55}\right)\left(\frac{u'_\Delta}{s_l^0}\right)^2, \tag{3.75}$$

$$f_\Delta = \left[\frac{27C_k\pi^{4/3}}{110}\left(f_{t,max}^{4/3} - 1\right)\right]^{0.5}, \tag{3.76}$$

$$f_{\mathrm{Re}} = \left[\frac{9}{55}\exp\left(-\frac{3}{2}C_k\pi^{4/3}\mathrm{Re}_\Delta^{-1}\right)\right]^{0.5}\mathrm{Re}_\Delta^{0.5}, \tag{3.77}$$

with $a = 0.6 + 0.2\exp\left(-0.1\frac{u'_\Delta}{s_l^0}\right) - 0.2\exp\left(-0.01F_{t,max}\right)$, $b = 1.4$ and 1.5 for the Kolmogorov constant C_k.

3.2.2.2 The FGM approach for three feed systems

Flames for the synthesis of nanoparticles are usually three feed systems. These systems consist of liquid or gaseous mixtures of a carrier fuel and a particle precursor, dispersed by an oxidizer stream and subsequently injected into a combustion chamber with a secondary heat source. Commonly, the fuel and precursor of the main flame are different from the fuel used for the secondary flame. The standard formulation of the FGM approach, based on one mixture fraction and progress variable, is not suited to describe the mixing and combustion of such three feed systems.

Therefore, in the present work the FGM approach for spray flames was extended to account for the mixing of three streams, namely (a) a premixed fuel/precursor composition, (b) a secondary fuel and stream (c) an oxidizer. Even though the approach is capable to account for three stream mixing and combustion, simplifying assumptions had to be made in the present approach: a) a unity Lewis number,i.e. equal diffusivity for all species and b) no heat exchange between the different streams. In contrast to laminar flames, in turbulent flames the assumption of equal diffusivity may be justified as molecular diffusion is dominated by turbulent mixing.

3.2.2.3 Mixture composition

If hydrocarbon fuels with different C/H ratios are described by a common two mixture fraction approach, cross terms between the mixture fractions need additional modelling. To avoid this, two element mass fractions Z_α are used as conserved scalars, to model mixing and combustion and as control variables for the table look-up. The element mass fraction according to Eq. (2.34) is used.

$$Z_\alpha = \sum_{j=1}^{N_s} a_{j,\alpha}\frac{W_\alpha}{W_j}Y_j \tag{3.78}$$

Common element mass fractions for the combustion of hydrocarbon fuels are Z_C, Z_H, Z_O and Z_N, (where Z_N may represent the sum of nitrogen and argon). In the presence of a particle precursor, an additionally element mass fraction needs to be accounted for, e.g. for the synthesis of silica particles Z_{Si}, for iron-oxide particles Z_{Fe} or for titania particles Z_{Ti}. At each time the sum of the element mass fractions must be unity $1 = \sum_\alpha Z_\alpha$. For synthesis flames, using the hydrogen or the carbon element mass fraction as a first control variable and the particle species as a second control variable is a good choice, as the particle species element mass fraction is zero outside of the main stream. Due to the aforementioned reason, interpolation errors from the

table look-up are minimized. In the presence of spray, the Favre filtered transport equation for the element mass fraction Z_α is given by the equation below.

$$\frac{\partial \overline{\rho}\widetilde{Z}_\alpha}{\partial t} + \frac{\partial \overline{\rho}\widetilde{Z}_\alpha \widetilde{u}_j}{\partial x_j} = \frac{\partial}{\partial x_j}\left(\overline{\rho} D_S \frac{\partial \widetilde{Z}_\alpha}{\partial x_j}\right) + \overline{\dot{\Gamma}}_{Z_\alpha} \tag{3.79}$$

3.2.2.4 Reaction progress

The progress of combustion is described by a joint reaction progress variable. For the cases with particle synthesis, the sum of carbon monoxide and carbon dioxide mass fractions is used as progress variable:

$$Y_P = Y_{CO_2} + Y_{CO}. \tag{3.80}$$

Water and hydrogen are not considered as reaction products in the definition of the reaction progress variable (for cases with particle synthesis). The formation of the particle monomer molecules is assumed to occur in the post flame zone by reactions with H_2O and H_2. These reactions reduce the mass fraction of water and increases the mass fraction of hydrogen, which might lead to a discontinuous correlation between the thermochemical properties and the control variable. As in the standard FGM approach, the Favre filtered transport equation with artificial flame thickening is solved to describe the evolution of the flame progress.

$$\frac{\partial \overline{\rho}\widetilde{Y}_P}{\partial t} + \frac{\partial \overline{\rho}\widetilde{Y}_P \widetilde{u}_j}{\partial x_j} = \frac{\partial}{\partial x_j}\left[\overline{\rho}\left(F_t E D_P + (1-\Omega) D_t\right)\frac{\partial \widetilde{Y}_P}{\partial x_j}\right] + \frac{E}{F_t}\overline{\dot{\omega}}_C + \overline{\dot{\omega}}_E \tag{3.81}$$

The normalized reaction progress variable C is defined the same way as described above, except that the minimum and maximum values of Y_P now depend on the two element mass fractions:

$$C = \frac{Y_{p,max}(Z_H, Z_{Si}) - Y_P}{Y_{p,max}(Z_H, Z_{Si}) - Y_{P,min}(Z_H, Z_{Si})} \tag{3.82}$$

Also as described before, the minimum reaction progress variable is zero, for the aforementioned definition of Y_P. The maximum progress variable $Y_{p,max}$ is stored in the 3D look-up tables.

3.2.2.5 Table generation

As described for the standard FGM approach, a set of 1D premixed flamelets is solved by varying the initial and inlet conditions. The inlet and initial composition of the flamelets are determined by varying the control variables Z_H and Z_{Si} (or Z_{Fe}) in equidistant steps of ΔZ_H and ΔZ_{Si} (or ΔZ_{Fe}). The resulting thermochemical variables are stored in a set of 2D look-up tables. During the table generation and for each 2D look-up table, the first control variable Z_H is kept constant and the second control variable Z_{Si} (or Z_{Fe}) is varied from a minimum to maximum value (e.g. $Z_H = x$, $Z_{Si,min}(Z_H(x)) = 0$ and $Z_{Si,max}(Z_H(x))$). An advantage of using the particle species as second element mass fraction is the fact that the minimum value of the second element mass fraction for a given value of the first element mass fraction is always 0. The maximum value of the second element mass fraction is determined before the table generation. The valid range of Z_H and Z_{Fe} for a set-up with iron-penthacarbonyl/ethanol as precursor/solvent, a premixed methane/air pilot and an air coflow is illustrated in Fig. 3.1. Tables generated according to the explained method result in partially filled tables, enable however a fast and simple generation and data access. Figure 3.2 illustrates the particle formation source term, tabulated as a function of the element mass fractions of hydrogen and iron. As described before, the first control variable Z_H is kept constant, the second and third control variables Z_{Fe} and $Y_{PN} = C$ are varied in equidistant steps. The last flamelet within the range of validity is used to fill the table for $Z_{Fe} > Z_{Fe,max}(Z_H)$. As in the standard FGM model, pure mixing is assumed outside of the flammability limits.

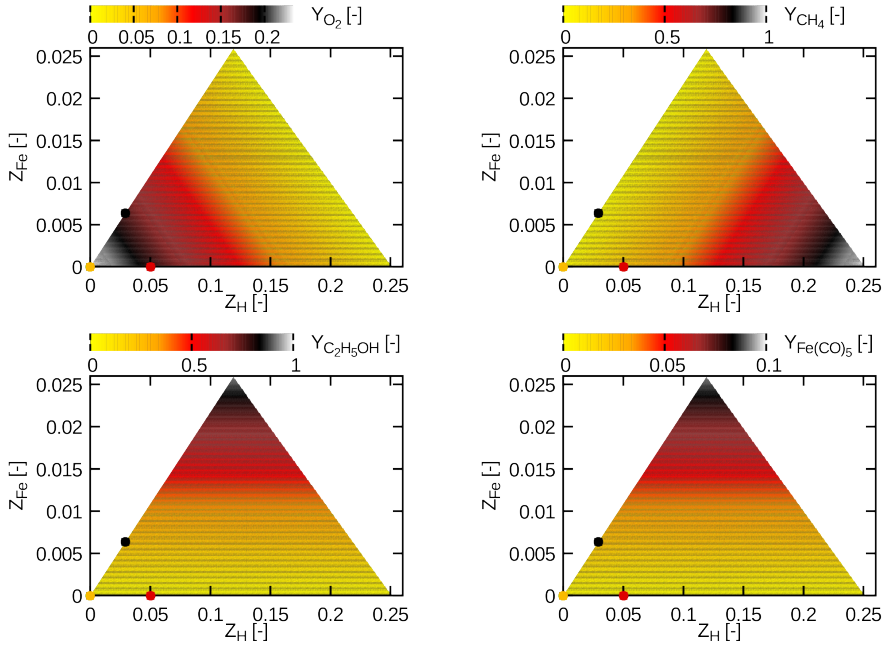

Figure 3.1: Range of validity of Z_H and Z_{Fe} illustrated by the mass fractions of oxygen, methane, ethanol and iron-pentacarbonyl [166].

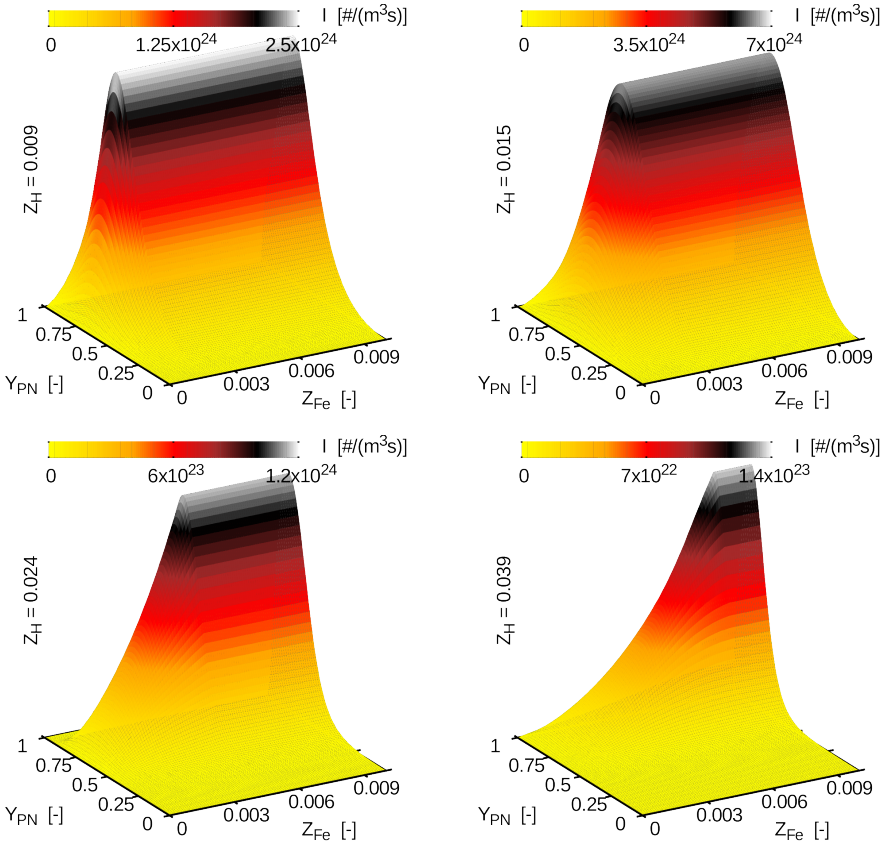

Figure 3.2: Particle formation source term I tabulated as a function of the element mass fractions of hydrogen Z_H and iron Z_{Fe} [166].

3.3 Modelling nanoparticle synthesis from the gas phase

A population of nanoparticles may be characterized by the size distribution for the corresponding particle properties, such as particle volume, diameter, fractal shape amongst others. The evolution of the size distribution in space and time for a particle property is described by a population balance equation as outlined and discussed in chapter 2. The general dynamics equation in discrete or continuous form (Eq. (2.71) or (2.74)) is a PBE for the particle synthesis from the gas phase. The GDE includes external processes, such as convection, diffusion, thermophoresis and internal processes, for example nucleation, coagulation, sintering, surface growth and condensation. The external processes lead to a change of the PSD in a sampling volume, but do not change the particle properties in contrast to the internal processes that describe the change of the particle properties due to interactions between the particles. The choice of the resolved physical phenomena depends on the investigated case and must be included in the models if necessary. In the particle synthesis from turbulent flames, the most important external processes are convection and particle diffusion. This diffusion process is, however, orders of magnitude smaller than convection. The most important internal aerosol processes are particle formation due to gas to particle conversion, coagulation and coalescence. The aforementioned external and three internal processes are included in the scope of the present work.

The numerical expenses are too high to solve the general dynamics equation, which describes the evolution of the size distribution for a particle property in space and time, parallel to CFD simulations. Therefore, many modelling approaches have been proposed, which approximate the GDE, either by resolving the particle size distribution (discrete models and sectional models), or models which solve for the moments of the GDE (the method of moment models, the bimodal and the monodisperse model), as illustrated in Fig. 3.3. Furthermore, in flames it may be assumed that the self preserving size distribution due to coagulation is attained after a specific residence time [99, 205]. The time needed to attain the self preserving size distribution depends on the thermochemical state and internal aerosol-dynamic processes involved in the particle formation.

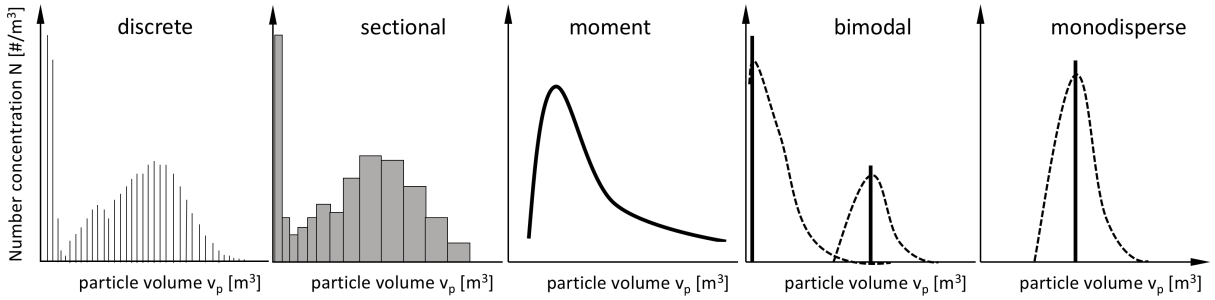

Figure 3.3: Illustration of the particle size distributions as obtained by the discrete, sectional, moment, bimodal and monodisperse models.

In the following section, first a brief overview about the models for the approximation of the GDE is given. Subsequently a detailed description of the used monodisperse, bimodal and sectional model is presented for the large eddy simulation methodology.

3.3.1 Population balance equation model overview

Discrete models

The discrete models are most accurate, since each particle property (e.g. particle volume, area, diameter or fractal shape) is represented by a particle size distribution, i.e. the number concentrations Q_k (particles per volume) for the corresponding particle property resolved in discrete intervals. Commonly, the first resolved particle property is the volume v_k and the number con-

centrations Q_k describe the number of particles with volume v_k in a reference volume. Therefore, one additional transport equation has to be solved for the number concentrations $Q_k(v_k)$ of each integer multiple k, where the discrete volume v_k is equal to the monomer volume times the integer number k, $v_k = k \times v_m$. The consideration of more physical phenomena, for example coalescence, increases not only the modelling effort but also the computational expenses tremendously. This model is not affordable for cases where wide particle size distributions have to be considered like in most practical applications. However, it may be useful to describe in detail nucleation and the initial particle growth and is often used for model validation [47].

Sectional models
The sectional models are based on a similar modelling approach as the discrete model, i.e. additional transport equations are solved for the number concentrations of the particle properties. In the simplest definition of the sectional model, the particle size distribution is given for the particle volume v_k by the corresponding number concentration Q_k. However, the model relaxes the assumption to represent each possible particle property (for example volume v_k) by one discrete size and rather summarizes particle properties in a reduced number of bins or sections, i.e. discretization in size space after continuity assumption, as illustrated in Fig. 3.3 by the PSD for the particle volume. The number of sections depends on the investigated case and the required accuracy. In the present work, the sectional model was applied using up to 75 sections, where section one represents the volume of the monomer particles and the particle volume space was resolved nonlinearly with increasing section number, more details on the resolution of the particle volume space is presented in the results section of this thesis.

Method of moments models
In contrast to the discrete and sectional models, the method of moments does not solve for the different sizes of the particle size distribution, but rather for the moments of the particle size distribution. (Usually, conservation equations are used to describe the evolution of the moments in space and time.) The moments M_k are defined based on the size distribution function n and the particle volume v_p, according to Eq. (3.83) [49, 93].

$$M_k = \int_0^\infty n(v_p) v_p^k \mathrm{dv_p} \tag{3.83}$$

Depending on the order of the moments, they represent different physical properties of the particle size distribution. The zeroth moment ($k = 0$) is the total particle number concentration $N_t = M_0$, with respect to the volume of the dispersion gas. The second moment times π is the surface area concentration of all particles $A_t = \pi M_2$ and the third moment times $\pi/6$ is the volume concentration of all particles $V_t = \pi/6 M_3$. After evaluating the moments by solving their conservation equations, the particle size distribution is subsequently modelled from the moments, based on different assumptions to determine the shape of the distribution function. Common approaches are based on assumed size distribution functions (e.g. normal or log-normal) [93]. The log-normal size distribution function can be calculated from the zeroth moment N_t, the averaged particle volume v_g and the standard deviation σ, according to Eq. (3.84).

$$n(v_p) = \frac{N_t}{3\sqrt{2}\ln\sigma} \exp\left[-\frac{1}{18}\left(\frac{\ln v_p/v_g}{\ln\sigma}\right)^2\right]\frac{1}{v_p} \tag{3.84}$$

More advanced models have been proposed to describe the shape of the size distribution function, e.g. based on stochastic methods [55]. A standard transport equation is used to solve for the moments M_k, with additional terms to describe nucleation, coagulation and sintering, amongst other processes. The three aforementioned moments are quite useful and can be found in the monodisperse and bimodal models (for a monomodal or bimodal particle size distribution, however). Sung et al. [184–186] applied a method of moments model to the prediction of the titania

formation from non-premixed flames in the LES context. In the LES context, the method of moments models are also popular for the modelling of soot [6, 126, 127].

Bimodal and monodisperse model
A special form of the moment models are the bimodal model [73] and the monodisperse model [98]. In the monodisperse model by Kruis et al. [98], nucleation, coagulation and sintering is described by the number concentration N, surface area concentration A and the volume concentration V of aggregate particles. These three quantities correspond to the moments of the particle size distribution function, for monodisperse particles with a monomodal size distribution. The bimodal model solves, additionally to the equations for the aggregation mode, the number concentration, area concentration and volume concentration of the nucleation mode. In the bimodal and monodisperse model, the size distribution is assumed to attain the self preserving size distribution [154] after a certain residence time. The monodisperse and bimodal model were first time applied to large eddy simulations in the present work (according to the authors knowledge).

3.3.2 Sectional model

Compared to the discrete models, the sectional model has the advantage of resolving the size distribution at moderate computational costs. In the current work, for each section k a transport equation for $\widetilde{Q}_k$ is solved, which represents the particle number concentration for particles with constant volume v_k. The model has been adapted from the works of Miller and Garrick [121] or Loeffler et al. [110], who derived the equations for the large eddy simulation approach. The Favre filtered transport equation for the particle number concentration in section k is outlined in Eq. (3.85).

$$\frac{\partial \overline{\rho}\widetilde{Q}_k}{\partial t} + \frac{\partial \overline{\rho}\widetilde{Q}_k \widetilde{u}_j}{\partial x_j} = \frac{\partial}{\partial x_j}\left(\overline{\rho}\left(D_{\widetilde{Q}} + D_t\right)\frac{\partial \widetilde{Q}_k}{\partial x_j}\right) + \overline{\rho}\overline{\dot{\omega}}_k^Q + \overline{\rho}\frac{E}{F_t}\overline{I}\eta_k \tag{3.85}$$

In the above equation, $D_{\widetilde{Q}}$ and D_t are the diffusivity of the particles and turbulent diffusivity respectively. The unclosed turbulent sub-filter fluxes have been modelled with an eddy viscosity approach, with $D_t = \nu_t/\mathrm{Sc_t}$, as proposed by Loeffler et al. [110]. To be consistent with the progress variable, artificial thickening E/F_t may be applied to the nucleation source term I. Section one represents the particle number concentration for monomer particles, hence, nucleation is only considered for the particles in section $k = 1$ with $\eta_{k=1} = 1$ and $\eta_{k\neq 1} = 0$. The coagulation source term $\overline{\dot{\omega}}_k^Q$ incorporates the "birth" and "death" of particles by coagulation and is determined according to Eq. (3.86).

$$\overline{\dot{\omega}}_k^Q = \begin{cases} \underbrace{-\sum_{i=1}^{N_s} \beta_{i1}\widetilde{Q}_i\widetilde{Q}_1}_{\widetilde{Q}_{\mathrm{death}}} & k = 1 \\ \underbrace{\frac{1}{2}\sum_{i=1}^{N_s}\sum_{j=1}^{N_s}\chi_{ijk}\beta_{ij}\widetilde{Q}_i\widetilde{Q}_j}_{\widetilde{Q}_{\mathrm{birth}}} - \underbrace{\sum_{i=1}^{N_s}\beta_{ik}\widetilde{Q}_i\widetilde{Q}_k}_{\widetilde{Q}_{\mathrm{death}}} & k > 1 \end{cases} \tag{3.86}$$

The term $\widetilde{Q}_{\mathrm{birth}}$ of $\overline{\dot{\omega}}_k^Q$ describes the "birth" of new particles in section k, i.e. an increase of the particle number concentration $\widetilde{Q}_k$. The particles added to the number concentration of section k originate from sections i and j, the coagulation kernel β_{ij} describes the collision frequency. The term $\widetilde{Q}_{\mathrm{death}}$ of $\overline{\dot{\omega}}_k^Q$ describes the "death" of particles in section k, i.e. a reduction of the particle number concentration $\widetilde{Q}_k$ due to coagulation of particles in section k with particles from the other section, their collision frequency is described by the coagulation kernel β_{ik}. The volume of

the particles which may not be directly added to section k is distributed to the section k and its neighboring sections $k+1$ or $k-1$. The choice of the coagulation kernel depends on the particle Knudsen number $\mathrm{Kn} = \lambda_{\mathrm{gas}}/\mathrm{r_C}$ (the ratio of the mean free path λ_{gas} of the gas to particle radius r_C) of the investigated case. If the particle Knudsen number is much larger than one ($\mathrm{Kn} \gg 1$), then the coagulation kernel for the free molecular regime can be used as given by Eq. (3.87).

$$\beta_{ij} = \left(\frac{3}{4\pi}\right)^{1/6} \left(\frac{6k_bT}{\rho_p}\right)^{1/2} \left(\frac{1}{v_i} + \frac{1}{v_j}\right)^{1/2} \left(v_i^{1/3} + v_j^{1/3}\right)^2 \tag{3.87}$$

In the previous equation, ρ_p, v_i and v_j are the bulk material density and the volume of the particles in section i and j, respectively. If small and large particles are expected in the investigated case ($\mathrm{Kn} \ll 1$ and $\mathrm{Kn} \gg 1$), the interpolation expression for the coagulation kernel as proposed by Fuchs [50] has to be used. Fuchs' expression of the coagulation kernel is valid for the free molecular to continuum and is determined from the particles diffusivity, diameters, velocities and the transition parameters, (D_i, d_i, c_i and g_i), according to Eq. (3.88).

$$\beta_{ij} = 2\pi \left(D_i + D_j\right)\left(d_i + d_j\right) \left[\frac{d_i + d_j}{d_i + d_j + 2\sqrt{g_i^2 + g_j^2}} + \frac{8\left(D_i + D_j\right)}{\left(d_i + d_j\right)\sqrt{c_i^2 + c_j^2}}\right]^{-1} \tag{3.88}$$

If the volume of the particles coagulating from sections i and j is not exactly the same as the volume of particles in section k, then the number concentrations removed from sections i and j ($\widetilde{Q}_{\mathrm{death}}$) is interpolated and added to the section k and its neighboring section $k+1$ for $v_k \leq (v_i + v_j) < v_{k+1}$ (or to sections k and $k-1$ for $v_{k-1} \leq (v_i + v_j) < v_k$). The interpolation function χ_{ijk} is determined as proposed by Miller and Garrick [121] and is outlined in Eq. 3.89.

$$\chi_{ijk} = \begin{cases} \frac{v_{k+1} - (v_i + v_j)}{v_{k+1} - v_k} & \text{for} \quad v_k \leq (v_i + v_j) < v_{k+1} \\ \frac{(v_i + v_j - v_{k-1})}{v_k - v_{k-1}} & \text{for} \quad v_{k-1} \leq (v_i + v_j) < v_k \\ 0 & \text{otherwise} \end{cases} \tag{3.89}$$

The transition parameter g_k, for the particles in section k, is determined from the particle diameter d_k and the mean free path of the particles L_k, according to Eq. (3.90).

$$g_k = \left[\left(d_k + L_k\right)^3 - \left(d_k^2 + L_k^2\right)^{3/2}\right] \left[3L_k d_k\right]^{-1} - d_k \tag{3.90}$$

For small particles, the transition parameter attains large values and the coagulation kernel accounts for the free molecular regime. For large particles, the transition parameter becomes small and the second part in Eq. (3.88) becomes important and β accounts for the continuum regime. The mean free path L_k of the particles in section k in Eq. (3.90) is determined from the particle diffusivity D_k and velocity c_k according to Eq. (3.91).

$$L_k = \frac{8D_k}{\pi c_k} \tag{3.91}$$

Equation (3.92) is used to calculate the particle velocity c_k, which depends on the gas phase temperature T and the mass of the particles m_k.

$$c_k = \sqrt{\frac{8k_bT}{\pi m_k}} \tag{3.92}$$

The particle diffusivity D_k is calculated according to the Einstein-Smoluchowski relation [108] as outlined below.

$$D_k = \frac{k_bT}{3\pi\mu d_k} C_S \tag{3.93}$$

To account for the inaccuracy of the Einstein-Smoluchowski relation when the particle size is in the order of the mean free path of the gas phase, the Cunningham slip flow correction factor was introduced [108] . In the previous equations, μ is the viscosity of the gas phase and C_S is the Cunningham slip flow correction factor, which is determined from the Knudsen number according to Eq. (3.94).

$$C_S = \frac{5 + 4\mathrm{Kn_k} + 6\mathrm{Kn_k^2} + 18\mathrm{Kn_k^3}}{5 - \mathrm{Kn_k} + (8+\pi)\mathrm{Kn_k^2}} \tag{3.94}$$

The nucleation source term I represents the number of newly produced monomer particles per time and volume and is defined as the change of the molar concentration C times the Avogadro number as outlined in Eq. (3.95).

$$I_m = \frac{\mathrm{dC_{NP}}}{\mathrm{dt}} N_A \tag{3.95}$$

In the present work, the nucleation source term is calculated prior to the CFD, within the freely propagating flames and is stored as a function of the control variables Z_α and Y_P in the look-up table.
The volume averaged particle diameter d_m is determined from averaged particle volume v_m:

$$v_m = \frac{\sum_{k=1}^{N_s} Q_k v_k}{\sum_{k=1}^{N_s} Q_k} \qquad \Rightarrow \qquad d_m = \left(\frac{6}{\pi} v_m\right)^{1/3}. \tag{3.96}$$

3.3.3 Monodisperse model

Kruis et al. [98] proposed the simple monodisperse model for the synthesis of nanoparticles from the gas phase, in which they introduced one additional transport equation for a) the total number concentration N, b) the total surface area concentration A and c) the total volume concentration V of the aggregate particles. As described previously for the moment models, N is proportional to the zeroth moment: $N \propto M_0$, A is proportional to the second moment: $A \propto M_2$ and V is proportional to the third moment: $V \propto M_3$. (The three moments (M_0, M_2 and M_3), however, represent a polydisperse population, in contrast to the monodisperse model where N, A and V correspond to aggregates with a monomodal size distribution.) In the original model the evolution of the particles was described by the coagulation of equally sized particles (or monodisperse particles) and the morphology of the particles by sintering. Coagulation and sintering are described separately in the transport equations for the number concentration and surface area concentration, respectively. The volume concentration is needed to determine different particle properties and diameters. In order to account for nucleation, Panda and Pratsinis [139] included the nucleation source term I in the monodisperse model, which is considered in each transport equation. The Favre filtered conservation equation for the particle number concentration $\widetilde{N}$ is outlined in Eq. (3.97).

$$\frac{\partial \overline{\rho}\widetilde{N}}{\partial t} + \frac{\partial \overline{\rho}\widetilde{N}\widetilde{u}_j}{\partial x_j} = \frac{\partial}{\partial x_j}\left(\overline{\rho}\left(D + D_t\right)\frac{\partial \widetilde{N}}{\partial x_j}\right) + \frac{E}{F}\overline{\rho} I - \frac{1}{2}\beta \overline{\rho}\widetilde{N}^2 \tag{3.97}$$

The unclosed turbulent sub-filter fluxes have been modelled, as for the sectional model, with an eddy viscosity approach, with $D_t = \nu_t/\mathrm{Sc_t}$. The two different coagulation kernels β, as described for the sectional model in Eqs. (3.87 and 3.88), have been used and investigated in the studies with the monodisperse model. The Favre filtered conservation equation for the surface area concentration $\widetilde{A}$ reads:

$$\frac{\partial \overline{\rho}\widetilde{A}}{\partial t} + \frac{\partial \overline{\rho}\widetilde{A}\widetilde{u}_j}{\partial x_j} = \frac{\partial}{\partial x_j}\left(\overline{\rho}\left(D + D_t\right)\frac{\partial \widetilde{A}}{\partial x_j}\right) + \frac{E}{F}\overline{\rho} I a_m - \frac{1}{\tau}\overline{\rho}\left(\widetilde{A} - \widetilde{A}_s\right). \tag{3.98}$$

The nucleation source term I is multiplied by the surface area of a monomer particle a_m, which is determined from the monomer volume as explained below. The specific sintering time τ in Eq. (3.98) depends on the investigated material system and is also explained below. If the surface area A approaches A_S (the surface area of a completely fused particle), the sintering source term becomes zero. The Favre filtered conservation of the volume concentration $\widetilde{V}$ is outlined in Eq. (3.99).

$$\frac{\partial \overline{\rho}\widetilde{V}}{\partial t} + \frac{\partial \overline{\rho}\widetilde{V}\widetilde{u}_j}{\partial x_j} = \frac{\partial}{\partial x_j}\left(\overline{\rho}\left(D + D_t\right)\frac{\partial \widetilde{V}}{\partial x_j}\right) + \frac{E}{F}\overline{\rho} I v_m \tag{3.99}$$

In the previous equation, v_m is the volume of a monomer particle, which is determined from the molar mass of the nanoparticle species W_{NP}, the density of the bulk material ρ_b and the Avogadro number N_A, respectively, according to the following equation.

$$v_m = \frac{W_{NP}}{\rho_b N_A} \tag{3.100}$$

The volume of the monomer particles v_m is assumed to be the volume of the corresponding particle molecules in gaseous state, the corresponding monomer diameter and area are determined from the monomer volume. The coagulation kernels used in the monodisperse model are calculated as described for the sectional model, however by assuming monosized particles with the same particle volumes, diameters, diffusivities, velocities and transition parameters, $v_i = v_j$, $d_i = d_j$, $D_i = D_j$, $c_i = c_j$ and $g_i = g_j$, respectively. Furthermore, the solid sphere diameter d_p (or d_a) is replaced with the collision diameter d_c, to account for the fractal shape of the particles [98]. The coagulation kernel for the free molecular regime is then determined from Eq. (3.101).

$$\beta = 4 d_p^2 \sqrt[2]{\frac{k_b T}{\frac{1}{6}\pi \rho_m d_c^3}} \tag{3.101}$$

The coagulation kernel for the free molecular to continuum regime and monodisperse particles is expressed according to Fuchs' interpolation formula, as outlined in Eq. (3.102).

$$\beta = 4\pi d_c \mathcal{D}\left[\frac{\frac{1}{2}d_c}{d_c + \sqrt{2}g} + \frac{\sqrt{2}\mathcal{D}}{c\frac{1}{2}d_c}\right]^{-1} \tag{3.102}$$

With the same assumption as for the coagulation kernel (monodisperse particles and replacing the particle diameter with the collision diameter), the transition parameter g, the mean free path of the particles L, the particle velocity and the particle diffusivity are calculated according to Eqs. (3.102-3.106).

$$g = \left[\left(d_c + L\right)^3 - \left(d_c^2 + L^2\right)^{1.5}\right] \;/\; \left[3\, L\, d_c\right] - d_c \tag{3.103}$$

$$L = \frac{8D}{\pi c} \tag{3.104}$$

$$c = \sqrt{\frac{8 k_b T}{\pi m}} \tag{3.105}$$

$$D = \frac{k_b T}{3\pi \mu d_c} \tag{3.106}$$

The applied specific sintering time τ is a linear function of the primary particle diameter d_p and an exponential function of the specific activation temperature T_a and the temperature of the fluid T, as outlined in Eq. (3.107).

$$\tau = a d_p e^{\frac{T_a}{T}\left(1 - \frac{d_{p,min}}{d_p}\right)} \tag{3.107}$$

The activation temperature and pre-exponential factor as proposed by Kingery [86] and applied by Tsantilis et al. [194] in the monodisperse model, with $a = 6.5 \times 10^{-17}$ and $T_a = 8.3 \times 10^4$, have been used in the present work to describe sintering of silica particles. The surface area concentration of the completely fused or sintered particles is determined according to Eq. (3.108).

$$A_S = \left(\frac{V}{N v_m}\right)^{\frac{2}{3}} N a_m \tag{3.108}$$

The aggregate particle diameter is calculated from the aggregate volume concentration and the aggregate number concentration according to Eq. (3.109).

$$d_a = \left(\frac{6V}{\pi N}\right)^{\frac{1}{3}} \tag{3.109}$$

The primary particle diameter is calculated from the aggregate volume concentration and the aggregate surface area concentration, as outlined by Eq. 3.110.

$$d_p = \left(\frac{6V}{A}\right) \tag{3.110}$$

The number of primary particles is determined from the equation below.

$$n_p = \frac{6V}{\pi N d_p^3} \tag{3.111}$$

The collision diameter is computed according to Eq.(3.112).

$$d_c = d_p n_p^{\frac{1}{d_f}} \tag{3.112}$$

3.3.4 Bimodal model

It is well known that the particle formation source term I in the monodisperse model leads to an underprediction of the particle diameter as new monomers after nucleation are added to the existing aggregates. For this reason Jeong and Choi [73] proposed "a simple bimodal model for the evolution of non-spherical particles undergoing nucleation, coagulation and coalescence" with two modes − based on Kruis' monodisperse model. The first mode (nucleation mode) describes the evolution of monomer particles due to nucleation and coagulation and is fully described by the monomer particle number-, area- and volume concentration N_1, A_1 and V_1, respectively. The second mode (aggregation mode) describes the evolution of aggregates due to coagulation and coalescence by the particle number-, area- and volume concentration of mode two, N_2, A_2 and V_2, respectively. The modes are coupled via inter-mode coagulation source terms, as explained in more detail below.
The number concentration of the nucleation moder changes due to particle formation (described by source term I), intra-mode coagulation of particles from the nucleation mode (the collision frequency is described by coagulation kernel β_{11}) and inter-mode coagulation of particles from nucleation mode with particles from aggregation mode (the collision frequency is described by coagulation kernel β_{12}). The Favre filtered transport equation for the particle number concentration is outlined in Eq. (3.113).

$$\begin{aligned}\frac{\partial \overline{\rho}\widetilde{N}_1}{\partial t} + \frac{\partial \overline{\rho}\widetilde{N}_1\widetilde{u}_j}{\partial x_j} =& \frac{\partial}{\partial x_j}\left(\overline{\rho}\left(D_1 + D_t\right)\frac{\partial \widetilde{N}_1}{\partial x_j}\right) + \\ & \frac{E}{F}\overline{\rho}I - \frac{1}{2}\beta_{11}\overline{\rho}\widetilde{N}_1\widetilde{N}_1\left(\frac{r}{r-1}\right) - \beta_{12}\overline{\rho}\widetilde{N}_1\widetilde{N}_2\end{aligned} \tag{3.113}$$

As the particles of the nucleation mode are considered to keep their morphology (no coalescence), the particle volume concentration and area concentration are calculated from the number concentration, the monomer area a_m and the monomer volume v_m, as given below.

$$\widetilde{A}_1 = \widetilde{N}_1 a_m \tag{3.114}$$

$$\widetilde{V}_1 = \widetilde{N}_1 v_m \tag{3.115}$$

Besides the transport equation for the number concentration of the nucleation mode $\widetilde{N}_1$, three additional transport equations are solved for the aggregation mode, i.e. the particle number concentration $\widetilde{N}_2$, the particle area concentration $\widetilde{A}_2$ and the particle volume concentration $\widetilde{V}_2$ of the aggregates, as outlined in Eqs. (3.116-3.117), (in a Favre filtered formulation).

$$\begin{aligned}\frac{\partial \overline{\rho}\widetilde{N}_2}{\partial t} + \frac{\partial \overline{\rho}\widetilde{N}_2\widetilde{u}_j}{\partial x_j} =& \frac{\partial}{\partial x_j}\left(\overline{\rho}\left(D_2 + D_t\right)\frac{\partial \widetilde{N}_2}{\partial x_j}\right) + \\ & \frac{1}{2}\beta_{11}\overline{\rho}\widetilde{N}_1\widetilde{N}_1\left(\frac{1}{r-1}\right) - \frac{1}{2}\beta_{22}\overline{\rho}\widetilde{N}_2\widetilde{N}_2\end{aligned} \tag{3.116}$$

The number concentration of the aggregation mode ($\widetilde{N}_2$) increases due to intra-mode coagulation of particles from the nucleation mode (described by the coagulation kernel β_{11}), and reduces due to intra-mode coagulation of particles from the aggregation mode (described by the coagulation kernel β_{22}).
The volume concentration of the aggregation mode ($\widetilde{V}_2$) increases due to intra-mode coagulation of particles from the nucleation mode (described by the coagulation kernel β_{11}) and due to inter-mode coagulation of particles from the nucleation mode with particles from the aggregation mode (described by the coagulation kernel β_{12}), as outlined in Eq. (3.117).

$$\begin{aligned}\frac{\partial \overline{\rho}\widetilde{V}_2}{\partial t} + \frac{\partial \overline{\rho}\widetilde{V}_2\widetilde{u}_j}{\partial x_j} =& \frac{\partial}{\partial x_j}\left(\overline{\rho}\left(D_2 + D_t\right)\frac{\partial \widetilde{V}_2}{\partial x_j}\right) + \\ & \frac{1}{2}\beta_{11}\overline{\rho}\widetilde{N}_1\widetilde{N}_1\left(\frac{r}{r-1}\right)v_m + \beta_{12}\overline{\rho}\widetilde{N}_1\widetilde{N}_2 v_m\end{aligned} \tag{3.117}$$

The area concentration of the aggregation mode increases due to particles coming from the nucleation mode by intra-mode coagulation (β_{11}), and due to particles from inter-mode coagulation of particles from nucleation and aggregation mode (β_{12}) and reduces due to sintering of particles in the aggregation mode, as outlined by the Favre filtered transport equation for $\widetilde{A}_2$.

$$\begin{aligned}\frac{\partial \overline{\rho}\widetilde{A}_2}{\partial t} + \frac{\partial \overline{\rho}\widetilde{A}_2\widetilde{u}_j}{\partial x_j} =& \frac{\partial}{\partial x_j}\left(\overline{\rho}\left(D_2 + D_t\right)\frac{\partial \widetilde{A}_2}{\partial x_j}\right) + \\ & \frac{1}{2}\beta_{11}\overline{\rho}\widetilde{N}_1\widetilde{N}_1\left(\frac{r}{r-1}\right)a_m + \beta_{12}\overline{\rho}\widetilde{N}_1\widetilde{N}_2 a_m - \frac{1}{\tau_p}\left(\widetilde{A}_2 - \widetilde{N}_2 a_{2,s}\right)\end{aligned} \tag{3.118}$$

The coagulation kernel β_{ij} (with $i\{1,2\}$ and $j\{1,2\}$) in Eqs. (3.113-3.118) is based on the same assumptions as in the two previous particle models. For the free molecular regime β_{ij} is computed according to Eq. (3.87), for the free molecular regime to continuum regime according to Fuchs' interpolation formula, as outlined by Eq. (3.88). The transition parameter g_i, the particle velocity c_i, the particle mean free path L_i and particle diffusivity D_i are calculated according to Eqs. (3.90-3.93). As described for the monodisperse model, the solid sphere diameter in the aforementioned equations is replaced by the collision diameter (for mode two, $i = 2$) to account for the fractal shape of the aggregate particles. The function r redistributes newly aggregated particles, whose size does not coincide with the particles in the nucleation or aggregation mode, so that the particle number and volume is conserved. The function r is determined as described

by Jeong and Choi [73]. Sintering in Eq. (3.118) is determined as described for the monodisperse model.
As in the monodisperse model, the aggregate diameter d_a, the primary particle diameter d_p, the number of primary particles n_p and the collision diameter d_c may be calculated from the number-, area- and volume concentration of mode two, as outlined below.

$$d_a = \left(\frac{6V_2}{\pi N_2}\right)^{\frac{1}{3}} \quad , \quad d_p = \left(\frac{6V_2}{A_2}\right) \quad , \quad d_c = d_p n_p^{\frac{1}{d_f}} \tag{3.119}$$

$$n_p = \frac{6V_2}{\pi N_2 d_p^3} \tag{3.120}$$

Besides the diameters of the monomer- and aggregate particles, the bimodal model also yields the volume averaged particle diameter d_{av}, which is obtained from the total volume concentration ($V_t = V_1 + V_2$) and the total number concentration ($N_t = N_1 + N_2$) based on the averaged particle volume $v_{av} = V_t/N_t$ according to Eq. (3.121).

$$d_{av} = \left(\frac{6}{\pi} v_{av}\right)^{1/3} = \left(\frac{6}{\pi}\frac{V_t}{N_t}\right)^{1/3} \tag{3.121}$$

3.3.5 Particle model assumptions

Particle model assumptions are made as in previous works by Sung et al. [185], Gröhn et al. [60], Mueller and Pitsch [126, 127] or Bisette et al. [6], where the particle diffusion is neglected due to their low diffusivity. The unresolved turbulent fluxes are modelled with an eddy diffusivity approach as proposed by e.g. Loeffler et al. [110]. Furthermore, it is assumed that gas phase molecules of the particle species represent particle monomers. Hence, the nucleation source term I is determined from the change of the molar concentration of particle species and the Avogadro number (as given by Eq. (3.95)) prior to the CFD simulations and is stored in the look-up tables as a function of the control variables Z_α and Y_{PN} ($I = f(Z_H, Z_{Si}, Y_{PN})$).

3.3.6 Sub-filter modelling of PBE models in LES

In the presented work, the sub-filter distributions of the nucleation source term, particle number concentration, particle area concentrations and particle volume concentrations were described by delta functions. Hence, a sub-filter model for the determination of the nucleation-, aggregation and sintering source term was neglected. For future work, it is recommended to develop and apply a sub-filter model for the aforementioned source terms. For the sake of simplicity, the distribution of the particles within the LES filter width is assumed to be homogeneous for the modelling of nucleation, agglomeration and sintering. As described in the ATF approach for combustion modelling, artificial thickening $\frac{E}{F}$ is applied to the source terms to be consistent with the gas phase distribution of the particle species which is looked-up depending on the normalized reaction progress variable.

3.3.7 Validation of the sectional, bimodal and monodisperse model

Space and time resolved statistics from in-situ measurements of the particle properties, such as diameter, number concentration, and size distribution are hard to obtain − especially together with gas phase and spray statics. This is in contrast to the standards of the turbulent flame community around the TNF [1] workshop, where detailed and complete sets of data are provided for the PDF's of velocity, temperature and gas species [8, 172], or the ECN community where statistics of the liquid droplets such as diameters and velocities are measured [57]. Therefore, a detailed comparison of the predicted particle properties to experimental data is not possible for the majority of lab-scale burners. Consequently, the validity and correctness of the models and their implementation must be proofed differently.

Chapter 4
Numerical treatment

The conservation equations for the flow field, the spray formation, the chemical kinetics and the aerosol dynamics describe a reacting multiphase flow with particle synthesis from an arbitrary flame. Analytical solutions for the derived or given conservation equations are not known must be solved by numerical treatment. Starting point is the partial differential equation for an arbitrary quantity ϕ, which consists of an accumulation term, convection term, diffusion term and source term, respectively, as outlined in Eq. (4.1). (For the sake of clarity, the numerical treatment is shown for the non filtered or averaged equations.)

$$\underbrace{\frac{\partial \rho\phi}{\partial t}}_{\text{accumulation}} + \underbrace{\frac{\partial \rho\phi u_j}{\partial x_j}}_{\text{convection}} = \underbrace{\frac{\partial}{\partial x_j}\left(\rho D_\phi \frac{\partial \phi}{\partial x_j}\right)}_{\text{diffusion}} + \underbrace{\dot{\omega}_\phi}_{\text{source}} \tag{4.1}$$

The methods applied in the numerical treatment for the solution of Eq. (4.1) depend on the different terms outlined in Eq. (4.1): spatial discretization is required for the convective and diffusive terms and temporal discretization for the accumulation term to advance the solution in time. The treatments applied to the aforementioned terms are summarized and discussed in the following sections, starting with the conservation equations in integral form for the arbitrary quantity ϕ as outlined below.

$$\int_V \frac{\partial \rho\phi}{\partial t}\mathrm{dV} + \int_\mathrm{V} \frac{\partial \rho\phi \mathrm{u_j}}{\partial \mathrm{x_j}}\mathrm{dV} = + \int_\mathrm{V} \frac{\partial}{\partial \mathrm{x_j}}\left(\rho \mathrm{D}_\phi \frac{\partial \phi}{\partial \mathrm{x_j}}\right)\mathrm{dV} + \int_\mathrm{V} \dot{\omega}_\phi \mathrm{dV} \tag{4.2}$$

4.1 Spatial discretization

In the present work, spatial discretization of the convective and diffusive fluxes is achieved by the finite volume method as in the majority of computational fluid dynamics codes.

4.1.1 Finite volume method

In the finite volume method (FVM), the conservation equations in integral form may be written for finite volumes ΔV. The volume integrals of the convection and diffusion terms are replaced by surface integrals using the divergence theorem, also known as Gauss theorem:

$$\int_\mathrm{dV} \frac{\partial F_j}{\partial x_j}\mathrm{dV} = \int_\mathrm{dA} \mathrm{F_j n_j dA}. \tag{4.3}$$

Replacing the volume integrals of the convection and diffusion terms, and writing the temporal derivative outside of the volume integral yields:

$$\frac{\partial}{\partial t}\left(\int_V \rho\phi \mathrm{dV}\right) + \int_A (\rho\phi u_j)\, n_j \mathrm{dA} = \int_\mathrm{A} \left(\rho \mathrm{D}_\phi \frac{\partial \phi}{\partial \mathrm{x_j}}\right)\mathrm{n_j dA} + \int_\mathrm{V} \dot{\omega}_\phi \mathrm{dV}. \tag{4.4}$$

In the finite volume method, the physical flow field is discretized by a large number of control volumes, which together form the numerical grid. In the present work, the finite volume cells are Cartesian and equidistant as sketched in Fig. 4.1. Due to the fact that the cell size Δ is equal

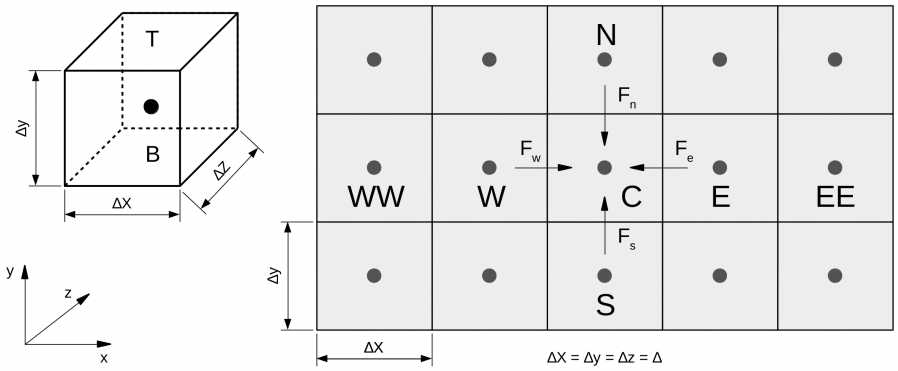

Figure 4.1: Illustration of a Cartesian numerical 2D mesh.

for all three directions, $\Delta = \Delta x = \Delta y = \Delta z$, the area of one face A_f and volume of one cell V_C are determined as outlined below.

$$V_C = \Delta^3 \qquad \text{and} \qquad A_f = \Delta^2 \tag{4.5}$$

The cell C is surrounded by its neighbours in the east E, west W, north N, south S, top T and bottom B, separated by the faces f in the corresponding direction of area A_e, A_w, A_n, A_s, A_t and A_b. The volume and surface integrals of ϕ in Eq. (4.4) are approximated by the mid-point rule (even though more sophisticated models are available) based on the values in the cell center and the cell face center according to

$$\int_V \phi \mathrm{dV} \approx \phi_\mathrm{C} \mathrm{V_C} \qquad \text{and} \qquad \int_\mathrm{A} \phi \mathrm{dA} \approx \phi_{\mathrm{S_l}} \mathrm{A_f}. \tag{4.6}$$

For the sake of simplicity, the equations in the following sections are given without density. The fluxes on the cell face centers F_f as shown in Fig. 4.1, are defined as the sum of the convective and diffusive flux, for example the flux on the western face is: $F_w = F_{w,C} + F_{w,D}$.

4.1.2 Convective fluxes

The convective fluxes of ϕ into cell C over the cell faces f are denoted as $F_{f,C}$ (with $F_{e,C}$, $F_{w,C}$, $F_{n,C}$, $F_{s,C}$, $F_{t,C}$ and $F_{b,C}$). With this, the surface integral of the convective term is approximated as the sum of the fluxes over cell faces, as given by Eq. (4.7).

$$\int_A (\phi u_j)\, n_j \mathrm{dA} \approx \sum_{\mathrm{f=e,w,n,s,t,b}} \mathrm{F_{f,C}} \tag{4.7}$$

These convective fluxes are computed from the velocities u_f on and normal to the face center, the face area A_f and the scalar quantity ϕ_f on face f, as outlined below.

$$F_{f,C} \approx \phi_f u_f A_f \tag{4.8}$$

The solution of Eq. (4.8) requires the knowledge of ϕ and u on the face center, although only the cell center values are known. The interpolation of the cell center values to the centers of the cell faces is achieved by different methods, which are more or less accurate and lead to more or less smoothening of the interpolated quantity ϕ. An overview about interpolation schemes in computational fluid dynamics is given for example by Versteeg and Malalasekera [206]. The methods applied in the scope of this work are summarized below.

The **upwind differencing scheme** (**UDS**) is first order accurate, most stable but leads to a strong smoothening of the solution. The smoothening needs to be avoided to reduce the numerical

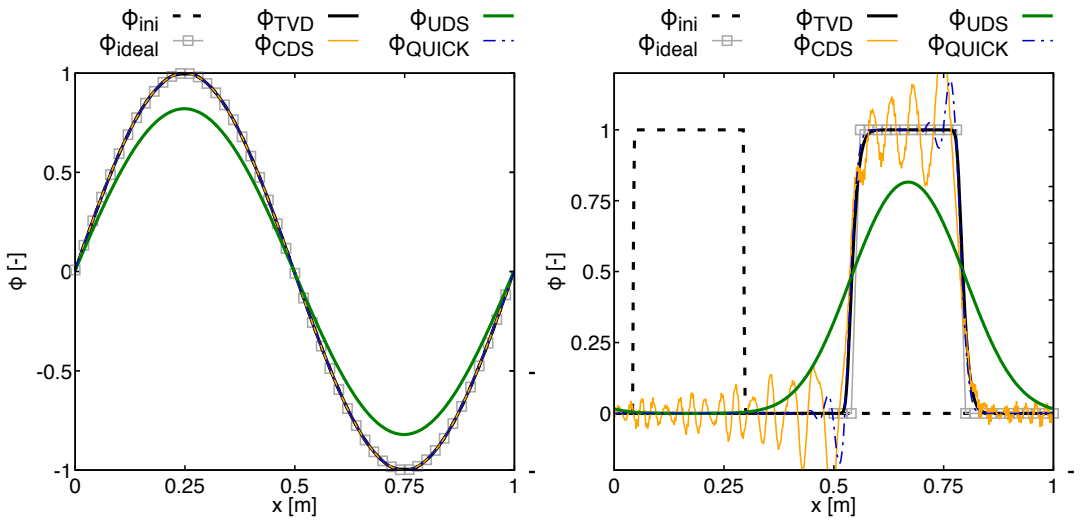

Figure 4.2: Illustration of the accuracy and stability of the numerical schemes for a ϕ field on an equidistant 1D mesh, initialized with a sin function (left) and a top-hat function (right). The numerical domain has a length of 1 m. A constant velocity of 1 m/s is used and periodic boundaries are applied. The simulation is performed for ten run-through times. An explicit third order Runge-Kutta scheme is used for temporal integration over 1 s, leading to the wave traveling one way length.

error. The velocity u_f and the scalar quantity ϕ_f on the cell face f are not interpolated from two neighbouring cells, but the cell center value upstream of f is substituted instead:

$$\phi_f = \phi_U. \tag{4.9}$$

The second order accurate **central differencing scheme** (**CDS**) may introduce instabilities. ϕ_f and u_f on the face center f are determined by a simple linear interpolation between the cell center values of the two neighbouring cells, here shown for ϕ located on the western cell face w.

$$\phi_w = \frac{\phi_W + \phi_C}{2} \tag{4.10}$$

The **quadratic upstream interpolation for convective kinematics** (**QUICK**) aims to improve the accuracy and reduce the smoothening of the UDS scheme. Therefore, the value of ϕ on the cell face is interpolated from the two bracketing nodes and one upstream node.

$$\phi_w = \begin{cases} \frac{6}{8}\phi_W + \frac{3}{8}\phi_C - \frac{1}{8}\phi_{WW} & u_w > 0 \quad \text{and} \quad u_e > 0 \\ \frac{6}{8}\phi_C + \frac{3}{8}\phi_W - \frac{1}{8}\phi_E & u_w < 0 \quad \text{and} \quad u_e < 0 \end{cases}. \tag{4.11}$$

The **total variation diminishing schemes** (**TVD**) aim to combine the advantages of the central differencing and upwind differencing schemes, i.e. high accuracy with low numerical instability. These properties are achieved by using the CDS as much as possible, especially in regions where the gradients of ϕ are small and the UDS in regions where high gradients would lead to numerical instabilities. A flux limiter function $\theta(r)$ is used to weight the portion of CDS and UDS of the numerical scheme, for example shown for ϕ on the western face.

$$\phi_w = \phi_U + \frac{\theta(r)\,(\phi_U - \phi_{UU})}{2} \tag{4.12}$$

The non-linear CHARM limiter function $\theta(r)$ [226] is used in the scope of this work, which depends on the gradient ratio of r.

$$\theta(r) = \frac{r^*(3r^* + 1)}{(r^* + 1)^2} \tag{4.13}$$

In Eq. (4.13), r^* is defined as $r^* = \max(r, 0)$ and the gradient ratio r is calculated from the cell center values downstream, upstream, and two nodes upstream of the node C as outlined below.

$$r = \frac{\phi_D - \phi_U}{\phi_U - \phi_{UU}} \tag{4.14}$$

Figure 4.2 illustrates the behaviour of the UDS, CDS, QUICK and TVD schemes applied to two simple test cases. The first test case (left) is the convective transport of a smooth sine function for ϕ with a constant velocity of $u = 1\text{m/s}$ through a one dimensional numerical domain with a total length of $L = 1\,m$ and a grid size of $\Delta = 2.5\text{mm}$. Periodic boundaries are used in the east and west. An explicit low storage Runge-Kutta scheme of third order accuracy is used for advancing the solution in time. The simulation is performed for ten run-through times. The CDS, QUICK and TVD schemes are able to conserve the shape of ϕ and do not introduce numerical oscillations. In contrast, the UDS scheme leads to a strong smoothening of ϕ and can not conserve the initial shape. The second test case (right) is the transport of a top-hat function with the same conditions as before. The UDS scheme again leads to strong smoothening, the CDS and QUICK schemes introduce numerical oscillations, and the applied TVD scheme conserves the shape of the initial function and does not lead to numerical instabilities.

4.1.3 Diffusive fluxes

The diffusive fluxes of ϕ into cell C over the cell faces A_f are denoted as $F_{f,D}$. The surface integrals in Eq. (4.4) are approximated based on the fluxes over the cell faces according to the approximation of convective fluxes.

$$\int_A \left(D_\phi \frac{\partial \phi}{\partial x_j} \right) n_j \mathrm{dA} \approx \sum_{\mathrm{f=e,w,n,s,t,b}} \mathrm{F_{f,D}} \tag{4.15}$$

With the equidistant and Cartesian cell, the diffusive flux over the cell face is approximated according to the mid point rule and can be written as outlined below (here shown for the western face A_w).

$$F_{w,D} A_w \approx \left(D_\phi \frac{\partial \phi}{\partial x} \right)_w A_w \tag{4.16}$$

The gradient of ϕ on the face center w is approximated with the central differencing scheme according to Eq. (4.17).

$$\left(\frac{\partial \phi}{\partial x} \right)_w \approx \frac{\phi_C - \phi_W}{\Delta} \tag{4.17}$$

4.2 Temporal discretization

Temporal discretization schemes may be separated into explicit schemes, i.e. the solution of a later time is completely calculated from the state of a previous time, and into implicit schemes, i.e. the solution of the later time is calculated from the previous and later time. While larger time steps may be used in implicit schemes, they are more complicated to implement and harder to solve. In the present work, the first order accurate, explicit Euler scheme and a third order accurate, explicit Runge-Kutta scheme are used, as discussed in this section.
Starting point is again the transport equation for an arbitrary quantity ϕ. The convection, diffusion and source term of Eq. (4.1) are discretized with the aforementioned methods, (are now known) and can be written as the RHS term as outlined in the equation below.

$$\frac{\partial \rho \phi}{\partial t} = \underbrace{- \frac{\partial \rho \phi u_j}{\partial x_j} + \frac{\partial}{\partial x_j} \left(\rho D_\phi \frac{\partial \phi}{\partial x_j} \right) + \dot{\omega}_\phi}_{\mathrm{RHS}} \tag{4.18}$$

In contrast to the RANS approach, the LES technique resolves the unsteady property of the flow variables, i.e. the accumulation term is resolved. Therefore, Eq. (4.18) must be integrated in time. The first order accurate explicit Euler scheme approximates the solution of $(\rho\phi)^{n+1}$ at the new time step $n+1$ from the known values of the previous time step n:

$$\frac{\partial \rho\phi}{\partial t} \approx \frac{\Delta\left(\rho\phi\right)}{\Delta t} = \frac{(\rho\phi)^{n+1} - (\rho\phi)^{n}}{\Delta t} = \mathrm{RHS}. \tag{4.19}$$

From the previous equation, the solution of the new time step can be written as outlined below.

$$(\rho\phi)^{n+1} = (\rho\phi)^{n} + \mathrm{RHS}\Delta\mathrm{t}. \tag{4.20}$$

In the large eddy simulation context, a stable and accurate solution of the equations is crucial. The Euler explicit scheme, however, is not able to fulfill these two conditions. More accurate and stable schemes are the Runge-Kutta schemes, in which the solution of the equations is still based on the known solution of the previous time step, but the integration of one time step is achieved in three subsequent intermediate steps ($m = 1, 2, 3$) [219].

$$\phi^{n_m} = \phi^{n_{m-1}} + b_m q_m \tag{4.21}$$

$$q_m = a_m q_{m-1} + \mathrm{RHS}(\phi^{\mathrm{n_{m-1}}}) \tag{4.22}$$

The equations that are solved for temporal integration are outlined below.

$$\begin{array}{lllllllll}
\phi^{n_1} & = & \phi^{n} & + & b_1\mathrm{RHS}(\phi^{\mathrm{n}})\Delta\mathrm{t} & & & & \\
\phi^{n_2} & = & \phi^{n_1} & + & a_2 b_2\mathrm{RHS}(\phi^{\mathrm{n}})\Delta\mathrm{t} & + & b_2\mathrm{RHS}(\phi^{\mathrm{n_1}})\Delta\mathrm{t} & & \\
\phi^{n_3} & = & \phi^{n_2} & + & a_2 a_3 b_3\mathrm{RHS}(\phi^{\mathrm{n}})\Delta\mathrm{t} & + & a_3 b_3\mathrm{RHS}(\phi^{\mathrm{n_1}})\Delta\mathrm{t} & + & b_3\mathrm{RHS}(\phi^{\mathrm{n_2}})\Delta\mathrm{t}
\end{array} \tag{4.23}$$

The weighting factors used in the previous equations are outlined below.

$$\begin{array}{llllll}
a_1 = 0; & b_1 = +\frac{1}{3}; & w_1 = +\frac{1}{3} \\
a_2 = -\frac{5}{9}; & b_2 = -\frac{15}{16}; & w_2 = +\frac{5}{12} \\
a_3 = -\frac{153}{128}; & b_3 = -\frac{8}{15}; & w_3 = +\frac{1}{4}
\end{array} \tag{4.24}$$

The weighting factors w_1 to w_3 are used to calculate the time during the three sub-steps in the Runge-Kutta method: $t_m = t_{m-1} + w_m \Delta t$.
The time step width must be small enough to ensure stability. This is usually achieved if the information transported by convection and diffusion does not skip any nodes. This is achieved based on the Courant-Friedrichs-Lewy condition/number (CFL).

$$\mathrm{CFL} = \frac{\max|\mathrm{u_i}|}{\Delta/\Delta\mathrm{t}} \qquad \Rightarrow \qquad \Delta\mathrm{t} = \frac{\Delta}{\max|\mathrm{u_i}|}\mathrm{CFL} \tag{4.25}$$

In explicit schemes, the CFL number is restricted to values smaller than one, to ensure the aforementioned condition. If the problem is dominated by diffusion, a further criterion must be introduced to limit the time step width as a function of the diffusive flux. This is achieved based on the diffusivity D, the grid size Δ and the dimensionality $d = \{1, 2, 3\}$ of the problem as given below [156].

$$\Delta t \leq 1\frac{\Delta^2}{D2d} \tag{4.26}$$

4.3 Pressure correction

In contrast to compressible codes, where the density ρ is directly calculated from solving the continuity equation and the pressure from the equation of state, Eq. (2.14), in the present low

Mach number formulation of the flow solver, the pressure gradient in the momentum equation, Eq. (2.5) needs to be determined. For the sake of simplicity the solution algorithm is explained for constant density and the unfiltered conservation equations first.

$$\frac{\partial \rho u_j}{\partial x_j} = 0 \tag{4.27}$$

$$\frac{\partial \rho u_i}{\partial t} = -\frac{\partial \rho u_i u_j}{\partial x_j} - \frac{\partial p}{\partial x_i} + \frac{\partial}{\partial x_j}\left(\mu\left(\frac{\partial u_i}{\partial x_j} + \frac{\partial u_j}{\partial x_i}\right) - \mu\frac{2}{3}\frac{\partial u_k}{\partial x_k}\delta_{ij}\right) + \rho g_i \tag{4.28}$$

Summarizing the right hand side of Eq. (4.28), except of the pressure gradient yields:

$$\frac{\partial \rho u_i}{\partial t} = \mathrm{RHS} - \frac{\partial \mathrm{p}}{\partial \mathrm{x_i}}. \tag{4.29}$$

Solving Eq. (4.29) by an explicit Euler scheme yields

$$(\rho u_i)^{n+1} + \left(\frac{\partial p}{\partial x_i}\Delta t\right)^{n+1} = (\rho u_i)^n + (\mathrm{RHS})^n \frac{\Delta t}{V} \tag{4.30}$$

The pressure term of the new time step is unknown. Therefore, in the first step of the predictor-corrector algorithm, the pressure term is neglected and a predicted momentum $(\rho u_i)^P$ is calculated from the known momentum and RHS of the previous time step.

$$(\rho u_i)^P = (\rho u_i)^{n+1} + \left(\frac{\partial p}{\partial x_i}\Delta t\right)^{n+1} = (\rho u_i)^n + (\mathrm{RHS})^n \frac{\Delta t}{V}. \tag{4.31}$$

The predicted momentum field does usually not fulfill the required continuity condition of the new time step:

$$\left(\frac{\partial \rho u_i}{\partial x_i}\right)^{n+1} = 0. \tag{4.32}$$

Rearranging Eq. (4.31) and substituting it into the previous equations yields the link between the pressure gradient of the new time step and the predicted divergence, i.e. the error in continuity, which is a Poisson type equation.

$$\frac{\partial}{\partial x_i}\left(\frac{\partial p}{\partial x_i}\right)^{n+1} = \frac{1}{\Delta t}\left(\frac{\partial \rho u_i}{\partial x_i}\right)^P \tag{4.33}$$

For reactive cases, the density depends also on the physical conditions of the gas phase and must be considered in calculating the pressure gradient of the new time step (derivation not shown here).

$$\frac{\partial}{\partial x_i}\left(\frac{\partial p}{\partial x_i}\right)^{n+1} = \frac{1}{\Delta t}\left(\frac{\partial \rho}{\partial t}\right) + \frac{1}{\Delta t}\left(\frac{\partial \rho u_i}{\partial x_i}\right)^P \tag{4.34}$$

Solution algorithm including predictor corrector method

Prediction

- Add new droplets to the Lagrangian particle list (in the first Runge-Kutta sub-step).
- Add the source terms $\overline{\dot{\omega}}_{\phi}^{n}$ to the predicted scalar quantities $(\overline{\rho}\widetilde{\phi})^{P}$, here: $(\overline{\rho}\widetilde{Z}_{\alpha})^{P}$, $(\overline{\rho}\widetilde{Y}_{P})^{P}$, $(\overline{\rho}\widetilde{N}_{i})^{P}$, $(\overline{\rho}\widetilde{A}_{i})^{P}$ and $(\overline{\rho}\widetilde{V}_{i})^{P}$.
- Solve the transport equations for $(\overline{\rho})^{P}$ and $\left(\overline{\rho}\widetilde{\phi}\right)^{P}$ with the velocity from the previous time step $\widetilde{u}^{n}$, to obtain the predicted and integrated variables, $(\rho)^{P*}$ $(\overline{\rho}\widetilde{Z}_{\alpha})^{P*}$, $(\overline{\rho}\widetilde{Y}_{P})^{P*}$, $(\overline{\rho}\widetilde{N}_{i})^{P*}$, $(\overline{\rho}\widetilde{A}_{i})^{P*}$ and $(\overline{\rho}\widetilde{V}_{i})^{P*}$.

Chemistry and particle dynamics

- Determine the thermochemical properties, for example the target density $\overline{\rho}^{S}$, viscosity μ and the chemical source term $\overline{\dot{\omega}}_{Y_P}^{n+1}$ for $\overline{\rho}\widetilde{Y}_{P}$, based on the predicted and integrated variables $\overline{\rho}^{P*}$, $(\overline{\rho}\widetilde{Z}_{\alpha})^{P*}$ and $(\overline{\rho}\widetilde{Y}_{P})^{P*}$. (The evaluation of the thermochemical properties depends on the combustion model.)
- Solve the population balance models to obtain the particle properties (e.g. d_{a}^{n+1} or n_{p}^{n+1}) and source terms (e.g. $\beta_{i,j}^{n+1}$) for $\widetilde{N}_{i}^{n+1}$, $\widetilde{A}_{i}^{n+1}$ and $\widetilde{V}_{i}^{n+1}$, based on the predicted and integrated variables $(\overline{\rho}\widetilde{N}_{i})^{P*}$, $(\overline{\rho}\widetilde{A}_{i})^{P*}$ and $(\overline{\rho}\widetilde{V}_{i})^{P*}$.

Projection

- Calculate the pressure field to satisfy continuity, the corrected velocity and momentum of the new time step $(\overline{\rho}\widetilde{u}_{i})^{n+1}$.
- Solve the ordinary differential equations of the Lagrangian fields to determine the droplet motion $x_{d,i}^{n+1}$, $v_{d,i}^{n+1}$ and $a_{d,i}^{n+1}$, mass transfer m_{d}^{n+1} and heat transfer T_{d}^{m+1} with the corresponding source terms for the Eulerian fields.

Correction

- Add the source terms $\overline{\dot{\omega}}_{\phi}^{n+1}$ to the scalar quantities $(\overline{\rho}\widetilde{\phi})^{n}$, here: $(\overline{\rho}\widetilde{Z}_{\alpha})^{n}$, $(\overline{\rho}\widetilde{Y}_{P})^{n}$, $(\overline{\rho}\widetilde{N}_{i})^{n}$, $(\overline{\rho}\widetilde{A}_{i})^{n}$ and $(\overline{\rho}\widetilde{V}_{i})^{n}$.
- Advance the transport equations of the conservative variables to obtain their corresponding fields at the new time step $(\overline{\rho}\widetilde{Z}_{\alpha})^{n+1}$, $(\overline{\rho}\widetilde{Y}_{P})^{n+1}$, $(\overline{\rho}\widetilde{N}_{i})^{n+1}$, $(\overline{\rho}\widetilde{A}_{i})^{n+1}$ and $(\overline{\rho}\widetilde{V}_{i})^{n+1}$.

Finalization

- Apply boundary treatment.
- Interpolate velocities at the cell faces from the momentum.
- Solve turbulence model for the velocity.

4.4 Lagrangian particles

The droplets of the diluted spray phase are described in a Lagrangian framework. In this work, each physical droplet is represented by one numerical particle, for which a set of ordinary differential equations is solved to describe the change of the location $x_{d,i}$, the velocity $u_{d,i}$, the acceleration $a_{d,i}$, the mass m_d and temperature T_d of the droplets d according to Eqs. (2.45,2.46,2.50,2.54). The numerical particles are stored in an array, its size is allocated during the initialisation of the particle routine. Subsequently and in the predictor step of the Euler time integration scheme or in the predictor step during each first Runge-Kutta sub-step new particles are added to the particle list (sourced). The solution of the ordinary differential equations is performed during each Euler step or Runge-Kutta sub-step − after the correction step. For an arbitrary quantity ϕ the Euler integration reads:

$$\phi^{n+1} = \phi^n + \mathrm{RHS}\Delta\mathrm{t} \tag{4.35}$$

The RHS that is integrated depends on the quantity ϕ, for which the equation is solved as summarized in table 4.1. The data exchange from the liquid phase to the gas phase is achieved by

Table 4.1: RHS for each solved droplet property.

ϕ	RHS
x_d	u_d
u_d	$\frac{f_1}{\tau_d}(u_i - u_{d,i}) + \left(1 + \frac{\rho}{\rho_d}\right)$
m_d	$-\frac{\mathrm{Sh}}{3\,\mathrm{Sc}}\frac{m_d}{\tau_d}\ln(1+\mathrm{B_m})$
T_d	$\frac{\mathrm{Nu\,c_p}}{3\,\mathrm{Pr\,c_{pl}}}\frac{(T_g - T_d)}{\tau_d}\frac{\ln(1+\mathrm{B_h})}{\mathrm{B_h}} + \frac{\dot{m}_d L_v}{m_d\, c_{pl}}$

trilinear interpolation of the droplet properties to the corresponding Eulerian field, as illustrated in Fig. 4.3 by a 2D sketch. The distribution of the particle quantity to the eight surrounding cells (in 3D) is outlined for the evaporated droplet mass $\dot{m}_d$ at the location (x, y, z), which is mapped to mixture fraction source term $\Gamma_{Z,ijk}$.

$$\begin{aligned}
\Gamma_{Z,\mathrm{i_m j_m k_m}} &= \alpha_{\mathrm{i_m}}\alpha_{\mathrm{j_m}}\alpha_{\mathrm{k_m}}\dot{m}_d \quad \Gamma_{Z,\mathrm{i_m j_m k_p}} &&= \alpha_{\mathrm{i_m}}\alpha_{\mathrm{j_m}}\alpha_{\mathrm{k_p}}\dot{m}_d \\
\Gamma_{Z,\mathrm{i_p j_p k_m}} &= \alpha_{\mathrm{i_p}}\alpha_{\mathrm{j_p}}\alpha_{\mathrm{k_m}}\dot{m}_d \quad \Gamma_{Z,\mathrm{i_p j_p k_p}} &&= \alpha_{\mathrm{i_p}}\alpha_{\mathrm{j_p}}\alpha_{\mathrm{k_p}}\dot{m}_d \\
\Gamma_{Z,\mathrm{i_m j_p k_m}} &= \alpha_{\mathrm{i_m}}\alpha_{\mathrm{j_p}}\alpha_{\mathrm{k_m}}\dot{m}_d \quad \Gamma_{Z,\mathrm{i_m j_p k_p}} &&= \alpha_{\mathrm{i_m}}\alpha_{\mathrm{j_p}}\alpha_{\mathrm{k_p}}\dot{m}_d \\
\Gamma_{Z,\mathrm{i_p j_m k_m}} &= \alpha_{\mathrm{i_p}}\alpha_{\mathrm{j_m}}\alpha_{\mathrm{k_m}}\dot{m}_d \quad \Gamma_{Z,\mathrm{i_p j_m k_p}} &&= \alpha_{\mathrm{i_p}}\alpha_{\mathrm{j_m}}\alpha_{\mathrm{k_p}}\dot{m}_d
\end{aligned} \tag{4.36}$$

Due to the fact that an orthogonal and equidistant mesh is used, the cell indices i_m, j_m, i_p and j_p for the corresponding particle position are simply determined from the grid size delta Δ, the location of the droplet $x_{d,i}$ and the number of the ghost cells n_G as outlined in the equation below for indices i_m and i_p.

$$i_m = \left\lfloor \frac{x_{d,1}}{\Delta} + n_G + 0.5 \right\rfloor \qquad \text{and} \qquad i_p = i_m + 1 \tag{4.37}$$

The weighting factors α_{ij} depend on the location of the droplets with respect to the surrounding grid cells and are calculated according to the following equations, only shown for x direction.

$$\alpha_{im} = i_p - n_G - 0.5 - \frac{x_{d,1}}{\Delta} \qquad \text{and} \qquad \alpha_{ip} = 1 - \alpha_{im} \tag{4.38}$$

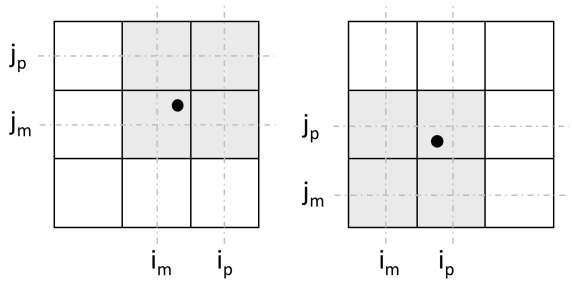

Figure 4.3: Sketch illustrating the trilinear interpolation of a droplet property to a grid in 2 dimensions.

Chapter 5

LES of the Sydney piloted spray flame series with the PFGM/ATF approach and different sub-filter models [164]

Authors: A. Rittler, F. Proch, A.M. Kempf
This chapter including all figures and tables was previously published in 'Combustion and Flame, 162(4), A. Rittler, F. Proch and A. M. Kempf, LES of the Sydney piloted spray flame series with the PFGM/ATF approach and different sub-filter models, 1575-1598, (2015) and is reprinted with permission from Elsevier.
The author A. Rittler developed the code for the spray treatment and the combustion model, produced the thermochemical manifolds, ran all the simulations, wrote the paper and generated all figures and tables.
The author F. Proch developed the code for the gas phase combustion model, and contributed through discussions and proof reading.
The author A. M. Kempf contributed corrections, discussions, proof-reading and the original code.

5.1 Abstract

Detailed numerical investigations of the Sydney spray flame series [57] are presented for ethanol flames referred to as "EtF3, EtF6 and EtF8", which feature identical ethanol mass flow rates but different carrier gas mass flow rates. Large eddy simulations (LES) are performed, where the gaseous and liquid phases are modelled by an Eulerian/Lagrangian approach. The turbulent sub-filter stresses (sgs) are modelled with Nicoud's sigma model [133] on grids with two different resolutions. Combustion is modelled with the premixed flamelet generated manifold approach (PFGM), which is combined with the artificially thickened flame (ATF) method. The sub-filter distributions of the control variables are modelled with (a) a β function (β-fdf) and (b) a top-hat function (TH). First, the influence of the variance in the mixture fraction and reaction progress variable is investigated separately, where the variances are either determined from an algebraic model or a transport equation model. Subsequently, the TH model is used to account for the joint impact of Z and Y_p. The results are compared against the experimental measurements and reference simulations without sub-filter model. The particle statistics are in good agreement with the experimental data. The variances predicted by the two algebraic models are quite similar, whereas the transport equation model predicts variances which are one order of magnitude higher. The results obtained with the TH and the β-fdf model are comparable. It is found that the impact of the sgs models for the mixture fraction and the progress variable increases with an increasing carrier gas mass flow rate.

5.2 Introduction

Liquid fuel spray combustion is found in many technical devices like gas turbines, internal combustion engines or nanoparticle synthesis reactors. The flow structure in these devices is often characterised by high Reynolds and Damköhler numbers. Complex physical phenomena on different time and length scales take place, especially turbulence, chemical reactions and particle interactions. This makes the numerical simulations of such multi-physics and multi-scale flows a challenging task.

The LES method, where the large scales are resolved and only the sub-filter scale quantities

are modelled, has been successfully applied to turbulent combustion: Recent overviews were given by Peters, Poinsot, Pitsch, Janicka and others [69, 144, 150, 151]. Researchers have also shown the suitability of LES for the prediction of reactive multiphase flows in research and engineering [25, 26, 75, 102, 173].

Several models describing the combustion processes in the case of two phase flows are available. Simple one-step models like the eddy break up model (EBU) [115] are used, e.g. for the simulation of coal combustion [45]. More advanced models have been applied to the LES of reactive multiphase flows, e.g. the LES probability density function approach (LES/PDF) [66], where a pdf transport equation is solved by a Lagrangian Monte-Carlo method. The flamelet generated manifold approach (FGM) has also been successfully applied to LES studies of gaseous flames [157, 202, 203], spray flames [25] and internal combustion engines [11]. The mixture fraction (Z), its variance (Z''^2), as well as the progress variable (Y_p) and its variance ($Y_p''^2$) are the usual control variables in the PFGM/ATF approach (for adiabatic conditions). Based on these aforementioned control quantities, the filtered thermo-chemical quantities are determined.

In single phase combustion, the mixture fraction and progress variable variances are commonly modelled as functions of their gradients and a characteristic length scale, that is usually set to the filter width times a model parameter. A constant value is often used for the model parameter, but dynamic models have also been proposed [7, 78]. Pera et al. [141] suggested to consider a spray source term in the equilibrium assumption between production and dissipation for the mixture fraction variance. In gas-phase combustion the variance production depends mainly on the gradient of the mixture fraction. However, in the presence of spray additional variance is produced due to evaporation. The proposed spray source term accounts for the evaporated mass from the liquid droplets. The dissipation is modelled assuming a linear relaxation for the sgs scalar dissipation rate. The model constants may be determined by a dynamic procedure [54]. The mixture fraction and progress variable variances can alternatively be obtained from an additional transport equation, where the spray source term and the sgs scalar dissipation rate remain as unclosed terms. The spray source term is commonly determined from the mixture fraction variance, the evaporated mass and a model constant, where again dynamic models may be applied to determine the constant [141]. Many different approaches have been proposed to determine the unresolved part of the scalar dissipation rate. It is commonly modelled assuming a linear relaxation between the variance and the length scale multiplied by the diffusivity [7, 28, 78, 147].

The specific objective of this work is the application of different models to determine the variances of the mixture fraction and the progress variable and the description of their sub-filter distributions, to investigate how well they work, how much they affect the flame, and to test how well the PFGM modelling concept works for diluted spray flames: first, we compare two different filtered density function (fdf) assumptions: a classical β function (β-fdf) approach for the sub-filter distribution and a top-hat (TH) model. Additionally, the suitability of the memory efficient TH approach for spray combustion is demonstrated. The assumed fdf is parameterized by the Favre-filtered mixture fraction or progress variable ($\widetilde{Z}$ or $\widetilde{Y_p}$) and the respective sub-grid variances ($\widetilde{Z''^2}$ or $\widetilde{Y_p''^2}$). Then, we compare different models for calculating the mixture fraction variance $\widetilde{Z''^2}$, where $\widetilde{Z''^2}$ is determined from (a) two different algebraic models and (b) a transport equation model. Combustion is described with the premixed flamelet generated manifold model combined with the artificial thickened flame approach and a flame sensor formalism [157, 202, 203]. This approach is applied to the well examined experimental spray flame by Gounder, Masri and coworkers [57], which has already been studied by other modellers, turning it into an ideal benchmark for model comparison and analysis [25, 66, 163, 196].

This chapter was first published [164] and is reprinted with permission of the journal

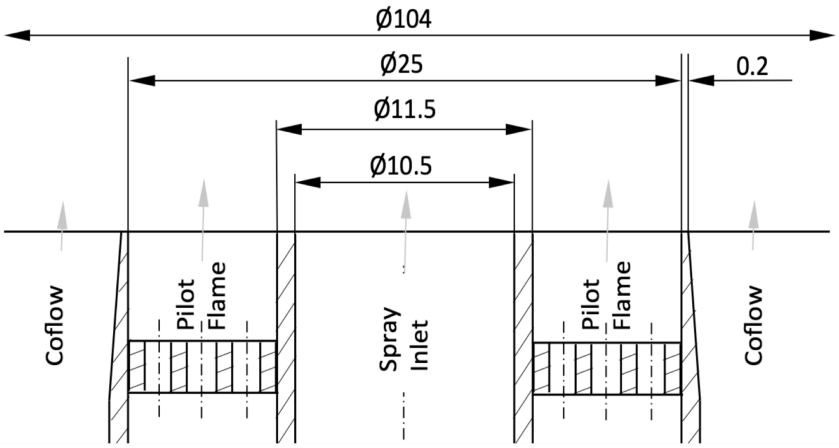

Figure 5.1: Illustration of the jet nozzle exit of the experimental burner setup, as used for the investigated spray flames.

5.3 Experiments

Non-reactive acetone sprays and reactive acetone and ethanol spray flames have been experimentally investigated with a laboratory scale burner by Masri et al. [57] at the University of Sydney. The jet nozzle exit region is sketched in Fig.5.1. The spray flames are stabilized by a concentric pilot flame. The composition of the pilot mixture is stoichiometric and premixed. The fuel used for the pilot flame has the same C/H ratio as the main jet.

The liquid droplets (referred to as particles) are produced by an ultrasonic nebulizer located 215mm upstream of the jet nozzle exit. The particles are initially fed into air with zero momentum. Some evaporation will already occur upstream of the jet nozzle exit. The particle statistics for axial and radial velocities, number density and volume flux are available from Laser Doppler velocimeter and phase-Doppler anemometer (LDV/PDA) measurements [57]. The measurements have been performed at several axial locations ($x/D = 0.3$, 5, 10, 15, 20, 25 and 30). The particles are clustered in five bin size groups (bg1 to bg5), summarizing the particles with diameters in the range of bg1: $0 - 10\,\mu m$, bg2: $10 - 20\,\mu m$ up to bg5: $40 - 50\,\mu m$. Additionally, one bin size group is provided which summarizes the statistics including all particles. The temperature was measured with thermocouples. Of the available fuel and mass flow combinations, we have chosen the ethanol flames referred to as "EtF3, EtF6 and EtF8" [57], with a constant ethanol mass flow rate but different jet mass flow rates. The conditions are summarized in table (5.3).

Table 5.1: Flow conditions for the investigated cases. Shown are the diameters, the mass flow rates, the velocities and the jet Reynolds numbers, as well as the equivalence ratios for the Ethanol flames 3, 6 and 8 (EtF3, EtF6 and EtF8).

CASE	EtF3	EtF6	EtF8
Jet diameter (mm)	10.5	10.5	10.5
Pilot diameter (mm)	25.0	25.0	25.0
Coflow diameter (mm)	104.0	104.0	104.0
Mass-flow carrier air (g/min)	**150**	**225**	**301**
Mass-flow ethanol liquid (g/min)	45	45	45
Mass-flow ethanol measured (g/min)	**30.7**	**41.3**	**36.6**
Bulk velocity jet (m/s)	**24.0**	**36.0**	**48.0**
Bulk velocity pilot, burned (m/s)	14.7	14.7	14.7
Reynolds number jet (1000)	**19.7**	**27.4**	**34.8**
Total equivalence ratio (-)	**2.7**	**1.8**	**1.3**

This chapter was first published [164] and is reprinted with permission of the journal

5.4 Modelling Approach

In the present work, the reactive multiphase flow is modelled using an Eulerian/Lagrangian approach. An equilibrium model is applied to describe the evaporation of the liquid phase. The phases are fully coupled through the exchange of mass and momentum. The gas-phase is described in an Eulerian framework, where the Favre-filtered governing equations for mass (5.1) and momentum (5.2) in the presence of a dilute spray are outlined below.

$$\frac{\partial \overline{\rho}}{\partial t} + \frac{\partial \overline{\rho}\widetilde{u}_j}{\partial x_j} = \dot{\Gamma}_{\overline{\rho}} \tag{5.1}$$

$$\frac{\partial \overline{\rho}\widetilde{u}_i}{\partial t} + \frac{\partial \overline{\rho}\widetilde{u}_i\widetilde{u}_j}{\partial x_j} = -\frac{\partial \overline{p}}{\partial x_i} + \frac{\partial \overline{\tau}_{ij}}{\partial x_j} + \frac{\tau_{ij}^{sgs}}{\partial x_j} + \dot{M}_p \tag{5.2}$$

In Eqs. (5.1) and (5.2), $\widetilde{u}_j$ is the Favre-filtered velocity, $\overline{\rho}$ the density and $\dot{\Gamma}_{\overline{\rho}}$ the evaporation mass source term. The term $\dot{M}_p = \dot{M}_{d_p} + \dot{M}_{\overline{\rho}}$ represents the combined drag and evaporation source terms, which appear to account for the presence of the spray droplets, and are determined from Eq. (5.3).

$$\dot{M}_p = \frac{1}{V}\sum_{i=1}^{N_p}\left(F_{d_p,i} + \dot{m}_{p,i}u_{p,i}\right) \tag{5.3}$$

In Eq. (5.3), $V = \Delta^3$ is the volume of the grid cell and N_p the number of particles that contribute to this cell. The calculation of the drag force (F_{d_p}) and the mass evaporation ($\dot{m}_{p,i}$) is described in section 5.4.5.

The mixture fraction $\widetilde{Z}$ and the progress variable $\widetilde{Y}_P$ are used to describe the chemical state of the mixture. The transport equation for the mixture fraction $\widetilde{Z}$ is given in Eq. (5.4).

$$\frac{\partial \overline{\rho}\widetilde{Z}}{\partial t} + \frac{\partial \overline{\rho}\widetilde{u}_i\widetilde{Z}}{\partial x_i} = \frac{\partial}{\partial x_i}\left(\overline{\rho}D_S\frac{\partial \widetilde{Z}}{\partial x_i}\right) + \dot{\Gamma}_{\widetilde{Z}} \tag{5.4}$$

The diffusion coefficient D_S in Eq. (5.4) is the sum of the molecular and turbulent diffusion $D + D_t$. The turbulent diffusivity is calculated according to $D_t = \nu_t/\mathrm{Sc}_t$, with a constant value of 0.7 for the turbulent Schmidt number Sc_t. The turbulent viscosity $\mu_t = \nu_t\rho$ is calculated with the σ-model which is further discussed in section 5.4.1. The evaporation source terms $\dot{\Gamma}_{\overline{\rho}}$ and $\dot{\Gamma}_{\widetilde{Z}}$ are identical and calculated according to Eq. (5.5).

$$\dot{\Gamma}_{\widetilde{Z}} = \dot{\Gamma}_{\overline{\rho}} = \frac{1}{V}\sum_{i=1}^{N_p}\dot{m}_{p,i} \tag{5.5}$$

The transport equation for the progress variable $\widetilde{Y}_P$, using a thickening procedure was described by e.g. Kuenne et al. [95] and Proch and Kempf [157] and is outlined in Eq. (5.6).

$$\begin{aligned}&\frac{\partial \overline{\rho}\widetilde{Y}_P}{\partial t} + \frac{\partial \overline{\rho}\widetilde{u}_i\widetilde{Y}_P}{\partial x_i} = \\ &\frac{\partial}{\partial x_i}\left(\left[FED_P + (1-\Omega)\frac{\mu_t}{\mathrm{Sc}_t}\right]\frac{\partial \widetilde{Y}_P}{\partial x_i}\right) + \frac{E}{F}\dot{\omega}_P + \dot{\omega}_{P,evp}\end{aligned} \tag{5.6}$$

The progress variable Y_P is defined as the sum of the mass fractions of CO_2, H_2O and H_2, $Y_P = Y_{CO_2} + Y_{H_2O} + Y_{H_2}$. The species used for the reaction progress variable has been successfully applied to large eddy simulations of dilute acetone spray flames by Chrigui et al. [25] - who divided

the mass fractions by the corresponding molar masses. Although more advanced formulations exist for Y_p [67, 134], we found that this definition works well for the investigated case. The thickening factor F is applied to Eq. (5.6) to resolve the thin reaction zone on the computational grid. It is determined from the filter-width Δ, the laminar flame thickness δ_l^0 and the flame sensor Ω, according to Eqs. (5.7) and (5.8).

$$F = 1 + \Omega(F_{max} - 1) \tag{5.7}$$

$$F_{max} = \max\left(\frac{n\Delta}{\delta_l^0}, 1\right) \tag{5.8}$$

The maximum value of F is determined from the number of grid points (n) on which the flame is resolved (as suggested by Charlette et al. [23], n is set to 5), the grid size and the laminar flame thickness. The lower limit for F_{max} of 1 is used to avoid the flame to be thinned if the grid is fine enough to resolve the flame. The efficiency function E accounts for the loss of flame wrinkling due to the artificial thickening of the flame. The source term due to evaporation ($\dot{\omega}_{P,evp}$) is set to zero in the present study. The normalized reaction progress variable C is determined according to Eq. (5.9).

$$C = \frac{Y_p - Y_p^{min}(Z)}{Y_p^{max}(Z) - Y_p^{min}(Z)} \tag{5.9}$$

The flame sensor Ω in Eq. (5.6) indicates the flame region and attains values between zero and one. Instead of the commonly used flame sensor which was proposed by Durand and Polifke [37], an alternative formulation for Ω as suggested by Proch [157] is used and outlined in Eq. (5.10).

$$\Omega = \Omega(C, Z) = \left[\frac{\frac{\mathrm{d}Y_p(x)}{\mathrm{d}x}}{\max\left(\frac{\mathrm{d}Y_p(x)}{\mathrm{d}x}\right)}\right]_{1-D} \tag{5.10}$$

For further information on the applied PFGM/ATF approach, please refer to recent work by Proch and Kempf [157].

The source term $\dot{\omega}_P$ is calculated a priori and stored in the table. Evaporating droplets can also influence the value of the progress variable [35], this can be considered by an additional evaporation source term $\dot{\omega}_{P,evp}$. In the investigated spray flames, however, it is assumed that the major part of the liquid phase evaporates before combustion. For this reason, the source term $\dot{\omega}_{P,evp}$ in Eq. (5.6) is set to zero. Neglecting $\dot{\omega}_{P,evp}$ in the LES of dilute spray flames has shown its suitability for predicting the correct flame behaviour [25, 26, 32].

A trilinear interpolation method in physical space is used to interpolate the source terms (in Eq. (5.1), (5.2) and (5.4)) to the Eulerian phase.

5.4.1 Sub-filter stress modelling

The sigma model, developed by Nicoud et al. [133], is used to account for the effect of the unresolved sub-filter fluctuations of the velocity field. Our previous testing [158, 162] has shown evidence that the model is superior to the static Smagorinsky model, and provided results of the same quality as the dynamic Smagorinsky model - at considerably lower computational costs. The model is particularly well suited for combustion simulations as, opposed to other models, it predicts zero turbulent viscosity and hence no turbulent diffusivity for solid body rotations (which does not matter if a model is only applied for a non-reacting flow without scalar transport). Furthermore, and in contrast to the Smagorinsky model, it predicts zero turbulent viscosity for thermal expansion. Baya-Toda et al. [10] recently showed the supeority of the σ-model over

the dynamic Smagorinsky model for the prediction of a pulsatile impinging jet in a turbulent cross-flow. The turbulent viscosity is calculated as outlined in Eq. (5.11).

$$\mu_t = \overline{\rho} \left(C_m \Delta\right)^2 D_m \tag{5.11}$$

The model parameter C_m is set to 1.5. The differential operator D_m is calculated from the singular values σ_i (with $\sigma_1 \geq \sigma_2 \geq \sigma_3$) according to Eq. (5.12).

$$D_m = \frac{\sigma_3 \left(\sigma_1 - \sigma_2\right) \left(\sigma_2 - \sigma_3\right)}{\sigma_1^2} \tag{5.12}$$

The singular values are identical to the square roots of the eigenvalues of G_{ij}. The tensor G_{ij} is calculated from the velocity gradient following Eq. (5.13).

$$G_{ij} = \frac{\partial u_k}{\partial x_i} \frac{\partial u_k}{\partial x_j} \tag{5.13}$$

The computational cost for the σ-model is approximately 7 times higher than for the Smagorinsky model, albeit at a quality that is similar to the still 4 times more expensive dynamic Smagorinsky model.

5.4.2 Combustion modelling

Combustion is modelled by the PFGM-approach, which is combined with the ATF-method. Within the flammable region, one dimensional simulations of premixed freely propagating flames were performed a priori to tabulate the thermo-chemical quantities as a function of the two control variables ($\phi = f(Z, C)$). Ideal mixing is assumed beyond the flammability limits. The mechanism library Cantera [56] has been used to solve a detailed kinetic mechanism with 57 species and 383 reactions for the combustion of ethanol, developed by Marinov et al. [118]. The thermo-chemical properties and the source terms are stored in a table with a resolution of 201 $\times$ 201 equidistant steps for the mixture fraction and the normalized reaction progress variable. The table ensures a high accuracy in the flammable region, while keeping storage requirements moderate. Without a sub-filter model, the filtered thermo-chemical quantities (ϕ = e.g. $\dot{\omega}$, ρ, D, ...) are only determined by a two-dimensional table lookup as a function of $\widetilde{Z}$ and $\widetilde{C}$: $\widetilde{\phi} = \phi(\widetilde{Z}, \widetilde{C})$. Figure 5.2(a) illustrates the two-dimensional table for the reaction progress variable source term ($\dot{\omega}_P$). The investigated spray flame consists of a cold ethanol/air jet, a hot pilot flame (which has the same C/H ratio as the main jet) and a cold coflow. The applied combustion model is well suited to describe simultaneously the mixing between the air/ethanol stream and the hot pilot, between the hot pilot and the coflow and the mixing between the coflow and the air/ethanol jet. Even though the standard flamelet equations for gas combustion have been applied to turbulent spray flames (e.g. [25, 26, 32]), there are suggestions to improve the FGM method for liquid fuel combustion. Neophytou and Mastorakos [132] performed one-dimensional simulations of n-heptane and n-decane flames and showed that the laminar flame speed is a function of the initial droplet diameter, the equivalence ratio and the particle residence time. According to Neophytou the laminar flame speed would then be additionally determined from the droplet-diameter in the FGM method. In the current work it is assumed that particles evaporate away from the flame front and the laminar flame speed is determined from the mixture fraction only.
Olguin and Gutheil [136] performed simulations of a mono-disperse laminar ethanol/air spray flame in a counter flow configuration and suggest to extend the FGM table by considering the evaporation rate as a third control variable. Two additional terms to account for evaporation and combined evaporation and mixing within the flamelet equation are proposed by the authors. However, the suitability of the proposed model and the suggested pdf shape for turbulent spray flames has not been proven yet.
Furthermore, Hasse and Peters [65] suggested to describe a three-feed system by a two mixture

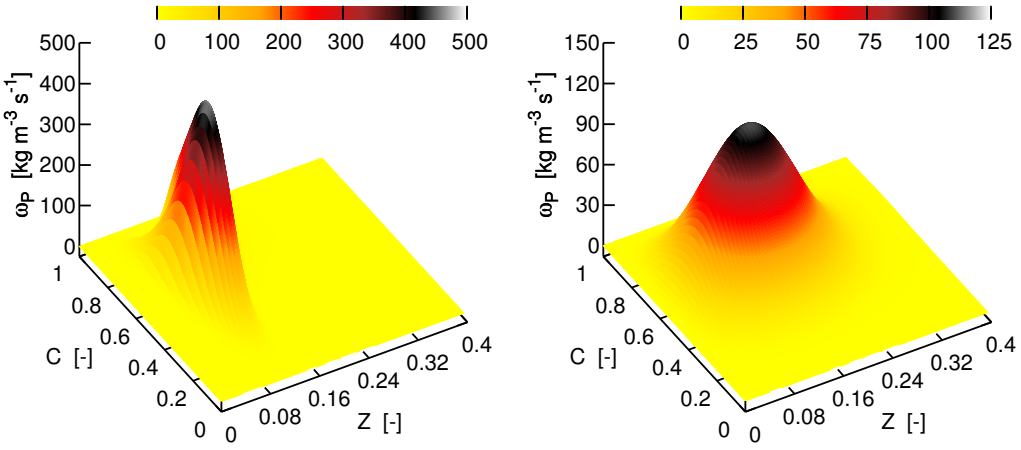

(a) (b)

Figure 5.2: Illustration of the flamelet generated manifold for the reaction progress variable source term $\dot{\omega}_{Y_p}$ (a). Figure (b) illustrates the table for the same quantity, as a function of the mixture fraction ($\widetilde{Z}$), the progress variable ($\widetilde{Y_p}$) and a mixture fraction variance $\widetilde{Z''^2}$ of 0.01 (used in β_{A1}, β_{A2} and β_{Tr}).

fraction approach, where each of them describes the mixing of the one fuel feed with the oxidizer feed. The authors derive two-dimensional flamelet equations to account for the mass and heat transfer between the two mixture fraction fields in the flamelet space. The proposed technique was applied to the simulation of a Diesel engine with a Common-Rail system utilizing a split injection with a main injection and a pilot, which are represented by the two mixture fractions.

5.4.3 Turbulence chemistry interaction

In the LES framework, however, only the filtered control variables are known and the sub-filter distributions remain unknown. A common closure approach is the assumption of a presumed sub-filter distribution for the control variables. In this work, these sgs distributions are described by (a) the commonly used β-fdf model and (b) by a TH model. Generally, the filtered variables are determined from the tabulated values weighted with the joint filtered density function $P(Z, C)$, according to Eq. (5.14).

$$\widetilde{\phi} = \int_{-\infty}^{+\infty} \int_{-\infty}^{+\infty} \phi(Z, C) P(Z, C) dZ dC \tag{5.14}$$

Assuming statistical independence of Z and C, the joint fdf simplifies to the product of two separate fdf's, $P(Z, C) = P(Z)P(C)$. The thermo-chemical quantities can then be determined from the integration over the mixture fraction and progress variable within their ranges of validity ($Z \in (0:1)$ and $C \in (0:1)$) according to Eq. (5.15).

$$\widetilde{\phi}_{ZC} = \int_{0}^{1} \int_{0}^{1} \phi(Z, C) P(Z) P(C) dZ dC \tag{5.15}$$

To study the influence of the sub-filter distribution of Z and C separately, a Dirac-δ function for either $P(Z)$ or $P(C)$ is applied to Eq. (5.15), and the thermo-chemical quantities are calculated according to either Eq. (5.16) or Eq. (5.17).

$$\widetilde{\phi}_{Z} = \int_{0}^{1} \phi(Z, C) P(Z) dZ \tag{5.16}$$

This chapter was first published [164] and is reprinted with permission of the journal

$$\widetilde{\phi}_C = \int_0^1 \phi(Z,C)P(C)dC \tag{5.17}$$

5.4.3.1 The β-fdf assumption

Within the β-fdf model, it is assumed that the sub-filter distributions $P(Z)$ and $P(C)$ can be described with the β function. The shape of the β function is described by Eq. (5.18) [144] (shown here for the mixture fraction and its variance).

$$P(Z) = \frac{Z^{\alpha-1}(1-Z)^{\beta-1}}{\Gamma(\alpha)\Gamma(\beta)}\Gamma(\alpha+\beta) \tag{5.18}$$

The two parameters α and β within the gamma (Γ) function are related to the Favre-filtered mean mixture fraction ($\widetilde{Z}$) and its variance ($\widetilde{Z''^2}$) (or $\widetilde{C}$ and $\widetilde{C''^2}$ respectively) as outlined in Eqs. (5.19) and (5.20).

$$\alpha = \widetilde{Z}\left[\frac{\widetilde{Z}(1-\widetilde{Z})}{\widetilde{Z''^2}} - 1\right] \tag{5.19}$$

$$\beta = (1-\widetilde{Z})\left[\frac{\widetilde{Z}(1-\widetilde{Z})}{\widetilde{Z''^2}} - 1\right] \tag{5.20}$$

To include the dependency on the variance of the mixture fraction and the variance of the progress variable as a third and fourth parameter, the chemistry table must be extended to three or four dimensions, at a very high memory requirement: Each additional dimension will increase the memory requirements by one to two orders of magnitude. Figure 5.2(b) illustrates the progress variable source term for a variance of $\widetilde{Z''^2} = 0.01$.

5.4.3.2 The TH-fdf assumption

In the top-hat approach, it is assumed that the real fields of Z and C are smooth with respect to the computational grid, so that they can be described by tri-linear interpolation between the support points. Floyd et al. [43] have estimated that this assumption is appropriate on grids that are sufficiently fine for an accurate LES. They applied the TH model to the LES of Sandia Flame D and highlighted the shortcomings of the β-fdf in the LES context. Olbricht et al. [135] performed LES of lifted flames in a gas turbine model combustor using the PFGM method with the TH model for the joint impact of the mixture fraction and progress variable variance.
Within the TH model the filtered density functions $P(Z,C)$, $P(Z)$ or $P(C)$ are expressed by top-hat functions which are built within the upper (u) and lower (l) limits of the control variables ($\widetilde{Z}_u$, $\widetilde{Z}_l$, $\widetilde{C}_u$ and $\widetilde{C}_l$ that were derived from Branley and Jones [18] standard gradient model (described in section 5.4.4). The filtered density function reads:

$$P(Z,C) = \begin{cases} \frac{1}{(\widetilde{Z}_u-\widetilde{Z}_l)(\widetilde{C}_u-\widetilde{C}_l)} & \widetilde{Z}_l \le \widetilde{Z} \le \widetilde{Z}_u \text{ and } \widetilde{C}_l \le \widetilde{C} \le \widetilde{C}_u \\ 0 & \text{for all other Z and C} \end{cases} \tag{5.21}$$

Equation (5.14) can then be written as:

$$\widetilde{\phi} = \frac{1}{(\widetilde{Z}_u-\widetilde{Z}_l)(\widetilde{C}_u-\widetilde{C}_l)} \int_{\widetilde{Z}_l}^{\widetilde{Z}_u}\int_{\widetilde{C}_l}^{\widetilde{C}_u} \phi(Z,C)dCdZ \tag{5.22}$$

Usually, a lookup table with $2N$-dimensions would be introduced where the N upper and N lower limits are used as input parameters. Such a $2N$-dimensional table would require excessive amounts

of memory, however, due to the properties of the TH function the $2N$ storage requirements can be reduced to $1N$ only: Instead of introducing new dimensions to the FGM-table, only the antiderivatives $\Phi(Z, C)$ are stored in the table which is integrated a priori according to Eq. (5.23).

$$\widetilde{\Phi} = \int_0^Z \int_0^C \phi(Z, C) dC dZ \tag{5.23}$$

The filtered thermo-chemical quantities $\widetilde{\phi}(\widetilde{Z}, \widetilde{C}, \widetilde{Z''^2}, \widetilde{C''^2})$ are determined from the antiderivatives according to Eq. (5.24).

$$\begin{aligned} \widetilde{\phi}_{ZC} = & \frac{1}{(\widetilde{Z}_u - \widetilde{Z}_l)(\widetilde{C}_u - \widetilde{C}_l)} \\ & \Big[\Phi(\widetilde{Z}_u, \widetilde{C}_u) - \Phi(\widetilde{Z}_u, \widetilde{C}_l) - \Phi(\widetilde{Z}_l, \widetilde{C}_u) + \Phi(\widetilde{Z}_l, \widetilde{C}_l)\Big] \end{aligned} \tag{5.24}$$

The TH approach may also be used to account for the variances in the mixture fraction space or progress variable space separately: the FDF in Eq. (5.21) simplifies to $1/(\widetilde{Z}_u - \widetilde{Z}_l)$ or $1/(\widetilde{C}_u - \widetilde{C}_l)$ respectively and the integration in Eq. (5.23) is performed over the mixture fraction or progress variable only. Generally, small (or zero) variances of $\widetilde{Z''^2}$ and $\widetilde{C''^2}$ lead to divisions by zero in Eq. (5.24). To account for small variances, the upper and lower limits may be expressed by a narrow interval (ϵ_Z and ϵ_C) and the TH may be built for $C_l = C - \epsilon_C$, $C_u = C + \epsilon_C$, $Z_l = Z - \epsilon_Z$ and $Z_u = Z + \epsilon_Z$. (alternatively, $\widetilde{\phi}(Z, C)$ may be determined using a Dirac-δ function). We recommend to implement the tabulation and table access with at least double precision to obtain accurate results. Further detailed information about the TH model and its implementation is given by Floyd et al. [43] or Olbricht et al. [135]. The derivation of the upper (u) and lower (l) limit of the control variables is discussed in the next section.

Figure 5.3(b) shows the integrated TH table for the progress variable source term ($\dot{\omega}_{Y_p}$), that was determined by integration over C. Figures 5.3(c) and 5.3(d) illustrate the tables for $\dot{\omega}_{Y_p}$, obtained by integration over Z and over both C and Z.

The standard β-fdf is built within the limits $Z_{min} = 0$ and $Z_{max} = 1$. In the presence of sprays, however, the upper physical limit for the mixture fraction depends on the vapour pressure of the evaporated fuel ($Z_{max} = f(T)$ or $Z_{max} = f(X, t)$), and thus the standard β-fdf is not valid for all locations. Therefore, Ge and Gutheil [52] proposed to extend the standard β-fdf and built the function within the physical limits $Z_{min} = 0$ and Z_{max}, for boiling droplets the upper limit becomes unity and the scaled function reduces to the standard function. Tyliszczak et al. [195] recently applied the scaled β-fdf to their LES/CMC (conditional moment closure) simulations of a liquid fueled swirl burner, where they set the upper limit to $Z_{max} = 0.7$. To account for the temperature dependency, an additional dimension would have to be introduced to the lookup table, which would again increase the storage requirements by 1-2 orders of magnitude.

The TH-fdf only accounts for the control variables within the physical limits (independent of e.g. the fuel vapour pressure). In contrast to the β-fdf approach, the lookup table in the TH approach remains its dimensionality if the variances of the control variables are used as additional input parameters. The TH assumption is robust, easy to implement and computationally cheap compared to the β-fdf approach.

5.4.4 Gas phase variance modelling

In the present study we compare two algebraic models (referred to as A1 and A2) and one transport equation model (referred to as Tr) to calculate the variance of $\widetilde{Z''^2}$. (The variance $\widetilde{C''^2}$ is determined with the algebraic model A2.)

This chapter was first published [164] and is reprinted with permission of the journal

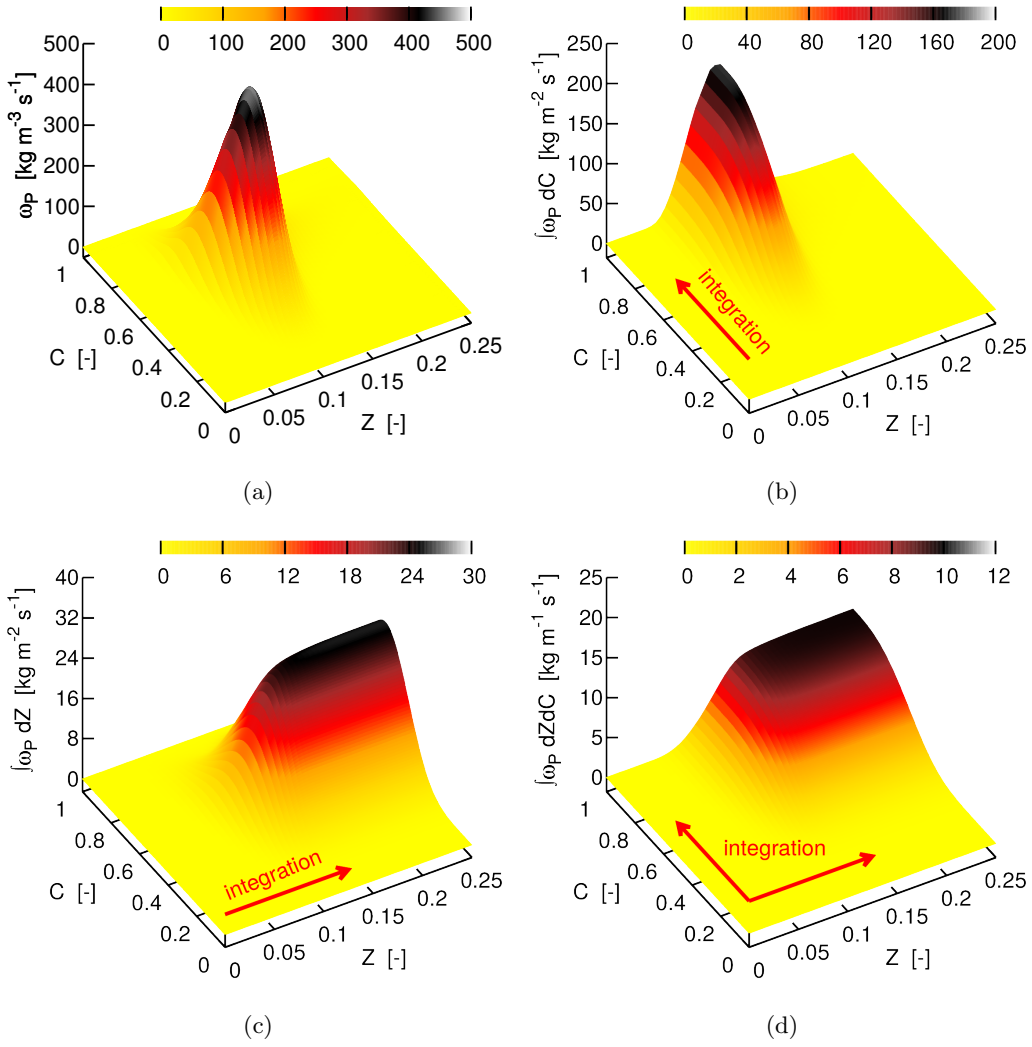

Figure 5.3: Illustration of the PFGM tables for the reaction progress variable source term $\dot{\omega}_{Y_p}$ for (a) the not integrated TH-fdf ($noSGS_C$ and $noSGS_F$) and the integrated tables (b)-(d). The integrations are performed over (b) the normalized reaction progress variable C (TH_C), (c) over the mixture fraction Z (TH_Z) and (d) over both, C and Z (TH_{CZ}).

This chapter was first published [164] and is reprinted with permission of the journal

The gradient model A1 has been proposed by Branley and Jones [18] and was successfully applied to large eddy simulations of spray flames by Chrigui et al. [26] and others. The model depends on the gradient of the filtered mixture fraction (or filtered reaction progress variable) only:

$$\widetilde{Z''^2} = C_{A1}\Delta^2 \left(\frac{\partial \widetilde{Z}}{\partial x_i}\right)^2 \tag{5.25}$$

In the present work, the coefficient C_{A1} is set to 0.15 (as applied to the LES of acetone and ethanol spray flames by Chrigui et al. [25, 26]). Branley and Jones [18] recommended a value of 0.1 for C_{A1}, but dynamic procedures are also available to determine the model parameter [147]. In the β-fdf approach, the filtered variance ($\widetilde{Z''^2}$ or $\widetilde{C''^2}$) is directly used as third input parameter for the table lookup. In the TH model the upper and lower limits of the control variables are required, which are determined from the filtered variances ($\widetilde{Z''^2}$ or $\widetilde{C''^2}$) according to Eq. (5.26), as suggested by Floyd et al. [43].

$$\widetilde{Z}_u = \widetilde{Z} + \frac{1}{2}\sqrt{12\widetilde{Z''^2}} \quad \text{and} \quad \widetilde{Z}_l = \widetilde{Z} - \frac{1}{2}\sqrt{12\widetilde{Z''^2}} \tag{5.26}$$

In the second algebraic model A2, the variances $\widetilde{Z''^2}$ and $\widetilde{C''^2}$ (as used as third input parameter in the β-fdf approach) result from the lower (l) and upper (u) limits of the filtered mixture fraction $\widetilde{Z}$ or filtered progress variable $\widetilde{C}$ according to Eq. (5.27) or (5.28).

$$\widetilde{Z''^2} = C_{A2}\left(\widetilde{Z}_u - \widetilde{Z}_l\right)^2 \tag{5.27}$$

$$\widetilde{C''^2} = C_{A2}\left(\widetilde{C}_u - \widetilde{C}_l\right)^2 \tag{5.28}$$

Within the model A2, the upper and lower values of the control variables ($\widetilde{Z}_u$, $\widetilde{Z}_l$, $\widetilde{C}_u$ and $\widetilde{C}_l$) are determined from the maximum and minimum values on the cell faces.

Floyd et al. [43] and Proch and Kempf [157] pointed out that for a linear profile of $\widetilde{Z}$ (or $\widetilde{C}$), the algebraic models A1 and A2 are identical. The model parameter C_{A2} is set to a value of 1/12.

It should be noted that the algebraic models can only recover the variance resulting from lean and rich gas streams, but not the fluctuations in the near particle region due to evaporation. However, with evaporating droplets the mixture fraction variance can increase, even in laminar flows. This effect of evaporation can be considered by solving a transport equation (Eq. 5.29) for the filtered mixture fraction variance, as given by Pera et al. [141].

$$\begin{aligned}\frac{\partial \overline{\rho}\widetilde{Z''^2}}{\partial t} + \frac{\partial \overline{\rho}\widetilde{u}_i\widetilde{Z''^2}}{\partial x_j} &= \frac{\partial}{\partial x_i}\left(\overline{\rho}D_S\frac{\partial \widetilde{Z''^2}}{\partial x_i}\right) \\ &+ 2\overline{\rho}D_t\left(\frac{\partial \widetilde{Z}}{\partial x_i}\right)^2 - 2\overline{\rho}\overline{S}\chi_{\widetilde{Z}} + \widetilde{\overline{\rho}\dot{W}^+}\end{aligned} \tag{5.29}$$

The term $\overline{S}\chi_{\widetilde{Z}}$ is the unresolved and dominant part of the scalar dissipation rate $\overline{\rho}\widetilde{\chi}$, commonly modelled according to Eq. (5.30).

$$\overline{S}_\chi = C_m D_t \frac{\widetilde{Z''^2}}{L^2} \tag{5.30}$$

The length scale L is usually set to the value of the filter width Δ, with a model constant value of $C_m = 2.0$ (as outlined by Tillou et al. [192] or others). For reactive multiphase flows, however, this

expression is known to lead to insufficient dissipation as the variance resulting from evaporation is normally not introduced on the filter scale but rather on the much smaller scale of the particle separation, leading to faster dissipation. To account for the aforementioned effect, the model constant C_m may be increased. Other approaches for increasing the dissipation rate are to use the maximum of turbulent and molecular diffusivity for D_t [32], or to use a dynamic procedure to determine C_m [7, 78]. In this work we apply a constant value of 8.0 for C_m, as suggested by De et al. [32] (for the same spray flame series).

The unclosed evaporation source term $\widetilde{\overline{\rho}\dot{W}}^{+}$ in Eq. (5.29) is determined according to Eq. (5.31) as suggested by Pera et al. [141].

$$\widetilde{\overline{\rho}\dot{W}}^{+} = \alpha \widetilde{Z''^2} \frac{\widetilde{\overline{\rho}\dot{W}}}{\widetilde{\overline{Z}}} \tag{5.31}$$

A constant value of 0.5 is used for α [192]. However, Pera et al. [141] suggested to use a dynamic procedure to determine the pre-factor α. The term $\widetilde{\overline{\rho}\dot{W}}$ is equal to $\dot{\Gamma}_{\widetilde{Z}}$ in Eq. 5.4.

5.4.5 The dispersed phase

The dispersed phase is modelled in a Lagrangian framework. In the present work, one numerical particle represents one physical droplet. For each particle p, a set of differential equations is solved, where the motion is determined from Eqs. (5.32,5.33).

$$\frac{\mathrm{d}x_{p,i}}{\mathrm{d}t} = u_{p,i} \tag{5.32}$$

$$\frac{\mathrm{d}u_{p,i}}{\mathrm{d}t} = a_{p,i} \tag{5.33}$$

The particle position $x_{p,i}$ and velocity $u_{p,i}$ are calculated from the acceleration $a_{p,i}$, which is modelled according to Eq. (5.34).

$$a_{p,i} = \frac{1}{\tau_p}\left(\widetilde{u}_i - u_{p,i}\right) + \left(1 - \frac{\overline{\rho}}{\rho_p}\right) g_i \tag{5.34}$$

In Eq. (5.34) ρ_p is the density of the liquid droplet, and g_i is the gravitational acceleration. The particle relaxation time τ_p relates the particle density ρ_p and diameter d_p to the gas-phase viscosity μ and the particle Reynolds number Re_p as outlined in Eq. (5.35). The typical particle response time τ_p represents the duration required to adjust the particle velocity to the surrounding flow velocity.

$$\tau_p = \frac{1}{18\mu} \frac{\rho_p d_p^2}{1 + \frac{3}{20}\mathrm{Re}_p^{0.687}} \tag{5.35}$$

The change of the particle diameter is calculated according to the d^2-law [2, 120], assuming equilibrium conditions as outlined in Eq. (5.36).

$$\frac{\mathrm{d}d_p^2}{\mathrm{d}t} = -4\frac{\overline{\rho}}{\rho_p}\mathcal{D}\log\left(1 + B_m\right)\mathrm{Sh} \tag{5.36}$$

The diffusion coefficient $\mathcal{D}$ of the ethanol vapor into the surrounding gas is calculated with the Chapman-Enskog theorem and tabulated prior to the simulation. The Spalding mass transfer number is defined as $B_m = (Y_S - Y_\infty)/(1 - Y_S)$, with the fuel mass fractions at the particle

surface Y_S and far away from the particle Y_∞. The Sherwood number Sh is calculated according to Eq. (5.37).

$$\mathrm{Sh} = 2 + \frac{(2 + 0.552\mathrm{Re}_p^{\frac{1}{2}}\mathrm{Sc}^{\frac{1}{3}}) - 2}{F_m} \tag{5.37}$$

To account for the relative change of the film thickness due to the Stefan flow, the correction factor F_m is used [2, 120]. The fuel vapor mass fraction at the droplet interface is determined from the fuel vapor mole fraction X_s, assuming equilibrium conditions, according to Eq. (5.38)

$$Y_s = Y_{S,eq} = \frac{X_s W_F}{\sum_i X_i W_i} \tag{5.38}$$

The saturated fuel vapor mass fraction X_s is calculated according to the Clausius-Clapeyron relation, as outlined in Eq. (5.39).

$$X_s = \frac{p_B}{p} \exp \frac{L_{evp} W_F}{\mathcal{R}} \left(\frac{1}{T_B} - \frac{1}{T_S} \right) \tag{5.39}$$

In the above equation p_B and T_B are the pressure and the temperature of the liquid fuel at the boiling point, the latent heat of evaporation L_{evp} is assumed to be constant, W_F is the molecular weight of the fuel and $\mathcal{R}$ is the universal gas constant.
The required Eulerian field properties are mapped onto the Lagrangian phase using a trilinear interpolation method in physical space.

5.4.6 Numerical setup and boundary conditions

The simulations have been performed with our LES in-house code PsiPhi [20, 82, 145]. The Favre-filtered conservation equations for mass, momentum, mixture fraction and the reaction progress variable are discretized and solved on an equidistant and orthogonal grid. A second order central differencing scheme (CDS) is used for the discretization of the convective terms of the momentum, and a total variation diminishing scheme (TVD) with a nonlinear CHARM limiter [226] for the discretization of the convective terms of other scalars. According to Swebys criterion [188] the applied limiter function yields a second order accurate TVD scheme. An explicit third order low storage Runge-Kutta scheme is used to advance the solution in time.
The velocity profiles provided by Gounder et al. [57] are used as boundary condition of the gas-phase velocity. The velocity of the burning pilot is determined from the mass flow rate. Pseudo turbulence is imposed at the inlet with a turbulent length scale (L_t) of 2.0 mm and a magnitude of 10 % for the velocity fluctuations of the bulk velocity, using the method proposed by Klein et al. [87]. In the pilot flame, the equivalence ratio and the progress variable are set to unity. The variances are initially set to zero at all locations.

The boundary conditions for the liquid phase are obtained from the experimental data. The particles are injected into the computational domain at the jet nozzle exit ($x/D = 0.0$), where they are randomly distributed over the plane with a size distribution fitted to the measured cumulative particle distribution, as illustrated in Figs. 5.4(a) and 5.4(b). The measured particle velocities of the five bin size classes are used as particle inlet velocities, as shown in Fig. 5.4 (c). Without evaporation and a domain length of 0.4 m, approximately 750,000 particles exist in the domain, which allows representation of each physical droplet by one numerical particle. The simulations without any sgs model are performed on a coarse and a fine grid with a resolution of 1.5 mm and 1.0 mm, referred to as $noSGS_C$ and $noSGS_F$, respectively. All simulations with sub-filter model are performed on grids with a resolution of 1.5 mm, since the sub-grid activity is expected to be highest for the coarse mesh. The performed simulations (summarized in table 5.2) were conducted on the Cray-XT6m computer at the University of Duisburg-Essen with up to 6 million cells on up to 192 cores within 110 hours (wall time).

This chapter was first published [164] and is reprinted with permission of the journal

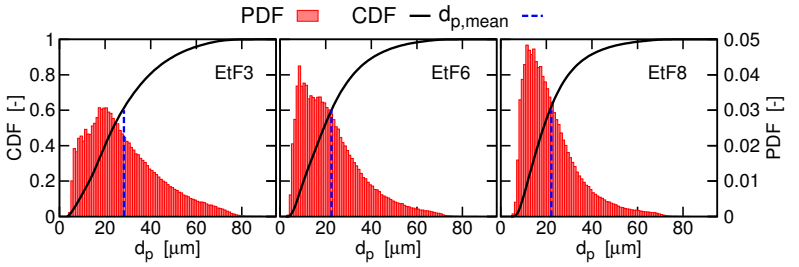

(a)

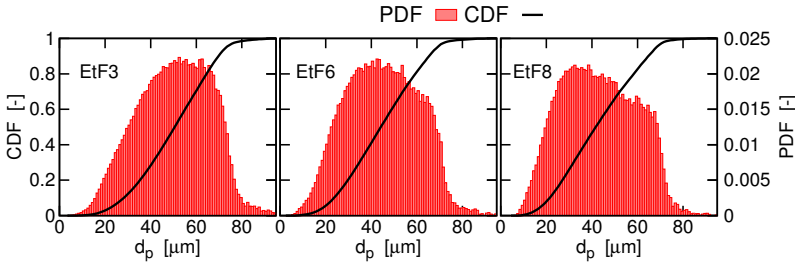

(b)

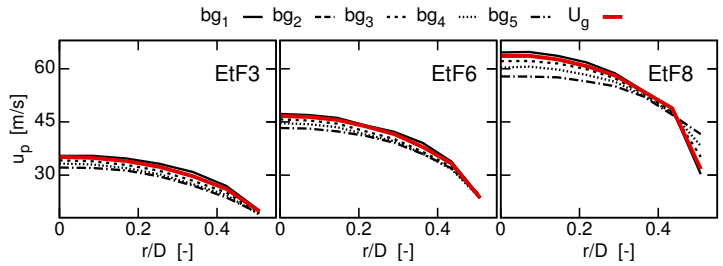

(c)

Figure 5.4: The probability density functions (PDFs) with its cumulative distribution functions (CDFs) (a) for the number of particles, the PDFs and the CDFs for the volume of the particles (b) and the velocities (c) for the five particle bin size groups (bg_1 to bg_5) as used as boundary conditions in the simulations.

Table 5.2: Sub-filter assumptions and variance models.

Name	Z_{sgs}	$Y_{p,sgs}$	Z''^2	C''^2
$noSGS_C$	-	-	-	-
$noSGS_F$	-	-	-	-
β_{A1}	β-fdf	-	algebraic 1	-
β_{A2}	β-fdf	-	algebraic 2	-
β_{Tr}	β-fdf	-	transport Eq.	-
TH_Z	TH-fdf	-	algebraic 2	-
TH_C	-	TH-fdf	-	algebraic 2
TH_{ZC}	TH-fdf	TH-fdf	algebraic 2	algebraic 2

5.5 Results

The investigated spray flames burn in a partially premixed combustion regime. The premixed and stoichiometric pilot provides the heat for the evaporation of the liquid phase and ignites and stabilizes the main flame. Depending on the rate of pre-evaporation, the flame tends to burn in a premixed or stratified combustion regime. Big particles persist up to far downstream locations and partially release their mass in the burned region. The following sections 5.5.1 and 5.5.2 give an overview of the results that were obtained assuming zero variance in mixture fraction and progress variable, providing reference data for the further modelling.

5.5.1 The spray flame characteristics

Figure 5.5 illustrates instantaneous snapshots of the Favre-filtered values for $\widetilde{Z}$, $\widetilde{Y_p}$ and $\widetilde{T}$ in a cross section through the center line. The investigated spray flames have the same initial droplet loading of $45g/min$, but different Reynolds numbers of $19,700$, $27,400$ and $34,800$, respectively. Due to the higher carrier gas mass flow rate, the mixture fraction is shifted towards stoichiometry (equivalence ratio of 2.7 for $EtF3$, 1.8 for $EtF6$ to 1.3 for $EtF8$). The laminar flame speed (S_l) increases with decreasing equivalence ratio and S_l competes with the increased carrier gas velocity. Figure 5.28 illustrates the laminar flame speed as a function of the mixture fraction within the flammable region, as computed with the flamelet equations for the gas phase. The impact of the mixture composition and the turbulence level on the flame structure can be seen in Fig. 5.5. Also the maximum temperature at the center line (predicted by the simulation) is reached earlier for flame EtF8 compared to flame EtF6, what is also substantiated by Fig. 5.10.

The maximum occurring mixture fraction for EtF3 and EtF6 is slightly below $\widetilde{Z}_{max} \approx 0.3$. For EtF8, $\widetilde{Z}_{max}$ is ≈ 0.2 due to the higher carrier gas mass flow rate. The axial location of the maximum mixture fraction is found at $x/D \approx 15$ for EtF3 and at $x/D \approx 20$ for EtF6 and EtF8.

Figures 5.6 (b,d,f) illustrate instantaneous snapshots of the Favre-filtered OH mass fraction for the three investigated flames compared to the laser induced fluorescence (LIF) images (a,c,e), as measured in the experiments. The OH concentration is a good indicator for the location and shape of the burned side of the flame front, and may be used as an indicator for the flame length and the flame lift-off heights. The structures of the OH mass fractions indicate an increase of the flame wrinkling with increasing Reynolds number, this trend is also captured by the simulations. Furthermore, the figure illustrates that the flame becomes shorter and narrower (which is a quantitative observation), and may be related to the increased flame wrinkling and the aforementioned effect of the carrier gas mass flow rate. Figures 5.7 and 5.8 show the radial profiles of the mean values for the Favre-filtered mixture fraction $\widetilde{Z}$ and the progress variable $\widetilde{Y_p}$. The evaporation of the particles increases in the shear layer region between the jet and the pilot due to the high temperatures of the combustion products from the pilot and the higher slip velocity between the particles and the gas-phase. Figure 5.9 illustrates the radial mean profiles

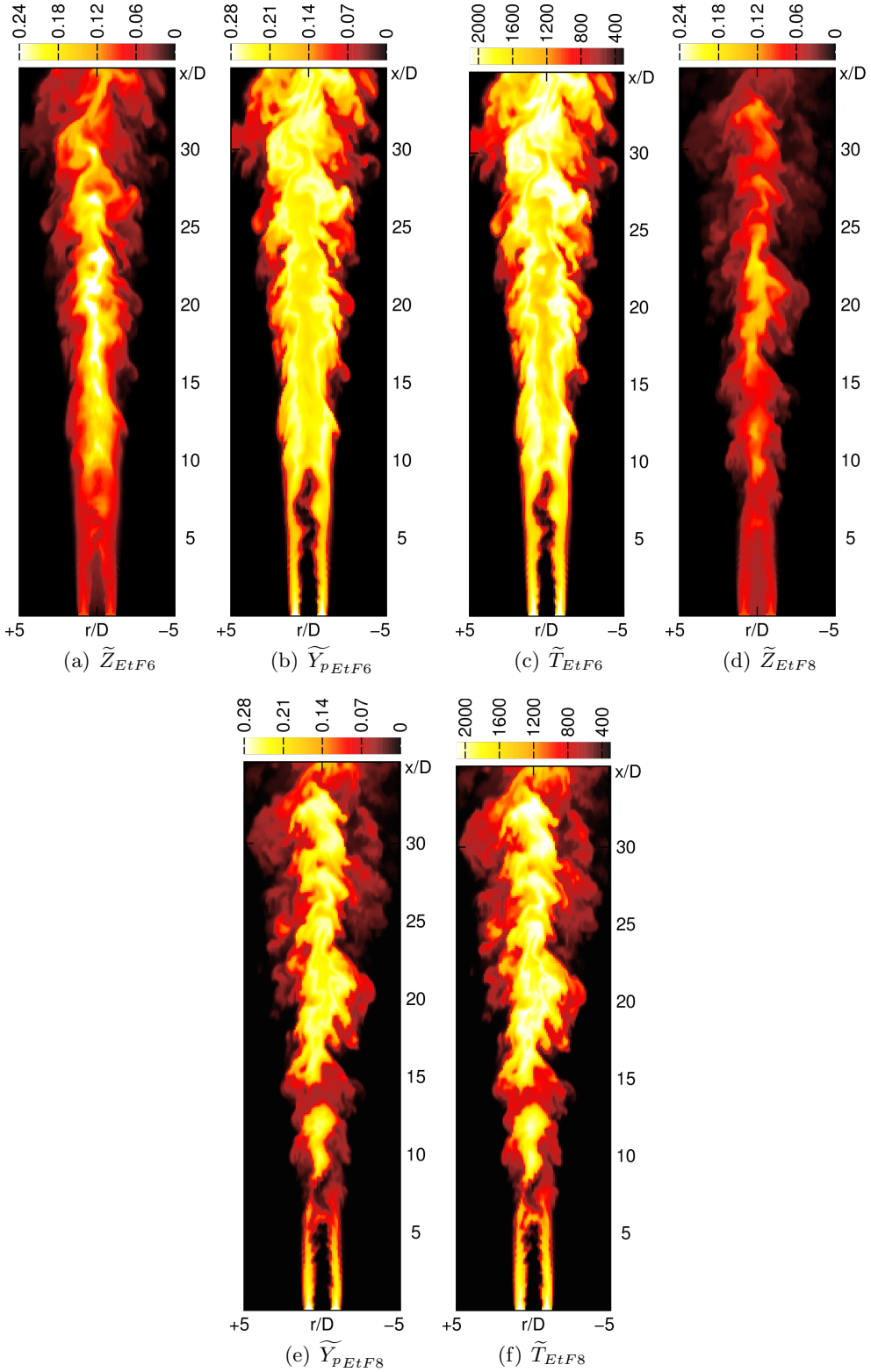

(a) $\widetilde{Z}_{EtF6}$ (b) $\widetilde{Y_p}_{EtF6}$ (c) $\widetilde{T}_{EtF6}$ (d) $\widetilde{Z}_{EtF8}$

(e) $\widetilde{Y_p}_{EtF8}$ (f) $\widetilde{T}_{EtF8}$

Figure 5.5: Instantaneous snapshots of the Favre-filtered mixture fraction ($\widetilde{Z}$), progress variable ($\widetilde{Y_p}$) and temperature ($\widetilde{T}$) on a cross-section through the center for EtF6 (a-c, $Re \approx 27,000$) and EtF8 (d-f, $Re \approx 35,000$). The results are obtained from the simulations without any sub-filter model on the fine grid.

This chapter was first published [164] and is reprinted with permission of the journal

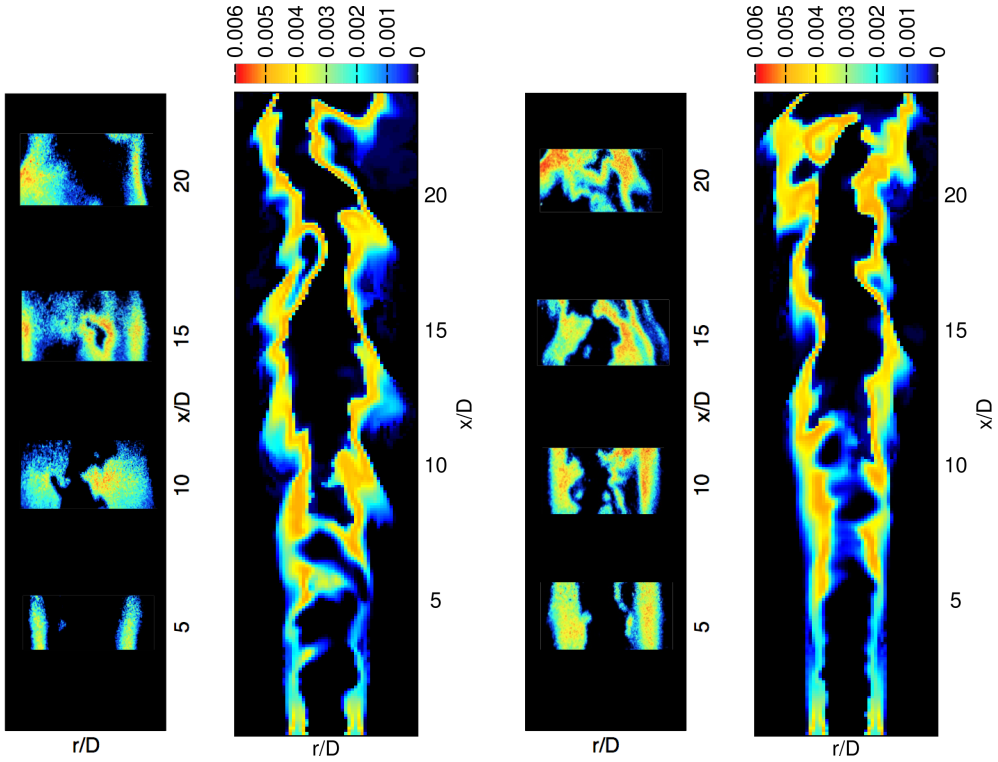

(a) $Y_{OH,EtF3}$ (b) $Y_{OH,EtF3}$ (c) $Y_{OH,EtF6}$ (d) $Y_{OH,EtF6}$

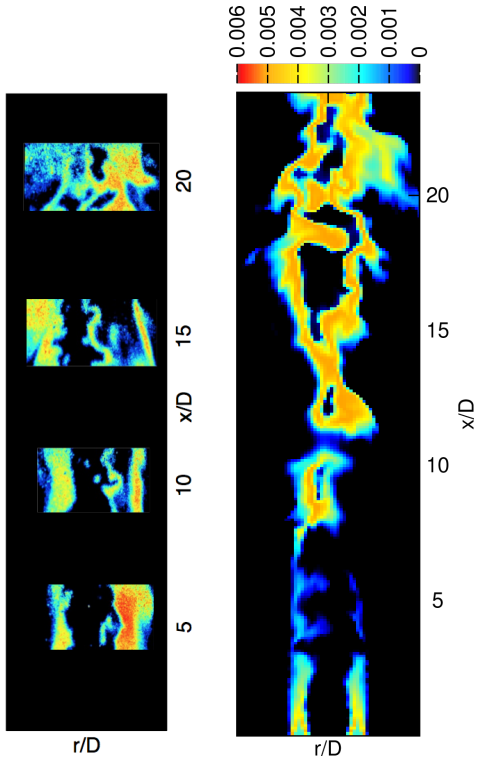

(e) $Y_{OH,EtF8}$ (f) $Y_{OH,EtF8}$

Figure 5.6: Instantaneous snapshots of the Favre-filtered OH mass fractions ($\widetilde{Y_{OH}}$) for the investigated cases EtF3 (a,b), EtF6 (c,d) and EtF8 (e,f) as obtained from the simulations (b,d,f) compared to the results obtained from the experiments (a,c,e).

This chapter was first published [164] and is reprinted with permission of the journal

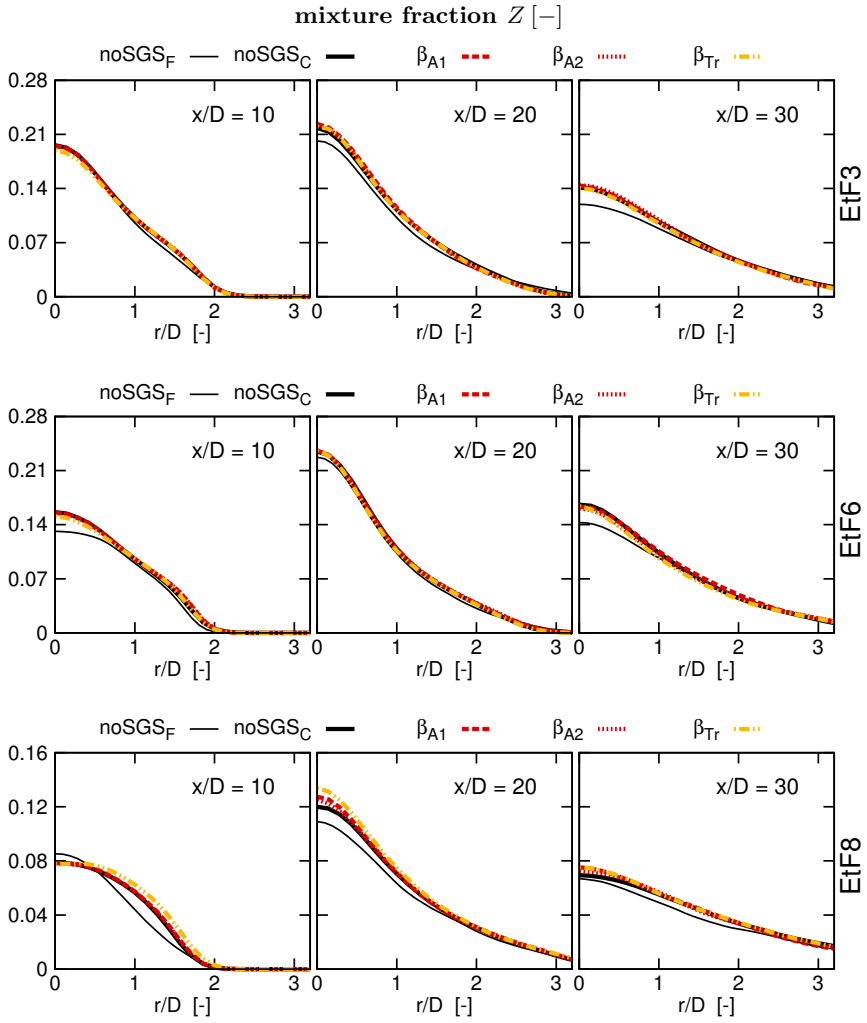

Figure 5.7: Radial profiles of the mean values for the Favre-filtered mixture fraction $\widetilde{Z}$ for the three investigated flames. Shown are the results for the coarse and the fine grid without sub-filter model ($noSGS_C$ and $noSGS_F$), along with the simulation results obtained with the β-fdf. The variances are calculated with the algebraic models and the transport equation model (β_{A1}, β_{A2} and β_{Tr}).

This chapter was first published [164] and is reprinted with permission of the journal

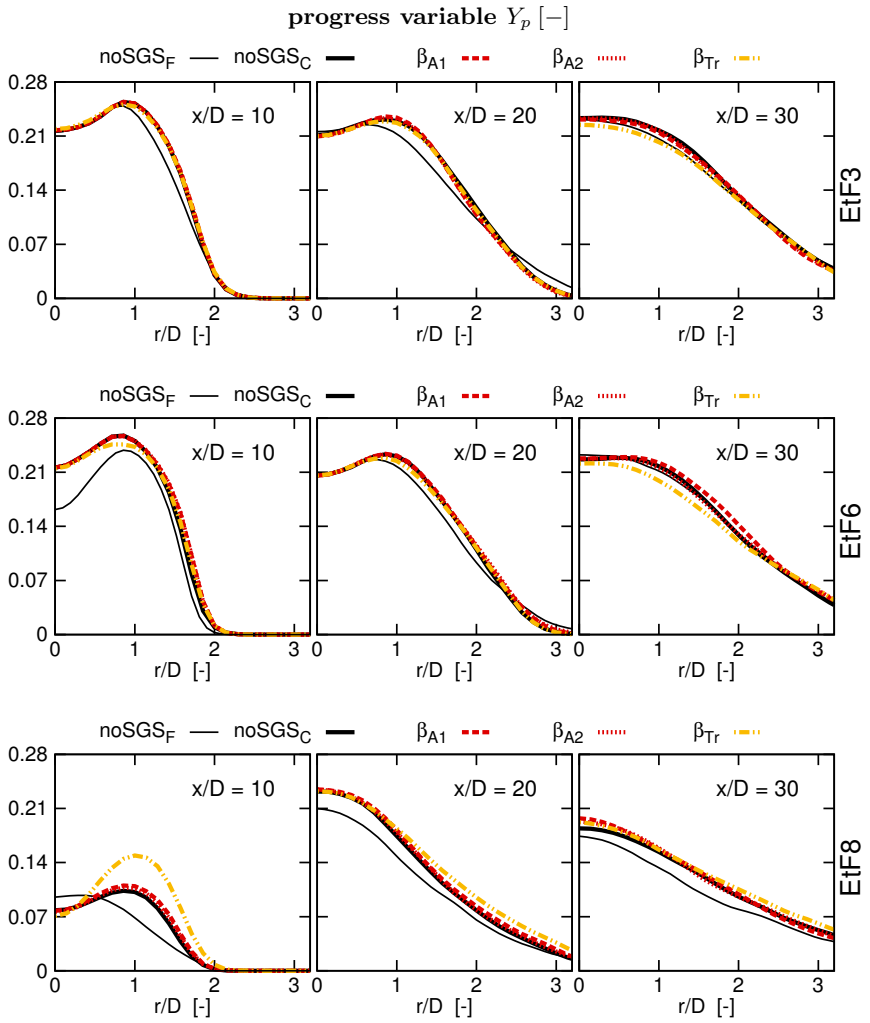

Figure 5.8: Radial profiles of the mean values for the Favre-filtered progress variable $\widetilde{Y_p}$ for the three investigated flames. Shown are the results for the coarse and the fine grid without sub-filter model ($noSGS_C$ and $noSGS_F$), along with the simulation results obtained with the β-fdf (β_{A1}, β_{A2} and β_{Tr}).

This chapter was first published [164] and is reprinted with permission of the journal

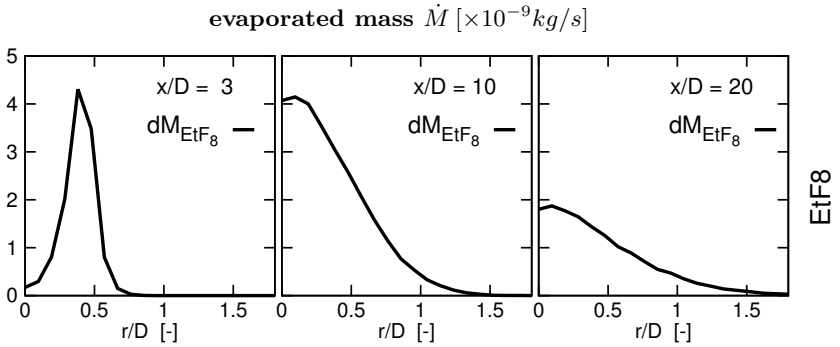

Figure 5.9: Radial profiles of the mean values for the released mass from the particles. Shown are the results for the fine grid without sub-filter model ($noSGS_F$).

of the mass released from the particles into the gas-phase for flame EtF8. Close to the jet nozzle exit the peak value is located between the pilot and the jet stream, further downstream the peak value shifts towards the center line. The mass released from the particles into the gas enriches the mixture fraction in the shear layer region, and the flame propagates from the pilot zone into the core jet region, as illustrated in Fig. 5.8. The maximum value of the progress variable depends on the mixture fraction ($Y_{p,max} \approx 0.287$ for a stoichiometric mixture fraction of $Z_S = 0.105$), and is found in the pilot and in the shear layer region at an axial location of approximately $x/D = 5$ to $x/D = 10$.

Figure 5.10 illustrates the radial profiles of the Favre-filtered temperature above the ambient temperature ($\widetilde{T} - T_0$). The temperature in the jet close to the center line increases further downstream with increasing mixture fraction and combustion progress. The aforementioned impact of the increasing carrier gas mass flow rate is also found for the flame temperature, which is determined by the table lookup as a function of Z and Y_p. The flame widths and the temperature trends are predicted accurately by the simulations, and the grid refinement improves the agreement of the results compared with the experimental data. However, the simulations overpredict the temperatures, especially in the core region of the jet, relative to the measurements conducted by thermocouples. Similar discrepancies are obtained by Masri et al. [25, 26], De et al. [32] and Ukai et al. [196]. According to Chrigui, Masri, Sadiki and Janicka [26] the discrepancies (especially at x/D=10) may be explained by the applied measurement technique. The error introduced by the used thermocouples is larger close to the jet nozzle exit. Ukai et al. [196] suggest that the cooling effect arises from the droplet collisions with the thermocouples.

5.5.2 Particle statistics

Figure 5.11 illustrates the radial profiles of the volume flux of the liquid phase at three different axial locations. The jet breakup angle is predicted well by the simulations for all three flames, as it can be seen from the radial mean velocity profiles in Fig. 5.13. The simulations overpredict the evaporation of the particles. However, it must be stressed that the uncertainties of the volume flux measurements are up to 20% [57]. Generally, similar results were obtained by the simulations with the coarse and fine grid size, except at $x/D = 10$ where the higher resolution yields a better accuracy.

Figure 5.12 illustrates the radial profiles of the Sauter mean diameter (SMD or d_{32}). Although the trend of d_{32} is predicted quite well for the three spray flames, its magnitude is underpredicted (especially at far downstream locations). The influence of the grid refinement on d_{32} is negligible. The experimental observation of an increasing d_{32} may be related to the faster evaporation of the small liquid droplets compared to the big droplets. A further cause for the growth could be the collision and coalescence of the particles. However, since all three investigated flames arise from diluted sprays, the major impact on the aforementioned finding may be attributed to the

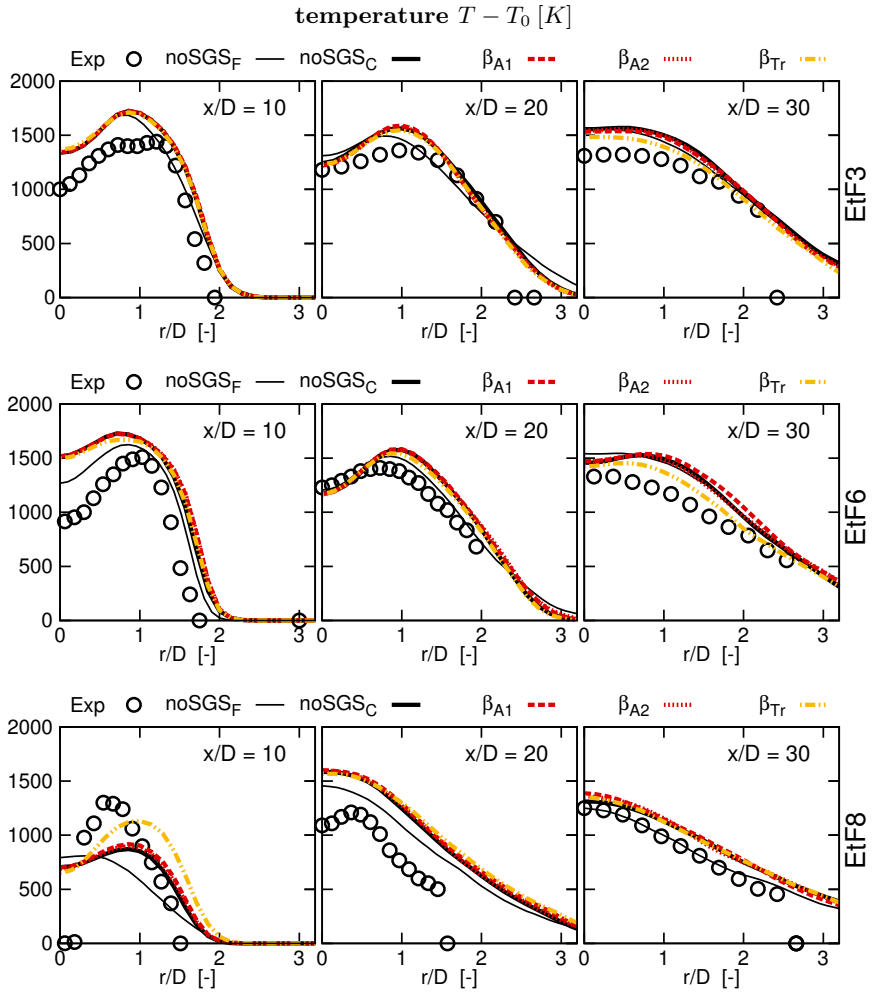

Figure 5.10: Radial profiles of the Favre-filtered temperature for the three investigated flames. Shown are the results for the coarse and the fine grid without sub-filter model ($noSGS_C$ and $noSGS_F$), along with the simulation results obtained with the β-fdf (β_{A1}, β_{A2} and β_{Tr}).

This chapter was first published [164] and is reprinted with permission of the journal

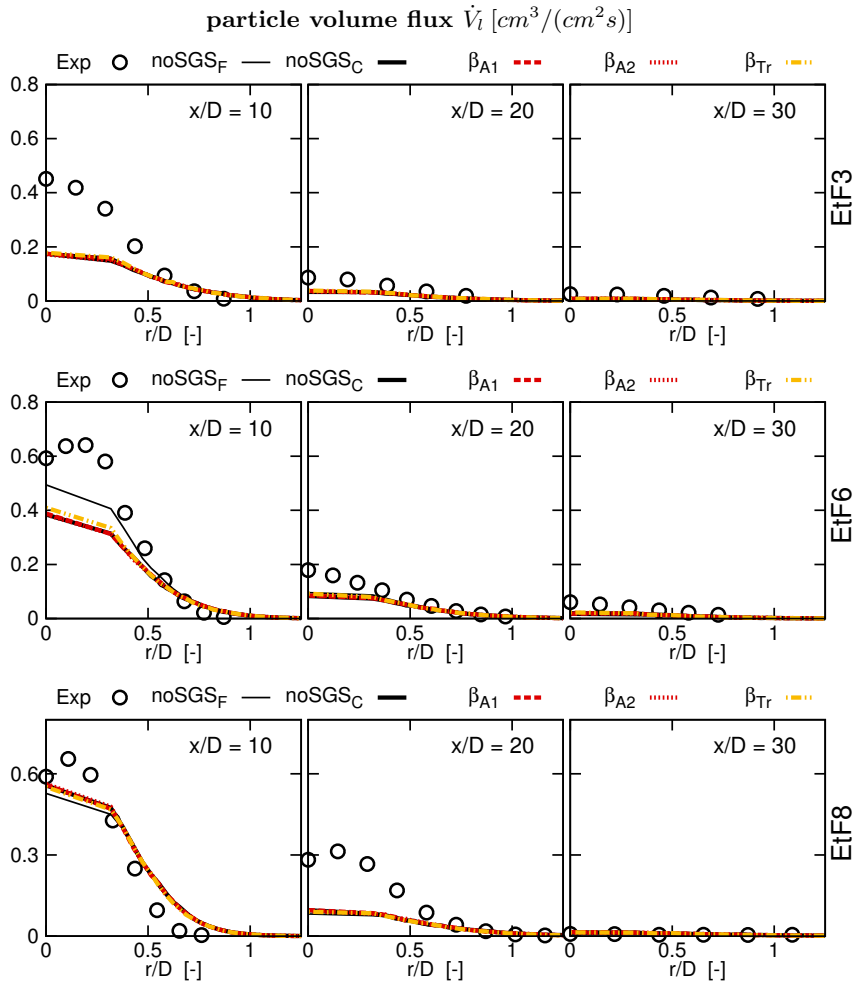

Figure 5.11: Radial profiles of the volume flux of the liquid phase for three investigated flames. Shown are the results for the coarse and the fine grid without sub-filter model ($noSGS_C$ and $noSGS_F$), along with the simulation results obtained with the β-fdf (β_{A1}, β_{A2} and β_{Tr}).

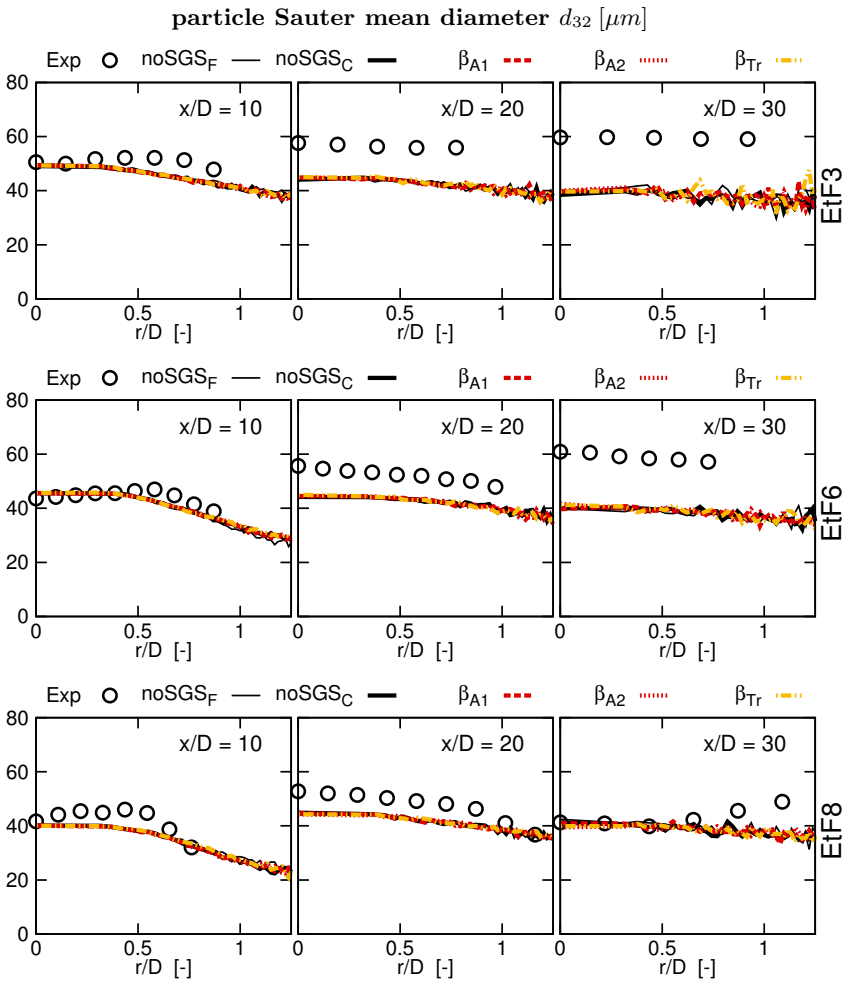

Figure 5.12: Radial profiles of the Sauter mean diameter (d_{32}) for the three investigated flames. Shown are the results for the coarse and the fine grid without sub-filter model ($noSGS_C$ and $noSGS_F$), along with the simulation results obtained with the β-fdf (β_{A1}, β_{A2} and β_{Tr}).

This chapter was first published [164] and is reprinted with permission of the journal

evaporation process [32], which is modelled in the present study with an equilibrium assumption. The increase of the Sauter mean diameter at a radial location of approximately $0.5 - 0.75$ (in the shear layer between the jet and the pilot) could be related to dispersion effects, small particles may escape quicker due to their lower inertia.

Figure 5.13 illustrates the radial profiles of the mean particle and the Favre-filtered gas-phase velocities. The velocities of the liquid particles at the jet nozzle exit depends on the size of the particles, where the smaller particles have the higher velocities (Fig. 5.4 and 5.13) (small particles are faster accelerated from the carrier mass on the way from the nebulizer to the combustion chamber). After leaving the jet nozzle, the particles decelerate initially due to the expansion of the jet, but then accelerate again due to the hot core zone where the heat is released.

The velocities of the small and big particles converge when they are accelerated again from the gas-phase. At far downstream locations ($x/D > 20$), the liquid phase is faster than the gaseous-phase as outlined in Fig 5.13. The experiments also confirm that the gas-phase (represented by the droplets smaller than $d_p = 10\ \mu m$ - squared symbols in Fig. 5.13), is faster than the droplets close to jet nozzle exit and is much slower at far downstream locations. This effect is more prominent for EtF3 and EtF6. This may again be attributed to the high inertia of the large particles, which are decelerated slower than the surrounding gas. Generally, the mean velocities are predicted quite well, except for EtF8 at $x/D > 20$. One reason for this finding may be related to the under-prediction of the gaseous-phase velocity [26]. Comparable results for the prediction of the velocities for similar cases have been achieved by other groups, [25, 26, 32].

Figure 5.14 illustrates the radial profiles of the axial velocity fluctuations at three axial locations. The velocity fluctuations of the particles are underpredicted at $x/D = 0.3$, probably due to the fact that no artificial fluctuations are superimposed to the liquid phase at the inlet. The fluctuations of the particle velocities predicted on the fine grid are in reasonable agreement with the experiments. The influence of the grid refinement is clearly visible for axial locations x/D greater than 20, where the simulations on the fine grid reproduce the experimental values more precisely.

Overall, a satisfactory agreement with the experiments is already achieved without any sub-filter modelling for the source term and the chemical state. The quality of these predictions is similar to the quality of the simulations by other groups [25, 26, 32], indicating that this data may well serve as a good reference for the subsequent studies, but also implying that the present test-case may not be very sensitive to the sub-filter modelling.

5.5.3 The influence of the variance model

In this section the impact of the variance model is illustrated and highlighted for the three investigated spray flames. The simulations are performed on the coarse grid, since the variance models have a stronger impact here. Results obtained from the β-fdf approach, where the variance is determined from an algebraic or a transport equation model (β_{A1}, β_{A2} and β_{Tr}) are compared against reference simulations ($noSGS_C$ and $noSGS_F$) and the available experimental data (Exp).

Figure 5.15 shows instantaneous snapshots of the mixture fraction variance (for EtF 8), obtained from the algebraic and transport equation models (A1, A2 and Tr). The transport equation model yields a variance which is approximately one order of magnitude higher than the variance predicted by the algebraic models (high variances are predicted over a wide region, not just in layers of steep scalar gradients). The algebraic model A1 predicts slightly higher variances compared to the algebraic model A2, since the model constant C_{A1} in A1 is higher than C_{A2} in A2. The shape of the filaments, which are aligned 45° to the flow direction of the jet, are similar for A1 and A2.

Figure 5.16 shows the radial profiles of rms values of the mixture fraction variance for the investigated flames. As outlined in Fig. 5.16 at $x/D = 10$ (for EtF3, EtF6 and EtF8), the mixture fraction variance increases in radial direction first, until it reaches a local maximum and

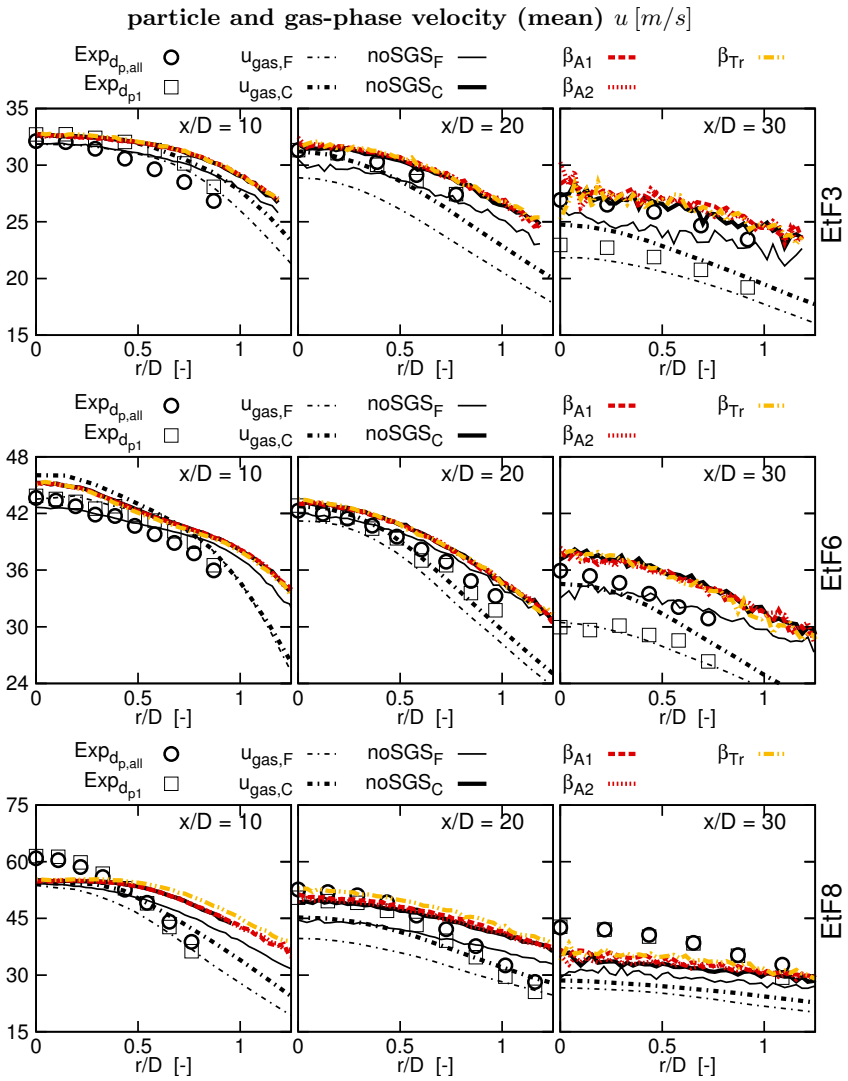

Figure 5.13: Radial profiles of the mean velocities for the liquid particles and the gas-phase. Shown are the results for the coarse and the fine grid without sub-filter model ($noSGS_C$ and $noSGS_F$), along with the simulation results obtained with the β-fdf (β_{A1}, β_{A2} and β_{Tr}). The gas-phase velocities are shown for the simulations without sub-filter model for the coarse and fine grid. The measured particle velocities are shown for the particle bin size group summarizing all particles ($d_{p,all}$) and for particles smaller than $10\mu m$ (d_{p1})

This chapter was first published [164] and is reprinted with permission of the journal

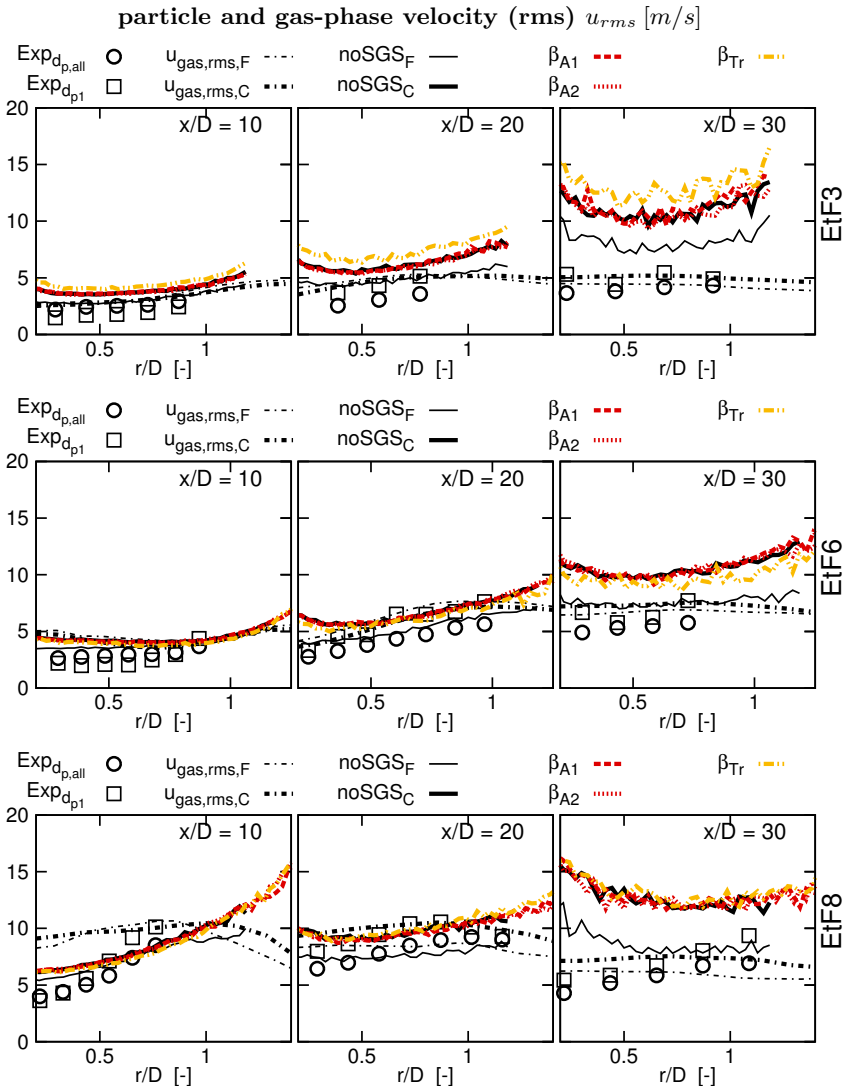

Figure 5.14: Radial profiles of the velocity fluctuations for the liquid particles and the gas-phase. Shown are the results for the coarse and the fine grid without sub-filter model ($noSGS_C$ and $noSGS_F$), along with the simulation results obtained with the β-fdf (β_{A1}, β_{A2} and β_{Tr}). The gas-phase velocities are shown for the simulations without sub-filter model for the coarse and fine grid. The measured particle velocities are shown for the particle bin size group summarizing all particles ($d_{p,all}$) and for particles smaller than $10\mu m$ (d_{p1})

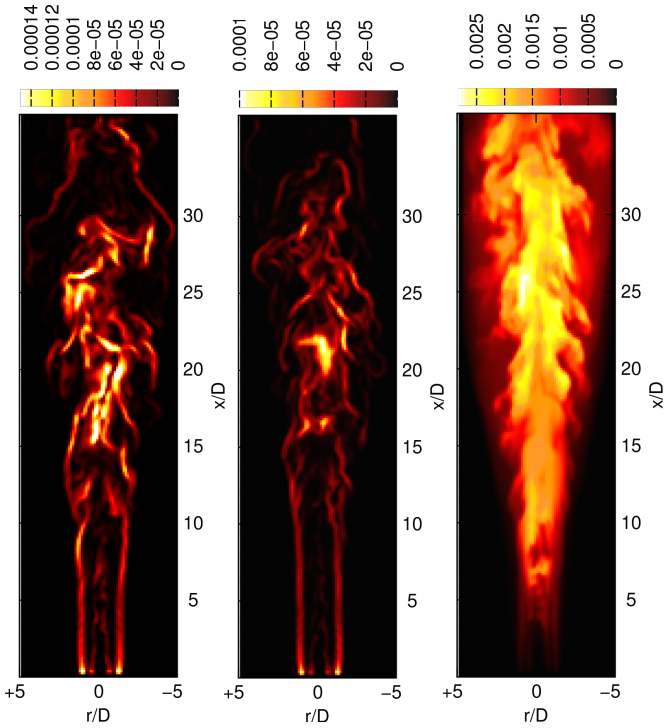

(a) $\widetilde{Z''^2_{A1}}$ (b) $\widetilde{Z''^2_{A2}}$ (c) $\widetilde{Z''^2_{Tr}}$

Figure 5.15: Instantaneous snapshots of the rms of the Favre-filtered variances ($\widetilde{Z''^2}$) for EtF8 on a cross-section through the center. The variances are modelled according to (a) the algebraic model A1, (b) the algebraic model A2 and (c) the transport equation model Tr.

subsequently decreases to zero again. In the algebraic models, the variance is determined from the gradients of the mixture fraction only. The first peak close to the center axis is caused by the mixture fraction gradients between the core region and the evaporated mass, the second peak is attributed to the difference in the mixture fraction fields between the pilot and the coflow. The transport equation model accounts for the evaporation source term and predicts a shift of the peak value (compared to the algebraic models) in radial direction. The local maximum of the variance is in the region of the hot pilot (where the particle mass is released) and not at the location of the gradients. Both model assumptions (A1 and A2 as well as Tr) predict a shift of the peak value towards the center line further downstream. In the transport equation model, the variance production competes with its dissipation.

Figures 5.7 to 5.14 show that both algebraic models A1 and A2 predict almost the same results for the gaseous and liquid phase, what is attributed to the prediction of the similar variances. The results predicted by the transport equation model deviate stronger from the reference simulations (than the result from the algebraic models A1 and A2), due to the high variances obtained by the Tr model. Furthermore, the largest deviations are found for EtF8 (as identified from the mixture fraction, progress variable and temperature fields Figs. 5.7 to 5.10). The particle statistics are only slightly affected by the variance models (outlined for the particle mean velocities and fluctuation, volume flux and d_{32} Figs. 5.11 to 5.14).

5.5.4 The influence of the sub-filter assumption

In this section, the results obtained from the TH approach for the mixture fraction only (TH_Z), the TH approach for the progress variable only (TH_C) and the joint TH-model (TH_{ZC}) are compared against the β-fdf (β_{A1} and β_{Tr}) model and the available experimental data.

Figure 5.17 shows radial profiles of the Favre-filtered mean mixture fraction obtained with

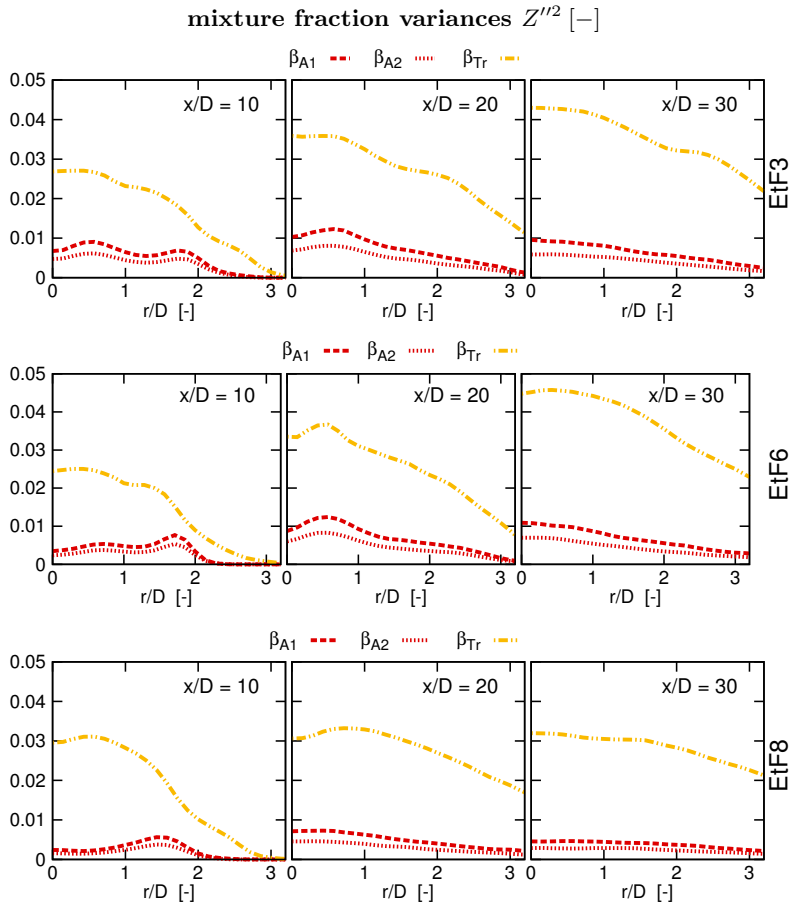

Figure 5.16: Radial profiles of the Favre-filtered mixture fraction variances $\widetilde{Z''^2}$ for the three investigated flames. Shown are the results obtained with the three investigated variance models β_{A1}, β_{A2} and β_{Tr}.

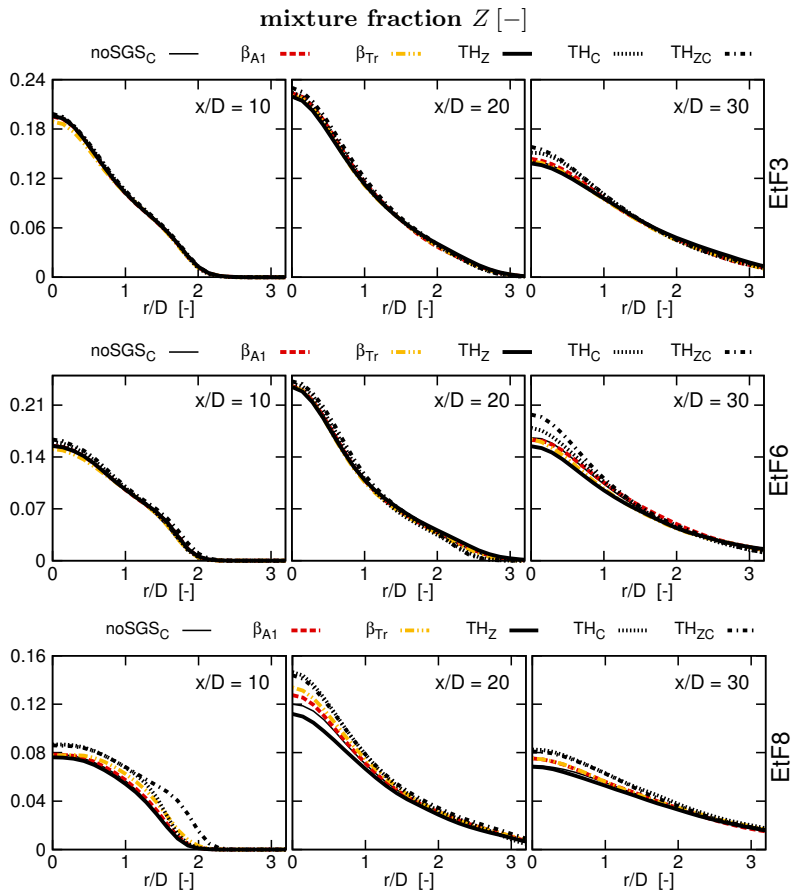

Figure 5.17: Radial profiles of the mean values for the Favre-filtered mixture fraction $\widetilde{Z}$ for the three investigated flames. Illustrated are the results obtained by the simulations with the β-fdf for the mixture fraction (β_{A1} and β_{Tr}) and the TH-fdf for the mixture fraction (TH$_Z$), the TH-fdf for the progress variable (TH$_C$) and the joint TH-fdf model for the mixture fraction and progress variable (TH$_{ZC}$).

This chapter was first published [164] and is reprinted with permission of the journal

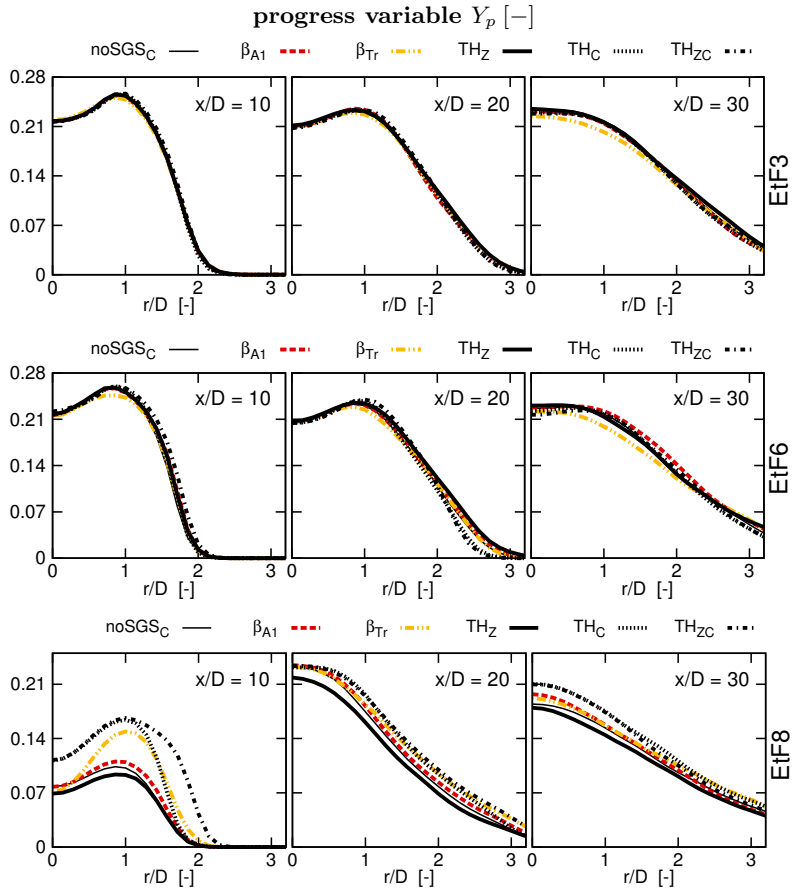

Figure 5.18: Radial profiles of the mean values for the Favre-filtered reaction progress variable $\widetilde{Y}_p$ for the three investigated flames. Illustrated are the results obtained by the simulations with the β-fdf (β_{A1} and β_{Tr}) and the TH-fdf (TH$_Z$, the TH$_C$ and TH$_{ZC}$).

the two different sub-filter approaches (β-fdf and TH-fdf). As already outlined before, there is no significant effect of the sub-filter distribution on the prediction of the mixture fraction for EtF3 and EtF6 up to $x/d \approx 20$. The impact of the variance model and the sub-filter model (on the prediction of the Favre filtered mixture fraction fields) increases with a higher carrier gas mass flow rate and distance from the jet nozzle exit as shown in Fig. 5.17. The models incorporating the variance for the progress variable (TH$_C$ and TH$_{ZC}$) predict larger deviations from the simulations without sub-filter model. It was found that the joint fdf model (TH$_{ZC}$) yields the biggest difference compared to the reference simulations (noSGS), what is attributed to the additional consideration of the variance of the progress variable. The impact of the sub-filter and variance models on the prediction of the mixture fraction is also mirrored in the prediction of the reaction progress variable $\widetilde{Y}_p$, as illustrated in Fig. 5.18. The deviation of the progress variable (compared to the reference simulations) increases in downstream direction and with increasing carrier gas mass flow rate. Furthermore, the models β_{A1}, β_{A2}, β_{Tr} and TH$_Z$ cause only a small deviation compared to noSGS. The highest deviations of $\widetilde{Y}_p$ are found for TH$_{ZC}$ followed by TH$_C$.

Radial profiles of the Favre-filtered temperatures above the ambient temperature are shown in Fig. 5.19. The temperature is determined from a table lookup as a function of the Favre-filtered mixture fraction, reaction progress variable and their variances. Worth mentioning is the strong influence of the sub-filter and variance models on the prediction of the temperature close to the nozzle exit, as shown in Fig. 5.19 for EtF8 at $x/D = 10$.

Figure 5.20 illustrates the mean profiles of the OH mass fractions Y_{OH}. The impact of the

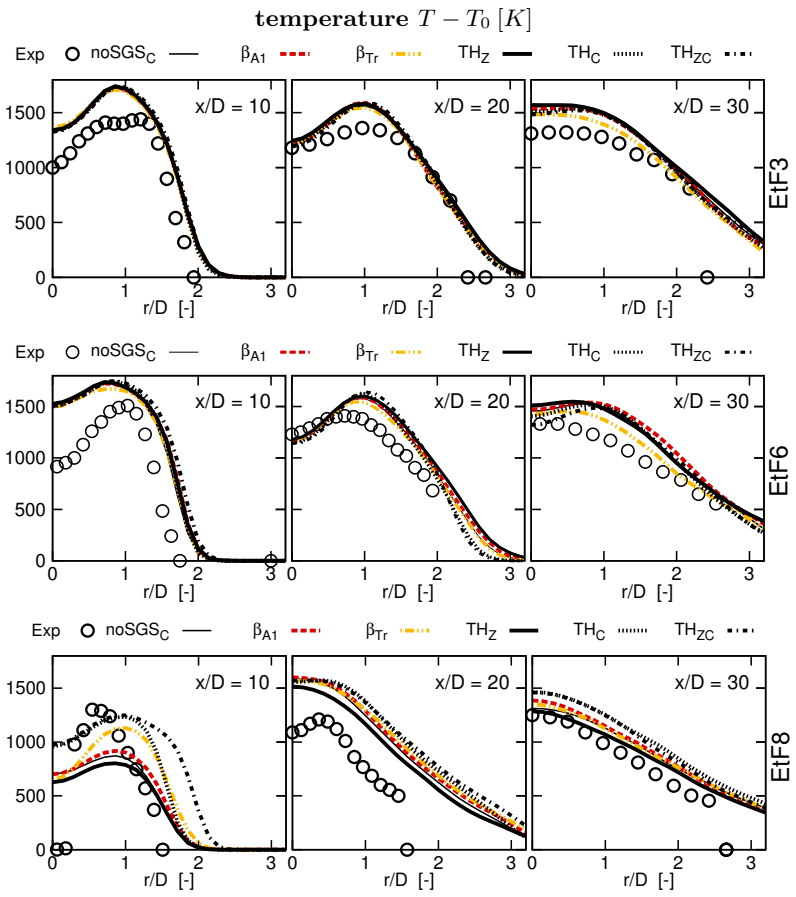

Figure 5.19: Radial profiles of the mean values for the Favre-filtered temperature above the ambient temperature ($\widetilde{T}-T_0$) for the three investigated flames. Illustrated are the results obtained by the simulations with the β-fdf (β_{A1} and β_{Tr}) and the TH-fdf (TH_Z, the TH_C and TH_{ZC}).

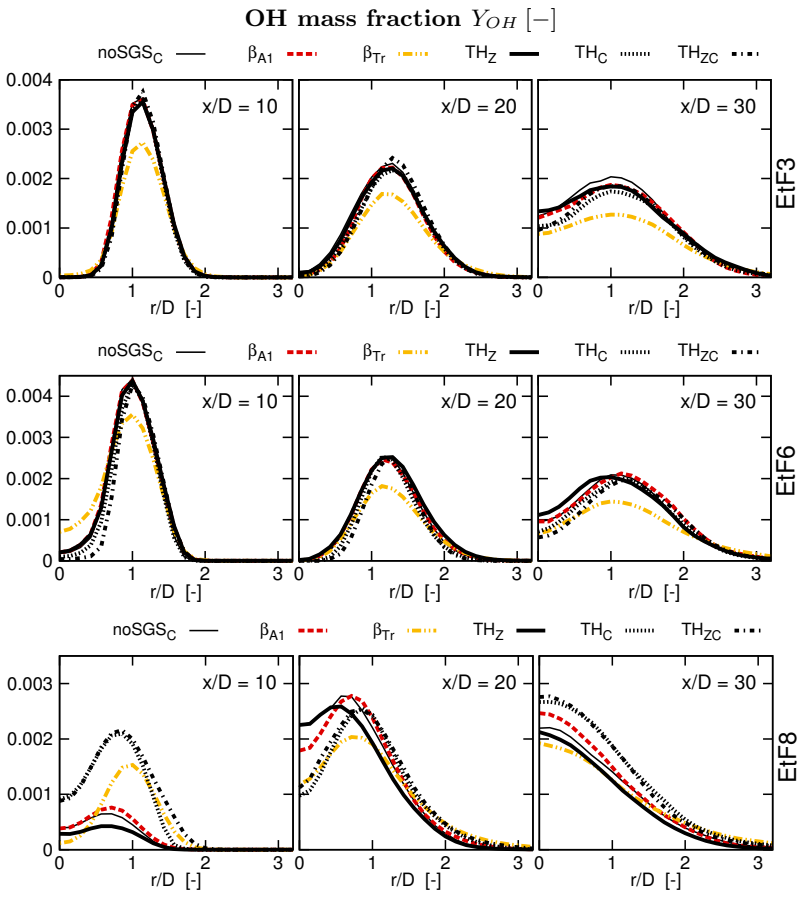

Figure 5.20: Radial profiles of the mean values for the Favre-filtered OH mass fractions ($\widetilde{Y}_{OH}$) for the three investigated flames. Illustrated are the results obtained by the simulations with the β-fdf (β_{A1} and β_{Tr}) and the TH-fdf (TH$_Z$, the TH$_C$ and TH$_{ZC}$).

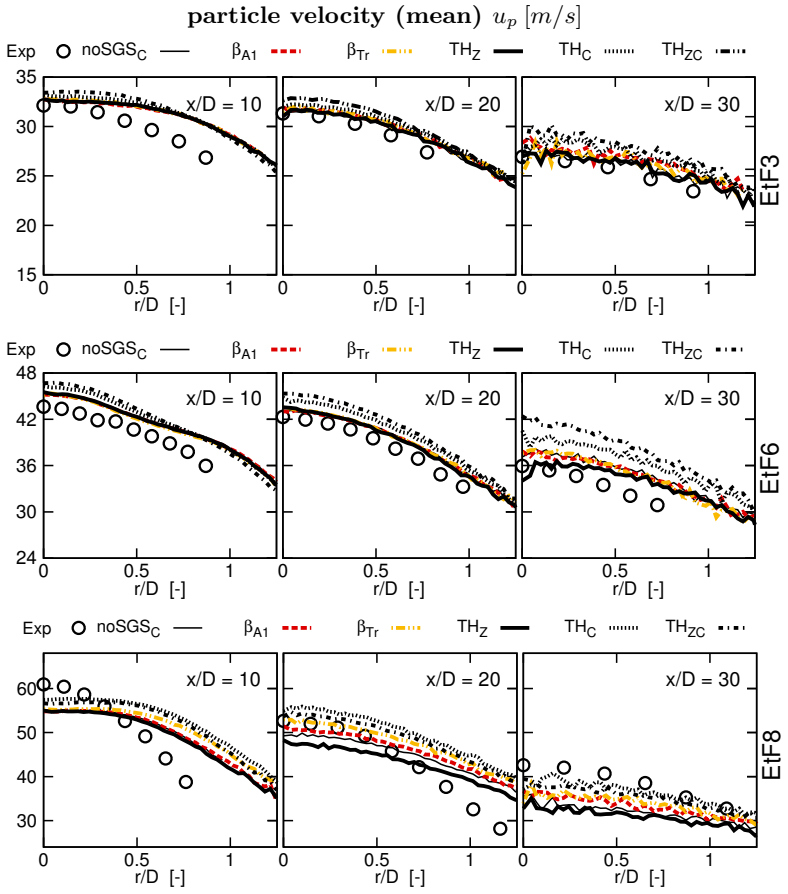

Figure 5.21: Radial profiles of the mean velocities for the liquid particles for the three investigated flames. Illustrated are the results obtained by the simulations with the β-fdf (β_{A1} and β_{Tr}) and the TH-fdf (TH$_Z$, the TH$_C$ and TH$_{ZC}$).

incorporated models on the prediction of Y_{OH} is significant, particularly for EtF8. Generally, it is found that with an increasing carrier gas mass flow rate and a growing distance from the jet nozzle exit the impact of the investigated models on the gas-phase statistics increases (outlined in Figs. 5.17 to 5.20). Due to the increase of the carrier gas mass flow rate but constant fuel mass flow rate the equivalence ratio is shifted from rich ($\Phi_{EtF_3,tot} = 2.7$) towards stoichiometry ($\Phi_{EtF_8,tot} = 1.3$). For this reason the table lookup is performed in a non-linear table region with higher gradients compared to the table lookup in the rich region. Even though similar variances are obtained for $EtF3$, $EtF6$ and $EtF8$, larger deviations are found for the flame close to stoichiometry. Another explanation may be the increase of the jet velocity and hence a shorter residence time of the particles leading to a reduced mixing time. A further effect of the increasing impact may be attributed to an increase of the local evaporation rate due to the higher slip velocity for particles which are leaving the jet. For the particle statistics the same trend is observed. Figure 5.21 illustrates the radial profiles of the mean particle velocities for the investigated flames. Of the investigated sgs models, the TH_{ZC} model shows the largest deviation from the simulations without sub-filter modelling. Interestingly, the influence of the sub-filter models on the particle velocities for EtF8 at $x/D = 10$ is almost negligible despite the high variances that are found for $\widetilde{Z}$, $\widetilde{Y_p}$ and $\widetilde{T}$. This may be related to the high inertia of the liquid particles that results in a small influence of the gas-phase velocity on the particle velocities. The radial profiles of the liquid volume flux and particle Sauter mean diameter obtained from the simulations with the different sgs models are attached to 5.9.

This chapter was first published [164] and is reprinted with permission of the journal

5.6 Conclusions

Large eddy simulations of diluted evaporating spray flames with a constant liquid mass flow rate and three different carrier gas mass flow rates were presented for two different grid sizes. An Eulerian/Lagrangian approach for the gas and liquid phase was applied. Combustion was modelled using the FGM technique combined with the ATF approach. The sub-grid stresses were described by the σ-model. The impact of two different approaches for the sub-filter distribution (β-fdf and TH-fdf) of the used control variables ($\widetilde{Z}$ and $\widetilde{C}$) was investigated. The variances were determined from (a) the standard algebraic gradient model (by Branley and Jones [18]) A1, (b) a second gradient model A2 and (c) a transport equation model Tr. The algebraic model A2 determined the variance based on the maximum and minimum cell face values of the control variables. The results from the two algebraic models within the β-fdf approach are similar.

The general flame characteristics and statistics were determined by analysing instantaneous snapshots of the Favre-filtered mixture fraction and variance, progress variable, temperature and OH mass fraction for the different flames. The flame lift-off height was found to depend on the pre-evaporation and the intensity of turbulence of the investigated flames. The simulations captured correctly the flame length and width for the three flames. Grid refinement was shown to slightly improve the prediction of the gas-phase properties and the droplet velocities, whereas the impact of the grid refinement on the Sauter mean diameter and droplet volume flux was rather small. Reasonable agreement for the temperature predictions with the experiments was achieved.

The prediction of the liquid phase statistics were compared against the experimental data. Reasonable agreement for the mean particle velocities and its variances was found for EtF3, EtF6 and EtF8. Some deviations occurred at far down stream locations for EtF8, which may be related to the prediction of the gas-phase velocity. The evaporation of the liquid phase was overpredicted and the Sauter mean diameter was underpredicted. This observation may be related to the overprediction of the flame temperature or the equilibrium assumption in the evaporation model. The spread of the liquid jet, however, was well captured by the simulations.

The influence of the variance model and the fdf-assumption on the prediction of the gaseous-phase for EtF3, EtF6 for locations $x/D < 20$ was shown to be small. At far downstream locations, the impact of the investigated models on the simulations increased for EtF3 and EtF6. The prediction of the mixture fraction, progress variable and temperature for EtF8 was stronger influenced by the incorporated variance model. The influence of the two different fdf-assumptions for the mixture fraction was found to be similar, for comparing the simulation results.

With regards to the sub-filter modelling, the chosen PFGM/ATF approach together with the TH-fdf assumption has shown to be robust and memory efficient, enabling multi-dimensional tabulation at little cost. A key question arising from the present paper is on better variance modelling for spray combustion, where different algebraic models and dissipation models (in the context of a transport equation) have lead to up to one order of magnitude difference in the variance. This must however be seen in the context of the present test case, where the predictions were not significantly affected. Overall, this robustness towards the sub-filter variance modelling may also be seen as a confirmation of the general strength of the concept of LES. The present work has confirmed, that the Sydney spray flames are well predicted by LES, and the TH-fdf approach has shown its suitability for the simulation of reactive multiphase flows. Where the suitability of different sub-filter modelling approaches was demonstrated, it has become apparent that the available experimental conditions and data are not sufficient to distinguish the quality of the different models - in fact not even to show their superiority over no modelling.

5.7 Acknowledgement

The authors gratefully acknowledge the financial support by the state North Rhine-Westphalia, Germany. We also thank the Center for Computational Sciences and Simulations (CCSS) of the

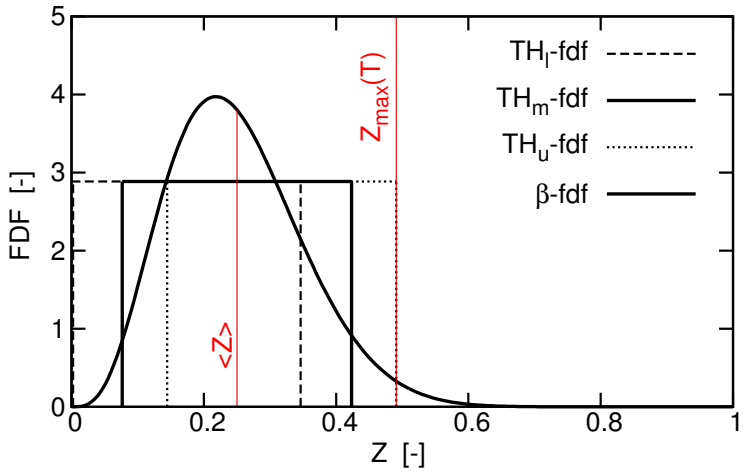

Figure 5.22: Illustration of an exemplary β-fdf function for $\widetilde{Z} = 0.25$ and $\widetilde{Z''^2} = 0.01$, in comparison to the possible fdf's from the TH approach. The TH_m-fdf is built assuming an equal sub-filter distribution in rich and lean mixture. The TH_l-fdf (TH_u-fdf) is built assuming a shift of the sub-filter distribution towards a lean (rich) mixture. The red vertical lines represent the Favre-filtered mixture fraction and the physical limit for the mixture fraction, which depends on the temperature and the partial pressure of the ethanol vapor.

University of Duisburg-Essen for providing the computational recourses.

5.8 Sub-Filter modelling

Figure 5.22 illustrates different possible fdf's (three TH-fdf's in comparison to the β-fdf) which are all built for a Favre mixture fraction of $\widetilde{Z} = 0.25$ and a variance of $\widetilde{Z''^2} = 0.01$. The red vertical line represent the maximum mixture fraction that can be found depending on the temperature. As described in section 5.4.3.1, the shape of the β function is defined by the Favre-filtered mean value and the variance of the control variable (here shown for Z). Due to the properties of the β function, the β-fdf assumption accounts for the control variables beyond their physical limits (as illustrated in Fig. 5.22 for the mixture fraction $Z \geq Z_{max}$). Furthermore, the β function has a positive skewness for $\widetilde{Z} \leq 0.5$ (or negative for $\widetilde{Z} \geq 0.5$) which may not always correctly describe the sub-filter distribution of the control variable.

The TH-fdf approach determines the sub-filter distribution by using the local maxima and minima of the control variable, and hence can not exceed the physical limit. The TH_m in Fig. 5.22 illustrates the sub-filter distribution for a Favre-filtered mixture fraction of 0.25 and a variance of 0.01. The upper and lower limits of the control variables are obtained by the algebraic variance model A1, as suggested by Floyd et al. [43]. A shift of the TH-fdf towards a lean (TH_l) or rich (TH_u) mixture is possible with the algebraic variance model A2, where the upper and lower limits are obtained from the maximum and minimum cell face values.

5.9 Liquid phase results

The radial profiles of the particle mean volume flux (Fig. 5.23) highlight that the influence of the variance model on the particle statistics is rather small compared to the influence on the gas-phase statistics. Also the models which predict a higher variance (β_{Tr}, TH_C and TH_{ZC}) have a rather small impact on the particle statistics. This finding may be attributed to the inertia of

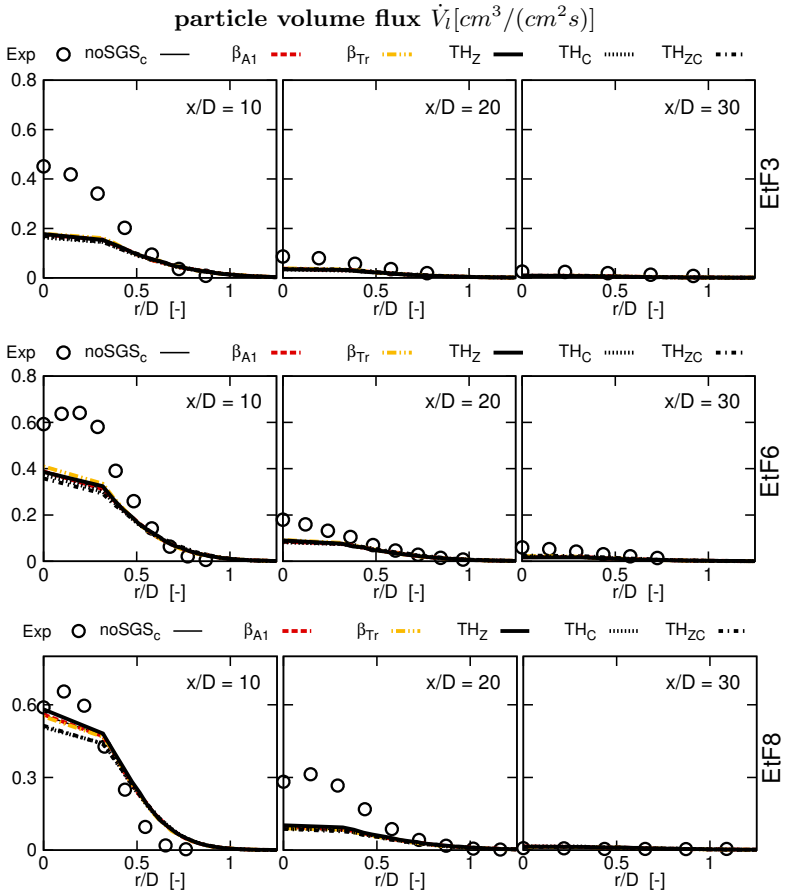

Figure 5.23: Radial profiles of the mean volume flux for the liquid particles for the three investigated flames. Illustrated are the results obtained by the simulations with the β-fdf (β_{A1} and β_{Tr}) and the TH-fdf (TH_Z, the TH_C and TH_{ZC}).

the particles.

5.10 Mesh quality

According to Pope [152] a LES is assumed to be of "good" quality if more than 80 % of the kinetic energy is resolved in the entire flow field. Celik et al. [21] proposed to express the quality of the LES as a non-linear function of the viscosity and the modelled turbulent viscosity. A viscosity ratio smaller than approximately 20 ($r_\nu = \nu_t/\nu \leq 20$) corresponds to a sufficient resolution of resolving more than 80 % [145] of kinetic energy, which is achieved for the entire flow field for $\Delta \leq 1\,mm$ (see Fig. 5.24). For the $0.5\,mm$ grid, the maximum viscosity ratio close to the jet nozzle exit is better than 5. The viscosity ratio obtained from the coarse grid simulations is quite good for the major part of the flow field, however for flame $EtF8$, r_ν locally exceeds 20 (but still more than 76 % of the kinetic energy is resolved). The region where r_ν is greater than 20 is close to the jet nozzle exit. With increasing grid size Δ the quality of the mesh is reduced.

$$IQ_{LES} \approx \frac{1}{1 + \alpha_V \left(1 + \frac{\nu_t}{\nu}\right)^n} \tag{5.40}$$

However, it must be stressed that this criterion by Celik is not sufficient, as the correctness of the test depends on a correct model and non-dissipative numerics.
The influence of the mesh on the simulation results is investigated for flame $EtF8$ without subfilter model. Figure 5.25 illustrates the radial profiles of the Favre-filtered temperature, the

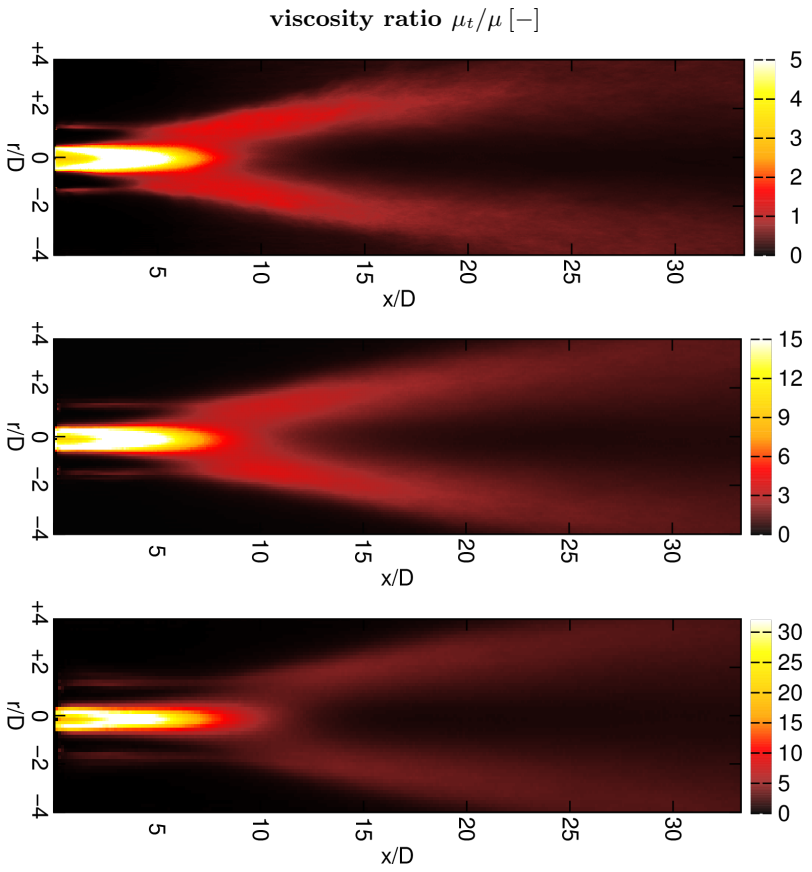

Figure 5.24: Ratio of the turbulent viscosity to the molecular viscosity μ_t/μ as a measure for the grid quality. Top: Simulation result as obtained with $\Delta = 0.5\,mm$, middle: $\Delta = 1\,mm$ and bottom: $\Delta = 1.5\,mm$ for $EtF8$ without sgs model.

This chapter was first published [164] and is reprinted with permission of the journal

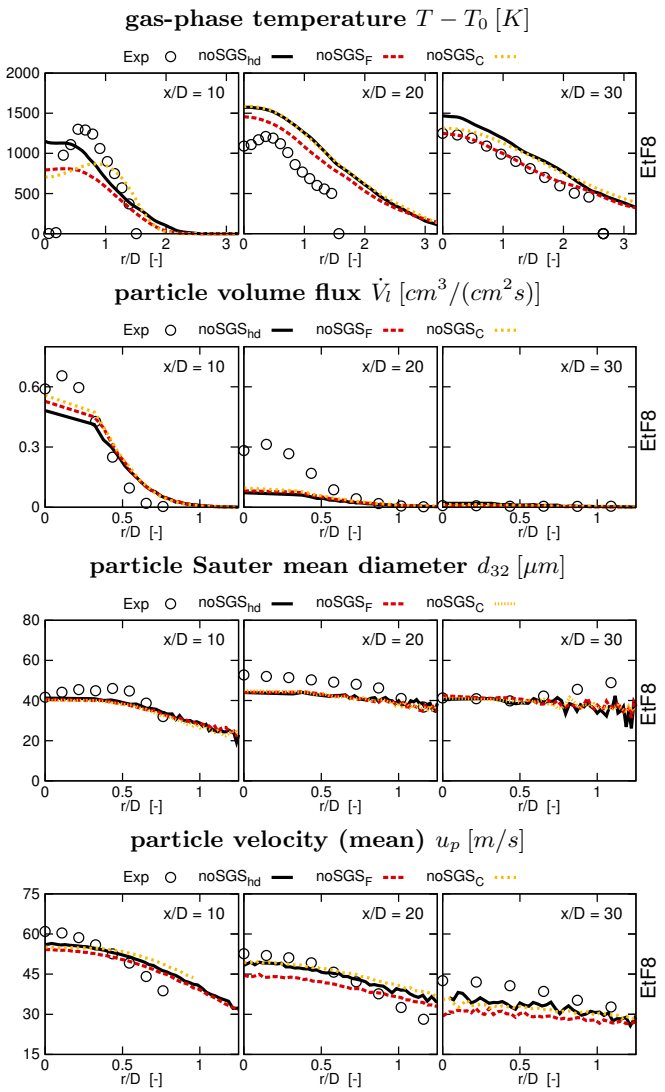

Figure 5.25: Radial profiles of the Favre-filtered temperature, particle volume flux, particle Sauter mean diameter and particle velocity (mean) for $EtF8$ as obtained without sub-filter model on the coarse and fine grid, compared against an even finer resolution (hd: $\Delta = 0.5\,mm$)

particle volume flux, the particle Sauter mean diameter and the particle mean velocity on three axial locations.

5.11 Lagrangian particle tracking

Figure 5.26 shows the number of tracked particles for $EtF8$ without any sub-grid model on three different axial locations. The statistics are performed for approximately $0.3\,s$ physical time which corresponds to 29 flow through times (for $u_p = 30$ and at $x/D = 30$). Each physical droplet is represented by one numerical particle, so that the plot represents both, the physical and numerical droplets. The graph summarizes the particles of all sizes.

5.12 Influence of the stochastic term on particle statistics

The figures shown in the results section are obtained without any sgs model for the particles. In this section the results for flame $EtF8$ on the coarse grid are compared for the simulations

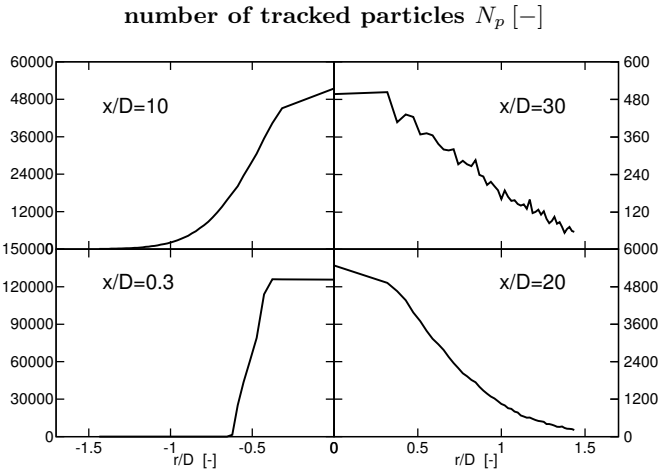

Figure 5.26: Radial profiles of the number of all tracked particles for EtF8.

without any sgs model for the particles with the results as obtained by applying a stochastic Wiener term. Figure 5.27 illustrates the radial profiles of the Favre-filtered temperature above the ambient temperature, the particle Sauter mean diameter, the particle mean velocity and its rms. The profiles suggest that the influence of the stochastic term is rather small.

5.13 Laminar flame speed

Figure 5.28 shows the laminar flame speed as a function of the mixture fraction within the flammable region. The maximum flame speed is observed for a slightly rich mixture, close to stoichiometry ($Z_S = 0.105$). Neophytou and Mastorakos [132] performed one-dimensional simulations of n-heptane and n-decane flames and showed that the laminar flame speed is a function of the initial droplet diameter, the equivalence ratio and the particle residence time. In the present study, however, the laminar flame speed is determined from the flamelet equations (for freely propagating flames) for gas-phase combustion.

This chapter was first published [164] and is reprinted with permission of the journal

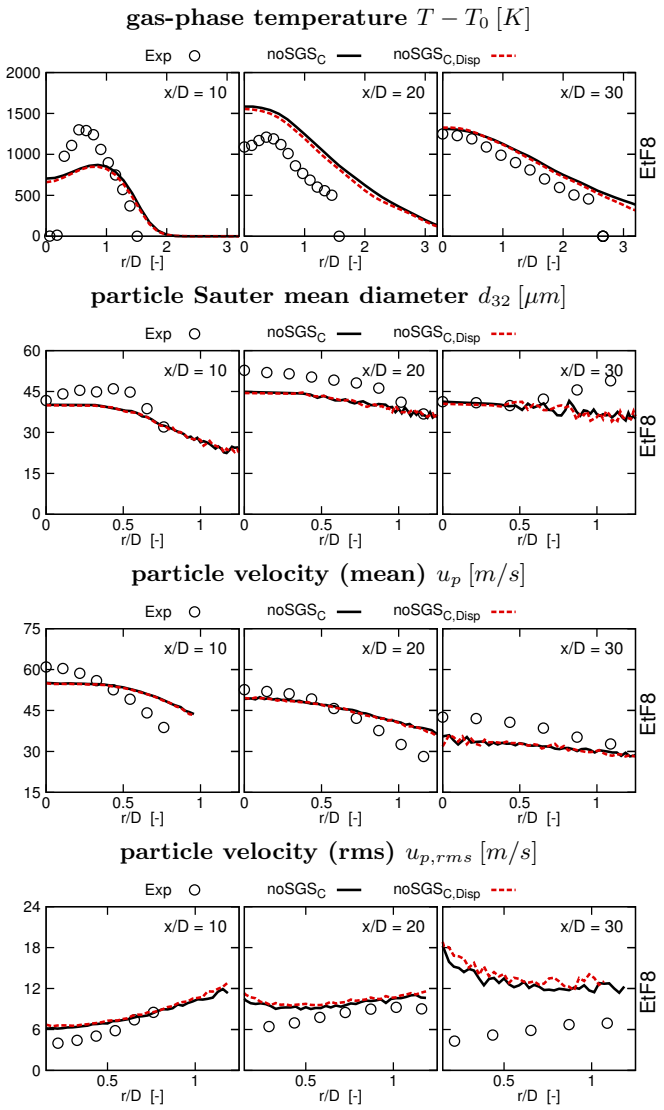

Figure 5.27: Radial profiles of the Favre-filtered temperature, particle Sauter mean diameter, particle mean velocity and particle rms velocity for $EtF8$ as obtained with and without stochastic dispersion model.

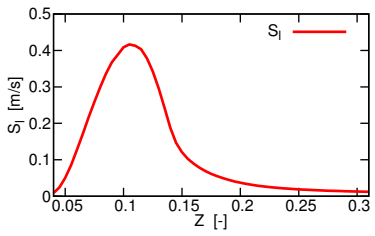

Figure 5.28: Illustration of the laminar flame speed as a function of the mixture fraction.

Chapter 6

Large eddy simulations of nanoparticle synthesis from flame spray pyrolysis [165]

Authors: A. Rittler, L. Deng, I. Wlokas, A.M. Kempf
This chapter including all figures and tables was previously published in 'Proceedings of the Combustion Institute, 36 (1), A. Rittler, L. Deng I. Wlokas and A. M. Kempf, Large eddy simulations of the nanoparticle synthesis from flame spray pyrolysis, 1077-1087, (2017) and is reprinted with permission from Elsevier.
The author A. Rittler developed the code for the spray treatment, the combustion- and particle model, developed the code to produce the thermochemical manifolds, ran all the simulations, wrote the paper and generated all figures and tables. The author L. Deng provided the DNS data for model comparison in section 6.5.
The author I. Wlokas provided the chemical mechanism for HMDSO and contributed through discussions and proof-reading.
The author A. M. Kempf contributed corrections, discussions, proof-reading and the original code.

6.1 Abstract

Large eddy simulations of the nanoparticle synthesis from flame spray pyrolysis are presented. A standard reactor is investigated, with ethanol/hexamethyldisiloxane (HMDSO) mixture as spray/precursor composition and oxygen as dispersion gas for the production of silica nanoparticles. Spray evaporation, ignition and stabilisation of the flame are achieved by a premixed methane/oxygen pilot flame. The gas, spray and nanoparticle phases are modelled with Eulerian, Lagrangian and Eulerian approaches, respectively. A modified tabulated chemistry model, adapted from the premixed flamelet generated manifold approach (PFGM) with artificial flame thickening (ATF) is proposed, tested and applied for the system. The control variables are the element mass fractions of hydrogen and carbon together with a joint progress variable. The population balance equation of the nanoparticles is modelled in terms of number, volume and surface area concentration, its subfilter distribution is modelled with a delta function. The combustion of HMDSO and formation of silica particle monomers is described by a two-step global mechanism. The nucleation source term is tabulated as a function of the control variables. The submodels for spray and combustion are validated separately to compensate for the shortage in detailed experimental data for nanoparticle spray flames. Subsequently, simulation results for the particles are presented and discussed, in particular the polydisperse particle size distributions resulting from turbulence.

6.2 Introduction

Flame spray pyrolysis (FSP) for the synthesis of ceramic powders (e.g. SiO_2, TiO_2 or Al_2O_3) permits a simple precursor injection into a hot flame and enables a rapid quenching of the aerosol formation [113]. The synthesis of silica nanoparticles from FSP has been the focus of many experimental and computational studies [39, 84, 113, 129], but the promising large eddy simulation (LES) approach has never been attempted for such systems before.

6.2.1 Nanoparticles from flame spray pyrolysis

In self sustaining FSP processes, a liquid precursor is solved in an organic liquid fuel. This mixture is fed into a hot environment, which is provided by a secondary heat source. Oxygen or air are used as dispersion and sheath gas for the stabilisation of the spray flame [113]. Common precursors for the gas-phase synthesis of silica include Silanes, cyclic and linear siloxanes and tetraethyl orthosilicate (TEOS), depending on the required properties [76, 113].

Solvents like ethanol, methanol or isopropanol are used, which also affect the particle properties. Mädler et al. [113] investigated the influence of the fuel and oxidizer composition and indicated the importance of the evaporation rate and total energy content of the precursor on the powder characteristics. Studies by Engel et al. [39] and Kilian et al. [84] investigated a modified version of the aforementioned spray burner, using a HMDSO/ethanol mixture, O_2 as dispersion and sheath gas and a near stoichiometric CH_4/O_2 mixture for the pilot flame. Laser-sheet based Mie scatter imaging, 2D-chemiluminescence imaging and coherent anti-Stokes Raman spectroscopy were applied to obtain the spatial distributions of $OH^\star$, $CH^\star$ and $SiO^\star$ radicals, the combustion and nucleation zones, as well as the temperature. In this work, HMDSO has been chosen as chlorine-free silica precursor, for which we expect more in situ data from future reactor experiments.

The FSP process can be divided into three main zones [214]: the spray is atomised in the shear layer between the liquid and surrounding environment and evaporated due to the heat of the pilot flame in zone A (Fig. 6.1). The turbulent flow enhances the mixing of the fuel/precursor vapor with the oxidizer and generates a flammable mixture that is burned in zone B, ignited by the pilot flame. The precursor is decomposed into intermediate species, which react and form SiO_2 molecules that nucleate in zone C. The nuclei coagulate and particles grow, followed by agglomeration and sintering. The modelling of this three zones is described in section 9.4. These process steps may happen simultaneously at one instant or place inside the flame, as a result of turbulence. As the methods for the experimental analysis of these processes in turbulent flames are limited and costly, deeper insights are likely to become available from detailed simulations by LES or direct numerical simulation (DNS). It should be noted, that the wide range of scales and the complexities of turbulence, aerosol dynamics and chemical kinetics are such that complete simulations with detailed models are not feasible for years. Any simulation must therefor apply a suitable set of simplifying assumptions and models and should be validated against suitable experiments.

6.2.2 Numerical studies of flame-made nanoparticles

The evolution of the nanoparticles from the gas phase for cases of practical interest is usually described by the general dynamics equation (GDE) for the continuous distribution function [49]. The GDE incorporates nucleation, growth, coagulation and coalescence as well as convection and diffusion and describes the particle size distribution in space and time. Several methods for the solution of the GDE have been proposed: The most accurate discrete models [46] introduce an additional differential equation (DE) for each discrete size or particle property. Sectional models [174, 222, 223] cluster particles of different sizes in classes and introduce additional DE's for the sections. Combinations of the discrete and sectional models have also been proposed [15]. The method of moments (MOM) and modified MOM models (e.g. QMOM, DQMOM [4, 5, 40, 47]) assume that the size distribution can be approximated with a presumed distribution function, i.e. a self-preserving [99] or as log-normal function [193], and solves for the moments of the GDE. Kruis et al. [98] proposed a simple model for the GDE, by introducing transport equations for the number, volume and surface area concentration of the aggregate particles. Coagulation and sintering are described separately in the equations for the number and surface area concentration. The morphology of the particles is considered by replacing the solid sphere diameter with the collision diameter in the coagulation kernel. Sintering is described with an empirical model that

correlates the sintering time to the primary particle diameter and temperature. In the present work, the modified Kruis-model with nucleation source term is applied [139, 194]. A detailed overview on models for the GDE is given by Tsantilis [193].

Numerical studies on the evolution of nanoparticles from flame synthesis are mainly limited to Reynolds averaged Navier-Stokes (RANS) simulations. However, in recent years LES studies of TiO_2 synthesis have been carried out by Raman et al. [184] or Fox et al. [185], who applied a QMOM for the solution of the GDE and investigated the influence of the chemical mechanism on nucleation. Sung et al. [186] extended the model to describe the evolution of the particles with a bivariate number density function. Related work has been published in the sooting flame community, e.g. by Bisetti et al. [6] or Pitsch and Müller [128].

The combination of the LES approach and the monodisperse model was chosen as a path to more accurate and detailed results that consider (at least) the major effects of turbulence, as a step forward from our previous work with RANS [214].

6.2.3 Particle distributions in turbulent flows

Moving to a turbulent flow problem, one must first discuss what the particle population actually means. Mathematically, a probability density function for the particle properties exists at every point and instant in a turbulent flame. The probability density can be interpreted as the expectation of the particle population within a sampling volume at this point and time, where the sampling volume must be smaller than the smallest scalar scale (Batchelor scale). This Batchelor scale can be orders of magnitudes smaller than the Kolmogorov scale of turbulence when nanoparticles are concerned. We will refer to this population as the *local instantaneous population* (LIP).

The LIP differs from what one is usually interested in, *the local time averaged population*, which may be the result of sampling at a point in an experiment. It is possible that a wide local time averaged population results from many local monodispers LIP's as a result of turbulence; or as a result of a wide LIP resulting from the agglomeration of polydisperse particles. Existing particle diagnostic techniques provide a time averaged local population, which makes it hard to determine the cause for a wide population. We present the first LES of the nanoparticle synthesis from FSP focusing on the effect of turbulence, i.e. many different LIPs are considered in the averaging. Each LIP, in turn, is described by the Kruis-model [98].

6.3 Setup of the experiments by Kilian et al. [84]

The investigated spray burner (Tethis S.p.A., Fig. 6.1) was used by many research groups before (e.g. [39, 60, 76, 84, 113, 114, 129, 191, 214]). The burner consists of a spray nozzle with a concentric annular gap for the dispersion gas, an annular gap for the pilot flame and a sintered matrix for the sheath gas supply. The capillary surmounts the other outlets by 0.5 mm to guarantee a constant spray angle independent of the liquid flow rate [113]. A solution of 5 ml/min ethanol with 0.5 mol/l HMDSO is fed through the capillary, dispersed by an oxygen stream with 5 l/min. The premixed methane/oxygen pilot with flow rates of 1.5 and 3 l/min is surrounded by oxygen sheath gas of 10 l/min (4). Mädler et al. [113] showed for a cold ethanol spray and a given inner nozzle gap that the median droplet mass diameter depends on the oxidant flow rate. The 3-D numerical domain starts 3 mm downstream of the jet-nozzle exit, as primary- and secondary break-up are not considered in the simulations, as shown in Fig. 6.1 and spans a region of 40 x 40 x 100 mm. A Rosin-Rammler distribution is assumed to describe the droplet diameters, which are used as initial and inlet conditions in the simulations (with a median diameter of ~ 8 μm). It is known that the burner is hard to adjust, so that a perfectly straight flame which is not leaning to one side is hard to achieve. As the simulated flame burns perfectly straight, we also provide results 5 mm off the centreline to have additional data for comparison to the experiments.

This chapter was first published [165] and is reprinted with permission of the journal

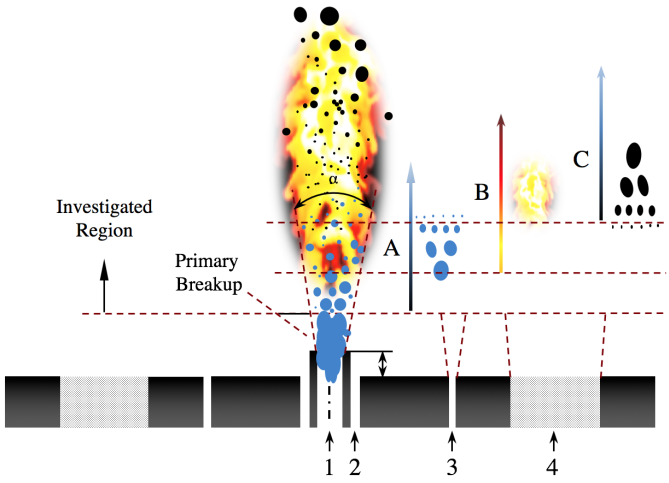

Figure 6.1: Sketch of the burner with inlet (1) for the fuel/precursor, (2) dispersion gas, (3) pilot and (4) the sheath gas supply with the zones A spray, B turbulent combustion and C particle synthesis.

6.4 Modelling Approach

The Favre filtered conservation equations for mass and momentum are solved accounting for spray evaporation as outlined below.

$$\frac{\partial \overline{\rho}}{\partial t} + \frac{\partial \overline{\rho}\widetilde{u}_j}{\partial x_j} = \dot{\Gamma}_{\overline{\rho}} \tag{6.1}$$

$$\frac{\partial \overline{\rho}\widetilde{u}_i}{\partial t} + \frac{\partial \overline{\rho}\widetilde{u}_i\widetilde{u}_j}{\partial x_j} = -\frac{\partial \overline{p}}{\partial x_i} + \frac{\partial \overline{\tau}_{ij}}{\partial x_j} + \frac{\tau_{ij}^{sgs}}{\partial x_j} + \dot{M}_{d,i} \tag{6.2}$$

In Eqs. (6.1) and (6.2), $\widetilde{u}_j, \overline{\rho}, \overline{p}, \overline{\tau}_{ij}$ and τ_{ij}^{sgs} denote the Favre filtered velocity, the filtered density, pressure and the viscous stress tensor, respectively. An eddy viscosity approach is used to model the residual stresses τ_{ij}^{sgs}, where the turbulent viscosity μ_t is determined with our implementation [162] of Nicoud's sigma model [133]. The source terms $\dot{\Gamma}_{\overline{\rho}}$ and $\dot{M}_d$ account for the exchange of mass and momentum with the spray and are evaluated for each droplet within a LES filter width and are applied to the Euler and Lagrangian phases through two way coupling based on trilinear interpolation.

6.4.1 Spray submodel - zone A

The spray is described in a Lagrangian framework [164], each physical droplet is represented by one numerical particle d for which a set of differential equations is solved. Motion and evolution of the droplet mass and temperature (assuming equilibrium conditions [2, 120]) are determined from Eqs. (6.3-6.6), where x_d, u_d, a_d, m_d and T_d are the position, velocity, acceleration, mass and temperature of the droplets, respectively

$$\frac{\mathrm{d}x_{d,i}}{\mathrm{d}t} = u_{d,i} \tag{6.3}$$

$$\frac{\mathrm{d}u_{d,i}}{\mathrm{d}t} = a_{d,i} = \frac{f_1}{\tau_d}\left(\widetilde{u}_i - u_{d,i}\right) + \left(1 - \frac{\overline{\rho}}{\rho_d}\right) g_i \tag{6.4}$$

$$\frac{\mathrm{d}m_d}{\mathrm{d}t} = -\frac{\mathrm{Sh}}{3\,\mathrm{Sc}}\frac{m_d}{\tau_d}\ln\left(1 + B_m\right) \tag{6.5}$$

$$\frac{\mathrm{d}T_d}{\mathrm{d}t} = \frac{\mathrm{Nu}\,c_p}{3\,\mathrm{Pr}\,c_{pl}}\frac{\left(T_g - T_d\right)}{\tau_d}\frac{\ln\left(1 + B_h\right)}{B_h} + \frac{\dot{m}_d L_v}{m_d\,c_{pl}} \tag{6.6}$$

This chapter was first published [165] and is reprinted with permission of the journal

Drag, gravity and buoyancy affect the drop acceleration with τ_d, f_1, ρ_d and g_i the relaxation time, correction factor for the drop drag coefficient, density and the gravitational acceleration, respectively. The specific heat at constant pressure of the gas c_p and liquid c_{pl} and the latent heat of vaporization L_v are used in Eq. 6.6 to determine the change of the droplet temperature. The droplet diameter, particle Reynolds number and gas viscosity (d_d, Re_d, μ) are used to determine τ_d and f_1.

$$\tau_d = \frac{\rho_d d_d^2}{18\mu} \qquad \text{and} \qquad f_1 = 1 + \frac{3}{20}\mathrm{Re}_d^{0.687} \tag{6.7}$$

The changes of the droplet mass and temperature are determined with the Schmidt, Prandtl, Sherwood, Nusselt and the Spalding numbers for mass and heat transfer $B_m = (Y_F^S - Y_F^\infty)/(1 - Y_F^\infty)$, $B_h = c_p(T - T_d)/L_v$. Two way coupling of the gas and liquid phase values is achieved by trilinear interpolation.

6.4.2 Combustion submodel - zone B

The premixed flamelet generated manifold approach (PFGM) [201, 202] is used, coupled with the artificial thickened flame (ATF) method [95]. Our PFGM/ATF implementation [157] for spray combustion [164] is extended to account for two fuel and one oxidizer species. The composition of the gas mixture is described by the element mass fractions of carbon and hydrogen (Z_C and Z_H) according to Eq. (6.8). The method works for fuels with different C/H ratios.

$$Z_\alpha = \sum_{i=1}^{N_{sp}} a_{\alpha,i}\frac{W_\alpha}{W_i}Y_i \tag{6.8}$$

The atomic or molecular weights of element α or molecule i are given by W_α and W_i respectively, Y_i is the mass fraction of molecule i, and $a_{\alpha,i}$ denotes the number of atoms α in molecule i. Assuming unity Lewis number [144], the filtered conservation equation for Z_α reads:

$$\frac{\partial\overline{\rho}\widetilde{Z}_\alpha}{\partial t} + \frac{\partial\overline{\rho}\widetilde{u}_i\widetilde{Z}_\alpha}{\partial x_i} = \frac{\partial}{\partial x_i}\left(\overline{\rho}D_S\frac{\partial\widetilde{Z}_\alpha}{\partial x_i}\right) + \dot{\Gamma}_{Z_\alpha} \tag{6.9}$$

In Eq. (6.9), $D_S = D + D_t$ is the sum of the molecular and turbulent diffusivity, D_t is calculated from the turbulent viscosity and turbulent Schmidt number $D_t = \mu_t/\mathrm{Sc}_t$. A joint progress variable $Y_P = Y_{CO_2} + Y_{CO}$ describes the progress of combustion.

$$\begin{aligned}&\frac{\partial\overline{\rho}\widetilde{Y}_P}{\partial t} + \frac{\partial\overline{\rho}\widetilde{u}_i\widetilde{Y}_P}{\partial x_i} = \\ &\frac{\partial}{\partial x_i}\left(\left[FED + (1-\Omega)\frac{\mu_t}{\mathrm{Sc}_t}\right]\frac{\partial\widetilde{Y}_P}{\partial x_i}\right) + \frac{E}{F}\dot{\omega}_C + \dot{\omega}_E\end{aligned} \tag{6.10}$$

In Eq. (6.10), F, E, Ω and $\dot{\omega}_C$ are the thickening factor, efficiency function, flame sensor and chemical source term [157], respectively. The thermochemical quantities (e.g. ρ, $\dot{\omega}_C$) are determined a priori by solving a set of 1D premixed flames with Cantera [56] - by varying the initial composition of the flamelets as functions of Z_H and Z_C in equidistant steps. The resulting quantities are interpolated from physical space to element mass fraction and progress variable space and stored in the 3D look-up table as functions of Z_C, Z_H, and the normalised progress variable Y_{PN}.

This chapter was first published [165] and is reprinted with permission of the journal

6.4.3 Population balance submodel - zone C

The GDE for aerosols [49] is described with the monodisperse model [98, 139], which describes the evolution of the number concentration, size and morphology of the particles through coagulation and coalescence. A narrow size distribution for the silica primary particles is assumed, as found by Boldridge [16] for aggregates, as a result of sintering at high temperatures. It may be expected that the particle size distribution attains the self preserving size distribution by coagulation [100], implied by the monodisperse model. Gröhn et al. [59] justified the application of the monodisperse model with the aforementioned assumptions in their RANS simulations for the SiO_2 synthesis from a turbulent methane/oxygen diffusion flame with a HMDSO precursor [59] and in the FSP process of ZrO_2 [60].

In the LES context, a particle size distribution can be derived from sampling in time at one point over monosized particles which have been exposed to different gas histories due to turbulence. Compared to RANS, the LES enables a more accurate description of the turbulent flow field and hence of the mixing and resulting thermochemical properties [128].

The Favre filtered, closure modelled transport equations for the particle number $\widetilde{N}$, surface area $\widetilde{A}$ and volume $\widetilde{V}$ concentration are outlined below. The assumption of a narrow size distribution is only needed on the sub-filter scales, but not for the resolved scales.

$$\frac{\partial \overline{\rho}\widetilde{N}}{\partial t} + \frac{\partial \overline{\rho}}{\partial x_j}(\widetilde{N}u_j - D_t\frac{\partial \widetilde{N}}{\partial x_j}) = \frac{E}{F}\overline{\rho}I - \frac{1}{2}\beta\overline{\rho}\widetilde{N}^2 \tag{6.11}$$

$$\frac{\partial \overline{\rho}\widetilde{A}}{\partial t} + \frac{\partial \overline{\rho}}{\partial x_j}(\widetilde{A}u_j - D_t\frac{\partial \widetilde{A}}{\partial x_j}) = \frac{E}{F}\overline{\rho}Ia_0 - \frac{\overline{\rho}(\widetilde{A} - A_s)}{\tau} \tag{6.12}$$

$$\frac{\partial \overline{\rho}\widetilde{V}}{\partial t} + \frac{\partial \overline{\rho}}{\partial x_j}(\widetilde{V}u_j - D_t\frac{\partial \widetilde{V}}{\partial x_j}) = \frac{E}{F}\overline{\rho}Iv_0 \tag{6.13}$$

The particle diffusion is neglected due to their low diffusivity [59, 60, 185], the turbulent diffusivity D_t is calculated as described above. The nucleation source term I describes the birth of particle monomers. It is assumed that particle monomers are represented by silica molecules [199]. A reduced reaction mechanism for the oxidation of HMDSO with 3 species and 2 reactions is solved together with a reduced mechanism for ethanol, originating from Marinovs mechanism [118]. The mechanism was adapted to reproduce the SiO LIF measurements by Feroughi et al. [36] and is outlined below (in CGS units).

$$C_6H_{18}Si_2O \;+\; OH \;\rightarrow\; 2\,SiO \;+\; 6CH_3 + H \tag{6.14}$$

$$with \quad 6.00 \times 10^{12} \;\; 0.46 \;\; 15000$$

$$SiO \;+\; H_2O \;\rightarrow\; SiO_2 + H_2 \tag{6.15}$$

$$with \quad 8.50 \times 10^{10} \;\; 0 \;\; 5650$$

The source term I is tabulated as a function of the control variables $I = f\,(Z_C, Z_H, Y_P)$, and is artificially thickened to be consistent with Y_P. In Eqs. (6.13 and 6.12), v_0 and a_0 are the monomer volume and surface, respectively. The coagulation frequency β is calculated with Eq. (6.16), the solid sphere diameter is replaced with the collision diameter d_c to account for the fractal shape of the particles [98].

$$\beta = 4\pi d_c \mathcal{D}\left[\frac{\frac{1}{2}d_c}{d_c + \sqrt{2}g} + \frac{\sqrt{2}\mathcal{D}}{c\frac{1}{2}d_c}\right]^{-1} \tag{6.16}$$

$$g = \left[(d_c + L)^3 - \left(d_c^2 + L^2\right)^{1.5}\right] \;/\; [3\,L\,d_c] - d_c \tag{6.17}$$

In Eqs. (6.16) and (6.17), $\mathcal{D} = (k_b T)/(3\pi\mu d_c)$,
$c = \sqrt{(8k_bT)/(\pi\rho_b\frac{V}{N})}$, k_b, T, ρ_b and $L = (8\mathcal{D})/(\pi c)$) are the particle diffusion, particle velocity,

Boltzmann constant, gas temperature, bulk density and mean free path of the particles, respectively. The characteristic sintering time τ for silica and the surface area of the completely fused particles A_S in Eq. (6.12) are calculated as outlined below [194, 223].

$$\tau = 6.5 \times 10^{-17} d_p \exp \frac{83000}{T} \left(1 - \frac{d_{p,min}}{d_p}\right) \tag{6.18}$$

$$A_S = \left(\frac{V}{N v_0}\right)^{\frac{2}{3}} N a_0 \tag{6.19}$$

The primary, aggregate and collision diameters (d_p, d_a and d_c) are obtained from Eqs. (6.20), with the number of primary particles $n_p = (6V)/(\pi N {d_p}^3)$ and a constant value of 1.8 for the fractal dimension d_f, as proposed by Tsantilis et al. [194].

$$d_p = \frac{6V}{A}, \quad d_a = \left(\frac{6V}{\pi N}\right)^{\frac{1}{3}} \text{ and } \quad d_c = d_p n_p^{\frac{1}{d_f}} \tag{6.20}$$

6.5 Testing

The complex global model must be validated, but the experimental investigations of flame spray pyrolysis processes do not provide enough data for it. This is different to the situation in the turbulent flame community around the TNF [1] workshop that provides complete and detailed measurements for one identical setup including the PDF's of velocity, composition and temperature [8, 9, 172]. The present case of flame spray pyrolysis is more complicated than these TNF-flames, which would necessitate even further measurements for model validation and development. Until such are available, we try to achieve a sufficient validation for the individual submodels as outlined below. *We would like to urge the nanoparticle flame synthesis community to work on the creation of one complete experimental dataset to enable a meaningful model validation or falsification.*

The presented study was performed with the LES in-house code PsiPhi, which was applied, tested and validated with many LES of non-premixed, premixed and partially premixed flames, for gaseous, solid or liquid fuels [20, 45, 82, 135, 157, 164].

A detailed validation of the spray submodel, as used in zone A, requires radial profiles of the droplet distribution, liquid mass or volume flow rate (evaporation rates), velocities and their fluctuations. Masri et al. [57] provided a detailed data set for ethanol spray flames with different equivalence ratios and turbulence levels, by LDV/PDA at different radial positions. The spray modelling in PsiPhi was validated with this dataset for different equivalence ratios and Reynolds numbers [164].

To show the effectiveness of the multi-mixture fraction PFGM model for zone B, it is applied to an artificial 2D test-case, where O_2, H_2 streams and a premixed CH_4/O_2 stream are fed through three inlets with velocities of 5 m/s - the geometry and mass fractions are shown together with the velocities in Fig. 6.2. The investigated test case is independent from the FSP reactor, and is only used for sub-model validation. The results obtained from the PFGM model are compared against the reference data from a direct simulation with finite rate chemistry [33] using Openfoam. The reduced mechanism DRM22 [48] is used in both. Figure 6.2 shows the satisfactory agreement between the PFGM/ATF combustion model and the finite rate chemistry.

6.6 Results

6.6.1 Spray combustion - zones A and B

As shown in Fig. 6.3, the spray evaporation and combustion in zones A and B overlap and interact between 5 and 25 mm above the burner. Figure 6.3a illustrates where the droplets

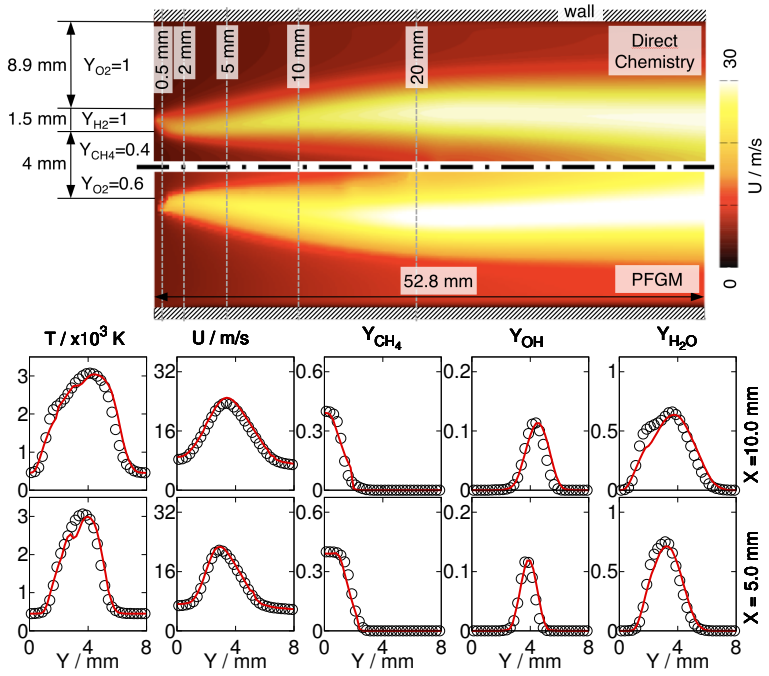

Figure 6.2: Top: contour plots of the velocity u_x; dimensions and mass fractions. Bottom: profiles of the temperature, axial velocity and mass fractions of CH_4, OH and H_2O at two axial locations (◯ finite rate chemistry, - PFGM) for the independent test case.

evaporate due to the heat from the pilot flame and the high slip velocities between the droplet and the environment with a maximum mass release at the outer radius of the spray jet. The major amount of the liquid is evaporated upstream of 15 mm, but drops with larger initial mass and droplets in the core of the jet evaporate further downstream into the burnt gases 6.3a. Spray evaporation was observed to be completely finished at 25 mm height above burner (HAB). The vapor increases the element mass fractions Z_H and Z_C as illustrated for Z_C in Fig. 6.3b. The progress variable Y_P (Fig. 6.3c) illustrates the flame front of the spray flame at 5 mm. The intermediate species SiO (Fig. 6.3d) is mainly predicted between 5 and 20 mm, which is in good agreement with the SiO* measurements by Kilian et al. [84]. An axial shift of SiO compared to the evaporated particle mass is observed since the evaporated mass is added to the unburnt mixture and subsequently burnt.

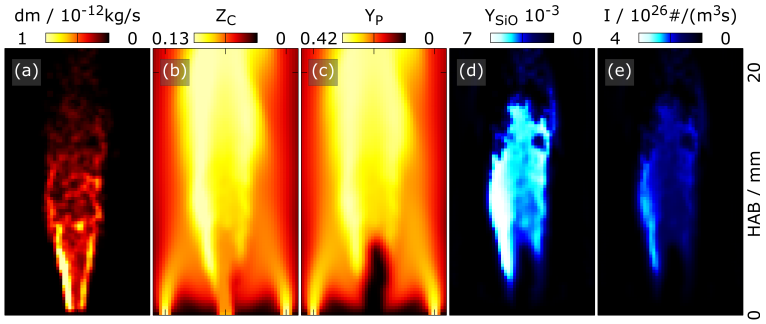

Figure 6.3: Snapshots of (a) evaporated mass dm_d, the Favre filtered (b) element mass fraction Z_C, (c) progress variable Y_P, (d) mass fraction Y_{SiO}, (e) the nucleation source term I.

Figure 6.4a shows a high mean temperature up to 3000 K in the premixed CH_4/O_2 pilot. Furthermore, a quick increase of the temperature in the spray flame at 5 mm is observed. The SiO mass fraction and its conversion to SiO_2 are shown in Fig. 6.4a. The decrease of Y_{SiO_2} is

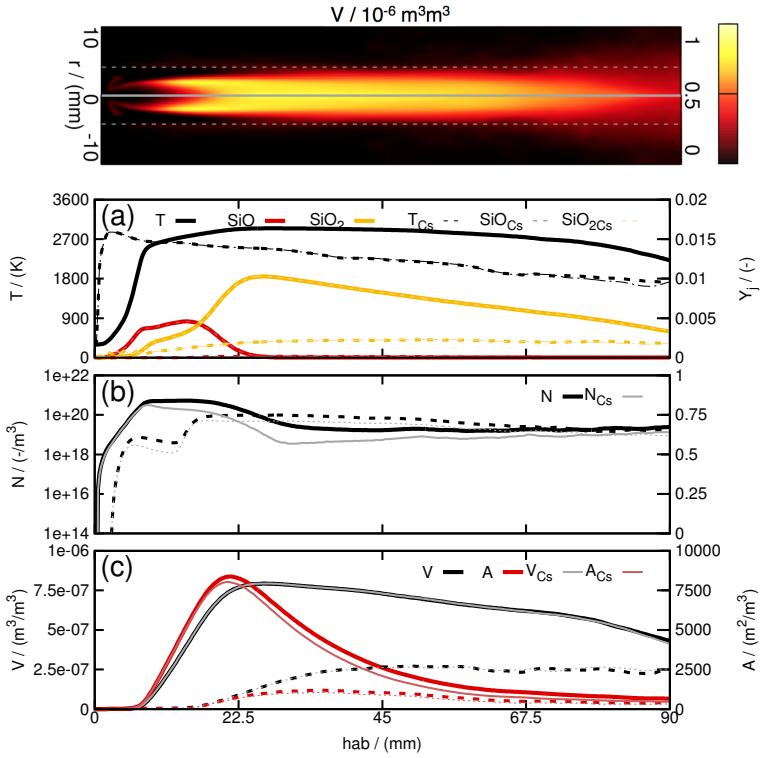

Figure 6.4: Axial profiles of the (a) temperature and SiO/SiO_2 mass fractions, (b) particle number concentration and (c) particle surface area concentration and volume concentration at the centerline (solid) and at a radius of 5 mm (dashed), obtained from the simulations with (labels with C_s) and without slip correction factor.

attributed to the spreading of the jet.

6.6.2 Particle synthesis - zone C

The particle number concentration N as shown in Fig. 6.4b and 6.5a, increases first due to the birth of monomer particles, and decreases afterwards as a result of coagulation. The surface area A shown in Fig. 6.4c and 6.5b and volume concentration V (Fig. 6.4c and 6.5c) rise sharply at $5-8\,\mathrm{mm}$ due to nucleation (Fig. 6.3e). Subsequent turbulent mixing with the environment leads to a slow reduction of the mean volume concentration V, as illustrated in Fig. 6.4c. The surface area concentration A decreases quickly because of sintering in the high temperature region, the curve flattens out with decreasing temperature.

Figure 6.5 illustrates the influence of turbulence downstream of 30 mm, where the particle laden flow is mixed with the environment. The model predicts that the primary particle diameter as illustrated in Fig. 6.5d starts to grow at $15-25\,\mathrm{mm}$, where the number of primary particles (Fig. 6.5e) is at a maximum and starts to decrease. This indicates the high impact of sintering by a reduction of A at almost constant V.

As shown in Fig. 6.6, a rather good agreement between the particles primary and aggregate diameter is observed for large HAB, which results from the fast sintering of the aggregates to larger primary particles. In contrast to the simulations, Kilian et al. [84] observed larger aggregates predominantly.

6.6.3 Sample averaged particle size distribution

Figure 6.6 illustrates size distributions (based on particle numbers) for the particle primary diameter (a), aggregate diameter (b) and collision diameter (c) obtained by the sampling over 256

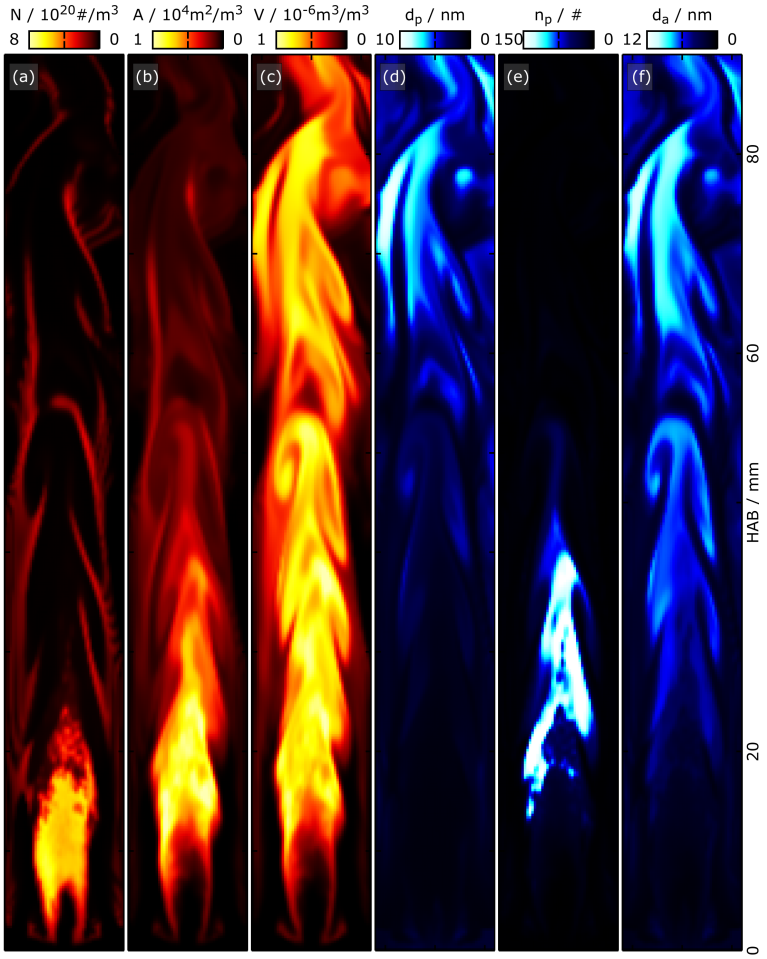

Figure 6.5: Snapshots of the Favre filtered (a) particle number N, (b) surface area A and (c) volume concentration V, (d) primary particle diameter d_p, (e) number of primary particles n_p, (f) aggregate diameter d_a.

instants within 0.01 s, which corresponds to 5-10 flow-through times with respect to the mean velocities at the sampling points. The sampling-volume is one filter volume with $(0.25\text{mm})^3$.

The sampled size distribution of the primary diameter on the centerline, as shown in Fig. 6.6a (dark bars), shows a narrow distribution of small particles up to 40 mm due to nucleation with some first influence of sintering with increasing primary diameter. At this location the aggregate and collision diameters (Fig. 6.6b and 6.6c) have a bimodal size distribution, indicating a large number of nucleated particles with small diameters and larger fractal shaped particles with larger diameters. The larger particles result from coagulation without sintering at this point. This bimodal shape is the result of particles which have been exposed to different histories due to turbulence. Further downstream, the distribution of the primary particles diameter is bimodal first, and the peak value is shifted towards larger values due to sintering. (The mean value changes into the same direction.) The peak value of the aggregate diameter and collision diameters are also shifted towards larger values. At 80 mm above the burner, the primary and aggregate particles still grow, and their size distributions converge towards each other. Furthermore, the distribution of the collision diameter highlights the location of nucleation, coagulation and sintering. A local maximum collision diameter is found at 40 mm, where nucleation seems to be finished and sintering gets dominant. Generally, turbulent mixing has increased at downstream locations, leading to a broader size distribution of the primary and aggregate particle diameters.

This chapter was first published [165] and is reprinted with permission of the journal

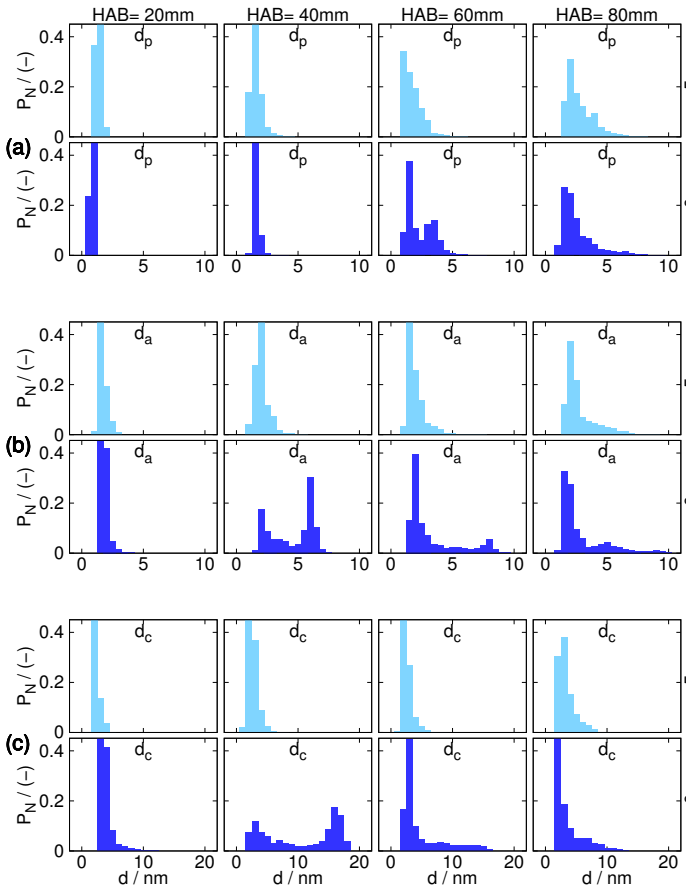

Figure 6.6: Particle size distribution (based on particle numbers) for the particle primary diameter (a), aggregate diameter (b) and collision diameter (c), at a radius of 0 (dark) and 5 mm (light), and at 20, 40, 60 and 80 mm HAB.

6.7 Conclusions

A large eddy simulation of the nanoparticle synthesis from flame spray pyrolysis was presented. The width of the sampled size distribution of the primary, aggregate and collision diameters was shown to be narrow first and increase especially at far downstream locations with increasing impact of turbulent mixing. In contrast to RANS simulations, the size distribution is the direct result of the time-resolved flow field, without applying further models such as presumed distribution functions.

The proposed approach is helpful in understanding the interaction between the spray evaporation, gas phase combustion and particle synthesis. Furthermore, the simulations with the global approach can be used to optimize a reactor such that the size distribution can become narrower by optimising the turbulent flow field. However, there is a case for better modelling in the future, and a strong need for more complete, detailed and repeated experimental reference data to enable the development, validation or falsification of existing or future models.

6.8 Acknowledgement

The authors gratefully acknowledge the financial support by the AiF (grant No. 18298N/3) and of the state North Rhine-Westphalia, Germany, as well as the Center for Computational Sciences and Simulations of the University Duisburg-Essen for the computational resources. We also thank Fabian Proch and Patrick Wollny for many helpful discussions.

This chapter was first published [165] and is reprinted with permission of the journal

This chapter was first published [165] and is reprinted with permission of the journal

Chapter 7

Comparison of population balance equation models for the gas phase synthesis of nanoparticles with mixing

Authors: A. Rittler, I. Wlokas, A.M. Kempf
This paper was submitted to the Journal of Aerosol Science (2017).
The author A. Rittler developed the code for the combustion and particle model, ran all the simulations, wrote the paper and generated all figures and tables.
The author I. Wlokas contributed through discussions and proof-reading.
The author A. M. Kempf contributed corrections, discussions and proof-reading.

This chapter was modified after the defence, according to a) the reviewer comments and b) the recommandations of Prof. Andreas Kronenburg. The modifiactions are made to the text and also to the figures und their captions. The modifications are indicated by footnotes.

7.1 Abstract

Nanoparticle formation from the gas phase is simulated to investigate the different models' capabilities in the presence of mixing. The population balance equation (PBE) is approximated by (a) a monodisperse model, (b) a bimodal model and (c) a sectional model, with a view of using them in three dimensional direct numerical- and large-eddy simulations of real (turbulent) flames and reactors. The sectional model accounts for nucleation and coagulation and resolves the size distribution of a particle property, but is typically too costly for CFD simulations. The monodisperse and bimodal models account for nucleation, coagulation and sintering, but only solve for the moments of either an aggregation mode (monodisperse) or an aggregation and a nucleation mode (bimodal).
First, the models are validated against a published reference case and the effect of the different model assumptions is tested. Then, the impact of mixing different particle populations is discussed and the evolution of the resulting population is analysed. Furthermore, the capability of the simple models compared to the sectional model is outlined. It is found that the monodisperse and bimodal models work reasonably well in predicting the mean particle diameters when very similar populations are mixed, but that the mean particle size may no longer be representative and that the size distribution may differ considerably from the normal self preserving distribution. Indeed, the sectional model is necessary if the real size distribution is of interest in cases with active mixing. Where mixing has only occurred "long ago", the monodisperse and bimodal models tend to be sufficient to produce a realistic, self preserving size distribution.

7.2 Introduction

The size distribution is the key parameter that controls the properties of nanoparticles, their functionality and their application [180]. Metal oxide particles such as titania (TiO_2), silica (SiO_2), zirconium-oxide (ZrO_2) or iron-oxide (Fe_2O_3) are commonly synthesized from the gas phase in laminar [76, 155, 204, 220] or turbulent gas [68, 76, 77, 130, 167, 210, 211, 221, 225] or spray flames [64, 113, 114, 129, 191]. In the processes, particles are nucleated at the supersaturated state in the post flame zone by the clustering of molecules to particle monomers. These particle monomers grow due to coagulation or aggregation, surface growth and coalescence [49]. Due to

the flow and chemical dynamics of turbulent (spray) flames, the aforementioned aerosol dynamic processes may occur simultaneously in space and time [165, 214]. The size distribution of the particle population is influenced by the aerosol dynamical processes to which the particles are exposed. The presence of recirculation zones or turbulence enhances the mixing of different particle populations and increases the width of the resulting particle size distribution.

The evolution of the particles from the gas phase is described by the general dynamics equation, a population balance equation (PBE) as outlined by Friedlander [49] and others. Several models for the approximation of the PBE have been proposed, like discrete models [46], sectional models [72, 109, 174, 222, 223], discrete-sectional models [15], models based on the method of moments [6, 40, 47, 116], bimodal models [73] and the simple monodisperse models [61, 98, 139, 165, 180, 194, 214], in order of decreasing model complexity and computational cost, but at the expense of model accuracy. (It should however be pointed out that most of the so called monodisperse models are actually just monomodal, as a self preserving size distribution of finite width is assumed.)

From the aforementioned models, a sectional, a monodisperse and a bimodal model and have been applied in the present work. These models were used before, to study the particle synthesis from turbulent flows, flames and turbulent spray flames, where mixing of particle populations with different histories obviously occurred. Gröhn et al. [59–61], Buddhiraje et al. [19], Weise et al. [214] or Rittler et al. [165] applied the monodisperse model for the prediction of SiO_2, TiO_2 and ZrO_2 from turbulent flames and spray flames. The sectional model was used by Miller and Garrick [121] for the prediction of the particle diameter in a planar jet, by Modem et al. [122] for the direct numerical simulation of particle coagulation in a temporal mixing layer, by Wang and Garrick [208] for the simulation of titania formation and growth in temporal mixing layers or by Das and Garrick [31, 110] for the investigation of the effects of turbulence on nanoparticle growth in turbulent reacting jets. These aforementioned studies did, however, not outline the impact of the mixing of different particle populations (with different histories) on the evolution of the particle size distributions.

The specific objective of this work is the assessment of three different PBE models, with a view of using them for the simulation and prediction in direct numerical- and large-eddy simulations (DNS and LES) when particle populations with different residence times and histories are mixed. The need of such a study can be seen from Fig. 7.1, illustrating the large-eddy simulation of particle synthesis from spray flames with a detailed sectional model, where the local particle size distribution (PSD) may be bimodal and the time averaged PSD is wider than the instantaneous PSD, indicating simultaneous nucleation and coagulation as well as mixing of fluids with different histories. The models considered are a) a sectional model [110, 121], b) a monodisperse model [98] and c) a bimodal model [73], which are described later. The models were implemented as modules for the in-house code PsiPhi [82, 157, 162, 164] and validated against a zero dimensional test case proposed by Spicer et al. [180]. In the first part of the study, the evolution of the particle population (diameters, number concentrations and size distributions) is discussed for a wide range of operating conditions against the reference data by Spicer, to quantify the abilities of the models without mixing. In the second part of the study, the models are tested when mixing of fluids with different histories and particle populations occurs, to test how the models react to mixing due to turbulence, recirculation, or the evaporation of fuel and precursor sprays.

7.3 Test case

A detailed and meaningful testing of the models based on experimental data is not feasible as time and space resolved measurements of particle diameters and particle size distributions are almost impossible to achieve. A numerical, well established test case in zero dimensions is used instead. The case by Spicer et al. [180] describes the formation of titania particles (TiO_2) from the gas phase, with titanium tetrachloride ($TiCl_4$) and oxygen (O_2) as precursor and oxidizer, respectively. At ambient pressure, three different (constant) temperatures T and three different

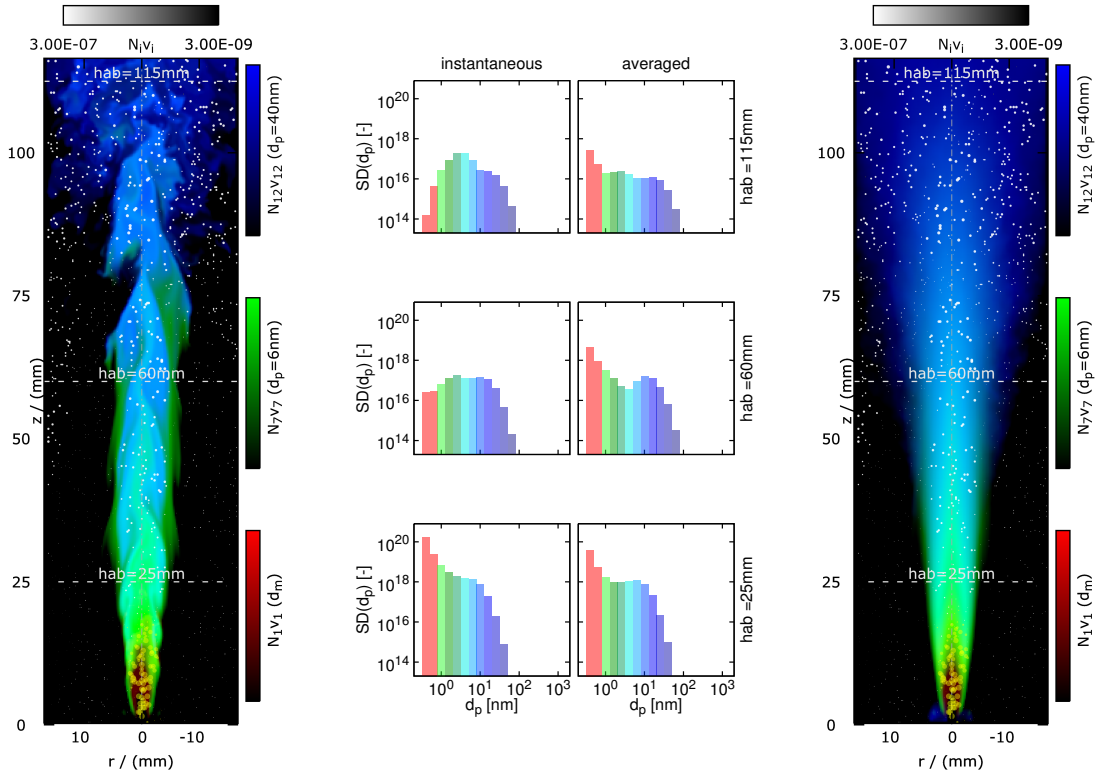

Figure 7.1: Large-eddy simulation results for the particle synthesis from a spray flame with a sectional model. Left and right: instantaneous and time averaged composed particle number concentrations of 3 sections (1, 7 and 12) illustrated together with spray droplets and nanoparticles. Diameters have been scaled by 5×10^7 and 5×10^5. Center: instantaneous and time averaged particle size distributions at 3 heights above the burner (hab).

initial precursor volume fractions ϕ_{ini} are used as operating conditions, as outlined in table 7.1. The reference work by Spicer et al. [180] studied the particle formation, nucleation, surface oxidation and coagulation based on a moving sectional model and the modified monodisperse model [98, 139, 180], with and without surface oxidation. Our work is based on the cases without surface oxidation, but goes beyond the work of Spicer by investigating the importance and effect of mixing, that is key to real (turbulent) synthesis flames, and the ability of different models to describe the mixing effects correctly.

		T [K]		
		1000	1400	1800
ϕ_{ini} [−]	0.01	1000-01	1400-01	1800-01
	0.10	1000-10	1400-10	1800-10
	0.50	1000-50	1400-50	1800-50

Table 7.1: Process parameters used for the nine setups: three temperatures T [K] and initial precursor volume fractions ϕ_{ini} [−] are used.

7.4 Theoretical background

7.4.1 Population balance equations

The evolution of particles from flames includes particle formation (i.e. nucleation of monomer particles from gas phase molecules), coagulation and coalescence (which may also be referred

to as sintering) of monodisperse or polydisperse particles and surface growth. Besides these forming processes (nucleation, coagulation, coalescence and surface growth), the particles are exposed to external processes like convection, diffusion, gravitational settling or thermophoresis, which usually do not change the size and morphology of the particles themselves, but their size distributions at a sampling point. The evolution of the complete particle population by the aforementioned processes for a transient problem in three dimensions is described by aerosol dynamics. The general dynamics equation (GDE) − here given in the continuous form − is used to describe the evolution of a complete particle population [49] and is outlined in Eq. (7.1).

$$\frac{\partial n(v)}{\partial t} + \frac{\partial n(v) u_j}{\partial x_j} - \frac{\partial}{\partial x_j}\left(D \frac{\partial n(v)}{\partial x_j}\right) = I(v)\delta(v - v_0) + \frac{1}{2}\int_0^v \beta(v - v', v') n(v - v') n(v) dv - \int_0^\infty \beta(v, v') n(v) n(v') dv' + \left[\frac{\partial n(v)}{\partial t}\right]_{\text{growth}} + \left[\frac{\partial n(v)}{\partial t}\right]_{\text{coalescence}} \tag{7.1}$$

In Eq. (7.1), $n\,[\mathrm{m}^{-3}]$ is the particle number concentration for a specific particle volume v and changes by convection and diffusion, the second and third term on the LHS. The five terms on the RHS of Eq. (7.1) describe particle formation due to nucleation, birth and death due to coagulation, surface growth and coalescence. Solving this GDE for each possible discrete particle size (expressed by e.g. the particle volume, diameter, ...) is not possible for the present case, due to computational limitations. Instead, three different modelling approaches are used to approximate the GDE, namely a) the numerically still expensive sectional model [15, 109, 121], b) a monodisperse model [60, 98, 139, 214] and c) a bimodal model [73]. The models are discussed in the following subsections.

7.4.1.1 Sectional model

The applied sectional model accounts for particle formation due to nucleation and coagulation of polydsiperse particles and divides the continuous space of a particle property, here the particle volume, into a finite number of (discrete) size classes, the sections. Therefore, N_s transport equations for the particle number concentrations Q_k of the corresponding particle volume v_k are solved, as outlined in Eq. (7.2) for a transient, three dimensional problem:

$$\frac{\partial \rho Q_k}{\partial t} + \frac{\partial \rho Q_k u_j}{\partial x_j} = \frac{\partial}{\partial x_j}\left(\rho D_k \frac{\partial Q_k}{\partial x_j}\right) + \rho \dot{\omega}_k^Q + \rho I \eta_k \tag{7.2}$$

Here, N_s is the number of sections and k indicates the section number. The diffusivity D of particles in section k is calculated with the Einstein-Smoluchowski relation [108] from the particle diameter d_k, the gas phase temperature T and viscosity μ, the Boltzmann constant k_b and the slip correction factor C_S as outlined below.

$$D_k = \frac{k_b T}{3\pi\mu d_k} C_S \tag{7.3}$$

The slip correction factor C_S is determined from the Knudsen number $\mathrm{Kn_k} = 2\,\lambda/\mathrm{d_k}$, with the mean free path λ of the gas as given in Eq. (7.4).

$$C_S = \frac{5 + 4\mathrm{Kn}_k + 6\mathrm{Kn}_k^2 + 18\mathrm{Kn}_k^3}{5 - \mathrm{Kn}_k + (8 + \pi)\mathrm{Kn}_k^2} \tag{7.4}$$

The coagulation source term $\dot{\omega}_k^Q$ accounts for the "birth" and "death" of particles in section k by coagulation and is determined according to Eq. (7.5).

$$\dot{\omega}_k^Q = \begin{cases} -\sum_{i=1}^{N_s} \beta_{i1} Q_i Q_1 & \text{for} \quad k = 1 \\ +\frac{1}{2} \sum_{i=1}^{N_s} \sum_{j=1}^{N_s} \chi_{ijk} \beta_{ij} Q_i Q_j - \sum_{i=1}^{N_s} \beta_{ik} Q_i Q_k & \text{for} \quad k > 1 \end{cases} \tag{7.5}$$

The coagulation frequency β_{ij} in Eq. (7.5) is modelled according to Fuchs' [50] expression for the free molecular to continuum regime and is calculated from the particle diffusivity, diameter and velocity D_i, d_i and c_i, respectively, as outlined in Eq. (7.6).

$$\beta_{ij} = 2\pi \left(D_i + D_j\right)\left(d_i + d_j\right) \left[\frac{d_i + d_j}{d_i + d_j + 2\sqrt{g_i^2 + g_j^2}} + \frac{8\left(D_i + D_j\right)}{\left(d_i + d_j\right)\sqrt{c_i^2 + c_j^2}} \right]^{-1} \tag{7.6}$$

The interpolation function χ_{ijk} in Eq. (7.5) accounts for new agglomerated particles, which do not have exactly the volume of a certain section and redistributes the particle volume to the neighbouring sections, to conserve the particle number and volume. The interpolation function χ_{ijk} is determined as proposed by Miller et al. [121] or Garrick et al. [109] and is outlined in Eq. 7.7.

$$\chi_{ijk} = \begin{cases} \frac{v_{k+1} - (v_i + v_j)}{v_{k+1} - v_k} & \text{for} \quad v_k \leq (v_i + v_j) < v_{k+1} \\ \frac{(v_i + v_j - v_{k-1})}{v_k - v_{k-1}} & \text{for} \quad v_{k-1} \leq (v_i + v_j) < v_k \\ 0 & \text{otherwise} \end{cases} \tag{7.7}$$

The particle velocity $c_k = \left[(8k_bT)/(\pi m_k)\right]^{0.5}$ in Eq. (7.6) increases with temperature and decreases with the particle mass m_k. The transition parameter g_k for the free molecular to continuum regime is determined from the particle diameters d_k and the mean free path of the particles $L_k = (8D_k)/(\pi c_k)$ according to Eq. (7.8).

$$g_k = \left[\left(d_k + L_k\right)^3 - \left(d_k^2 + L_k^2\right)^{3/2} \right] \left[3 L_k d_k\right]^{-1} - d_k \tag{7.8}$$

In the sectional model, the volume averaged particle diameter d_m is determined from the averaged particle volume v_m:

$$v_m = \frac{\sum_{k=i}^{N_s} Q_k v_k}{\sum_{k=i}^{N_s} Q_k} \qquad \Rightarrow \qquad d_m = \left(\frac{6}{\pi} v_m\right)^{1/3}. \tag{7.9}$$

The numerical cost of the sectional model results from solving a transport equation for each section and dominantly from calculating the coagulation source term $\dot{\omega}_k^Q$ for each cell of the three dimensional computational domain. In the present work, the cost is much reduced by focussing on a zero dimensional domain.

7.4.1.2 Monodisperse model

The monodisperse model as proposed by Kruis et al. [98] and modified to account for nucleation [139] describes the evolution of the number concentration, size and morphology of the particles through nucleation, coagulation and coalescence of locally monosized particles. The fractal shape of the particles is considered by replacing the solid sphere diameter with the collision diameter

[98]. Three transport equations are solved for the aggregate number concentration N, the surface area concentration A and the volume concentration V, as outlined in Eqs. (7.10-7.12).

$$\frac{\partial \rho N}{\partial t} + \frac{\partial \rho N u_j}{\partial x_j} = \frac{\partial}{\partial x_j}(\rho D_p \frac{\partial N}{\partial x_j}) + \rho I - \frac{1}{2}\beta \rho N^2 \tag{7.10}$$

$$\frac{\partial \rho A}{\partial t} + \frac{\partial \rho A u_j}{\partial x_j} = \frac{\partial}{\partial x_j}(\rho D_p \frac{\partial A}{\partial x_j}) + \rho I a_m - \frac{\rho}{\tau_p}(A - A_s) \tag{7.11}$$

$$\frac{\partial \rho V}{\partial t} + \frac{\partial \rho V u_j}{\partial x_j} = \frac{\partial}{\partial x_j}(\rho D_p \frac{\partial V}{\partial x_j}) + \rho I v_m \tag{7.12}$$

In our implementation of the monodisperse model, the gas phase density ρ is considered in the transport equations, as in the work of Gröhn et al. [59–61]. The particle diffusivity D_p in Eqs. (7.10-7.12) is calculated as described for the sectional model, however by replacing the particle diameter of section k by the collision diameter d_c (to account for the shape of the particles [98]), as outlined in Eq. (7.13).

$$D_p = \frac{k_b T}{3\pi\mu d_c} C_S \tag{7.13}$$

The collision frequency β in the monodisperse model is also determined according to Fuchs' expression for the free molecular to continuum regime. Assuming collisions of monodisperse particles only ($D_i = D_j$, $d_i = d_j$, $g_i = g_j$ and $c_i = c_j$) and by replacing the particle diameter by the collision diameter d_c, Eq. (7.6) reduces to Eq. (7.14).

$$\beta = 4\pi d_c D_p \left[\frac{\frac{1}{2}d_c}{d_c + \sqrt{2}g} + \frac{\sqrt{2}D_p}{c\frac{1}{2}d_c} \right]^{-1} \tag{7.14}$$

Alternatively the coagulation diameter may be calculated based on the definition for the free molecular regime only (with the solid particle density ρ_p), which is outlined by the equation below.

$$\beta = 4d_c^2 \sqrt{\frac{6k_b T}{\rho_p d_c^3}} \tag{7.15}$$

The collision diameter is also used for the calculation of the Knudsen number Kn and transition parameter g, respectively, as given by Eqs. (7.16,7.17).

$$\mathrm{Kn} = 2\lambda / d_c \tag{7.16}$$

$$g = [(d_c + L)^3 - (d_c^2 + L^2)^{1.5}] \,/\, (3\, L\, d_c) - d_c \tag{7.17}$$

In the monodisperse model, the diameter of an aggregate particle is determined from the volume of one aggregate ($v_a = V/N$), and may be compared to the volume averaged diameter of the sectional model. The diameter of the primary particles d_p is determined from the aggregate particles volume and the corresponding area. The collision diameter is determined from the number of primary particles per aggregate as outlined below.

$$d_a = \left(\frac{6}{\pi} v_a\right)^{\frac{1}{3}}, \quad d_p = \frac{6V}{A} \quad \text{and} \quad d_c = d_p n_p^{d_f} \tag{7.18}$$

The number of primary particles per aggregate is the ratio of the aggregate particle volume to the primary particle volume.

$$n_p = \frac{v_a}{v_p} = \frac{V}{N} \frac{6}{\pi d_p^3} \tag{7.19}$$

In this work, the fractal dimension d_f is set to a value of $d_f = 3$, which corresponds to spherical particles, to enable a comparison to the sectional model, which does not account for sintering. The particle formation source term I in the monodisperse model leads to an underprediction of the particle diameter as new monomers are added to the aggregates - a key shortcoming of the extended monodisperse model.

7.4.1.3 Bimodal model

To resolve the monodisperse model's weakness of underpredicting the particle diameter when nucleation and aggregation occur simultaneously, Jeong and Choi [73] proposed "a bimodal model for the evolution of non-spherical particles undergoing nucleation, coagulation and coalescence" with two modes − based on Kruis' monodisperse model. The first mode describes the evolution of monomer particles due to nucleation and coagulation and is fully described by the particle number-, area- and volume concentration with N_1, A_1 and V_1, respectively. The second mode describes the evolution of aggregates due to coagulation and coalescence by the particle number-, area- and volume concentration of mode two with N_2, A_2 and V_2, respectively. The number concentration in mode one changes due to particle formation I, intra-mode coagulation of particles in mode one with β_{11} and inter mode coagulation of particles in modes one and two with β_{12} as outlined in Eq. (7.20).

$$\frac{\partial \rho N_1}{\partial t} + \frac{\partial \rho N_1 u_j}{\partial x_j} = \frac{\partial}{\partial x_j}(\rho D_1 \frac{\partial N_1}{\partial x_j}) + \rho I - \frac{1}{2}\beta_{11}\rho N_1 N_1 \left(\frac{r}{r-1}\right) - \beta_{12}\rho N_1 N_2 \tag{7.20}$$

As the particles in mode one are considered to maintain their size, the particle volume and area are calculated from the number concentration and the monomer area a_m and monomer volume v_m:

$$A_1 = N_1 a_m \qquad \text{and} \qquad V_1 = N_1 v_m \tag{7.21}$$

Further transport equations are solved for the particle number-, area- and volume concentration of mode two as outlined in Eqs. (7.22-7.24).

$$\frac{\partial \rho N_2}{\partial t} + \frac{\partial \rho N_2 u_j}{\partial x_j} = \frac{\partial}{\partial x_j}(\rho D_2 \frac{\partial N_2}{\partial x_j}) + \frac{1}{2}\beta_{11}\rho N_1 N_1 \left(\frac{1}{r-1}\right) - \frac{1}{2}\beta_{22}\rho N_2 N_2 \tag{7.22}$$

$$\frac{\partial \rho A_2}{\partial t} + \frac{\partial \rho A_2 u_j}{\partial x_j} = \frac{\partial}{\partial x_j}(\rho D_2 \frac{\partial A_2}{\partial x_j}) + \frac{1}{2}\beta_{11}\rho N_1 N_1 \left(\frac{r}{r-1}\right) a_m + \beta_{12}\rho N_1 N_2 a_m - \frac{1}{\tau_p}\left(A_2 - N_2 a_{2,s}\right) \tag{7.23}$$

$$\frac{\partial \rho V_2}{\partial t} + \frac{\partial \rho V_2 u_j}{\partial x_j} = \frac{\partial}{\partial x_j}(\rho D_2 \frac{\partial V_2}{\partial x_j}) + \frac{1}{2}\beta_{11}\rho N_1 N_1 \left(\frac{r}{r-1}\right) v_m + \beta_{12}\rho N_1 N_2 v_m \tag{7.24}$$

The coagulation frequency β_{ij} (with $i \in \{1,2\}$ and $j \in \{1,2\}$) in Eqs. (7.20-7.24) is calculated with the same assumptions as in the two previous models, for the free molecular to continuum regime according to Eq. (7.6), and the particle diffusivity D_i according to Eq. (7.3). As described for the monodisperse model, the collision diameter replaces the solid sphere diameter to account for the fractal shape of the particles and is used to calculate the collision frequency β_{ij}, the particle diffusivity D_i, the transition parameter g_i and the Knudsen number Kn_i of the aggregates. The function r redistributes new aggregated particles whose size does not coincide with the particles in mode one or two, so that the particle number and volume is conserved. Besides the diameter of the aggregates and the monomers, the bimodal model also yields the volume averaged particle diameter, d_{av}, which is obtained from the total volume concentration $V_t = V_1 + V_2$ and number

concentration $N_t = N_1 + N_2$, based on the averaged particle volume $v_{av} = V_t/N_t$, according to Eq. (7.25):

$$d_{av} = \left(\frac{6}{\pi} v_{av}\right)^{1/3} = \left(\frac{6}{\pi}\frac{V_t}{N_t}\right)^{1/3} \tag{7.25}$$

7.4.2 Reaction mechanism and particle formation

The gas phase oxidation of titanium tetrachloride ($TiCl_4$) and oxygen (O_2) is described by a global one step reaction, according to the following equation [180].

$$TiCl_4 + O_2 \rightarrow TiO_2 + 2Cl_2 \tag{7.26}$$

In our current work, the surface reactions are neglected and the molar concentration C of titanium tetrachloride is reduced according to Eq. (7.27), with $k_{TiCl_4} = 8.26 \times 10^4 \exp(-10681/T)$.

$$\frac{\mathrm{d}C}{\mathrm{d}t} = -k_{TiCl_4} C \tag{7.27}$$

A simple model for the particle formation is used, assuming that titania molecules represent the first particle monomers; therefore the nucleation source term I is calculated as given by Spicer et al. [180]:

$$I = -\frac{\mathrm{d}C}{\mathrm{d}t} N_A = k_{TiCl_4} C N_A. \tag{7.28}$$

7.4.3 Modelled particle size distribution

The particle size distributions in the monodisperse (MM) and bimodal (BM) model are modelled with an assumed log normal size distribution for each mode, parameterised by the mean particle diameter of mode one d_{g1} (MM) and the mean diameters of modes one and two d_{g1} and d_{g2} (BM) and the corresponding particle number concentrations N, N_1 and N_2:

$$n(d_p) = \frac{N_i}{\sqrt{2\pi}\ln(\sigma)} \exp\left[-\frac{1}{2}\left(\frac{\ln(d_p/d_{gi})}{\ln(\sigma)}\right)^2\right]/d_p \tag{7.29}$$

The PSD may also be obtained from the particle volumes according to Eq. (7.30):

$$n(v_p) = \frac{N_i}{3\sqrt{2\pi}\ln(\sigma)} \exp\left[-\frac{1}{18}\left(\frac{\ln(v_p/v_a)}{\ln(\sigma)}\right)^2\right]/v_p \tag{7.30}$$

A constant value of 1.4 is used for the geometric standard deviation σ.

7.4.4 Quantification of modelling error

To estimate the deviation of monodisperse and bimodal models from the sectional model, an error E is defined that is calculated from the number concentrations Q_i from the sectional model and the number concentrations N_i from the modelled log-normal size distribution of the monodisperse and bimodal model:

$$E_d = \frac{\sqrt{\int_{d_m}^{d_{\max}} (Q_i - N_i)^2 \,\mathrm{d}d_p}}{\sqrt{\int_{d_p=v_m}^{d_p=v_{\max}} (Q_i)^2 \,\mathrm{d}d_p}}. \tag{7.31}$$

Alternatively, the error may be determined based on the particle volume v_p as outlined in Eq. (7.32):

$$E_v = \frac{\sqrt{\int_{v_m}^{v_{\max}} (Q_i - N_i)^2 \,\mathrm{d}v_p}}{\sqrt{\int_{v_p=v_m}^{v_p=v_{\max}} (Q_i)^2 \,\mathrm{d}v_p}}. \tag{7.32}$$

7.4.5 Mixing related phenomena

The mixing cases certainly raise the question of how well the models are able to describe a non-uniform spatial or temporal distribution of the particle populations that may require modeling in LES or RANS simulations of turbulent flows. This RANS or LES modeling is beyond the scope of the present paper. The effect of temporal and spatial fluctuations of the particle population on RANS and LES simulations is however demonstrated in the appendix, which shows that better RANS and LES models will be required.

7.5 Results

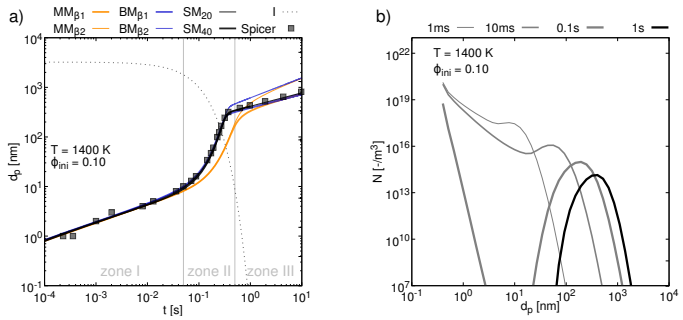

Figure 7.2: Illustration of a) the temporal evolution of the particle diameter predicted by the monomodal (MM), bimodal (BM) and sectional (SM) models (with β_1 and β_2 in the MM and BM model; results of the sectional model are shown for 20 and 40 sections) and b) the particle size distribution obtained with the sectional model (SM) with 40 sections after different residence times (for reference case 1400-10, with $T = 1400\,\mathrm{K}$ and an initial precursor volume fraction of $\phi_{ini} = 0.1$).[1]

7.5.1 Particle evolution

Particle diameter

The evolution of the particle diameter is discussed for case 1400-10 ($T = 1400\,\mathrm{K}$ and $\phi_{ini} = 0.1$)[2]. Figure 7.2a illustrates the predicted volume averaged particle diameters over the particle residence time[3] t. The initial number concentrations for the different models are assumed to be zero $N_{ini} = 0$; the calculated initial particle diameter $d_m = 0.4\,\mathrm{nm}$, representing monomer particles. In the log-log plot of $d_p(t)$, three different particle growth rates may be identified. The linear slope of $d_p(t)$ in zone I is explained by the slow reduction of the precursor concentration C or consequently the slow growth of the number concentration. In zone II, the nucleation source term drops, which is caused by the reduction of the precursor concentration and leads to an increase of the particle number concentration due to particle formation. This internal nucleation process competes with coagulation, which leads to a reduction of the number concentration and subsequently a growth of the particle diameter, explaining the steeper gradient $\partial d_p/\partial t$ in the second zone. The aforementioned finding is also supported by the particle size distribution as outlined in Fig. 7.2b. In zone III, the slope flattens as the precursor gets consumed completely, also shown by the particle size distribution in Fig. 7.2b by the curve for a residence time of 1 ms.

[1] Figure and figure caption were modified to improve the quality of the paper.

[2] ϕ replaced by ϕ_{ini}

[3] The term residence time is used to be consistent with the work of Spicer, even if it may be imprecise in zero dimensions.

Particle size distribution

The evolution of the particle size distribution is discussed for the same case, 1400-10 (T = 1400 K and ϕ_{ini} = 0.1). Figure 7.2b illustrates the predicted particle size distribution as obtained with the sectional model with 40 sections after residence times of 1 ms, 10 ms, 0.1 s and 1 s, respectively. The sectional model shows the bimodal particle size distribution, with a nucleation mode and an aggregation mode. The nucleation mode vanishes for a residence time of 1 s. Interestingly, from a residence time of 0.1 s to a residence time of 1 s, particles with intermediate diameters between 2 nm and 20 nm are hardly found, just small particles from nucleation and large particles from coagulation.

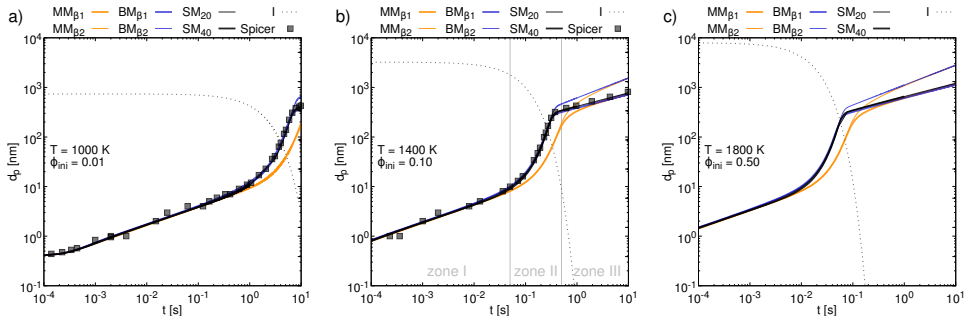

Figure 7.3: Illustration of the temporal evolution of the particle diameter predicted by the monomodal (MM), bimodal (BM) and sectional (SM) models for varying process parameters (cases 1000-01, 1400-10 and 1800-50, with process temperatures T of 1000 K, 1400 K and 1800 K and initial precursor volume fractions ϕ_{ini} of 0.01, 0.1 and 0.5, respectively).[4]

Impact of the process parameters

The particle synthesis is now investigated for three different temperatures and initial precursor concentrations – the case with the lowest temperature and precursor concentration (case 1000-01), the case with a medium temperature and precursor concentration (case 1400-10) and the case with the highest temperature and precursor concentration (case 1800-50). The evolution of the particle diameter is outlined in Fig. 7.3. The increased temperature leads to a quicker reduction of the precursor concentration with a faster reduction of the nucleation source term and therefore a steeper gradient of $d_p(t)$ with a faster particle growth. The particle diameter predicted for the maximum residence time of t = 10 s and the three illustrated cases, increases as a result of the increased precursor concentration, the increased temperature leads just to a faster particle growth.

7.5.2 Performance and convergence of the sectional model

To justify the number of used sections for the further study, the well known impact of section spacing is also investigated in the present study.[6] The performance and convergence of the sectional model is investigated based on case 1400-10. Figure 7.2 has shown that the results for the particle diameter predicted with the sectional model compare very well with the particle diameter of the reference data by Spicer et al. [180]. The particle size distribution is illustrated in Fig. 7.4 for different numbers of sections, from N_s = 10 to N_s = 75, respectively. By reducing the number of sections, the resolution and hence accuracy of the particle diameter space (or particle volume space) is coarsened as the maximum resolved diameter (or volume) was kept constant. The predicted size distributions of the sectional model with 75 and 40 sections is in very good agreement with the reference data, which was obtained by Spicer with a moving sectional method

[4]Figure and figure caption were modified to improve quality of the paper.
[5]Figure and figure caption were modified to improve quality of the paper.
[6]This information was added after defense.

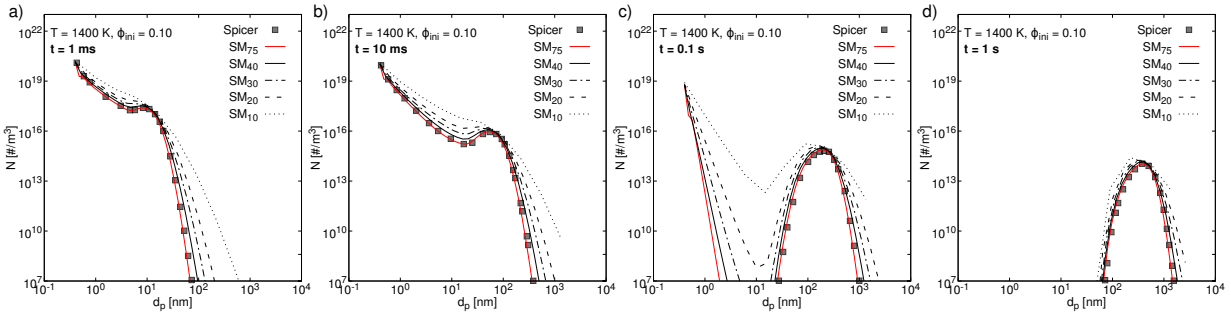

Figure 7.4: Illustration of the particle size distribution obtained with the sectional model (SM) after residence times of 1 ms, 10 ms, 0.1 s and 1 s for the simulations with 10, 20, 30, 40 and 75 sections in comparison to the reference data by Spicer et al. [180] for the reference case with $T = 1400\,K$ and an initial precursor volume fraction of $\phi_{ini} = 0.1$.[5]

[53, 85, 97]. This indicates that resolution independence in size space is reached with 40 sections for this case. It must be stressed, however, that for the investigated cases a wide range of particle diameters, of up to 100 μm with a very long residence time had to be covered. The residence time in real flames is usually shorter, leading to a narrower particle size distribution, so that less sections would be required. The shorter residence time would lead to a narrower particle size space that needs to be resolved and subsequently a reduced number of required sections.

The coarsening of the resolution of the particle diameter space leads to a widening of the size distribution. The trend and the volume averaged particle diameter are predicted well with 10 and 20 sections already, as illustrated in Fig. 7.2a.

7.5.3 Performance of the bimodal and monodisperse model

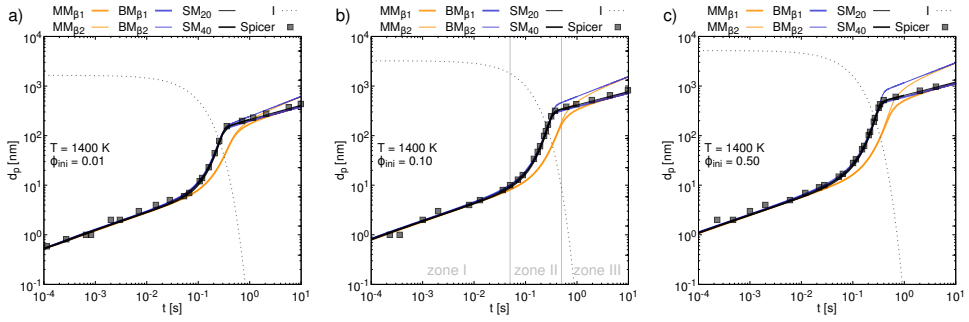

Figure 7.5: Temporal evolution of the particle diameter predicted by the monomodal (MM), bimodal (BM) and sectional (SM) models (with β_1 and β_2 in the MM and BM model) for the case with $T = 1400\,\mathrm{K}$ and increasing initial precursor volume fraction ϕ_{ini} of 0.01, 0.1 and 0.5, respectively. Results of the sectional model (SM) are shown for 20 and 40 sections.[7]

The performance and validity of the bimodal and monodisperse models are investigated for the cases with a process temperature of 1400 K and for all three initial precursor concentrations. Up to a short residence time (zone I), when the nucleation mode is dominant over the coagulation mode, the bimodal and monodisperse model are able to predict the same volume averaged diameter as the sectional model, as illustrated in Fig. 7.5, (for the number concentrations and diameters, refer to Fig. 7.6). With a further growth of the aggregated particles and ongoing nucleation

[7] Figure and figure caption were modified to improve quality of the paper.
[8] Figure and figure caption were modified to improve quality of the paper.

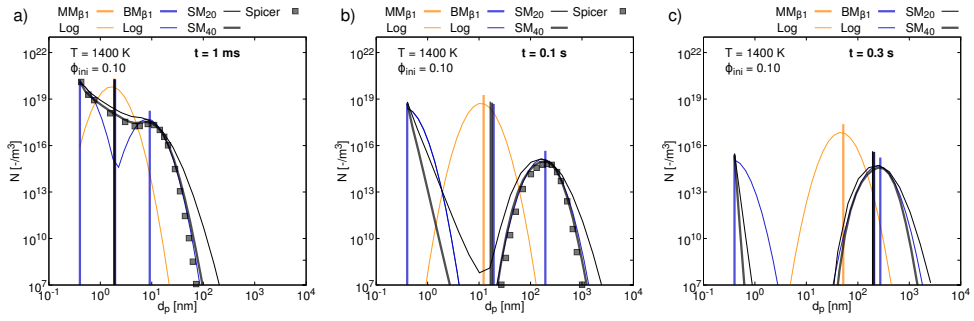

Figure 7.6: Particle size distributions for case 1400-10 (for $T = 1400\,\mathrm{K}$ and an initial precursor volume fraction of $\phi_{ini} = 0.1$) after residence times of a) 1 ms, b) 0.1 s and c) 0.3 s, respectively, together with the aggregate diameter predicted by the MM model, the monomer-, aggregate- and averaged diameter obtained from the BM model and the volume averaged diameter as predicted by the SM model. Additionally shown are log-normal distribution for the aforementioned diameters.[8]

(zone II, Fig. 7.6c), the bimodal model is still able to predict the volume averaged particle diameter in good agreement with the sectional model. The bimodal model is even able to capture the correct diameter of the aggregates. The monodisperse model, however, under-predicts the particle diameters strongly. This under-prediction is attributed to the model property of having only one mode, and adding the nucleation source term to the aggregate particles. Even if the model predicts the right average diameter, the particles predicted by the monodisperse model may not be representative as only larger and smaller particles exist, as illustrated in Fig. 7.6b. In zone III, where nucleation has completed and coagulation is the determining aerosol process, the diameters predicted by the monodisperse model converge towards the diameters predicted by the bimodal and sectional model. This also indicates that for cases where nucleation and coagulation do **not** occur simultaneously, the monodisperse model is a good alternative to the bimodal or sectional model. This finding is also supported by Fig. 7.14, which illustrates the evolution of the particle diameter for a case with an initial number concentration and without nucleation, the monodisperse model predicts the same diameter as the sectional model for all residence times. Figure 7.6 also illustrates the assumed size distributions superimposed to the number concentrations and diameters of the monomers and aggregates for the MM and BM models. These log-normal distribution functions are determined from Eqs. (7.29) and (7.30). The modeled size distribution of the BM model predicts the aggregates reasonable well compared to the sectional model, the SD of the monodisperse model is not representative for the illustrated residence times.

One parameter affecting the performance of the monodisperse and bimodal model is the coagulation kernel. The improper choice of this can lead to a strong over prediction for large particles after long residence times as shown in Fig. 7.5.

The errors of the bimodal and monodisperse model, relative to the sectional model, can be quantified according to Eqs. (7.31) and (7.32). The error of the bimodal model is small as it accounts for an inception mode, the error of the monodisperse model is much higher, especially as long as nucleation and coagulation occur simultaneously, as outlined in Fig. 7.9a. The error of the monodisperse model, however, converges towards the error of the bimodal model for high residence times, when nucleation has less impact.

7.6 Impact of mixing

In the presence of mixing due to turbulence or recirculation zones, an increased mixing of fluid volumes with different particle populations occurs. Depending on the geometry of the burner and

housing, particle populations with histories of a few seconds may be mixed with newly formed particles.[9] Figure 7.1 illustrates exemplarily results for the particle synthesis from a spray flame based on a large-eddy simulation with the sectional model and 20 sections. The left part of the figure illustrates instantaneous snapshots of the composed particle number concentrations for the monomers and particles with a diameter of 6 nm and 40 nm respectively, on a 2D cross section of the 3D simulation. The figure in the center illustrates instantaneous and sample averaged particle size distributions on the centreline for three different heights above the burner. The PSD in the center of the figure indicates that a) nucleation and coagulation occurs simultaneously and b) that mixing occurs for all investigated locations. The mixing of two particle populations with different histories raises the question how well the different models are able to describe a further evolution of the particle properties, e.g. the diameter for turbulent reacting flows. It needs to be stressed, that the rate of particle mixing is very small in laminar flows due to the small Schmidt numbers, but that it is greatly enhanced by turbulence, typically by several orders of magnitude (which is why most chemical processes that require mixing are designed to feature strong levels of turbulence). The parameter "mixing" could be quantified by the coagulation and nucleation time or length scales.[10] This quantification, however, would require very detailed and costly direct numerical simulations.[11] These simulations would greatly extend the scope and volume of the present paper and are part of our future work.[12]

Generic test cases are now developed which consider the mixing of particle populations from the previous simulations at different residence times − as a realistic representation of the mixing of "old recirculated fluid" with "fresh, just reacted fluids". The five new cases are based on the process with $T = 1400\,\mathrm{K}$ and $\phi_{ini} = 0.1$, and describe the evolution of the particle population starting from a bimodal/trimodal size distribution that results from mixing. As it is known that the sectional model is capable of describing the population that results from mixing, the data from the sectional model is used as the reference against which the monomodal and bimodal models are tested.

Mixing of populations with similar residence times without nucleation

The first test case and particle size distribution is obtained by mixing the particle populations of case 1400-10 at a residence time of 1 ms with the population after 10 ms, respectively. Nucleation is not considered, the initial particle size distribution is shown in Fig. 7.7a. (Such a configuration may be found in a setup with a fast consumption of a precursor and a small recirculation zone.) The mixing of these populations leads to a trimodal population, which cannot be described by the mono- and bimodal models. The trimodal shape of the population changes first to a bimodal distribution at $t = 1\,\mathrm{ms}$, which converges towards the self preserving size distribution due to coagulation, as illustrated in Figs. 7.7c and 7.7d. The bimodal and monodisperse models predict the evolution of the mean particle diameter reasonably well in comparison to the sectional model. For long residence times, the presumed log-normal size distributions of the monodisperse and bimodal models are in good agreement with the predicted PSD from the sectional model. However, for an early residence time the width of the PSD cannot be represented by simple log-normal distributions.

The errors of the monodisperse and bimodal models for the case without nucleation but mixing particle populations with similar residence times are high directly after mixing, but decrease for longer residence times as the particle size distribution can attain the self preserving size distribution, undisturbed by nucleation or mixing, as shown in Fig. 7.9b. As nucleation is not included in this case, the error results from mixing only, and hence, the bimodal model is not superior to

[9] This information was added aftre defense.
[10] This information was added after defense.
[11] This information was added after defense.
[12] This information was added after defense.
[13] Figure and figure caption were modified to improve quality of the paper.

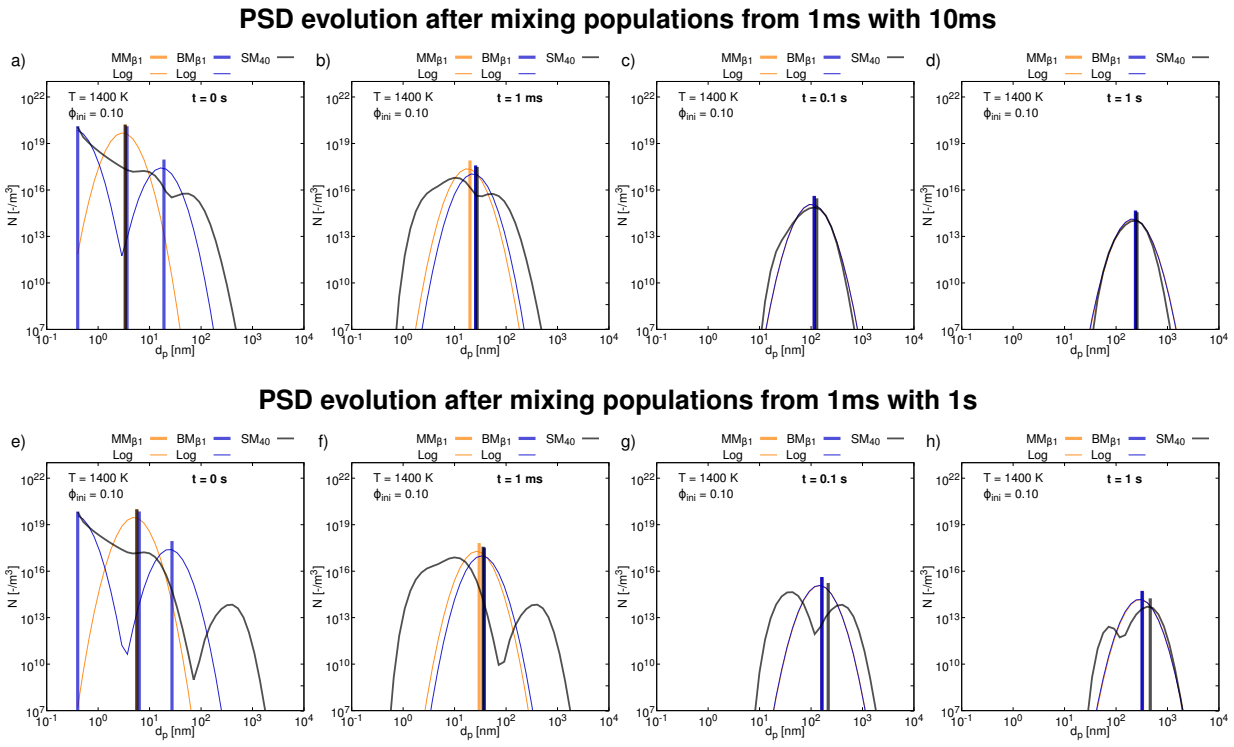

Figure 7.7: Illustration of new particle populations as obtained by mixing the populations from case 1400-10 (for $T = 1400\,\mathrm{K}$ and an initial precursor volume fraction of $\phi_{ini} = 0.1$) after 1 ms with 10 ms (Fig. a)-d)) and 1 ms with $t = 1\,\mathrm{s}$ (Fig. e)-h)), respectively without nucleation.[13]

the monodisperse model.

Mixing of populations with different residence times without nucleation

The second test case is obtained by mixing the particle populations of case 1400-10 at residence times of 1 ms and 1 s, respectively. This case excludes nucleation, the initial size distribution is illustrated in Fig. 7.7e. (This configuration may be found in a setup with a fast consumption of the precursor, as in the previous configuration, but with a large recirculation zone.) From the mixing, a trimodal distribution results, which changes first to a bimodal distribution, which is conserved for a much longer residence time up to $t = 1\,\mathrm{s}$. The bimodal and monodisperse models predict the evolution of the mean particle diameter well. However, neither the monodisperse nor the bimodal model are able to capture the diameters of the modes. The bimodal model can't capture the second mode, as it is not a nucleation mode. The shape and the width of the particle size distribution cannot be represented by a presumed PSD determined from the monodisperse and bimodal model for an early residence time.

If the strength of mixing is increased, the errors of the monodisperse and bimodal models have the same trend as with less mixing, i.e. the high error directly after mixing drops with times, but the error is and remains larger, as illustrated in Fig 7.9c. Here again, the error results from mixing only and the bimodal model is not superior to the monodisperse model.

Mixing of populations with different residence times, with medium nucleation

The previous test cases excluded nucleation, which is now included: The setup is obtained by mixing the particle populations and precursor concentrations of case 1400-10 after residence times of $t = 1\,\mathrm{ms}$ and $t = 1\,\mathrm{s}$, however with medium nucleation as outlined in Figs. 7.8a to 7.8d. The nucleation rate is calculated according to Eq. (7.28) as in the previous study, however

[14]Figure and figure caption were modified to improve quality of the paper.

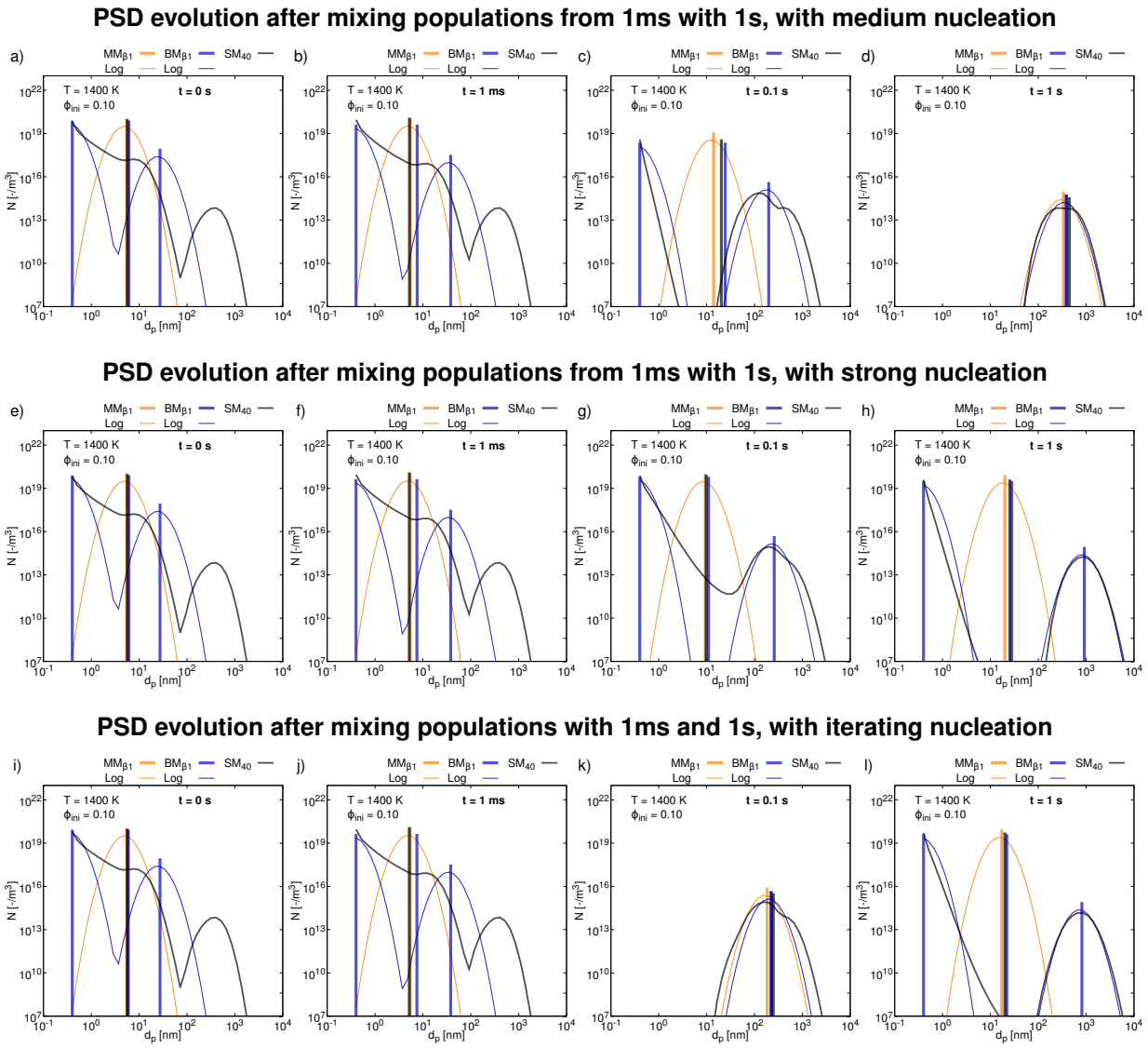

Figure 7.8: Illustration of new particle populations as obtained by mixing the particle size distributions and precursor concentrations for the case with $T = 1400\,\mathrm{K}$ and an initial precursor volume fraction of $\phi_{ini} = 0.1$ at residence time of $t = 1\,\mathrm{ms}$ with $t = 1\,\mathrm{s}$. The nucleation rate is calculated from (Fig. a-d) the precursor concentration after mixing, (Fig. e-h) the precursor concentration after mixing which was artificially set constant and (Fig. i-l) the precursor concentration after mixing which was artificially and iteratively set constant or to zero.[14]

from the precursor concentration after mixing.[15] (Such a setup may be found in flames with large recirculation zones, flames with a slow precursor consumption or in spray flames where the precursor is continuously supplied over a large physical range). Again, a trimodal size distribution results from mixing, which is conserved over a longer residence time as compared to the two previous setups. In the presence of nucleation and mixing, the bimodal model is able to capture the volume averaged particle diameter, as well as the diameters of the monomers and aggregates after longer residence times. The monodisperse model predicts the averaged particle diameter well, it is, however, far off the diameter of the aggregates or monomers. The presumed particle size distribution from the bimodal model cannot represent the real SD directly after mixing, for longer residence times, however, the agreement between the modelled and real PSD is improved. The SD from the monodisperse model is only in agreement with the real PSD after very long

[15] This information was added after defense.

residence times, when the SD attains the self preserving distribution undisturbed.

The error for the setup with mixing and medium nucleation is much higher for the monodisperse model than for the bimodal model, as outlined in Fig. 7.9d, which is however, higher as the error for the setup without mixing (compare Figs. 7.9a and 7.9d).

(It must be stressed that the total mass of the particles and the gas phase is conserved for the previously investigated cases. The following two cases are canonical test-cases to highlight the behaviour of the models in the limit of very strong nucleation.).[16]

Mixing of populations with different residence times with strong nucleation

As in the previous setup, mixing of populations with different residence times is considered in this case, just with strong nucleation. The nucleation rate is calculated according to Eq. (7.28) as in the previous study, however from the precursor concentration after mixing which was artificially set to a constant value.[17] (It must be stressed that for this set-up, the mass fractions may be not conserved, but this case represents a suitable well-defined canonical test-case.)[18] Both simple models predict the averaged diameter well, as shown in Figs. 7.8e to 7.8h. As for the previous setup, the bimodal model predicts the correct aggregate diameter for longer residence times. Directly after mixing, however, the bimodal model is not able to predict the aggregate diameter correctly, as shown in Fig. 7.8f. The modelled particle size distributions determined from both simple models fail to predict the real PSD up to a residence time of 0.1 s. For longer residence time, a good agreement of the PSD predicted by the bimodal model is observed. The monodisperse model also fails to predict the correct PSD for long residence times, as illustrated in Fig. 7.8h.

In the presence of strong nucleation and initial mixing of particle populations, the error of the bimodal model appears to be smaller than for the setup with less nucleation, but only due to a stronger impact of the nucleation mode and hence a relatively weaker effect of the agglomerate mode, as illustrated in Fig. 7.9e. Because of the strong impact of nucleation, the error of the monodisperse model increases continuously.

Mixing of populations with different residence times with repeated nucleation

Finally, the impact of initial mixing and repeated nucleation is investigated and shown in Figs. 7.8i to 7.8l. As in the two previous cases, the nucleation rate is calculated from the precursor concentration after mixing.[19] In this case however, the precursor concentration was artificially and repeatedly set to a constant value or to zero.[20] (Also for this case it must be stressed that the mass fractions may be not conserved, but this set-up represents a suitable well-defined canonical test-case.)[21] As outlined for the previous setups, the volume averaged particle diameters predicted by all three models are in good agreement. The particle size distribution obtained from the bimodal model represents the real PSD reasonably well after longer residence times when nucleation and coagulation occur simultaneously. The PSD predicted by the monodisperse model is in reasonable agreement when nucleation and coagulation do **not** occur simultaneously.

The error resulting from initial mixing and iterative nucleation is shown in Fig. 7.9f: while nucleation is present, the impact of mixing on the error of the bimodal model appears to be small. The error of the monodisperse model increases when nucleation occurs.

Findings

[16] This information was added after defense.
[17] This information was added after defense.
[18] This information was added after defense.
[19] This information was added after defense.
[20] This information was added after defense.
[21] This information was added after defense.
[22] Figure and figure caption were modified to improve quality of the paper.

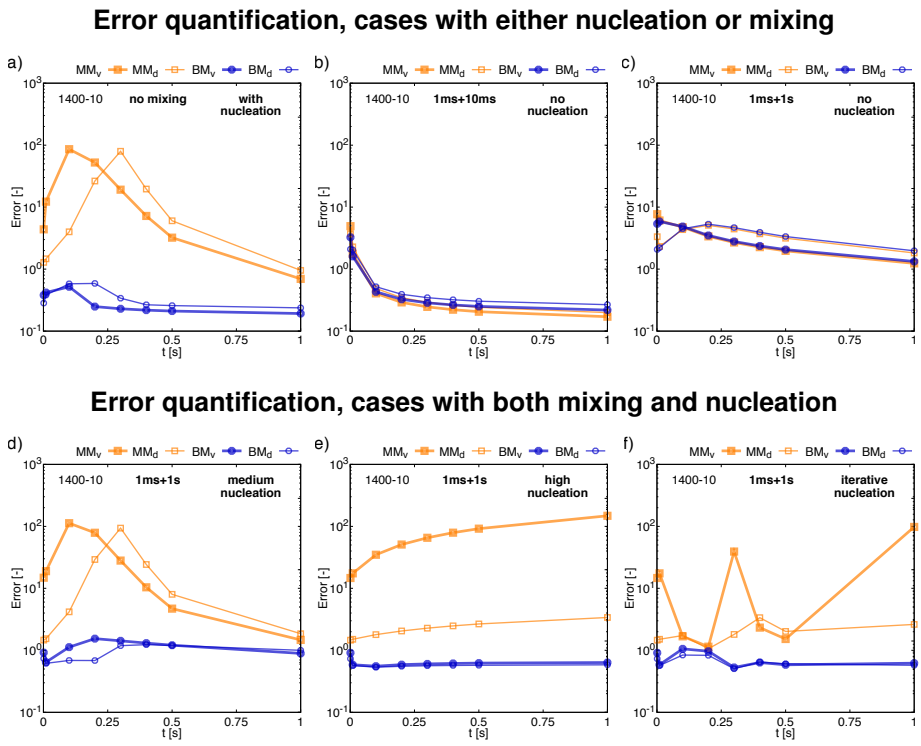

Figure 7.9: Evolution of the errors of the monodisperse (MM) and bimodal (BM) model on basis of the particle diameter d and particle volume v determined according to Eqs. (7.31) and (7.32), respectively. Illustration of the error quantification for a) the reference case 1400-10, b) case 1400-10 with mixing of populations after 1 ms with 10ms without nucleation, c) case 1400-10 with mixing of populations after 1 ms with 1 s without nucleation, d) case with mixing the populations after 1ms with 1s with medium nucleation, e) high nucleation and f) repeated nucleation.[22]

The error measure indicates a) that nucleation strongly increases the error of the monodisperse model (as expected), b) that the impact of mixing leads to a reduced accuracy of the monodisperse model but also of the bimodal model, c) the need for a model that accounts for mixing and d) that the error drops as soon as mixing and nucleation cease - leading to a self preserving size distribution after a sufficiently long time. These findings indicate that the simple monodisperse and bimodal model are suitable for cases where the particles are exposed to long residence times after mixing, so that the PSD may return to the self preserved distribution again. But it also indicates that in recirculation zones and turbulent flows with simultaneous nucleation, coagulation and mixing, an elaborated particle model may be inevitable, as the PSD is prevented from attaining the self preserving distribution again.

7.7 Conclusions

A sectional-, a bimodal- and a monodisperse model have been compared for cases with and without mixing. The models were validated against an artificial reference case by Spicer et al. [180], which described the synthesis of TiO_2 from $TiCl_4$ in O_2 by a global one step reaction and a simple nucleation model. The evolution of the particle properties and the impact of the process parameters have been discussed based on the particle diameter, particle size distribution and the particle number concentrations. An error measure was introduced, based on the particle size distribution from the sectional model and the simple models, to analyse the evolution of the error in time. Furthermore, the importance of a proper turbulence model for the aggregation source term was illustrated for an idealized intermittent case.

Very good agreement of the particle size distribution could be achieved with our implementation of the static sectional model in comparison to the reference data [180]. A too low resolution of the particle volume space lead to a light widening of the particle size distribution, but did not influence the prediction of the volume averaged particle diameter. The bimodal model was able to capture the diameters of the aggregates and the averaged particle diameters for all cases with simultaneous nucleation and coagulation, the monodisperse model was only able to capture the averaged particle diameters for a dominant nucleation or coagulation mode. It was also shown that the particle size distribution constructed from a presumed distribution function represents the real particle size distribution reasonably well for cases without nucleation and mixing.

The impact of mixing was investigated for five generic test-cases based on combining two different populations and monitoring their evolution. Results of the sectional model were considered as a reference. The size distributions predicted by the monodisperse and bimodal model strongly deviate right after mixing, but return to a good agreement eventually, well after mixing had finished, when a monodisperse or bimodal model would suffice again. This means that cases dominated by mixing will require a sectional method, whereas cases with negligible mixing can be described reasonably well with the bimodal or even monodisperse model.

7.8 Acknowledgement

The authors gratefully acknowledge the financial support by the AiF (grant No. 18298N/3) and of the state North Rhine-Westphalia, Germany, as well as the Center for Computational Sciences and Simulations of the University Duisburg-Essen for the computational resources. We also thank Fabian Proch for many helpful discussions.

Appendix

[23] Figure 7.10 illustrates the evolution of the particle diameter for the complete set of investigated test-cases. The particle evolution as discussed in the previous section is also found for the cases that were not discussed in detail in the paper.

Impact of time-averaging or spatial filtering

Simulations of turbulent flows normally reduce the computational effort by only considering time-averaged $<\phi>$ or spatially filtered $\overline{\phi}$ quantities ϕ, using the RANS (Reynolds Averaged Navier Stokes) or LES (Large-Eddy Simulation) approaches. This means that for a point or a filter volume, the distribution of the quantity ϕ is not known, but only a mean value (time-averaged or spatially filtered). The distribution of the quantity ϕ does, however, affect averaged or filtered quantities that non-linearly depend on ϕ. Therefore, the knowledge of the mean value is not enough. In RANS, the distribution of ϕ is known as the PDF (Probability Density Function), in LES as the FDF (Filtered Density Function). In the context of nanoparticle synthesis, the agglomeration term depends not just on the mean particle number density, but actually on its distribution, which hence affects the evolution of the time-averaged or filtered particle distribution. Thus, the development of suitable turbulence models is necessary

The effect of the distribution is demonstrated in the following section for an idealised intermittent case. In this case, the mean number concentration $<N_i>$ (or the filtered concentration $\overline{N}_i$) is obtained as the average of samples of a high value $N_i^h = <N_i> / \alpha$ with a probability of α and samples of a low value $N_i^l = 0$ with the probability of $1 - \alpha$. (For example in RANS, one could think of a time series that repeatedly takes the value of N_i^h for α seconds and of N_i^l for $(1 - \alpha)$ seconds.) This means that either a high concentration N_i^h exists or a zero one ($N_i^l = 0$) − with

[23] All figures in the appendix were modified to improve the quality of the paper.

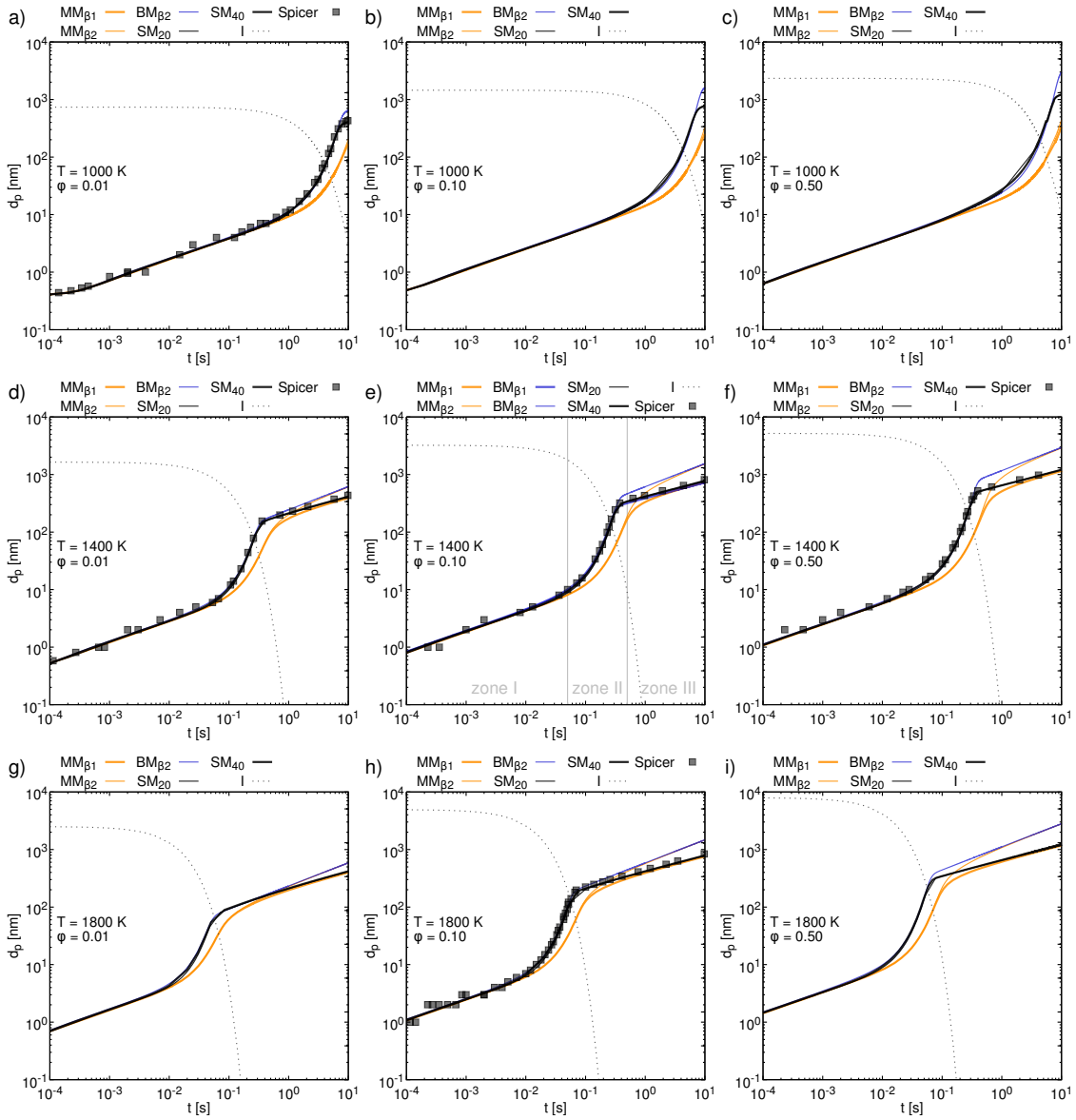

Figure 7.10: Evolution of the volume averaged particle diameter with respect to time for three different temperature regimes and three different initial volume fractions. Comparison of the simulation results against the results by Spicer et al. [180].

a corresponding effect on aggregation that depends non-linearly on the number concentration as $\beta N_i N_j$. The difference between correctly computing the evolution of the particle population based on the intermittent concentration (either N_i^h or $N_i^l = 0$) and of incorrectly computing it from the constant mean value $<N_i>$ is illustrated in Figs. 7.16a to 7.16d, for $\alpha \in \{1, 0.1, 0.01, 0.001\}$. This clearly shows that the very high instantaneous (or spatial) concentrations lead to a very fast agglomeration and hence increase of particle size and reduction of particle number. A quantitative representation of the evolution of the error with time is illustrated in Figs. 7.16e to 7.16h, showing that the error is zero to start with, increases rapidly and then drops off slowly after the agglomeration has slowed down due to very few remaining particles. It also needs to be pointed out that very considerable errors can result, depending on the intermitency factor α – errors that can well exceed the error caused by a simplistic model (e.g. monodisperse) even for a complicated size distribution function. This means that further work on proper turbulence modelling for nanoparticle synthesis is needed, although the LES tends to yield smaller errors than RANS, as much of the fluctuations are resolved.

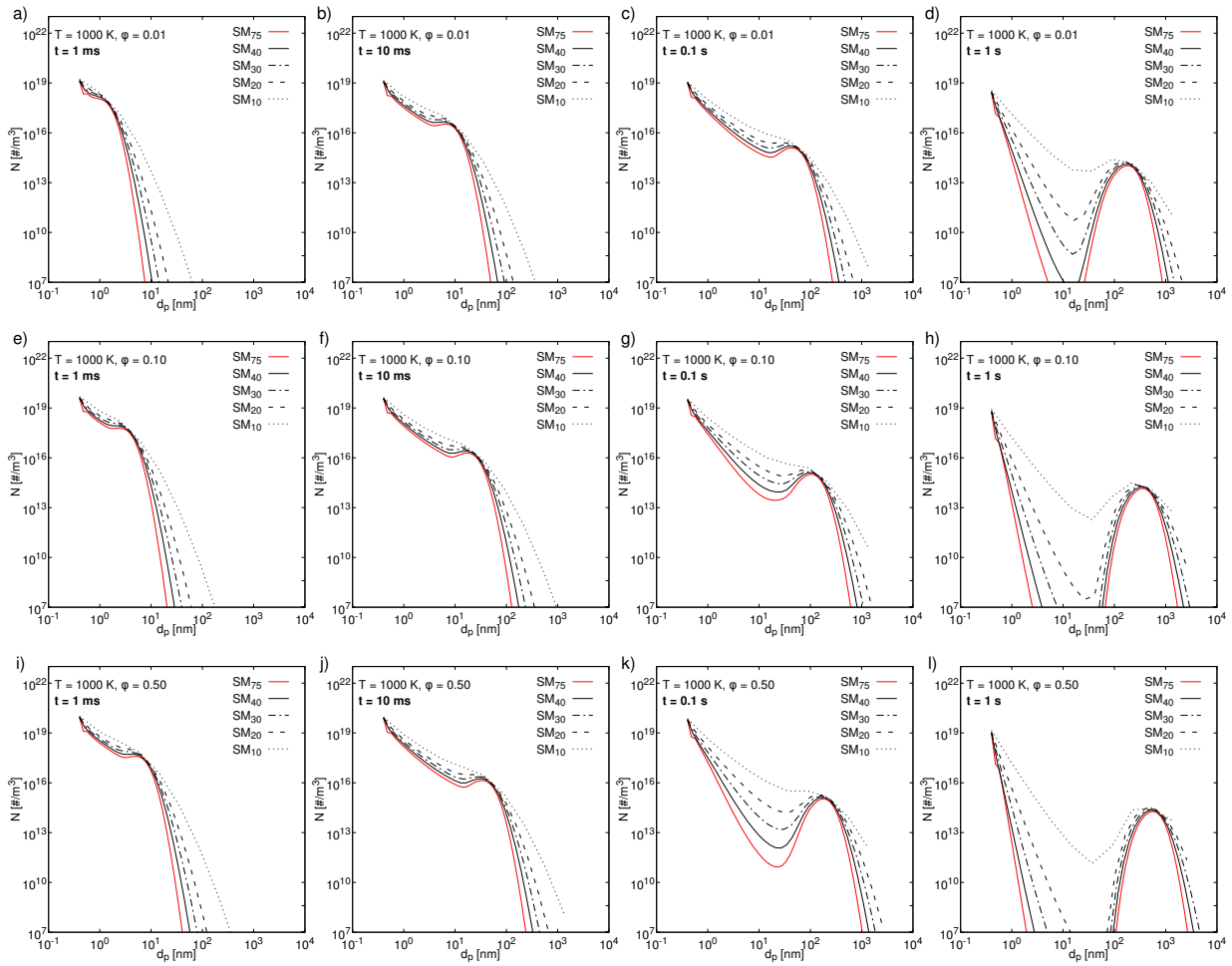

Figure 7.11: Particle size distribution for the case with 1000 K and all initial precursor concentrations. The PSD are shown for four different residence times and for the sectional model with 75, 40, 30, 20 and 10 sections compared against the simulation results by Spicer et al. [180].

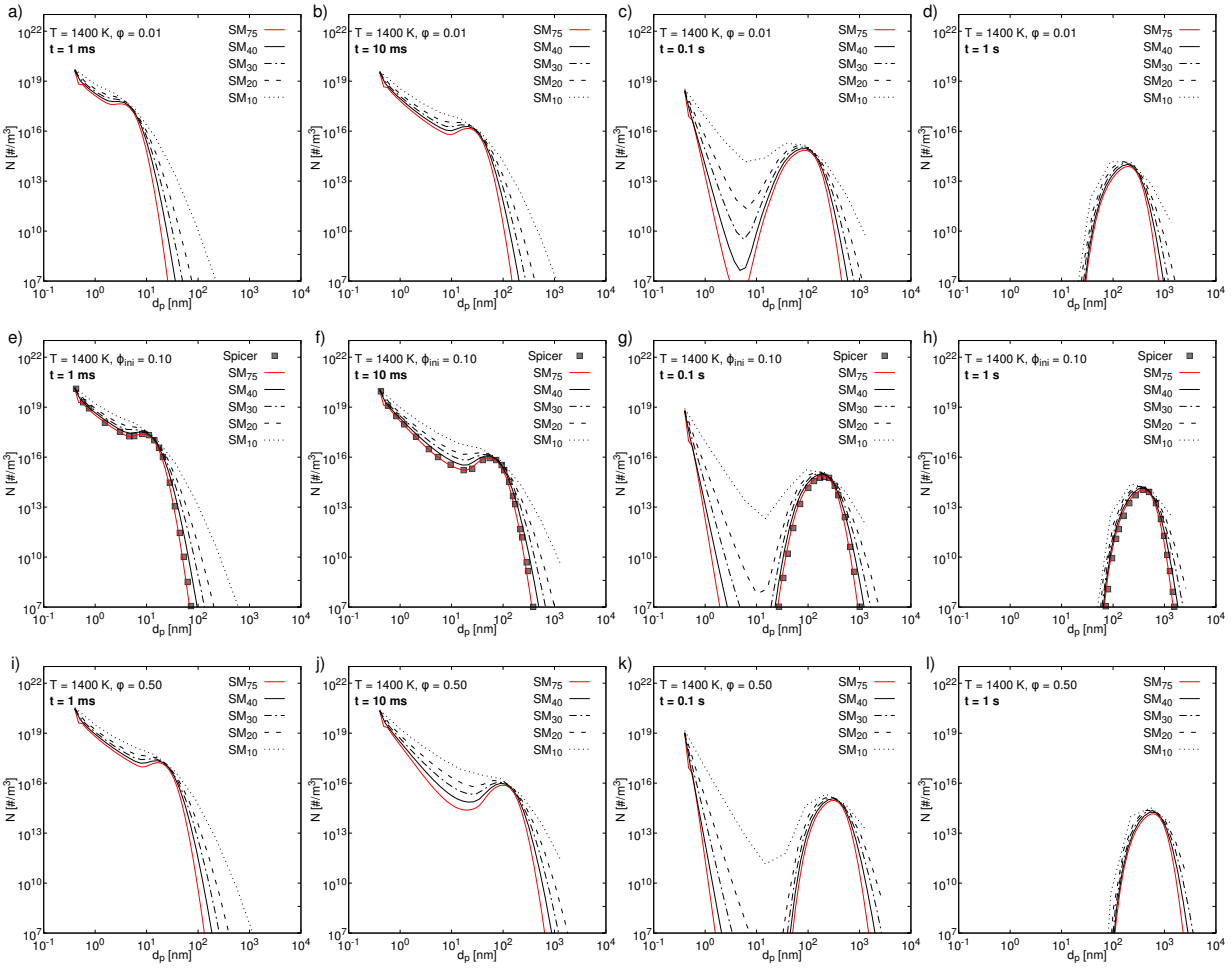

Figure 7.12: Particle size distribution for the case with 1400 K and all initial precursor concentrations. The PSD are shown for four different residence times and for the sectional model with 75, 40, 30, 20 and 10 sections compared against the simulation results by Spicer et al. [180].

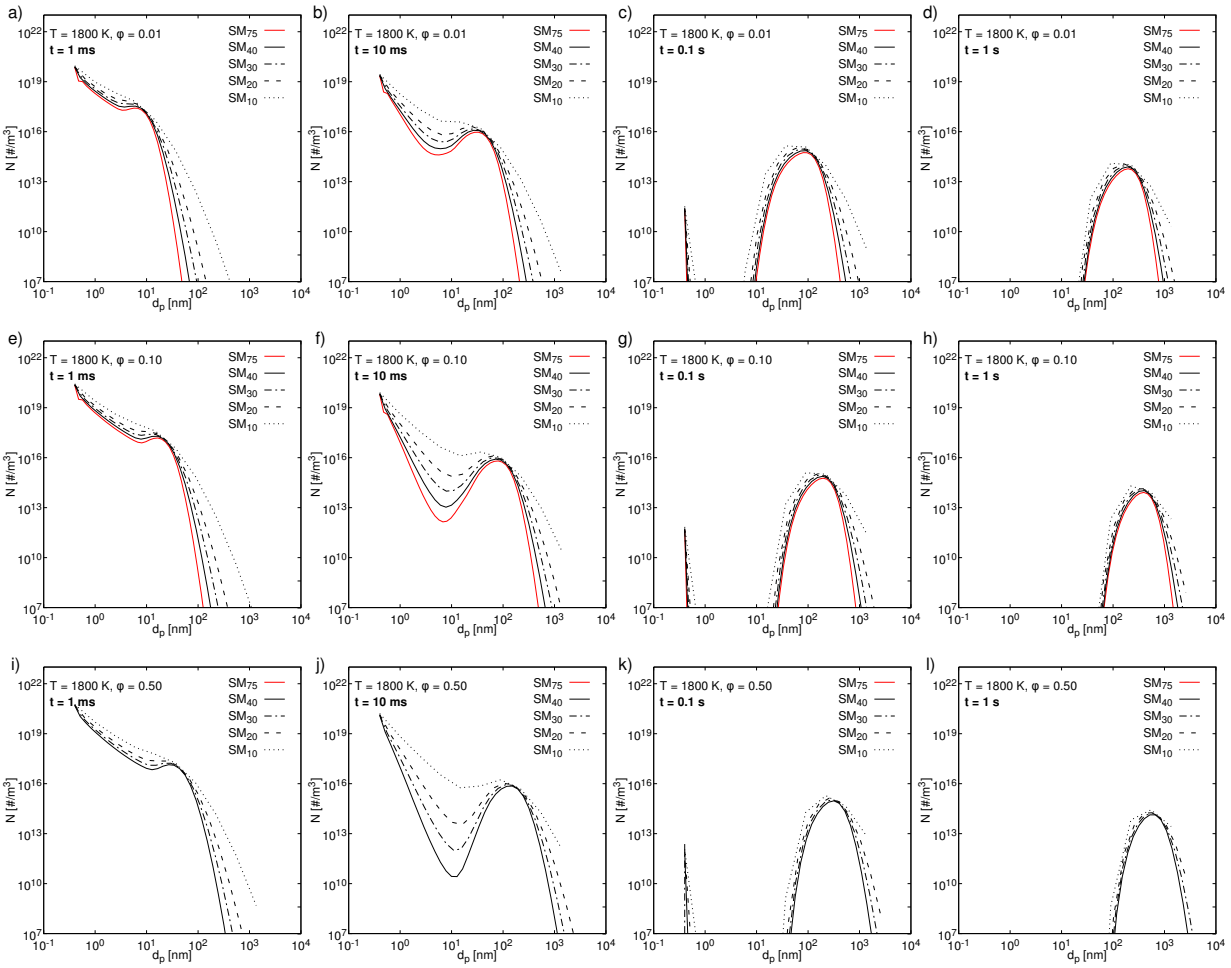

Figure 7.13: Particle size distribution for the case with 1800 K and all initial precursor concentrations. The PSD are shown for four different residence times and for the sectional model with 75, 40, 30, 20 and 10 sections compared against the simulation results by Spicer et al. [180].

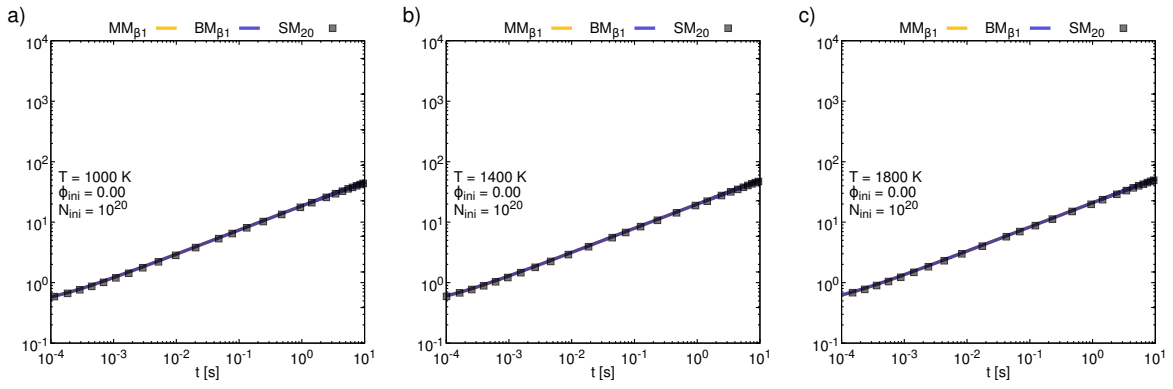

Figure 7.14: Evolution of the particle diameter without nucleation, as predicted by the sectional, bimodal and monodisperse model.

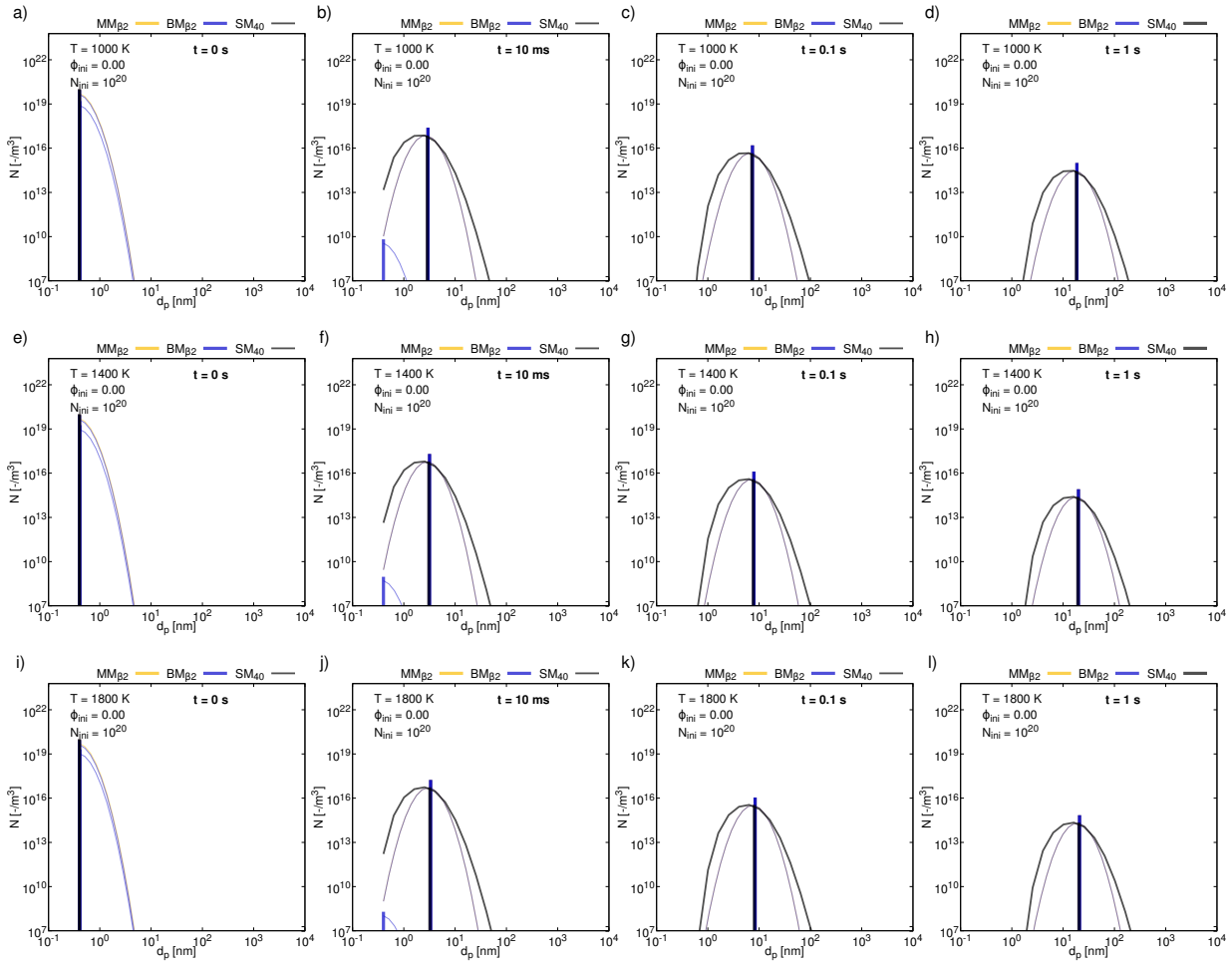

Figure 7.15: Evolution of the particle diameter without nucleation, as predicted by the sectional, bimodal and monodisperse model.

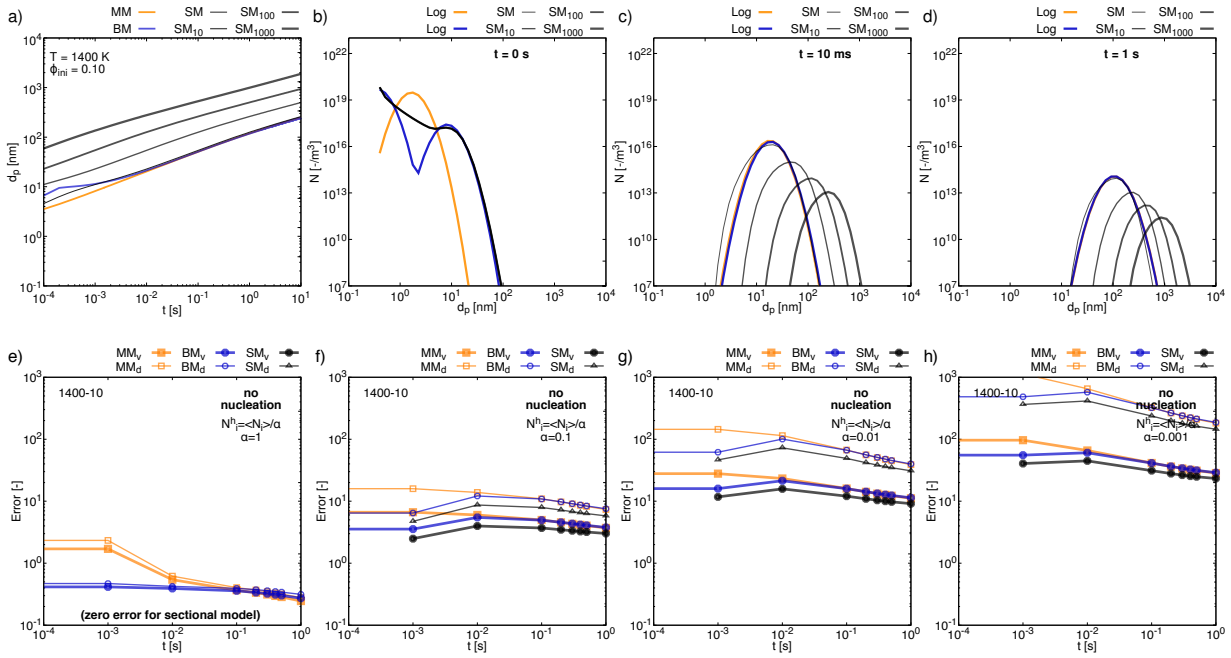

Figure 7.16: Evolution of a) the particle diameter, b)-d) the particle size distribution and e)-h) the error index for case 1400-10 without nucleation or mixing, but with an α^{-1} times higher initial number concentration for the sectional model. (The number concentrations in the simulations with the monodisperse and bimodal model are the same as in the original setup. It should be noted that for plotting the graphs the resulting PSD's for the initial scaled PSD's are devided by α^{-1}).

Chapter 8

Large Eddy Simulation of Iron-Oxide Nanoparticle Synthesis from Spray Flame Pyrolysis [166]

Authors: A. Rittler, I. Wlokas, A.M. Kempf
This chapter including all figures and tables was previously published in 'Proceedings of the European Combustion Meeting, A. Rittler, I. Wlokas and A. M. Kempf,. Large Eddy Simulation of Iron-Oxide Nanoparticle Synthesis from Spray Flame Pyrolysis. (2017)
The author A. Rittler developed the code for the spray treatment, the combustion- and particle model, developed the code to produce the thermochemical manifolds, ran all the simulations, wrote the paper and generated all figures and tables.
The author I. Wlokas provided the chemical mechanism for iron-pentacarbonyl and contributed through discussions and proof-reading.
The author A. M. Kempf contributed corrections, discussions, proof-reading and the original code.

8.1 Abstract

Large eddy simulation results are presented for the iron-oxide synthesis from a spray flame process. The liquid iron precursor is dissolved in ethanol and injected into a combustion chamber, dispersed by an air stream and subsequently evaporated and ignited by a premixed methane air pilot flame. The simulations are performed with the LES and DNS in-house code PsiPhi. Combustion is modelled with the flamelet generated manifold approach, coupled with the artificially thickened flame method (FGM/ATF). The evolution of the nanoparticle population is described by a) a monodisperse model and b) a sectional model. Results are presented for diameters, number concentrations and particle size distributions. The reactor was investigated for a wide range of operating conditions.

8.2 Introduction

The flame spray pyrolysis (FSP) for the synthesis of metal oxide particles (e.g. SiO_2, TiO_2, Al_2O_3, ZrO_2 or Fe_2O_3) allows a simple precursor supply into a hot flame with a rapid quenching of the particle formation [113] and overcomes the limits of the partial pressures of the precursor. The synthesis of iron oxide nanoparticles from FSP has been investigated by many experiments ([58, 105, 183]), but numerical investigations have not been reported for iron oxide formation from spray flames. Iron oxide formation from laminar flames, however, was investigated by numerical simulations (e.g. Wlokas et al. [220]), based on a detailed reaction mechanism for the oxidation of iron pentacarbonyl and the simple monodisperse model for approximating the population balance equation.

In the flame spray pyrolysis process, the liquid precursor is solved in an organic liquid fuel, which is injected into a combustion chamber with a pilot flame as a secondary heat source. Usually, air or oxygen are used as dispersion and sheath gas [113]. Precursors that have been used for the gas-phase synthesis of iron oxide particles are include iron pentacarbonyl, iron acetylacetonate, iron propionate or iron (III) nitrate solved in ethanol or xylene, a good overview is given by Mädler et al. [191].

In the spray flame process, the liquid spray is atomised in the shear layer between the liquid and surrounding gas and subsequently evaporated due to the heat of the pilot flame. The mixing

This chapter was first published in the proceedings of the European Combustion Meeting and is reprinted with permission of the journal

of the fuel and precursor vapor with the environment is enhanced due to turbulence of the flow field. This mixture is ignited by the pilot flame. During the combustion of the main flame, the iron containing precursor is decomposed into intermediate species, which react to Fe_2O_3 molecules. These molecules nucleate and form the first particle monomers, which coagulate, grow, agglomerate and coalesce. The aforementioned fluid dynamic and aerosol dynamic process steps may happen simultaneously in space and time inside the flame, due to the impact of turbulence.

Direct and large-eddy simulations are promising tools to allow deeper insight into the underlying processes, as experiments are costly and limited. It must be stressed however, that complete simulations with detailed models for the fluid dynamics, spray formation, chemistry and aerosol dynamics will not be feasible for years. The simulations must therefore apply a set of simplifying assumptions.

The aim of the presented work is the development, implementation and validation of a model for the prediction of the nanoparticle sysnthesis from a spray flame in the LES context [165]. Subsequently, the process parameters of the synthesis reactor are varied and the particle evolution is investigated for different process parameters.

8.3 Experimental setup

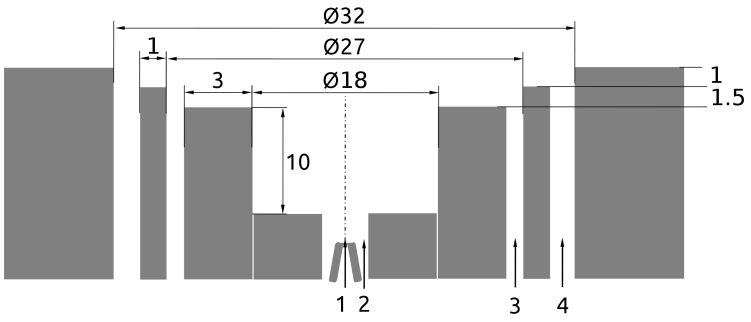

Figure 8.1: Illustration of the investigated spray synthesis burner (at the "Institut für Energie- und Umwelttechnik e. V." (IUTA) in Duisburg, Germany).

The investigated burner consists of four concentric inlets, which are illustrated in Fig. 8.1. The liquid precursor and solvent mixture is injected through inlet 1, dispersed by air supplied through the concentric inlet 2. The heat for evaporation of the liquid droplet, as well as the ignition and stabilisation of the spray flame is achieved by the pilot flame which consists of a premixed methane air mixture and is supplied through concentric inlet 3. An air sheath gas is supplied through concentric inlet 4. The operating conditions are summarized in the table below.

Inlet	Species	flow rate	unit
1	ethanol	400	g/h
1	ironpentacarbonyl	100	g/h
2	air	18	slm
3	methane	4	slm
3	air	24	slm
4	air	90	slm

Table 8.1: Operating conditions of the standard setup for iron pentacarbonyl.

Except of the spray angle, the boundary conditions for the droplets are unknown. In the

This chapter was first published in the proceedings of the European Combustion Meeting and is reprinted with permission of the journal

simulations, the spray angle at the inlet is set to 20°, the droplet size distribution is prescribed by a Rosin Rammler distribution with a diameter of 40 μm at the 80th percentile.

8.4 Modelling Approach

An Eulerian-, Lagrangian- and Eulerian specification of the flow field is used to describe the gas-, liquid- and particle phase, respectively. In the LES context, the Favre filtered conservation equations are solved as discussed below. The continuity and momentum equation with source terms for mass ($\dot{\Gamma}_{\overline{\rho}}$) and momentum exchange ($\dot{M}_{d,i}$) between the phases are outlined below.

$$\frac{\partial \overline{\rho}}{\partial t} + \frac{\partial \overline{\rho}\widetilde{u}_j}{\partial x_j} = \dot{\Gamma}_{\overline{\rho}} \tag{8.1}$$

$$\frac{\partial \overline{\rho}\widetilde{u}_i}{\partial t} + \frac{\partial \overline{\rho}\widetilde{u}_i\widetilde{u}_j}{\partial x_j} = -\frac{\partial \overline{p}}{\partial x_i} + \frac{\partial \overline{\tau}_{ij}}{\partial x_j} + \frac{\tau_{ij}^{sgs}}{\partial x_j} + \dot{M}_{d,i} \tag{8.2}$$

In Eqs. (8.1) and (8.2), $\widetilde{u}_j, \overline{\rho}, \overline{p}, \overline{\tau}_{ij}$ and τ_{ij}^{sgs} represent the Favre filtered velocity, the filtered density, pressure and the viscous stress tensor, respectively. Two way coupling between the gas and liquid phase is achieved based on a trilinear interpolation method. The residual stresses τ_{ij}^{sgs} are determined based on an eddy viscosity approach from the turbulent viscosity μ_t, which is calculated with our implementation [162] of Nicoud's sigma model [133].

In the **Spray phase model**, the Lagrangian specification is used to describe the evolution of liquid droplets. A set of differential equations is solved for each numerical particle d, which represent the liquid droplets. Assuming equilibrium conditions [2, 120], the motion and the evolution of the droplet mass and temperature are described by Eqs. (8.3-8.6), with x_d, u_d, a_d, m_d and T_d denoting the position, velocity, acceleration, mass and temperature of the droplets, respectively.

$$\frac{\mathrm{d}x_{d,i}}{\mathrm{d}t} = u_{d,i} \tag{8.3}$$

$$\frac{\mathrm{d}u_{d,i}}{\mathrm{d}t} = a_{d,i} = \frac{f_1}{\tau_d}\left(\widetilde{u}_i - u_{d,i}\right) + \left(1 - \frac{\overline{\rho}}{\rho_d}\right) g_i \tag{8.4}$$

$$\frac{\mathrm{d}m_d}{\mathrm{d}t} = -\frac{\mathrm{Sh}}{3\,\mathrm{Sc}}\frac{m_d}{\tau_d}\ln\left(1 + B_m\right) \tag{8.5}$$

$$\frac{\mathrm{d}T_d}{\mathrm{d}t} = \frac{\mathrm{Nu}\,c_p}{3\,\mathrm{Pr}\,c_{pl}}\frac{\left(T_g - T_d\right)}{\tau_d}\frac{\ln\left(1 + B_h\right)}{B_h} + \frac{\dot{m}_d L_v}{m_d\,c_{pl}} \tag{8.6}$$

The droplet acceleration is calculated from drag, gravity and buoyancy forces, where τ_d, f_1, ρ_d and g_i are the particle relaxation time, the correction factor for the drop drag coefficient, the density and the gravitational acceleration, respectively. The gas viscosity, the droplet diameter and Reynolds number (μ, d_d, Re_d) are used to determine τ_d and f_1 as outlined below.

$$\tau_d = \frac{\rho_d d_d^2}{18\mu} \qquad \text{and} \qquad f_1 = 1 + \frac{3}{20}\mathrm{Re}_d^{0.687} \tag{8.7}$$

The Schmidt, Prandtl, Sherwood, Nusselt and the Spalding numbers for mass transfer $B_m = (Y_F^S - Y_F^\infty)/(1 - Y_F^\infty)$ and heat transfer $B_h = c_p(T - T_d)/L_v$ are used to determine the changes of the droplet mass and temperature.

In the **Combustion model**, the thermochemical state of the gas phase is determined based on the flamelet generated manifold approach (FGM) [201, 202] coupled with the artificial thickened flame (ATF) method [95]. Our implementation of the FGM/ATF approach for spray combustion [157, 164] was extended to account for 2 fuels and 1 oxidizer [165].

This chapter was first published in the proceedings of the European Combustion Meeting and is reprinted with permission of the journal

In the present work, the mixture composition is described by the element mass fractions of hydrogen and iron (Z_H,Z_{Fe}), which are determined from the atomic and molecular weights of atom α and species i (W_α, W_i), the species mass fraction (Y_i) and the corresponding number of atoms α in species i ($a_{\alpha,i}$).

$$Z_\alpha = \sum_{i=1}^{N_{sp}} a_{\alpha,i} \frac{W_\alpha}{W_i} Y_i. \tag{8.8}$$

With the eddy diffusivity approach, a unity Lewis number assumption for all species [144] and accounting for spray evaporation by the source term $\dot{\Gamma}_{Z_\alpha}$, the Favre filtered equation for the element mass fraction of species α reads

$$\frac{\partial \overline{\rho}\widetilde{Z}_\alpha}{\partial t} + \frac{\partial \overline{\rho}\widetilde{u}_i\widetilde{Z}_\alpha}{\partial x_i} = \frac{\partial}{\partial x_i}\left(\overline{\rho} D_e \frac{\partial \widetilde{Z}_\alpha}{\partial x_i}\right) + \dot{\Gamma}_{Z_\alpha}. \tag{8.9}$$

The effective diffusivity D_e in Eq. (8.9), is determined from the molecular and turbulent diffusivity: $D_e = D + D_t$. The turbulent diffusivity is the ratio of the turbulent viscosity and Schmidt number: $D_t = \nu_t/\mathrm{Sc}_t$. The progress of combustion is described by the joint progress variable Y_P, in the present work the sum of carbon dioxide and monoxide mass fractions: $Y_P = Y_{\mathrm{CO}_2} + Y_{\mathrm{CO}}$. The Favre filtered transport equation for Y_P, with the thickening factor, efficiency function, flame sensor, the chemical and evaporation source term [157] F, E, Ω, $\dot{\omega}_C$ and $\dot{\omega}_E$ reads

$$\begin{aligned} &\frac{\partial \overline{\rho}\widetilde{Y}_P}{\partial t} + \frac{\partial \overline{\rho}\widetilde{u}_i\widetilde{Y}_P}{\partial x_i} = \\ &\frac{\partial}{\partial x_i}\left(\left[FED + (1-\Omega)\frac{\mu_t}{\mathrm{Sc}_t}\right]\frac{\partial \widetilde{Y}_P}{\partial x_i}\right) + \frac{E}{F}\dot{\omega}_C + \dot{\omega}_E. \end{aligned} \tag{8.10}$$

The thermochemical quantities, such as ρ, $\dot{\omega}_C$ or the particle source term I, as illustrated in Fig. (8.2) bottom row, are determined a priori by solving 1D premixed flames with Cantera [56]. Detailed reaction mechanisms for ethanol and iron-pentacarbonyl [137, 220] were combined, resulting in mechanism with 79 species and over 400 reactions. In the 1D simulations, the inlet composition of the flamelets are varied as functions of Z_H and Z_{Fe} in equidistant steps. The resulting thermochemical variables are interpolated from physical to element mass fraction and progress variable space and stored in 3D look-up table as functions of Z_{Fe}, Z_H, and Y_{PN}.

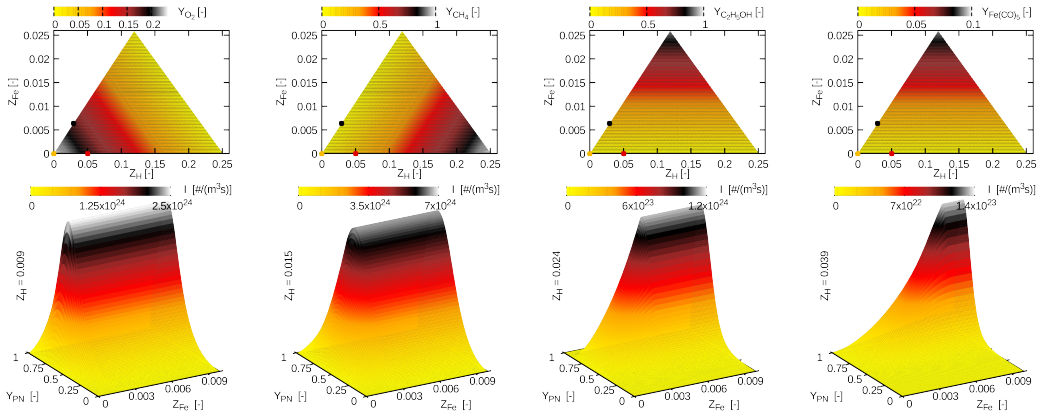

Figure 8.2: Top: validity range of Z_H and Z_{Fe}, with the mass fractions of O_2, CH_4, C_2H_5OH and $Fe(CO)_5$. Bottom: nucleation source term I for constant hydrogen mass fractions, $Z_H = 0.009$, $Z_H = 0.015$, $Z_H = 0.024$ and $Z_H = 0.039$.

This chapter was first published in the proceedings of the European Combustion Meeting and is reprinted with permission of the journal

The **population balance models** approximate the general dynamics equation either by resolving the particle size space and polydispersity, or assume monodispersity and model the size distribution based on their moments, i.e. the total number-, area- and volume concentration of the aggregates. The two applied particle models are described below.

The **sectional model** [72, 110, 121] describes the particle evolution due to nucleation and coagulation of a polydsiperse particle population. Therefore, N_s Favre filtered transport equations are solved for the particle number concentrations Q_k in sections k as given by Eq. (8.11).

$$\begin{aligned}\frac{\partial \overline{\rho}\widetilde{Q}_k}{\partial t} + \frac{\partial \overline{\rho}\widetilde{Q}_k\widetilde{u}_j}{\partial x_j} =& \frac{\partial}{\partial x_j}\left(\rho D_{kt}\frac{\partial \widetilde{Q}_k}{\partial x_j}\right) \\ &+\overline{\rho}\widetilde{\dot{\omega}}_k^Q + \frac{E}{F}\overline{\rho}\widetilde{I}\eta_k\end{aligned} \tag{8.11}$$

The particle diffusivity $D_k = \frac{k_b T}{3\pi\mu d_k} C_S$ is determined from the Boltzmann constant k_b, the slip correction factor C_S,

$$C_S = \frac{5 + 4\mathrm{Kn}_k + 6\mathrm{Kn}_k^2 + 18\mathrm{Kn}_k^3}{5 - \mathrm{Kn}_k + (8+\pi)\mathrm{Kn}_k^2}, \tag{8.12}$$

the Knudsen number $\mathrm{Kn}_k = 2\lambda/d_k$ and the mean free path of the gas λ. The coagulation source term $\dot{\omega}_k^Q$ accounts for the change of the number concentrations of particles in sections i and j.

$$\dot{\omega}_k^Q = \begin{cases} -\sum_{i=1}^{N_s} \beta_{i1} Q_i Q_1 & k = 1 \\ +\frac{1}{2}\sum_{i=1}^{N_s}\sum_{j=1}^{N_s} \chi_{ijk}\beta_{ij} Q_i Q_j - \sum_{i=1}^{N_s} \beta_{ik} Q_i Q_k & k > 1 \end{cases} \tag{8.13}$$

The coagulation kernel β_{ij}, according to Fuch's expression for the free molecular to continuum regime and is calculated with the particle diffusivity, diameter and velocity (D_i, d_i, $c_i = [(8k_bT)/(\pi m_k)]^{0.5}$) according to:

$$\begin{aligned}\beta_{ij} = &2\pi\left(D_i + D_j\right)\left(d_i + d_j\right) / \\ &\left[\frac{d_i + d_j}{d_i + d_j + 2\sqrt{g_i^2 + g_j^2}} + \frac{8\left(D_i + D_j\right)}{\left(d_i + d_j\right)\sqrt{c_i^2 + c_j^2}}\right]\end{aligned} \tag{8.14}$$

Aggregated particles which do not fit into one specific section are redistributed by the interpolation function χ_{ijk}, to conserve the particle number and volume [110] - χ_{ijk} is determined as proposed by Miller et al. or Loeffler et al. [110, 121] as outlined in Eq. (8.15).

$$\chi_{ijk} = \begin{cases} \frac{v_{k+1} - (v_i + v_j)}{v_{k+1} - v_k} & \text{for} \quad v_k \le (v_i + v_j) < v_{k+1} \\ \frac{(v_i + v_j - v_{k-1})}{v_k - v_{k-1}} & \text{for} \quad v_{k-1} \le (v_i + v_j) < v_k \\ 0 & \text{otherwise} \end{cases} \tag{8.15}$$

The transition parameter g_k for the free molecular to continuum regime is determined from the particle diameters and the mean free path of the particles $L_k = (8D_k)/(\pi c_k)$ according to Eq. (8.16).

$$g_k = \left[\left(d_k + L_k\right)^3 - \left(d_k^2 + L_k^2\right)^{3/2}\right] / \left[3L_k d_k\right] - d_k \tag{8.16}$$

This chapter was first published in the proceedings of the European Combustion Meeting and is reprinted with permission of the journal

Besides the particle volumes and diameters of the N_s sections, also the averaged particle volume v_m and diameter d_m are determined by the sectional model.

$$v_m = \frac{\sum_{k=i}^{N_s} Q_k v_k}{\sum_{k=i}^{N_s} Q_k} \qquad \text{and} \qquad d_m = \left(\frac{6}{\pi} v_m\right)^{1/3} \tag{8.17}$$

The **monodisperse model** [98, 139] describes the evolution of the particle size and morphology through nucleation, coagulation and coalescence based on the number-, surface area- and volume concentration of an aggregation mode. It is expected that the particle population attains the self preserving size distribution by coagulation [100]. Gröhn et al. [59–61] and Weise et al. [214] applied the monodisperse model in their numerical studies based on the Reynolds averaged (RANS) approach for the prediction of SiO_2 and ZrO_2 from turbulent spray flames without any further closures; Rittler et al. [165] applied the monodisperse model in the large-eddy simulation context for a FSP process of SiO_2. The Favre filtered transport equations for the particle number-, surface area- and volume concentration ($\widetilde{N}$, $\widetilde{A}$ and $\widetilde{V}$) are outlined below.

$$\frac{\partial \overline{\rho}\widetilde{N}}{\partial t} + \frac{\partial \overline{\rho}}{\partial x_j}(\widetilde{N}u_j - D_t\frac{\partial \widetilde{N}}{\partial x_j}) = \frac{E}{F}\overline{\rho}I - \frac{1}{2}\beta\overline{\rho}\widetilde{N}^2 \tag{8.18}$$

$$\frac{\partial \overline{\rho}\widetilde{A}}{\partial t} + \frac{\partial \overline{\rho}}{\partial x_j}(\widetilde{A}u_j - D_t\frac{\partial \widetilde{A}}{\partial x_j}) = \frac{E}{F}\overline{\rho}Ia_0 - \frac{\overline{\rho}(\widetilde{A} - A_s)}{\tau} \tag{8.19}$$

$$\frac{\partial \overline{\rho}\widetilde{V}}{\partial t} + \frac{\partial \overline{\rho}}{\partial x_j}(\widetilde{V}u_j - D_t\frac{\partial \widetilde{V}}{\partial x_j}) = \frac{E}{F}\overline{\rho}Iv_0 \tag{8.20}$$

As in the sectional model, the coagulation kernel is determined according to Fuch's expression for the free molecular to continuum regime. Assuming only mono-sized particles, with $D_i = D_j$, $d_i = d_j$, $c_i = c_j$ and $g_i = g_j$, and by replacing the solid sphere diameter by the collision diameter d_c [98], the coagulation kernel and transition parameter can be written as:

$$\beta = 4\pi d_c \mathcal{D}\left[\frac{\frac{1}{2}d_c}{d_c + \sqrt{2}g} + \frac{\sqrt{2}\mathcal{D}}{c\frac{1}{2}d_c}\right]^{-1} \tag{8.21}$$

$$g = \left[(d_c + L)^3 - \left(d_c^2 + L^2\right)^{1.5}\right] \;/\; [3\,L\,d_c] - d_c \tag{8.22}$$

The characteristic coalescence time τ for iron oxide particles [220] and the surface area of the completely fused particles A_S in Eq. (8.19) are calculated as outlined below.

$$\tau = 8 \times 10^{16} d_p^4 \exp\frac{30000}{T} \tag{8.23}$$

$$A_S = \left(\frac{V}{N v_0}\right)^{\frac{2}{3}} N a_0 \tag{8.24}$$

The primary, aggregate and collision diameters (d_p, d_a and d_c) are obtained from:

$$d_p = \frac{6V}{A}, \quad d_a = \left(\frac{6V}{\pi N}\right)^{\frac{1}{3}}; \quad d_c = d_p n_p^{\frac{1}{d_f}} \tag{8.25}$$

The number of primary particles is obtained from $n_p = (6V)/(\pi N {d_p}^3)$ and a constant value of 1.8 for the fractal dimension d_f is used.

Particle model assumptions are made as in previous work: particle diffusion is neglected due to their low diffusivity [59, 60, 165, 185] and the unresolved turbulent fluxes in Eqs. (8.11, 8.18-8.20) are modelled with an eddy diffusivity approach [110, 165]. Furthermore, it is assumed that Fe_2O_3 molecules represent particle monomers, and hence, the nucleation source term I is

This chapter was first published in the proceedings of the European Combustion Meeting and is reprinted with permission of the journal

determined from the change of the molar concentration of Fe_2O_3 and the Avogadro number a priori to the simulations and is stored in the look-up tables, $I = f(Z_H, Z_{Fe}, Y_P)$.

$$I = -\frac{\mathrm{d}C_{Fe_2O_3}}{\mathrm{d}t} N_A, \tag{8.26}$$

The distribution of the particles within the LES filter width is assumed to be homogeneous for the modelling of agglomeration. Artificial thickening is applied.

8.5 Results and Discussions

Figure 8.3 (a) illustrates the Favre filtered axial velocity u, (b) iron element mass fraction Z_{Fe}, (c) temperature T, (d) particle nucleation source term I, (e) particle number concentration N and (f) the aggregate particle diameter d_a on a 2D cross section. Theses results have been obtained by the simulations with the monodisperse particle model. Due to the high inertia of the main jet, including the liquid droplets, the pilot stream and the co-flow stream are entrained towards the centerline as shown by Fig. 8.3 (a). The majority of the liquid droplets evaporate due to the heat of the pilot upstream of 100 mm and lead to an increase of the element mass fraction of iron as outlined in Fig. 8.3 (b). The spray flame is found to have a length and diameter of approximately 150 mm and 40 mm, respectively. The nucleation source term I as shown in Fig. 8.3 (d) indicates that particle formation occurs within a large region of the flame, which is attributed to the continuous evaporation of the liquid droplets and the subsequent combustion of its vapour. The particle number concentration N, as outlined in Fig. 8.3 (e), increases due to nucleation and decreases due to coagulation simultaneously. The monodisperse particle model predicts an aggregate particle diameter d_a (Eq. (8.25)) below 10 nm on the centerline and above 10 nm off the centerline, in the investigated flow region. The different particle diameters on and off the centerline are explained by the different residence times and different process parameters (temperature and iron concentration) to which the particles are exposed.

Figure 8.4 (b) and (d) illustrate the particle number concentrations of section 1 (N_{01}) and 6

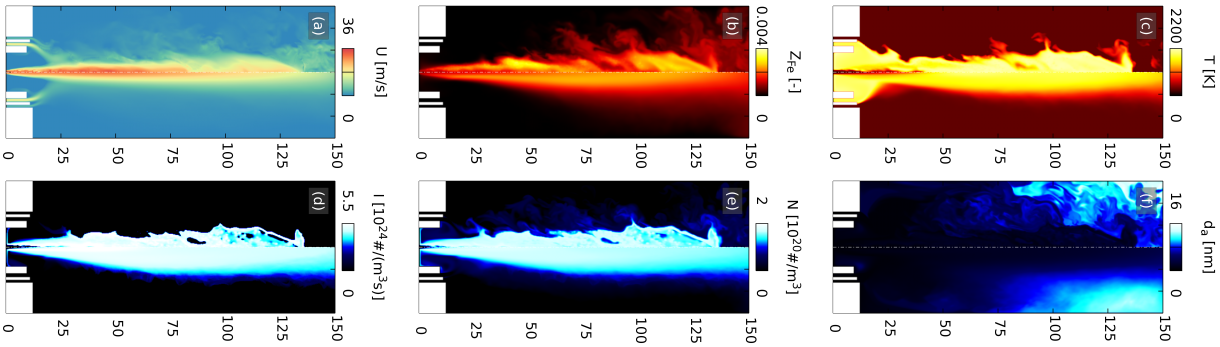

Figure 8.3: Top row: instantaneous snapshots of the Favre filtered element mass fractions Z_H and Z_{Fe} and temperature T. Bottom row: the snapshots of the Favre filtered nucleation source term, the number concentration and the resulting aggregate particle diameter d_a.

(N_{06}) as predicted by the sectional model. These two sections represent the monomer particles and particles with a diameter of 12.8 nm. As also found with the monodisperse model, particle formation occurs within a large physical space. The sectional model predicts an volume averaged particle diameter (d_m, Eq. (8.17)) of around 10 nm on the centerline and above 20 nm off the centerline, as illustrated in Fig. 8.4 (f). The volume averaged particle diameter predicted by the sectional model is larger than by the monodisperse model. This difference may result from the fact that the monodisperse model does not account for different modes, and the nucleation source term is added to the aggregates.

This chapter was first published in the proceedings of the European Combustion Meeting and is reprinted with permission of the journal

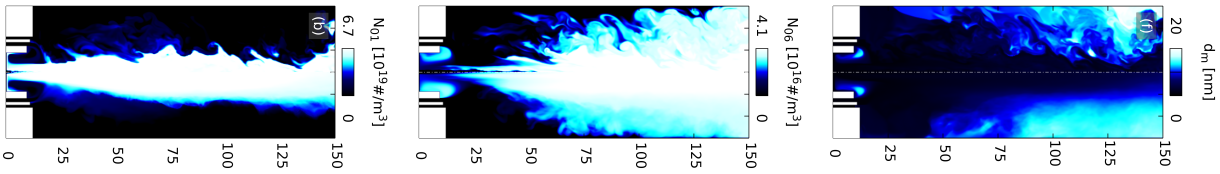

Figure 8.4: Instantaneous snapshots of the Favre filtered particle number concentrations of section 1 (N_{01}) and 6 (N_{06}) with particle diameters of the monomers and 12.8 nm, as well as the volume averaged particle diameter d_m.

The **particle size distribution** obtained by the sectional model is illustrated in Fig. 8.5, for three axial and two radial locations. Close to centerline and to the burner exit ($x = 50, r = 0$ mm and $x = 50, r = 15$ mm), nucleation is the determining process and small particles are predominant. For further downstream locations on the centerline, new particles are nucleated and larger particles are aggregated, what leads to a widening of the PSD and a shift towards larger particles. Off the centerline aggregation gets dominant, the nucleation mode disappears and the number concentrations are reduced.

Figure 8.6 illustrates the PSD as obtained from the monodisperse model. This size distribution represents the particle number concentrations of the aggregates obtained from the monomodal model over 256 time steps in sampling volumes of $v_s = (2\Delta)^3$. The findings discussed for the PSD of the sectional model, are also found for the monodisperse model: simultaneous nucleation and aggregation on the centerline with a widening of the PSD; predominant aggregation off the centerline for downstream locations, with a shift of the PSD towards larger particles and a reduction of the corresponding number concentrations.
Additionally shown in Figs. 8.5 and 8.6 are the modelled PSD for each mode. Therefore, a log-normal distribution function was assumed with a constant value of 1.4 for the geometric standard deviation. Superimposed to the presumed log-normal PSD for each mode of the monodisperse and sectional model is a PSD, which results from the sum of the concentrations of the presumed size distributions. This PSD predicted by the monodisperse model is too narrow if nucleation and coagulation occurs simultaneously, compared to the sectional model. When coagulation is dominant the PSD's of the monodisperse model is in a better agreement with the results from the sectional model. The presumed PSD as determined for the mean volume averaged particle diameter (sectional) and the sample averaged aggregate particle diameter (monodisperse) are also too narrow as compared to the PSD from the sectional model. For the mono-disperse model, this difference can be identified as the effect of the large-scale turbulence resolved by the LES, demonstrating that turbulence has a very strong effect on the width of the particle size distribution that must be included in simulations.

8.6 Conclusions

The resolved (sectional) and modelled particle size distributions (monodisperse) were shown to be narrow close to the burner exit and widen for downstream locations. The monodisperse model under-predicted the particle diameter relative to the sectional model, and over-predicted the particle number concentration. The particle size distributions obtained by the monodisperse and monomodal model are in a reasonable agreement with the polydisperse and sectional model, as long as aggregation is dominant with a similar shape of the distribution. When nucleation and aggregation occurred simultaneously the PSD of the simple model is too narrow, the diameter too small and the concentration too high. The effect of turbulence on the size distribution was found to be significant and must be properly included in the simulations.

This chapter was first published in the proceedings of the European Combustion Meeting and is reprinted with permission of the journal

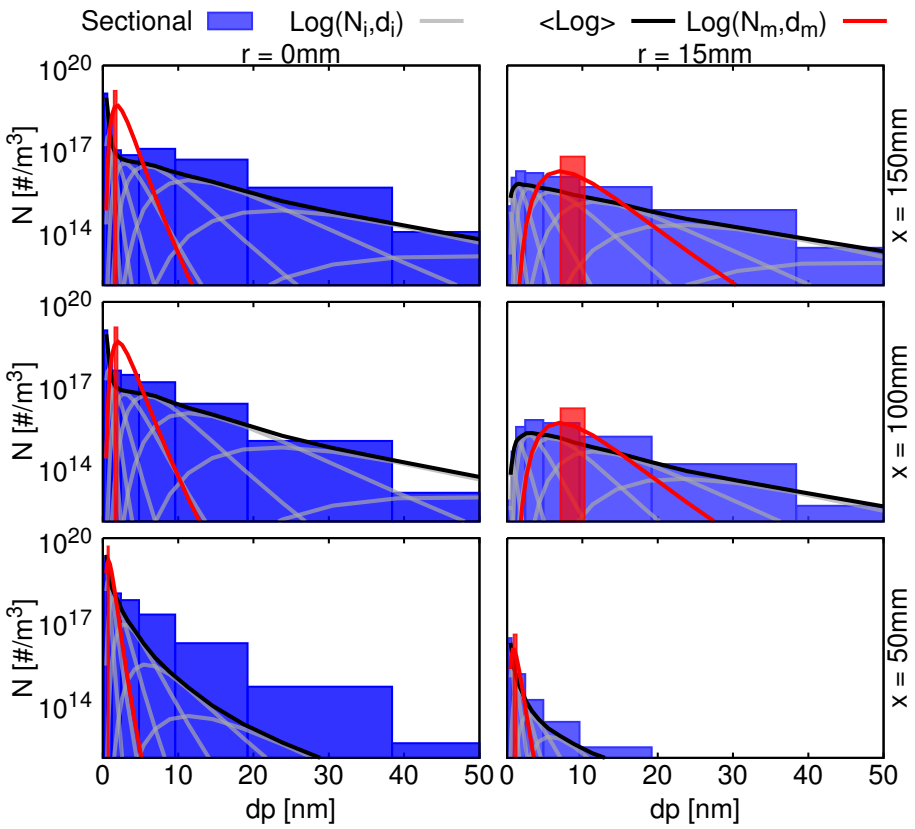

Figure 8.5: PSD's predicted by the sectional model. Shown are the calculated concentrations (blue boxes), presumed log-normal distributions for each section (grey), the resulting distribution for the sum of the concentrations of the presumed SD's (black) and the SD for the volume averaged diameter (red).

8.7 Acknowledgements

We gratefully acknowledge the financial support by the AiF (grant No. 18298N/3) and the computing time granted by the Center for Computational Sciences and Simulation (CCSS) of the University of Duisburg-Essen and provided on the supercomputer magnitUDE (DFG grants INST 20876/209-1 FUGG, INST 20876/243-1 FUGG) at the Zentrum für Informations- und Mediendienste (ZIM).

This chapter was first published in the proceedings of the European Combustion Meeting and is reprinted with permission of the journal

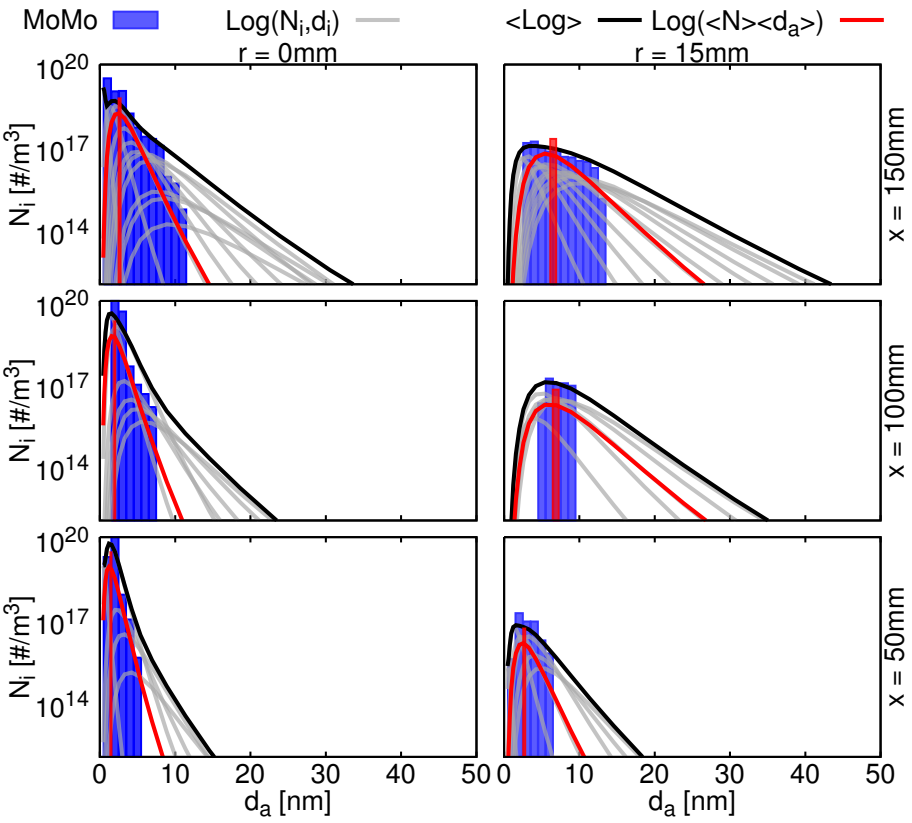

Figure 8.6: PSD for the temporal resolved modes of the monodisperse model. Shown are the calculated concentrations (blue boxes), presumed log-normal distributions for each aggregate (grey), the resulting distribution for the sum of the concentrations of the presumed SD's (black) and the SD for the mean aggregate diameter (red).

This chapter was first published in the proceedings of the European Combustion Meeting and is reprinted with permission of the journal

Chapter 9

Large Eddy Simulation with Sectional Modelling of Silica Nano-Particle Flame Synthesis

Authors: A. Rittler, I. Wlokas, A.M. Kempf
This paper is in preperation for submission to the Journal of Aerosol Science.
The author A. Rittler developed the code for the spray treatment, the combustion- and particle model, developed the code to produce the thermochemical manifolds, ran all the simulations, wrote the paper and generated all figures and tables.
The author I. Wlokas developed the reaction mechanism for HMDSO and contributed through discussions and proof-reading.
The author A. M. Kempf contributed corrections, discussions, proof-reading and the original code.

9.1 Abstract

Large eddy simulations of the nanoparticle synthesis from a spray flame are presented with hexamethyldisiloxane/ethanol as precursor/spray composition dispersed in oxygen for the synthesis of silica particles. A premixed methane/oxygen pilot flame is used as secondary heat source for spray evaporation, ignition and stabilization of the flame. The spray, gas and particle phases are described by Lagrangian, Eulerian and Eulerian approaches, respectively. A premixed flamelet generated manifold approach with artificial flame thickening (PFGM/ATF) is proposed and applied to model combustion. The control variables are the element mass fractions for hydrogen, silicon and a joint progress variable. Accounting for nucleation and coagulation, the general dynamics equation of the particles is approximated by a) a polydisperse sectional model and b) a monodisperse moment model that accounts additionally for coalescence. The evolution of the particles and their size distribution is discussed based on instantaneous and sample averaged results which are obtained from both models. The studies highlight the differences of the particle properties and the particle size distributions predicted by the two models and show the validity of the simple monodisperse model - for the investigated test case, but also the feasibility of applying a detailed, sectional model in the LES of spray flame synthesis for nanoparticles.

9.2 Introduction

Nanoparticles on a large-scale are commonly produced by the simple and cost efficient flame synthesis processes [167], which enable an effective supply of the precursor into a hot environment, i.e. the reaction zone of the flame. The synthesis of ceramic-powders is usually based on the combustion of a precursor injected into a premixed or non-premixed gaseous flame or in partially premixed spray flames [76, 113, 154, 167]. The particles produced by flame pyrolysis processes are of high purity and have a relatively narrow particle size distribution (PSD) [113, 154]. This size distribution of the particles depends mainly on the thermochemical state, i.e. the temperature, the saturation pressure and the relevant species concentrations and the residence time, during which the particles are exposed to aforementioned thermochemical state. The particle size and morphology is relevant for several particle properties, since it affects the ratio between the particle volume and particle surface area. Therefore, controlling the PSD is one of the key parameters to control the particle properties.

In laminar flames, all particles gathered in a sampling volume are exposed to the same thermochemical state, have the same residence time and histories. Therefore, the measured PSD in laminar flames results from the interaction of different sized particles (polydisperse particles) only. In turbulent flames however, the measured PSD is not only the result of the interaction of polydisperse particles but the particles are also exposed to different states and residence times. In turbulent flame experiments, it is difficult to differentiate the impact of pure particle dynamics and turbulence on the particle size distribution. Hence, numerical methods are promising tools to investigate the impact of turbulence and polydisperse particle dynamics independently.

9.2.1 The flame spray pyrolysis process

A liquid precursor is commonly solved in an liquid fuel, in a self-sustaining flame spray pyrolysis (FSP) processes. This liquid mixture is injected into a hot environment, provided by a secondary heat source, to evaporate the liquid and ignite the main spray flame. Air or oxygen are used as dispersion gas, for the stabilisation of the spray flame and as sheath gas to protect the reactor walls [113]. Depending on the required particle properties, the gas-phase synthesis of silica is obtained from different precursors including Silanes, linear and cyclic siloxanes and tetraethyl orthosilicate (TEOS) [76, 113]. The choice of the solvent like methanol, ethanol or isopropanol amongst others also affects the particle properties. Also the evaporation rate and the total energy content of the precursor is known to influence the powder characteristics, what was investigated by Mädler et al. [113] by varying the precursor and solvent composition for different dispersion gas flow rates. Recent studies by Engel et al. [39] and Kilian et al. [84] used a modified version of Mädler's standard spray flame reactor for their studies producing silica particles from an HMDSO/ethanol mixture, pure oxygen as dispersion and sheath gas and a premixed CH_4/O_2 mixture as pilot flame composition. Engel and Kilian et al. [39, 84] applied coherent anti-Stokes Raman spectroscopy (CARS), 2D-chemiluminescence imaging and laser-sheet based Mie scatter imaging to measure the temperature, the combustion and nucleation zones as well as the spatial distributions of $OH^\star$, $CH^\star$ and $SiO^\star$ radicals. In our work, the chlorine-free silica precursor HMDSO was chosen, for which we expect more in situ data from future reactor experiments [165].

Weise et al. proposed to separate the FSP process into three main zones (as outlined in Fig. 9.1): in zone (A) the spray droplets are atomized in the shear layer between the environment and the liquid and is subsequently evaporated due to the heat of the pilot flame. In zone (B), the fuel/precursor vapor is mixed with the surrounding oxidizer, ignited by the pilot flame and subsequently burned to decompose the precursor into intermediate species which finally form SiO_2 molecules. These molecules nucleate to monomer particles in zone (C), which further downstream coagulate, coalesce and aggregate.

In sections 9.4.2, 9.4.3 and 9.4.4 detailed discussions of the sub-models for the liquid phase in zone (A), the gas-phase combustion in zone (B) and for the particles synthesis in zone (C) are given. As a result of turbulence, the aforementioned processes usually happen simultaneously at certain instants and locations inside the flame. Detailed numerical studies by LES or even direct numerical simulations (DNS) are promising techniques to obtain deeper insights into the underlying physical processes of the FSP, as the methods for the experimental analysis in turbulent flames are limited and costly. It should however be noted, that complete simulations with detailed models are not feasible for years due to the complexities of the wide range of scales of turbulence, chemical kinetics and aerosol dynamics. Therefore, any simulation must apply a set of suitable simplifying assumptions.

9.2.2 Numerical studies of flame-made nanoparticles

The general dynamics equation (GDE) for the continuous distribution function [49] describes the evolution of nanoparticles from the gas phase for cases of practical interest. The evolution of particles by nucleation, growth, coagulation and coalescence as well as their transport through

diffusion and convection in space and time are incorporated in the GDE. Including the aforementioned models in the solution method for the GDE, influences the predicted particle properties and size distribution. Many, more or less accurate, models have been proposed to solve the GDE. Firtsly, discrete aerosol models [46] resolve the particle property space by introducing and solving one additional differential equation (DE) for each possible particle size (volume, diameter, ...) or property. The discrete models are known to be most accurate, however due to the high computational costs their usage is limited to certain applications and it is often used for model validation. Secondly, sectional models [109, 121, 174, 222, 223] introduce and solve additional DE's for a finite number of sections or bins, which cluster and represent particles within a certain size range. The discrete and sectional models are quite similar except of the degree they resolve the particle property range. Hence, also combinations of the two aforementioned models have been proposed [15] where the small particles are resolved directly by the discrete model and the larger particles are clustered in sections. A further popular group of models are the method of moment models [40, 44, 47, 116, 184–186], which introduce and solve transport equations for several moments of the GDE. The method of moments (MOM) and their successors (e.g. QMOM or DQMOM) determine the size distribution based on presumed functions, e.g. self-preserving [99] or log normal [193], or use stochastic methods. The monodisperse model proposed by Kruis et al. [98] and modified by Pratsinis et al. [139], accounts for nucleation, coagulation and coalescence and introduces three additional transport equations for the aggregate number-, surface area and volume concentrations, respectively. The monodisperse model assumes that the particle size distribution may be represented by a mean particle diameter and a presumed function.

The aerosol models described before, have been mainly applied to numerical studies using the Reynolds Averaged Navier-Stokes (RANS) equations as basis for turbulence modelling. The downside of the computationally cheap RANS based turbulence model and simulation technique is the fact that the complete energy spectrum of turbulence has to be modelled and a function must be presumed to describe the distribution of a quantity at a given point. We use the LES approach for the current studies, as, in contrast to RANS, it resolves the major effects of turbulence and a huge amount of the energy contained in the small turbulent structures and is therefore more accurate in describing the mixing, combustion and the resulting thermochemical state [128].

9.2.3 Specific objective

The present study investigates the particle formation from a spray flame pyrolysis process by numerical techniques. The impact of the state and flow field on the particle size distribution is outlined and discussed. The LES approach is used as turbulence model, with our implementation [162] of Nicouds σ-model [133], which yields the same accuracy as the dynamic Smagorinsky model at much lower numerical cost [164]. For the solution of the GDE equation two different particle models are coupled to the 3D LES in-house code PsiPhi [165], a) a polydisperse sectional model [121] and b) a simple monodisperse moment-model [98]. The unresolved turbulent fluxes are determined as additional diffusion terms as suggested by Garrick et al. [109]. Sample averaged PSD obtained from the two different particle models within 256 sample steps in sampling volumes of 0.25^3 mm^3 are discussed and compared. The sample averaged PSD from the monodisperse model is only a result of turbulence, while the sample averaged PSD obtained with the sectional model results from particle dynamics and turbulence. Subsequently, instantaneous PSD from the sectional model, where only the particle dynamics is accounted for, is compared to the sample averaged PSDs. Furthermore the validity of the monodisperse and sectional models for the investigated FSP reactor are discussed.

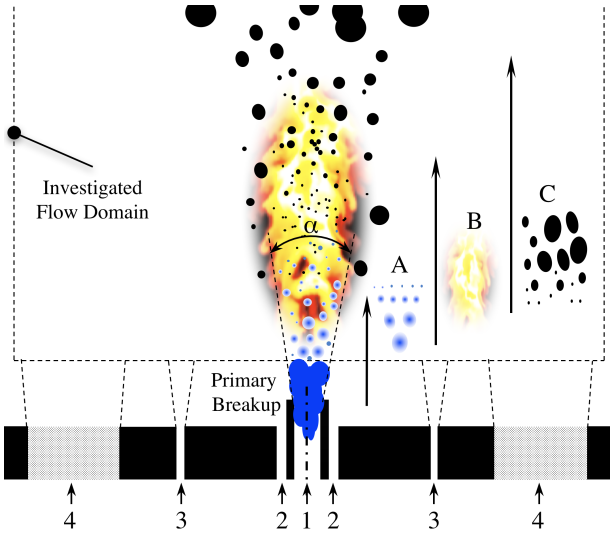

Figure 9.1: Sketch of the burner near region with inlet (1) for the fuel/precursor, (2) dispersion gas, (3) pilot and (4) the sheath gas supply with the zones A spray, B turbulent combustion and C particle synthesis [165, 214].

9.3 Investigated experiments and numerical setup

The investigated spray flame reactor was originally developed and designed by Mädler et al. for the *Controlled synthesis of nanostructured particles by flame spray pyrolysis* [113]. The original burner and a variety of it with several modifications is used by many research groups for the synthesis of metal oxide nanoparticles, as for example SiO_2, TiO_2, Bi_2O_3 ,Al_2O_3, $BaTiO_3$ as reported in [39, 60, 76, 84, 113, 114, 129, 191, 214]. The burner may be operated with and without housing to control the operating pressure and to provide a safe environment and consists of a spray nozzle, two concentric annular gaps and a sintered matrix as illustrated in Fig 9.1. A liquid mixture of 5 ml/min ethanol with 0.5 mol/l HMDSO is fed through the capillary, which surmounts the other outlets by 0.5 mm to allow for a constant spray angle independent of the liquid flow rate [113]. The liquid solution is dispersed by an oxygen stream with 5 l/min, which is supplied through the inner annular gap (inlet 2). A premixed methane/oxygen pilot with flow rates of 1.5 and 3 l/min is fed through the second annular gap (inlet 3) and is surrounded by an oxygen sheath gas of 10 l/min, which is fed through the sinter matrix (inlet 4). In the studies of Mädler et al. [113] it was shown that the median droplet mass diameter depends on the oxidant flow rate - for a cold ethanol spray and a given inner nozzle gap.

In the simulations, the primary- and secondary break-up of the liquid core are not considered and hence the 3-D numerical domain starts 3 mm downstream of the jet-nozzle exit as shown in Fig. 9.1. The simulation domain covers a region of $70 \times 70 \times 220$ mm and is discretized by an equidistant orthogonal mesh with a spacing of $\Delta = 0.25$ mm throughout the hole domain. The LES in-house code PsiPhi is used as in many previous studies [82, 157, 164, 165]. The convective fluxes of the moment equations are discretized by a second order central differencing scheme (CDS) and the convective fluxes of the scalars by a second order total variation diminishing scheme (TVD) with a nonlinear CHARM limiter [188, 226]. An explicit third order Runge-Kutta scheme is used for temporal integration. Artificial inflow fluctuations are superimposed to the mean profiles of the velocities at the inlet [83, 87]. A Rosin-Rammler distribution is assumed to describe the droplet diameters, which are used as initial and inlet conditions in the simulations (with a median diameter of $\sim 10\,\mu$m) [113].

9.4 Modelling approach

9.4.1 Gas phase equations

The large eddy simulation approach is well suited for simulating turbulent reacting flows [69, 143, 150]. In the presence of a second phase with mass, momentum and energy exchange the conservation equations have to be modified [71, 173]. The underlying equations and their modifications are discussed in the following chapter.

In the LES technique, the low-pass filtered conservation equations for mass and momentum are solved. To decompose the small scales from the large scales - which are directly solved on the numerical grid - a density weighted filtering operation, i.e. Favre filtering, is applied to the aforementioned conservation equations. An arbitrary filtered quantity $\widetilde{\phi}$ is obtained by applying the filtering kernel $G(x_i - r_i)$ as outlined in Eq. (9.1), to the corresponding unfiltered quantity ϕ.

$$\widetilde{\phi}(x_i, t) = \frac{1}{\overline{\rho}} \int \rho\phi(x_i, t) G(x_i - r_i) \mathrm{d}x_i \tag{9.1}$$

The Favre filtered continuity equation is then given by Eq. (9.2).

$$\frac{\partial \overline{\rho}}{\partial t} + \frac{\partial \overline{\rho}\widetilde{u}_j}{\partial x_j} = \dot{\Gamma}_{\overline{\rho}} \tag{9.2}$$

In the previous equation, $\overline{\rho}$ is filtered density (non density weighted) and $\widetilde{u}_j$ is the filtered gas phase velocity in direction of j (density weighted). To account for the exchange of mass from the evaporating droplet to the gas phase, the source term $\dot{\Gamma}_{\overline{\rho}}$ arises in Eq. (9.2), which is discussed later. The Favre filtered conservation equation for momentum is outlined in Eq. (9.3)

$$\frac{\partial \overline{\rho}\widetilde{u}_i}{\partial t} + \frac{\partial \overline{\rho}\widetilde{u}_i\widetilde{u}_j}{\partial x_j} = -\frac{\partial \overline{p}}{\partial x_i} + \frac{\partial \widetilde{\tau}_{ij}}{\partial x_j} + \frac{\tau_{ij}^{sgs}}{\partial x_j} + \dot{M}_{d,i}, \tag{9.3}$$

where $\overline{p}$, $\widetilde{\tau}_{ij}$, τ_{sgs} and $\dot{M}_{d,i}$ are the pressure, the viscous stress tensor based on the resolved quantities, the sub-filter stress tensor and a source term to account for the exchange of momentum between the spray and the gas phase. The viscous stress tensor $\widetilde{\tau}_{ij}$ is determined from the strain rate $\widetilde{S}_{ij}$ and the dynamic viscosity μ according to Eq. (9.4).

$$\widetilde{\tau}_{ij} = \mu\widetilde{S}_{ij} = \mu\left(\frac{\widetilde{u}_i}{x_j} + \frac{\widetilde{u}_j}{x_i}\right) \tag{9.4}$$

The sub-filter stress tensor τ_{sgs} is solved with our implementation [162] of Nicouds σ-model [133], where the turbulent viscosity μ_t is determined from the model parameter C_m, the grid size Δ and the differential operator D_m as outlined in the equation below.

$$\mu_t = \overline{\rho}(C_m\Delta)^2 D_m \tag{9.5}$$

The differential operator D_m is determined from the singular values σ_i (where $\sigma_1 \geq \sigma_2 \geq \sigma_3$) according to

$$D_m = \frac{\sigma_3(\sigma_1 - \sigma_2)(\sigma_2 - \sigma_3)}{\sigma_1^2}, \tag{9.6}$$

where the singular values are equivalent to the square roots of the eigenvalues of tensor G_{ij}, which is defined according to Eq. (9.7).

$$G_{ij} = \frac{\partial u_k}{\partial x_i}\frac{\partial u_k}{\partial x_j} \tag{9.7}$$

The σ-model has the well known advantages to a) predict zero turbulent viscosity for solid body rotation and b) to predict zero turbulent viscosity for thermal expansion, in contrast to the Smagorinsky model [164]. Furthermore, compared to the dynamic Smagorinsky model the σ-model requires approximately 25% of the computation time and yields the same accuracy. Artificial turbulences at the inlet are superimposed to the mean velocity profiles, generated with Kempf's inflow generator [83, 87].

9.4.2 Liquid phase equations

The dispersed liquid phase is described by the Lagrangian specification of the flow equations. In the present work each physical droplet is represented by one numerical particle. Therefore, a set of differential equations has to be solved for each physical droplet d. The motion of the particles is described by Eqs. (9.8) and (9.9).

$$\frac{\mathrm{d}x_{d,i}}{\mathrm{d}t} = u_{d,i}, \tag{9.8}$$

where $x_{d,i}$ is the location of droplet d in direction of i, with the corresponding droplet velocity $u_{d,i}$.

$$\frac{\mathrm{d}u_{d,i}}{\mathrm{d}t} = a_{d,i} = \frac{f_1}{\tau_d}\left(\widetilde{u}_i - u_{d,i}\right) + \left(1 - \frac{\overline{\rho}}{\rho_d}\right) g_i \tag{9.9}$$

The droplet velocity $u_{d,i}$ is calculated from the forces acting on them, here represented by the acceleration $a_{d,i}$. Relevant and here considered forces are the drag, gravitational and buoyancy force. The drag force is calculated from the correction factor for the droplet drag coefficient $f_1 = 1 + \frac{3}{20}\mathrm{Re}_d^{0.687}$, the droplet relaxation time τ_d and the slip velocity between the gas phase and drolet velocity $\widetilde{u}_i - u_{d,i}$. The droplet relaxation time represents the time required to adjust the droplet velocity to the surrounding gas phase velocity and is determined from the gas phase viscosity, the droplet diameter d_d and density ρ_d according to Eq. (9.10).

$$\tau_d = \frac{\rho_d d_d^2}{18\mu} \tag{9.10}$$

In the present work, the change of the droplet mass is determined from the Schmidt number Sc, the Sherwood number $\mathrm{Sh} = 2 + 0.552\mathrm{Re}_d^{1/2}\mathrm{Sc}^{1/3}$ and the Spalding mass transfer number $B_m = (Y_S - Y_\infty)/(1 - Y_S)$ (with the fuel mass fraction Y at the droplet surface S and the far-field ∞) as outlined in Eq. (9.11).

$$\frac{\mathrm{d}m_d}{\mathrm{d}t} = -\frac{\mathrm{Sh}}{3\,\mathrm{Sc}}\frac{m_d}{\tau_d}\ln\left(1 + B_m\right) \tag{9.11}$$

The change of the droplet temperature T_d is determined from the Prandtl number Pr, the Nusselt number $\mathrm{Nu} = 2 + 0.552\mathrm{Re}_d^{1/2}\mathrm{Pr}^{1/3}$ and the Spalding number for heat transfer $B_h = c_p(T - T_d)/L_v$ according to the following equation.

$$\frac{\mathrm{d}T_d}{\mathrm{d}t} = \frac{\mathrm{Nu}\,c_p}{3\,\mathrm{Pr}\,c_{pl}}\frac{(T_g - T_d)}{\tau_d}\frac{\ln\left(1 + B_h\right)}{B_h} + \frac{\dot{m}_d L_v}{m_d\,c_{pl}} \tag{9.12}$$

In Eq. (9.12), c_p and c_{pl} are the specific heat at constant pressure of the gas phase and the liquid and L_v is the latent heat of vaporization, respectively. The source terms arising in the transport equations for mass and momentum, Eqs. (9.2) and (9.3) are calculated as outlined below.

$$\dot{\Gamma}_{\overline{\rho}} = \frac{1}{V}\sum_{j=1}^{N_d}\left(\dot{m}_{d,j}\right) \tag{9.13}$$

$$\dot{M}_{d,i} = \frac{1}{V}\sum_{j=1}^{N_d}\left(F_{d,i,j} + \dot{m}_{d,i,j}u_{d,i,j}\right) \tag{9.14}$$

In the previous equations, $V = \Delta^3$ is the volume of one cell, N_d is the number of droplets which contribute to the volume and $F_{d,i,j}$ is the drag force of of droplet j in direction of i. The coupling between the liquid and gas phase is achieved by trilinear interpolation.

9.4.3 Combustion modeling

The combustion model used for the present study is based on the premixed flamelet generated manifold approach (PFGM) as proposed by van Oijen et al. [201, 202]. To resolve the flame on the numerical grid the PFGM technique is coupled with the artificial thickened flame (ATF) method [95]. Our implementation of the PFGM/ATF method for pure gas-phase combustion [157] was extended for spray combustion [164] with additional source terms in the transport equations to account for evaporation, and subsequently modified to account for two different fuel species [165]. The element mass fractions of hydrogen and silicon (Z_H and Z_{Si}) are used to describe the mixture composition, which are defined according to Eq. (9.15).

$$Z_\alpha = \sum_{i=1}^{N_{sp}} a_{\alpha,i} \frac{W_\alpha}{W_i} Y_i \tag{9.15}$$

In Eq. (9.15) $a_{\alpha,i}$ denotes the number of elements α in molecule i, with the corresponding elemental or molecular masses W_α and W_i and species mass fractions Y_i, respectively. With the unity Lewis number assumption [144], the Favre-filtered transport equation for Z_α is outlined in Eq. (9.16).

$$\frac{\partial \overline{\rho} \widetilde{Z}_\alpha}{\partial t} + \frac{\partial \overline{\rho} \widetilde{u}_i \widetilde{Z}_\alpha}{\partial x_i} = \frac{\partial}{\partial x_i} \left(\overline{\rho} D_S \frac{\partial \widetilde{Z}_\alpha}{\partial x_i} \right) + \dot{\Gamma}_{Z_\alpha} \tag{9.16}$$

The unclosed turbulent fluxes are modeled with the eddy viscosity approach, introducing an effective diffusivity as the sum $D_S = D + D_t$ of the molecular D and turbulent D_t diffusivity, which is calculated from the turbulent viscosity and Schmidt number $D_t = \mu_t / \mathrm{Sc}_t$. The reaction progress of a given mixture composition Z_H and Z_{Si} is described by a joint progress variable Y_P. In this work the mass fractions of carbon-monoxide CO and carbon-dioxide CO_2 are used as progress variable species $Y_P = Y_{CO_2} + Y_{CO}$. The Favre-filtered transport equation for Y_p is outlined in Eq. (9.17)

$$\frac{\partial \overline{\rho} \widetilde{Y}_P}{\partial t} + \frac{\partial \overline{\rho} \widetilde{u}_i \widetilde{Y}_P}{\partial x_i} = \frac{\partial}{\partial x_i} \left(\left[FED + (1 - \Omega) \frac{\mu_t}{\mathrm{Sc}_t} \right] \frac{\partial \widetilde{Y}_P}{\partial x_i} \right) + \frac{E}{F} \dot{\omega}_C + \dot{\omega}_E, \tag{9.17}$$

where F, E, Ω and $\dot{\omega}_C$ denote the thickening factor, efficiency function, flame sensor and chemical source term [157], respectively. A priori to the LES simulations, a set of 1D premixed flames with different initial and inlet conditions is solved with the open source library Cantera [56] and the resulting thermo-chemical quantities ϕ (e.g. ρ, T, $\dot{\omega}_C$) are stored in 3-D look-up tables as functions of the control variables Z_H and Z_{Si} and the normalized reaction progress variable Y_{PN}, respectively.

9.4.4 Population balance equations

Nucleation of monomer particles from gas molecules, coagulation, coalescence and surface growth are the most relevant aerosol processes in flames. Furthermore, the particle population changes as a result of external processes as for example convection, diffusion, gravitational settling or thermophoresis. The external processes do not change the size and morphology of the particles, but the particle size distribution at a certain sampling point. The general dynamics equation

(GDE) of the aerosol dynamics describes the evolution of a complete particle population for a three dimensional and transient problem. The GDE in the continuous form [49] is outlined below.

$$\underbrace{\frac{\partial n(v)}{\partial t}}_{\text{accumulation}} + \underbrace{\frac{\partial n(v)u_j}{\partial x_j}}_{\text{convection}} - \underbrace{\frac{\partial}{\partial x_j}\left(D\frac{\partial n(v)}{\partial x_j}\right)}_{\text{diffusion}} = \underbrace{I(v)\delta(v-v_0)}_{\text{nucleation}} + \underbrace{\frac{1}{2}\int_0^v \beta(v-v',v')n(v-v')n(v)dv}_{\text{coagulation birth}} - \underbrace{\int_0^\infty \beta(v,v')n(v')dv'}_{\text{coagulation death}} + \underbrace{\left[\frac{\partial n(v)}{\partial t}\right]}_{\text{growth}} + \underbrace{\left[\frac{\partial n(v)}{\partial t}\right]}_{\text{coalescence}} \tag{9.18}$$

The second and third term on the LHS of the previous equation are convection and diffusion of the particle number concentration n (i.e. particles per reference volume) for a specif particle volume v. Nucleation, the birth and death of particles due to coagulation, particle growth and coalescence are described by the five term on the RHS of Eq. (9.18). Due to computational limitations it is (at the current state) not possible to solve the GDE for each particle property. Therefore, two modeling approaches are used to approximate the general dynamics equation, namely a) the numerically still expensive sectional model [15, 109, 121] and b) a monodisperse model [60, 98, 139] which are outlined and discussed below.

9.4.4.1 Sectional model

Sectional models discretize the particle property space into a finite number (N_s) of intervals, the sections. Accounting for nucleation and coagulation of polydisperse particles, the sectional model solves N_s additional transport equations for the particle number concentration Q of sections k and is outlined for a three dimensional and transient problem in Eq. (9.19).

$$\frac{\partial \rho Q_k}{\partial t} + \frac{\partial \rho Q_k u_j}{\partial x_j} = \frac{\partial}{\partial x_j}\left(\rho D_k \frac{\partial Q_k}{\partial x_j}\right) + \rho\dot{\omega}_k^Q + \rho I \eta_k \tag{9.19}$$

The Einstein-Smoluchowski relation [108] is used to calculate the particle diffusivity D in section k from the particle diameter d_k, gas temperature T, gas viscosity μ, the Boltzmann constant k_b and the slip correction factor C_S as given by Eq. (9.20).

$$D_k = \frac{k_b T}{3\pi\mu d_k} C_S \tag{9.20}$$

The Knudsen number $\mathrm{Kn_k} = 2\lambda/\mathrm{d_k}$ with the mean free path of the gas λ is used to determine the slip correction factor C_S as outlined in Eq. (9.21).

$$C_S = \frac{5 + 4\mathrm{Kn}_k + 6\mathrm{Kn}_k^2 + 18\mathrm{Kn}_k^3}{5 - \mathrm{Kn}_k + (8+\pi)\mathrm{Kn}_k^2} \tag{9.21}$$

Coagulation of particles in section k is described by the source term $\dot{\omega}_k^Q$, which accounts for the "birth" and "death" of the particles and is determined according to Eq. (9.22).

$$\dot{\omega}_k^Q = \begin{cases} -\sum_{i=1}^{N_s} \beta_{i1} Q_i Q_1 & k = 1 \\ +\frac{1}{2}\sum_{i=1}^{N_s}\sum_{j=1}^{N_s} \chi_{ijk}\beta_{ij} Q_i Q_j - \sum_{i=1}^{N_s} \beta_{ik} Q_i Q_k & k > 1 \end{cases} \tag{9.22}$$

Fuch's expression [50] is used to calculate the coagulation frequency β_{ij} in Eq. (9.22) for the free molecular to continuum regime from the particle diffusivity, particle diameter and particle velocity D_i, d_i and c_i respectively as outlined in Eq. (9.23).

$$\beta_{ij} = 2\pi \left(D_i + D_j\right)\left(d_i + d_j\right)\left[\frac{d_i + d_j}{d_i + d_j + 2\sqrt{g_i^2 + g_j^2}} + \frac{8\left(D_i + D_j\right)}{\left(d_i + d_j\right)\sqrt{c_i^2 + c_j^2}}\right]^{-1} \tag{9.23}$$

New agglomerated particles with volume $v_k^\star$, which do not have the exactly the volume v_k of a certain section k are redistributed by the interpolation function χ_{ijk} to the neighbouring sections, to conserve the particle number and volume. The interpolation function χ_{ijk} proposed by Miller et al. [121] or Garrick et al. [109] is determined as outlined in Eq. (9.24).

$$\chi_{ijk} = \begin{cases} \frac{v_{k+1} - (v_i + v_j)}{v_{k+1} - v_k} & \text{for} \quad v_k \leq (v_i + v_j) < v_{k+1} \\ \frac{(v_i + v_j - v_{k-1})}{v_k - v_{k-1}} & \text{for} \quad v_{k-1} \leq (v_i + v_j) < v_k \\ 0 & \text{otherwise} \end{cases} \tag{9.24}$$

The particle velocity c_k in Eq. (9.23) is determined from the gas temperature, the particle mass m_k and the van Boltzmann constant k_b as outlined below.

$$c_k = \left(\frac{8 k_b T}{\pi m_k}\right)^{0.5} \tag{9.25}$$

The particle diameter d_k and the mean free path of the particles $L_k = (8D_k)/(\pi c_k)$ are used calculate the transition parameter g_k for the free molecular to continuum regime according to Eq. (9.26).

$$g_k = \left[\left(d_k + L_k\right)^3 - \left(d_k^2 + L_k^2\right)^{3/2}\right]\left[3 L_k d_k\right]^{-1} - d_k \tag{9.26}$$

Applying the filtering procedure as explained in section 9.4.1 to Eq. (9.19) yields the transport equation for the low pass filtered particle number density as outlined in Eq. (9.27), with the unclosed terms for the turbulent fluxes and source terms.

$$\frac{\partial \overline{\rho}\widetilde{Q}_k}{\partial t} + \frac{\partial \overline{\rho}\widetilde{Q}_k \widetilde{u}_j}{\partial x_j} = \frac{\partial}{\partial x_j}\left(\rho D_k \frac{\partial \widetilde{Q}_k}{\partial x_j}\right) + \overline{\rho}\left(\widetilde{\dot{\omega}}_k^Q + \left(\dot{\omega}_k^Q\right)^{sgs}\right) + \overline{\rho}\left(\widetilde{I} + I^{sgs}\right)\eta_k - \frac{\partial}{\partial x_j}\overline{\rho}\left(\widetilde{u_j Q_k} - \widetilde{u}_j \widetilde{Q}_k\right) \tag{9.27}$$

The turbulent flux term and the source terms in Eq. (9.27) are closed as proposed in the work of Garrick et al. [109], with a turbulent viscosity approach as given in Eq. (9.28) and assuming a equal distribution for the source term.

$$-\frac{\partial}{\partial x_j}\overline{\rho}\left(\widetilde{u_j Q_k} - \widetilde{u}_j \widetilde{Q}_k\right) = +\frac{\mu_t}{\mathrm{Sc}_t}\frac{\partial \widetilde{Q}_k}{\partial x_j}, \tag{9.28}$$

The final solved transport equation for the filtered number density $\widetilde{Q}$ of section k reads:

$$\frac{\partial \overline{\rho}\widetilde{Q}_k}{\partial t} + \frac{\partial \overline{\rho}\widetilde{Q}_k \widetilde{u}_j}{\partial x_j} = \frac{\partial}{\partial x_j}\left(\overline{\rho} D_{k,sum}\frac{\partial \widetilde{Q}_k}{\partial x_j}\right) + \overline{\rho}\widetilde{\dot{\omega}}_k^Q + \frac{E}{F}\overline{\rho}\widetilde{I}\eta_k \tag{9.29}$$

The volume averaged particle diameter d_m is determined from averaged particle volume v_m

$$v_m = \frac{\sum_{k=i}^{N_s} Q_k v_k}{\sum_{k=i}^{N_s} Q_k} \qquad \Rightarrow \qquad d_m = \left(\frac{6}{\pi} v_m\right)^{1/3} \tag{9.30}$$

Using the sectional model for a three dimensional and transient problem leads to high computational costs, which result from solving additional transport equations of each section Q_k (here 20) and dominantly from solving the coagulation source term $\dot{\omega}_k^Q$ in each numerical cell (here approximately 80,000,000 cells). The modified monodisperse model [98, 139], overcomes the numerical expenses and reduces the model complexity.

9.4.4.2 Monodisperse model

Accounting for nucleation, coagulation, sintering and the particle morphology the monodisperse model solves three additional transport equations for the aggregate number concentration N, aggregate area concentration A and the aggregate volume concentration V. The model assumes locally monosized particles. Including the gas phase density, the additional transport equations are outlined in Eqs. (9.31-9.33) [59, 60, 165].

$$\frac{\partial \rho N}{\partial t} + \frac{\partial \rho N u_j}{\partial x_j} = \frac{\partial}{\partial x_j}(\rho D_p \frac{\partial N}{\partial x_j}) + \rho I - \frac{1}{2}\beta \rho N^2 \tag{9.31}$$

$$\frac{\partial \rho A}{\partial t} + \frac{\partial \rho A u_j}{\partial x_j} = \frac{\partial}{\partial x_j}(\rho D_p \frac{\partial A}{\partial x_j}) + \rho I a_m - \frac{1}{\tau_p}(A - A_s) \tag{9.32}$$

$$\frac{\partial \rho V}{\partial t} + \frac{\partial \rho V u_j}{\partial x_j} = \frac{\partial}{\partial x_j}(\rho D_p \frac{\partial V}{\partial x_j}) + \rho I v_m \tag{9.33}$$

The surface and volume of a monomer particle are denoted as a_m and v_m, respectively, in the previous equations. To account for the fractal shape of the particles [98], the particle diffusivity D_p in Eqs. (9.31-9.33) is calculated from the collision diameter d_c as outlined in Eq. (9.34).

$$D_p = \frac{k_b T}{3\pi\mu d_c} C_S \tag{9.34}$$

As described for the sectional model, the collision frequency β in Eq. (9.31) is determined according to Fuchs's expression for the free molecular to continuum regime, however by replacing the solid sphere diameter d_k with the collision diameter d_c. Assuming collisions of monodisperse particles only ($D_i = D_j$, $d_i = d_j$, $g_i = g_j$ and $c_i = c_j$), Eq. (9.23) reduces to Eq. (9.35).

$$\beta = 4\pi d_c D_p \left[\frac{\frac{1}{2}d_c}{d_c + \sqrt{2}g} + \frac{\sqrt{2}D_p}{c\frac{1}{2}d_c} \right]^{-1} \tag{9.35}$$

The collision diameter is also used for the calculation of the Knudsen number Kn and transition parameter g, respectively givne by Eqs. (9.36,9.37).

$$\mathrm{Kn} = 2\lambda / d_c \tag{9.36}$$

$$g = \left[(d_c + L)^3 - (d_c^2 + L^2)^{1.5} \right] / (3\, L\, d_c) - d_c \tag{9.37}$$

Favre filtering of Eqs. (9.31-9.33), with the assumptions described for the sectional model, yields the transport equations for the LES technique $\widetilde{N}$, $\widetilde{A}$ and $\widetilde{V}$ [165], respectively.

$$\frac{\partial \overline{\rho}\widetilde{N}}{\partial t} + \frac{\partial \overline{\rho}\widetilde{N}\widetilde{u}_j}{\partial x_j} = \frac{\partial}{\partial x_j}(\overline{\rho} D_t \frac{\partial \widetilde{N}}{\partial x_j}) + \frac{E}{F}\overline{\rho} I - \frac{1}{2}\beta \overline{\rho}\widetilde{N}^2 \tag{9.38}$$

$$\frac{\partial \overline{\rho}\widetilde{A}}{\partial t} + \frac{\partial \overline{\rho \widetilde{A} \widetilde{u}_j}}{\partial x_j} = \frac{\partial}{\partial x_j}(\overline{\rho} D_t \frac{\partial \widetilde{A}}{\partial x_j}) + \frac{E}{F}\overline{\rho} I a_0 - \frac{\overline{\rho}(\widetilde{A} - A_s)}{\tau} \tag{9.39}$$

$$\frac{\partial \overline{\rho}\widetilde{V}}{\partial t} + \frac{\partial \overline{\rho}\widetilde{V}\widetilde{u}_j}{\partial x_j} = \frac{\partial}{\partial x_j}(\overline{\rho} D_t \frac{\partial \widetilde{V}}{\partial x_j}) + \frac{E}{F}\overline{\rho} I v_0 \tag{9.40}$$

The diameter of the aggregate particles is determined from the aggregate volume $v_a = V/N$ and may be compared to the volume averaged diameter d_m of the sectional model (Eq. (9.30)). The

primary particle diameter d_p is calculated from the volume concentration V and area concentration A of the aggregates. The number of primary particles per aggregate n_p is the determined from the aggregate particle volume and the primary particle volume.

$$d_a = \left(\frac{6}{\pi} v_a\right)^{\frac{1}{3}} \quad , \quad d_p = \frac{6V}{A} \quad , \quad n_p = \frac{v_a}{v_p} = \frac{V}{N}\frac{6}{\pi d_p^3} \tag{9.41}$$

To account for the fractal shape of the aggregate particles the fractal dimension d_f is used to calculate the collision diameter d_c as outlined below.

$$d_c = d_p n_p^{d_f} \tag{9.42}$$

In this work, the fractal dimension d_f is set to a value of $d_f = 1.8$ as proposed by Tsantilis et al. [194].

9.4.4.3 Particle model assumptions

Particle model assumptions are made as in previous work: particle diffusion is neglected due to the very low diffusivity in contrast to the turbulent diffusivity [59, 60, 165, 185] and the unresolved turbulent fluxes in Eqs. (9.29, 9.38-9.40) are modelled with an eddy diffusivity approach [109, 165]. Furthermore, it is assumed that SiO_2 molecules represent particle monomers, and hence, the nucleation source term I is determined from the change of the molar concentration of SiO and the Avogadro number a priori to the simulations and is stored in the look-up tables, $I = f\left(Z_H, Z_{Si}, Y_{PN}\right)$.

$$I = -\frac{\mathrm{d}C_{SiO_2}}{\mathrm{d}t} N_A \tag{9.43}$$

The distribution of the particles within the LES filter width is assumed to be homogeneous for the modelling of agglomeration, justified by the small grid size and the fact that particle formation occurs over a wide range of equivalence ratios. (Accounting for the sub-filter distribution of the particles within a LES filter width is part of our future work). Artificial thickening $\frac{E}{F}$ is applied to the source terms to be consistent with the progress variable.

9.5 Results

In the following section first the droplet dynamics and gas phase combustion is briefly discussed and subsequently a detailed investigation on the evolution of the particle properties is presented. The particle dynamics is first discussed based on the monodisperse model. Further insight on the particle size distribution is then presented based on the results from the sectional model.

9.5.1 Flame dynamics

Figure 9.2a illustrates the mass evaporated from the liquid droplets and highlights that the spray transport and evaporation occurs mainly below 25 mm above the burner. A minor number of droplets survives to a further downstream location and releases a fresh and unburned precursor/fuel mixture in the flame zone. Furthermore, it can be seen that the droplets start to evaporate at the outer radius first. This finding is explained by the high slip velocities between the droplet and the environment in the shear region and more relevant due to the heat of the pilot flame [165]. It can be seen that spray evaporation is completely finished at 35 mm above the burner.

Figure 9.2b illustrates the axial component of the velocity. A small recirculation zone is observed close to the burner exit between the main spray jet and pilot flame. A maximum

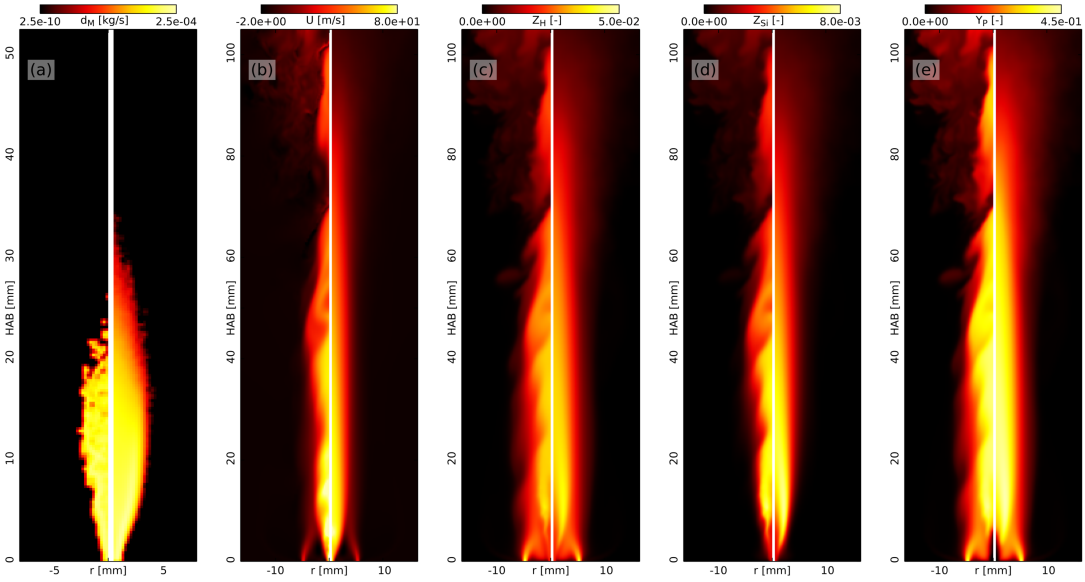

Figure 9.2: Instantaneous (left half) and sample averaged (right half) Favre filtered fields on a 2D cross section. Shown are (a) the mass evaporated from the liquid droplets dM, (b) the axial gas phase velocity U, (c) and (d) the element mass fraction of hydrogen Z_H and silicon Z_{Si} and (e) the progress variable Y_P.

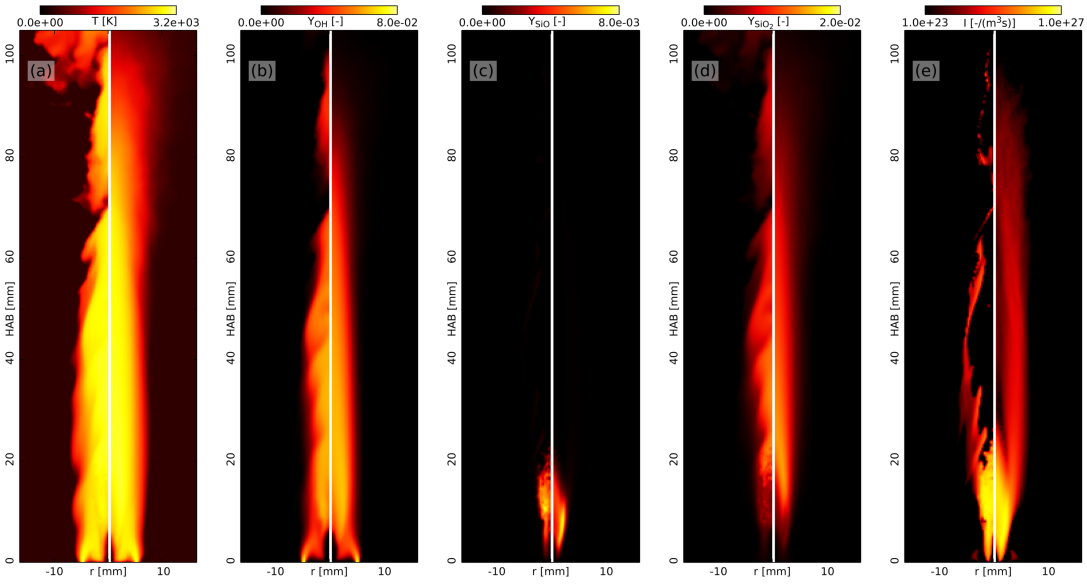

Figure 9.3: Instantaneous (left half) and sample averaged (right half) Favre filtered fields on a 2D cross section. Shown are (a) the gas temperature T, (b) to (d) the mass fractions of OH, SiO and SiO_2 and (e) the nucleation source term I.

velocity of approximately 90 m/s is predicted between 10 mm and 40 mm in the center of the jet, which is the region where the spray vapor is burned. The fuel vapor released from the droplets increases the element mass fractions of hydrogen Z_H and silicon Z_{Si} as illustrated in Figs. 9.2c and 9.2d. As observed for the droplet mass, the element mass fractions increase at the outer radius first and up to approximately 35 mm. Downstream of 35 mm, the jet breakup leads to a redistribution of Z_H and Z_{Si} from the center of the jet in radial direction. The main spray flame is ignited at approximately 5 mm downstream of the jet nozzle exit, as illustrated in Fig. 9.2e by the reaction progress variable Y_P [165]. The maximum temperature for the investigated flame is

approximately 3000 K as illustrated in Fig. 9.3a. The mass fractions of the intermediate species SiO and OH are outlined in Fig. 9.3b and 9.3c. Silicon-Oxide is mainly predicted between 5 mm and 20 mm - which is found to be in good agreement with the SiO* measurements by Kilian et al. [84]. Downstream of approximately 20 mm, Silicon-Oxide is converted to Silicon-Dioxide as illustrated in Figs. 9.3c and 9.3d. As described by Eq. (9.43), the change of SiO to SiO_2 is considered as nucleation source term, which is illustrated in Fig. 9.3e.

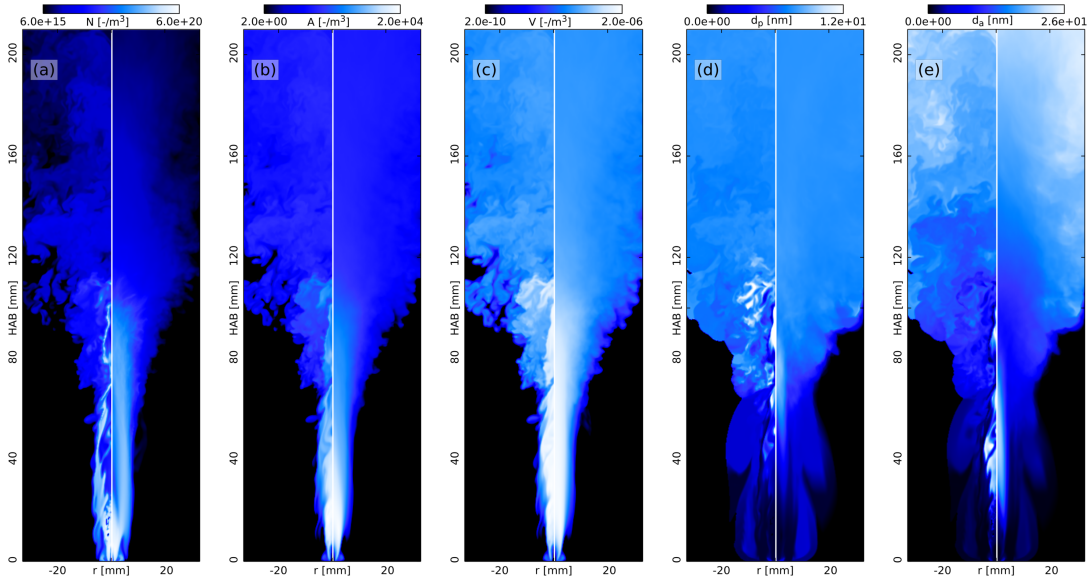

Figure 9.4: Instantaneous (left half) and sample averaged (right half) Favre filtered fields on a 2D cross section. Shown are the aggregate particle (a) number concentration N, (b) area concentration A and (c) volume concentration V, as well as the diameters of the (d) primary particles d_p and (e) aggregate particles d_a predicted by the monodisperse model.

9.5.2 Particle synthesis

Particle monomer molecules are formed by the conversion of the intermediate species SiO to species SiO_2 in the flame front, which is indicated by the nucleation source term I and illustrated in Fig. 9.3e. Nucleation is found to occur mainly in the region where the spray is evaporated and subsequently burned, i.e. in the central jet and below 35 mm HAB (height above the burner). The nucleation source term increases the number concentration of the aggregate particles N first, with a maximum value of approximately 6×10^{20} particles per m^3 at 25 mm HAB in the central jet, as illustrated in Fig. 9.4a. Further downstream, the aggregate number concentration decreases as a consequence of particle growth by coagulation. The structures of the nucleation source term I can also be found in the instantaneous fields of N, which disappear for larger heights above the burner (HAB $>$ 100 mm). The surface area concentration A and the volume concentration V of the aggregate particles increases rapidly at 5 mm to 8 mm as a result of nucleation, compare Figs. 9.4b and 9.4c. In the high temperature regions, sintering with coalescence of particles leads to a quick reduction of the surface area concentration A, further downstream the area concentration is only reduced as a result of turbulent mixing with the environment. The aggregate volume concentration V reduces for further downstream location only as a result of the jet break-up and due to turbulent mixing with the environment [165].

The primary particle diameter, illustrated in Fig. 9.4d, starts to grow at approximately 25 mm above the burner and reaches a maximum value of approximately 12 nm in the flame. The growth of the primary particles results from sintering with a reduction of the surface area concentration

A at almost constant volume concentration V [165]. In the post flame zone, where the impact of sintering is of minor importance, the primary particle diameter remains constant. The aggregate particle diameter, illustrated in Fig. 9.4e, represents the volume averaged particle diameter and starts to grow at 15 mm HAB. In contrast to the primary particle diameter, the aggregate particle diameter grows also for further downstream locations (for HAB $>$ 100 mm) and attains a maximum value of 22 nm for the investigated region. The aggregate particles outside of the central jet are larger than the aggregate particles found close to the centreline. This finding is attributed to the longer residence times of the particles away from the central jet.

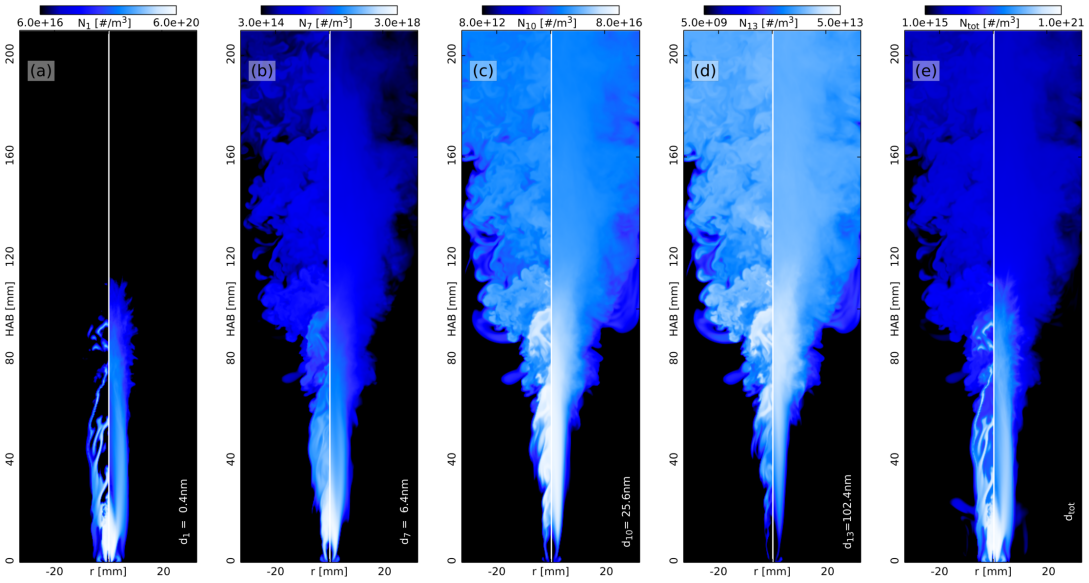

Figure 9.5: Instantaneous (left half) and sample averaged (right half) Favre filtered fields on a 2D cross section. Shown are the particle number concentrations for particles with diameters of (a) $d_p = 0.4\,\text{nm}$, (b) $d_p = 6.4\,\text{nm}$, (c) $d_p = 25.6\,\text{nm}$, (d) $d_p = 102.4\,\text{nm}$ and (e) the total number concentration predicted by the sectional model.

Figures 9.5a to 9.5d illustrate the number concentrations for particles with diameters of a) 0.4 nm, b) 6.4 nm, c) 25.6 nm, d) 102.4 nm and Fig. 9.5e the number concentration of all particles. The figures indicate nicely that a) a much higher number of small particles is found for the investigated region and b) the reduction of the number concentrations of small particles leads to an increase of the number concentrations of the larger particles as a result of coagulation. The major particle volume, however, is found for particles with a diameter of $d_p = 10\,\text{nm}$ to $d_p = 40\,\text{nm}$, as illustrated in Figs. 9.6a to 9.6d for the particle volume concentrations of particles with diameters of a) 1.0 nm, b) 6.4 nm, c) 25.6 nm and d) 102.4 nm. The volume averaged particle diameter d_m, illustrated in Fig. 9.6e, starts significantly to grow at HAB $= 15\,\text{mm}$ and reaches a maximum of $d_m = 26\,\text{nm}$ for the investigated region. The volume averaged particle diameters, d_a predicted by the monodisperse model and d_m obtained from the sectional model, are in a good agreement. The monodisperse model underpredicts the particle diameter slightly as the nucleated particles are added to the aggregates.

9.5.2.1 Particle size distribution

The spatial evolution of the volume- and time averaged particle diameters ($< d_a >$ and $< d_m >$) and the corresponding particle size distributions for the monodisperse model and the sectional model are illustrated in Figs. 9.7a and 9.7b. As described in the previous section, a good agreement is found for the mean particle diameters predicted by the two different models for far downstream locations. As long as "new" particles from nucleation and "old" particles from

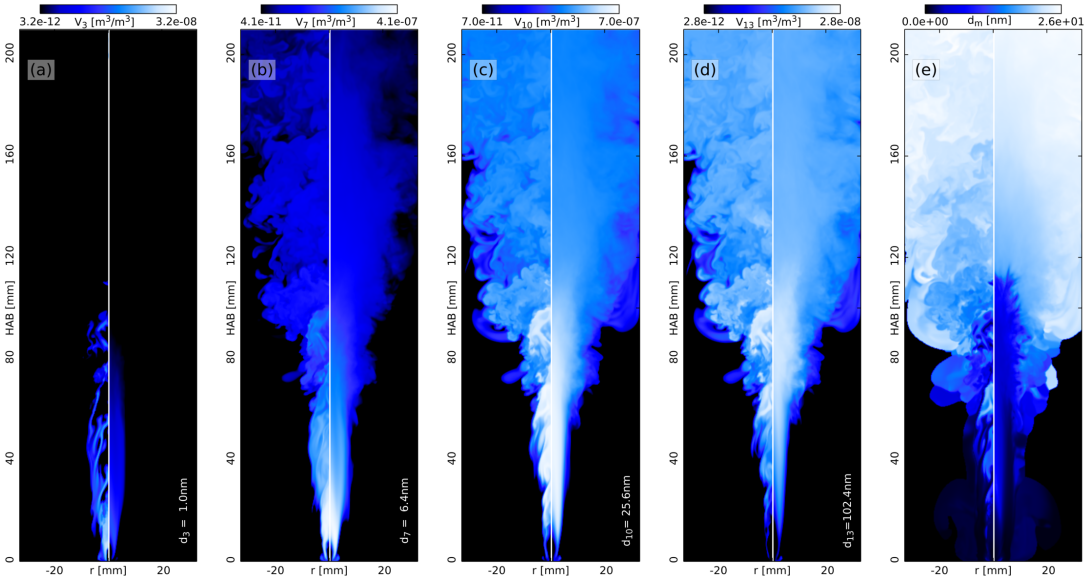

Figure 9.6: Instantaneous (left half) and sample averaged (right half) Favre filtered fields on a 2D cross section. Shown are the particle volume concentrations for particles with diameters of (a) $d_p = 0.4\,\mathrm{nm}$, (b) $d_p = 6.4\,\mathrm{nm}$, (c) $d_p = 25.6\,\mathrm{nm}$, (d) $d_p = 102.4\,\mathrm{nm}$ and (e) volume averaged particle diameter d_m predicted by the sectional model.

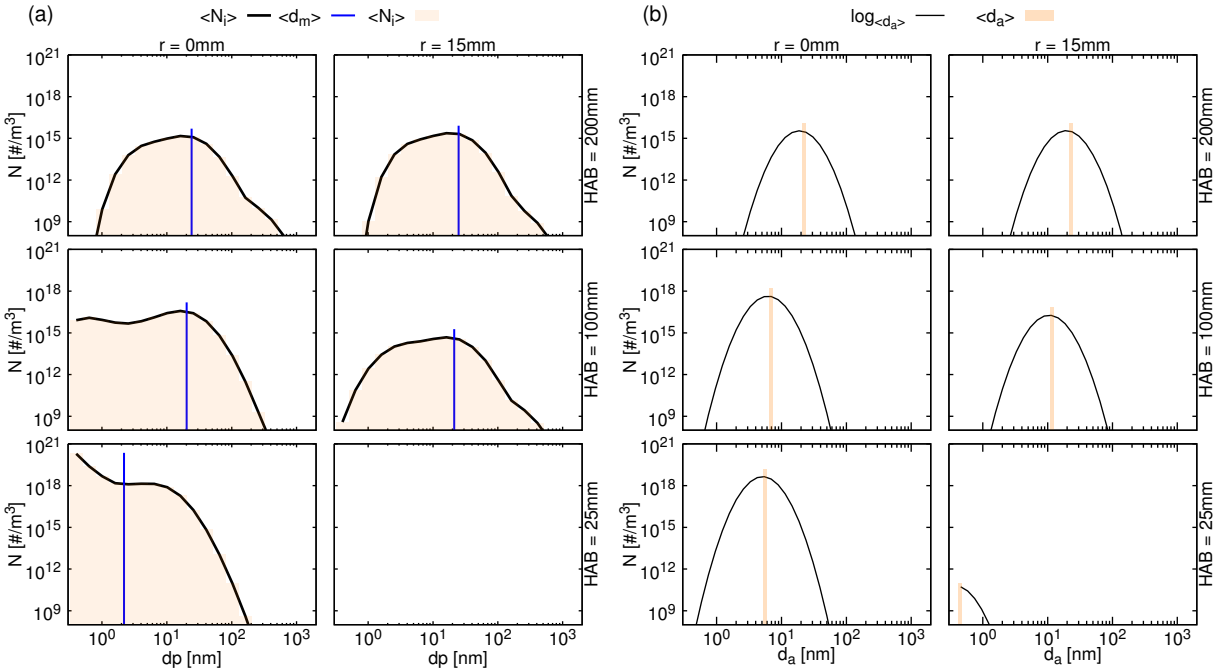

Figure 9.7: Evolution of the particle diameter and particle size distribution obtained from the sectional model (left) and the monodisperse model (right). Shown are the volume- and time averaged particle diameters $< d_m >$ and $< d_a >$, the resolved and time averaged size distribution predicted by the sectional model and a presumed log-normal size distribution around $< d_a >$ predicted by the monodisperse model, for three axial and two radial locations.

coagulation are present, however, the monodisperse model predicts to small diameters as shown in Figs. 9.7a and 9.7b at HAB $= 100\,\mathrm{mm}$ for both radial locations.

The time averaged particle size distribution obtained from the sectional model shows a bimodal size distribution in the central jet and close to the burner (HAB $= 25\,\mathrm{mm}$ and HAB $= 100\,\mathrm{mm}$)

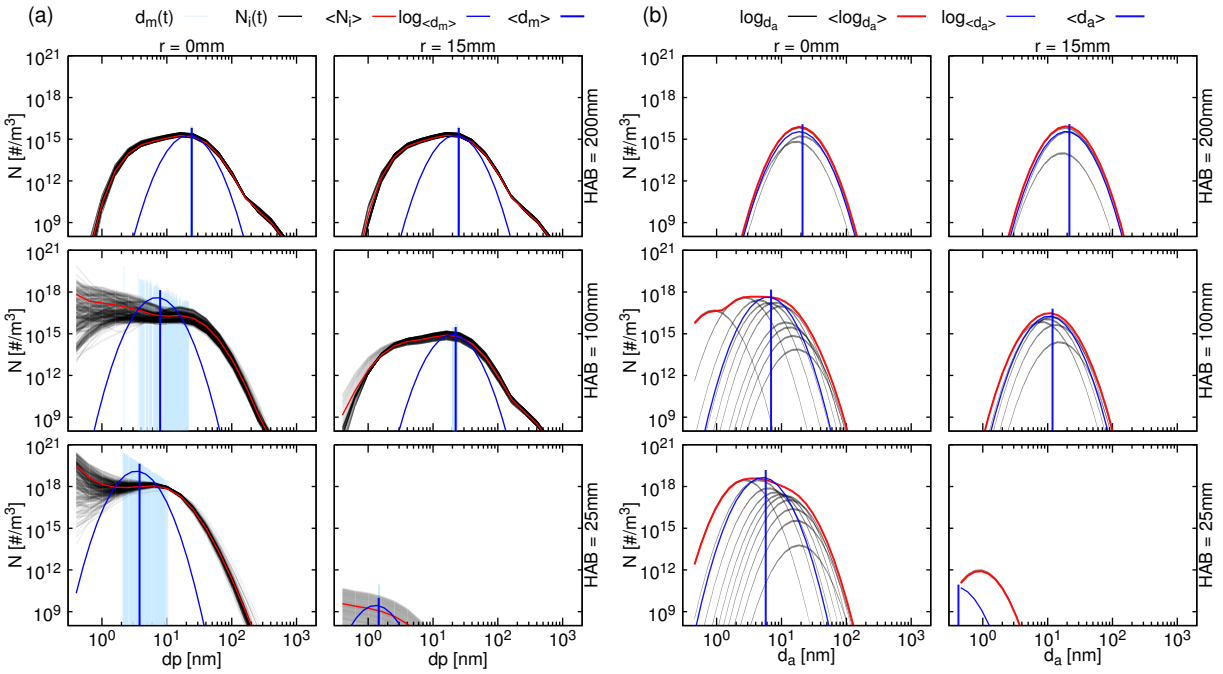

Figure 9.8: Particle size distribution obtained from the sectional model for two radial and four axial locations.

as a result of simultaneous nucleation and coagulation. With reducing impact of the inception mode, the bimodal distribution changes to a monomodal distribution off the centerline and for larger HAB, as illustrated in Fig. 9.7a. The size distribution also highlights that in the central jet small and large particles are found while a shift of the size distribution towards larger particles is observed further downstream. Furthermore, the PSD converges towards the self-preserving distribution as a result of coagulation only at HAB = 200mm for both illustrated radial locations.

A presumed log-normal size distribution from the monodisperse model has been obtained from the time averaged aggregate diameter d_a, the time averaged aggregate number concentration N and a standard deviation of 1.4. The predicted PSD is much too narrow, compared to the PSD from the sectional model, as long as two modes are present, compare Figs. 9.7a and 9.7b. Although the aggregate diameter d_a compares well with the volume averaged diameter d_m, for pure coagulation, the presumed log-normal size distribution from the monodisperse model is still too narrow for further downstream locations. For longer residence times and pure coagulation, it can however be assumed that a presumed log-normal size distribution represents the real PSD reasonably well.

The temporal variation of the particle size distributions is illustrated in Figs. 9.8a and 9.8b for 256 samples, which have been obtained over a sampling period of 10 ms. The instantaneous PSDs from the sectional model highlights the more or less distinct bimodal shape at HAB = 25 mm and HAB = 100 mm. For the investigated case, it is observed that dominantly the number concentrations of the small particles vary, especially close to the burner and in the central jet (HAB = 25 mm and HAB = 100 mm). For large HAB the particle size distribution is found to be stable. Also the volume averaged particle diameter varies close to the burner within a range of approximately 10 nm.

Figure 9.8b illustrates the presumed particle size distributions from time averaged particle number densities, as obtained from the monodisperse model. The particle diameter range has bin separated into 20 sections, for which 20 presumed log-normal distributions ($\log_{d_a}$) have been constructed. The resulting PSD ($< \log_{d_a} >$) captures the different states to which the particles have been exposed and is wider than the PSD around the averaged particle diameter ($\log_{<d_a>}$),

it is however still narrower than the real size distribution ($< N_i >$) predicted by the sectional model. Due to the fact that the investigated burner is only mildly turbulent the variations of the particle diameter and particle size distribution is found to be small especially for large heights above the burner. This finding is supported by both PSD predicted by the sectional model and the monodisperse model.

9.6 Conclusions

The nanoparticle formation and evolution from spray flame synthesis was investigated with the large eddy simulation technique. A modified version of the flamelet generated manifold approach combined with the artificial thickened flame model was proposed and used to describe combustion and precursor oxidation. A polydisperse sectional model accounting for nucleation and coagulation and a simple monodisperse model accounting for nucleation, coagulation and coalescence where used to approximate the general dynamics equation.

Particle nucleation, coagulation and sintering where shown to occur simultaneously for low heights above the burner. Sintering where shown to be only present in the high temperature region of the flame. Due to coalescence, primary particles with a diameter of up to 12 nm were observed. Larger aggregated particles and volume averaged particles of up to 26 nm were predicted by the simulations. The instantaneous and time averaged particle size distribution was shown to be bimodal as long as nucleation and coagulation occurred simultaneously. The bimodal distribution converged towards the self-preserving size distribution for conditions with pure coagulation. Temporal variations of the volume averaged particle diameter and the particle size distribution were shown especially for smaller particles close to the burner and in the jet break-up region, which results from different gas-phase and particle histories.

The simple monodisperse particle model predicted the volume averaged particle diameter well. The presumed log-normal size distribution obtained from the monodisperse model did however not capture the shape and width of the real size distribution from the sectional model, especially for low heights above the burner. Turbulence was shown to affect the particle size distribution, the impact of the aerosol dynamics was found to be of major importance.

The proposed global approach can be used to understand the interaction between the spray evaporation, gas phase combustion and particle synthesis. The numerical expenses of the sectional model limits its applications to a small domains, the numerical cheaper monodisperse model is however not able to capture to correct size distribution for conditions with simultaneous nucleation and coagulation.

9.7 Acknowledgement

The authors gratefully acknowledge the financial support by the AiF (grant No. 18298N/3) and of the state North Rhine-Westphalia, Germany, as well as the Center for Computational Sciences and Simulations of the University Duisburg-Essen for the computational resources.

Chapter 10
Summary and outlook

The nanoparticle formation from spray flame synthesis was investigated by highly resolved large eddy simulations (LES) using tabulated chemistry and both simple and detailed population balance equation models (PBE) in a three dimensional implementation.

First, a Lagrangian particle method was implemented in the LES flow solver PsiPhi − which was originally developed by Kempf [81] and extended by Proch [156] for massive parallel computations − to describe the spray transport and spray evaporation in turbulent reactive flows. The standard implementation of the flamelet generated manifold (FGM) approach coupled with the artificial thickened flame (ATF) method was modified to account for spray combustion. The FGM/ATF model for spray combustion was validated by detailed comparisons against a lab scale spray burner [57]. Subsequently the FGM/ATF approach for spray combustion was extended to account for two different fuels. A simple monodisperse model was included into PsiPhi to approximate the general dynamics equation (GDE) in the continuous form, to describe the particle synthesis from the gas phase by simultaneous nucleation, coagulation and sintering. The combination of the modified FGM/ATF approach and the monodisperse model was applied to describe the silica particle formation from an ethanol/hexamethyldisiloxane spray flame pyrolysis process (FSP). The findings of this study raised the question how well the monodisperse model is suited to describe the particle formation for cases with simultaneous aerosol-dynamics and mixing. In a next step, the more advanced sectional and bimodal PBE models were implemented into PsiPhi, which describe the particle evolution also by nucleation, coagulation and sintering, but these models are able to resolve the particle property space more accurate than the monodisperse model. The three PBE models were validated by a detailed comparison with results from a generic reference case [180]. Afterwards, the models capabilities in predicting the particle properties were tested in the presence of simultaneous nucleation, coagulation and mixing of particle populations with different histories. To show the applicability of the detailed and simple models for spray flames in the LES context and to demonstrate the differences of the models, they were used to describe the silica and iron-oxide synthesis from lab scale burners.

In the **first part** of the thesis, the modified version of the FGM/ATF approach was applied to investigate three diluted ethanol spray flames with varying equivalence ratios from the Sydney piloted spray flame series [57]. The liquid ethanol droplets were produced upstream of the burner by an ultrasonic nebulizer and injected into the combustion chamber, where the heat of a premixed pilot flame evaporated the droplets and subsequently ignited and stabilized the spray flame. A model for the spray transport and an equilibrium evaporation model were implemented into PsiPhi in a Langrangian framework [164]. The standard flow solver and the FGM/ATF combustion model were extended by source terms in the density, momentum and mixture fraction to account for mass-, momentum- and heat- exchange between the evaporating liquid droplets and the gas phase. Two dimensional look-up tables were generated a priori to the simulations. Therefore, a set of one dimensional premixed freely propagating flames was solved for ethanol and air with varying mixture compositions at the inlet. The thermochemical properties were stored in the look-up tables as functions of the control variables, here the mixture fraction and the reaction progress variable. Furthermore, the sub-filter distributions of the control variables were described by presumed filtered density functions (FDF). The variances of the control variables were either calculated by algebraic models or by a transport equation model. Overall good and

satisfactory results were obtained for the gas phase and liquid droplet statistics compared to the experimental results. The impact of the presumed FDF-shape and the variances of the control variables on the flow field were shown to be small. Further, the impact of the grid resolution was investigated and it was shown that a finer grid could slightly improve the predictions of the gas phase statics, whereas the impact on the liquid statistics was shown to be negligible. The presented studies of the Sydney piloted spray flame series indicated the suitability of the applied models for spray combustion, lead to a peer-reviewed journal publication and were necessary to be able to describe reactive two phase flows with the LES methodology.

In the **second part** of the study, the silica particle formation from the spray flame pyrolysis process of hexamethyldisiloxane as precursor was investigated numerically by utilizing a modified version of the FGM/ATF approach and a simple monodisperse particle model. In the investigated flame spray pyrolysis process, the liquid precursor was dissolved in ethanol and injected into a combustion chamber, where the liquid was subsequently evaporated, ignited and stabilized by a premixed methane/oxygen flame. To describe the aforementioned system with two fuels (hexamethyldisiloxane and methane), the FGM/ATF approach, developed and implemented in the first part of the thesis, was extended by a second mixture fraction. The mixture composition was described by the element mass fractions for carbon and hydrogen (instead of two standard mixture fractions) and the progress of combustion by one joint reaction progress variable. The three dimensional look-up table for the oxidation of hexamethyldisiloxane, ethanol and methane in pure oxygen were generated by solving one dimensional freely propagating flames, by varying the initial conditions of the fuel and oxidizer mass fractions as functions of the element mass fractions. To also account for the chemistry of the precursor in the manifolds, an existing reaction mechanism for the oxidation of ethanol was extended by a sub-mechanism for hexamethyldisiloxane, which was developed by Wlokas et al. [42]. The evolution of the particle population by simultaneous nucleation, coagulation and coalescence by sintering, was described by solving transport equations for the number concentration, area concentration and volume concentration of aggregate particles, which are proportional to the zeroth, first and third moments of the general dynamics equation. The nucleation source term was determined a priori to the simulations during the flamelet calculations and stored in the look-up table as a function of the control variables. The particle formation was investigated and discussed in terms the three moments and the resulting aggregate and primary particle diameters. The developed and presented global simulation approach enables a deeper understanding of the interactions of the spray formation, the gas phase combustion and particle synthesis and is suitable for simulations and optimizations of real synthesis reactors [165]. Furthermore, a particle size distribution (PSD) was obtained as a result of turbulence − even from the monodisperse particle model − which was shown to be narrow close to the burner exit and widen further downstream with locally bimodal distributions. The obtained local size distributions are the result of monodisperse particles exposed to different histories and do not result from the synthesis of polydisperse particle populations. A key question that arose from this study is: how important is the impact of turbulence and polydispersity on the resulting particle size distribution? This point was addressed in the forth and fifth part of the thesis. Furthermore, a validation of the implemented monodisperse model by a comparison to experimental data could not be performed, as space and time resolved measurements of particle diameters and size distributions are hard to obtain in turbulent spray flames.

In the **third part** of this thesis, the formation of titania particles from gas phase synthesis was simulated with the simple monodisperse model, a more advanced bimodal model and a detailed sectional model to a) validate and b) further investigate the models' capabilities in the presence of mixing. The three models were first implemented into PsiPhi and then validated by a detailed comparison against the results from a published reference case, which describes the titania particle formation from the oxidation of titanium-tetrachloride in pure oxygen [180]. The oxidation

of titanium tetrachloride was described, as in the reference case, by a global one step reaction. Particle formation was modelled as the change of the gas phase precursor to titania molecules. The applied bimodal model described the evolution of the particle population by nucleation, coagulation and sintering and solves transport equations for the number concentration of a nucleation mode, and transport equations for the number-, area- and volume concentration of an aggregation mode. The implemented sectional model described the particle formation by nucleation and coagulation and resolved the particle property space by solving transport equations for particle number concentrations of different particle volumes. A very good agreement of the predicted particle diameter and size distributions from the sectional model was obtained in comparison to the reference data for all investigated process conditions and residence times. The bimodal model predicted the diameter of the monomer molecules, aggregates and the volume averaged particle diameter very well for all investigated cases and residence times. The monodisperse model however, under predicted the particle diameter as long as nucleation and coagulation occurred simultaneously. Presumed log-normal PSDs were determined from the particle diameters and number concentration from the monodisperse- and bimodal model, which were compared to the real PSD from the sectional model. The presumed PSDs were shown to be in a good agreement as long as coagulation is the driving internal aerosol dynamic process and the real PSD converges towards the self-preserving PSD. To investigate the models' capabilities in the presence of simultaneous nucleation, coagulation and mixing, five generic cases were designed in which particle size distributions obtained from the reference case after different residence times were mixed. Nucleation was neglected in the first two cases, but considered in the third to fifth test case. The further evolution of the resulting particle size distribution and particle diameter predicted by the bimodal and monodisperse model were compared against the results from the sectional model. It was shown that the particle diameter and size distributions predicted by the monodisperse and bimodal model strongly deviate right after mixing, but also that the PSD returns to a good agreement for longer residence times after mixing had finished. The studies indicated a) the accuracy of the implemented models, b) the need of a more detailed particle model when nucleation, coagulation and mixing occurred simultaneously, c) that the simple models may by sufficient as long as mixing may be negligible and d) the importance of a proper sub-filter model for coagulation.

In the **fourth part** of the thesis, the developed FGM/ATF approach coupled with the sectional model and the monodisperse model were applied to investigate the iron-oxide particle synthesis from iron pentacarbonyl and to show the suitability of the developed methods also for a different material system. Iron oxide particles were produced by the spray flame pyrolysis process of iron pentacarbonyl solved in ethanol, which was injected into a combustion chamber, where a premixed methane air flame provided the heat for evaporation, ignition and stabilization of the spray flame. The element mass fractions of iron and hydrogen were used as control variables in the FGM/ATF approach. The look-up tables were produced by solving one dimensional freely propagating flames for varying inlet conditions. An existing reaction mechanism for the oxidation of ethanol was extended by a sub-mechanism for iron pentacarbonyl, which was developed by Wlokas et al. [220]. Particle diameters and presumed log-normal particle size distributions obtained from the simple monodisperse model were compared against the results from the detailed sectional model. The diameters predicted by the monodisperse model were slightly smaller than the diameters predicted by the sectional model. Narrow particle size distributions were found by both models close to the burner exit, which widened further downstream only as a result of turbulence. The presumed and predicted PSDs from the monodisperse model were too narrow compared to the real PSDs from the sectional model. The studies presented in the fourth part of this thesis indicated the material independency of the developed global simulation approach.

In the **fifth part** of the thesis, the developed FGM/ATF approach coupled with the sectional

model and the monodisperse model were applied to improve the investigations of the silica particle synthesis from the spray flame pyrolysis described in part two. The studies showed that the particle formation, coagulation and sintering (with the monodisperse model) occurred simultaneously for low heights above the burner, and coagulation is the dominant process further downstream. (Primary particles of up to 12 nm and larger aggregates of up to 26 nm were found in the investigated flow domain). A bimodal particle size distribution from simultaneous nucleation and coagulation could be shown by the sectional model for low heights above the burner, which converged towards a self preserving size distribution further downstream as a result of pure coagulation. The studies also highlighted the impact of turbulence and polydispersity on the evolution of the PSD and outlined the differences of the simple and detailed sectional model.

In summary, it was shown that tabulated chemistry approaches combined with PBE models and the large eddy simulation methodology is a suitable tool to numerically investigate spray flames with subsequent nano particle synthesis. Therefore, the presented work may be seen as a step towards the detailed modelling of the spray flame synthesis of nanoparticles. However, there are still open research questions to be worked on: a) how to incorporate the sub-filter distribution of the particle population in the modelling of coagulation and sintering, b) how to improve the modelling of diffusion in the monodisperse and bimodal model for low turbulent or laminar cases, c) how should the gas and particle phases be treated for flows with a high particle loading and d) how can the accuracy of the sectional model and the numerical efficiency of the monodisperse model be combined.

Bibliography

[1] http://www.sandia.gov/TNF/abstract.html, 2000.

[2] B. Abramzon and W. Sirignano. Droplet vaporization model for spray combustion calculations. *International journal of heat and mass transfer*, 32(9):1605–1618, 1989.

[3] P. P. Ahonen, J. Joutsensaari, O. Richard, U. Tapper, D. P. Brown, J. K. Jokiniemi, and E. I. Kauppinen. Mobility size development and the crystallization path during aerosol decomposition synthesis of tio 2 particles. *Journal of aerosol science*, 32(5):615–630, 2001.

[4] J. Akroyd, A. J. Smith, L. R. McGlashan, and M. Kraft. Comparison of the stohastic fields method and dqmom-iem as turbulent reaction closures. *Chemical Engineering Science*, 65: 1915 – 1924, 2010.

[5] J. Akroyd, A. J. Smith, R. Shirley, L. R. McGlashan, and M. Kraft. A coupled cfd-population balance approach for nanoparticle synthesis in turbulent reacting flows. *Chemical Engineering Science*, 66:3792 – 3805, 2011.

[6] A. Attili, F. Bisetti, M. E. Mueller, and H. Pitsch. Formation, growth, and transport of soot in a three-dimensional turbulent non-premixed jet flame. *Combustion and Flame*, 161 (7):1849 – 1865, 2014. ISSN 0010-2180. doi: 10.1016/j.combustflame.2014.01.008. URL `http://www.sciencedirect.com/science/article/pii/S0010218014000133`.

[7] G. Balarac, H. Pitsch, and V. Raman. Development of a dynamic model for the subfilter scalar variance using the concept of optimal estimators. *Physics of fluids*, 20:035114, 2008.

[8] R. Barlow and J. Frank. Effects of turbulence on species mass fractions in methane/air jet flames. *Symposium (International) on Combustion*, 27(1):1087–1095, 1998.

[9] R. S. Barlow and A. N. Karpetis. Measurements of scalar variance, scalar dissipation, and length scales in turbulent piloted methane/air jet flames. *Flow, Turbulence and Combustion*, 72(2-4):427–448, 2004. ISSN 1386-6184. doi: 10.1023/b%3aappl.0000044405.96071.e1.

[10] H. Baya Toda, O. Cabrit, K. Truffin, G. Bruneaux, and F. Nicoud. Assessment of subgrid-scale models with a large-eddy simulation-dedicated experimental database: The pulsatile impinging jet in turbulent cross-flow. *Physics of Fluids (1994-present)*, 26(7):075108, 2014. doi: 10.1063/1.4890855. URL `http://scitation.aip.org/content/aip/journal/pof2/26/7/10.1063/1.4890855`.

[11] C. Bekdemir, E. Rijk, L. Somers, d. L. Goey, and B. Albrecht. On the application of the flamelet generated manifold (fgm) approach to the simulation of an igniting diesel spray. *SAE Technical Papers*, (2010-01-0358):2010–01, 2010.

[12] A. T. Bell. The impact of nanoscience on heterogeneous catalysis. *Science*, 299(5613): 1688–1691, 2003.

[13] R. W. Bilger, S. H. Stårner, and R. J. Kee. On reduced mechanisms for methane-air combustion in nonpremixed flames. *Combustion and Flame*, 80(2):135 – 149, 1990. ISSN 0010-2180. doi: 10.1016/0010-2180(90)90122-8. URL `http://www.sciencedirect.com/science/article/pii/0010218090901228`.

[14] B. R. Bird, W. E. Stewart, and E. N. Lightfoot. *Transport phenomena*. John Wiley & Sons, 2nd edition, 2002.

[15] P. Biswas, C. Y. Wu, M. R. Zachariah, and B. McMillin. Characterization of iron oxide-silica nanocomposites in flames: Part ii. comparison of discrete-sectional model predictions to experimental data. *Journal of Materials Research*, 12:714–723, 1997. ISSN 2044-5326. doi: 10.1557/jmr.1997.0106. URL `http://journals.cambridge.org/article_S0884291400039017`.

[16] D. Boldridge. Morphological characterization of fumed silica aggregates. *Aerosol Science and Technology*, 44(3):182–186, 2010. doi: 10.1080/02786820903499462.

[17] J. V. Boussinesq. Essai sur la théorie des eaux courantes. *Mémoires présentés par divers savant à l'Académie des Sciences de l'Institut de France*, 23:1 – 680, 1877.

[18] N. Branley and W. P. Jones. Large eddy simulation of a turbulent non-premixed flame. *Combustion and Flame*, 127(1-2):1914–1934, Oct. 2001.

[19] V. S. Buddhiraju and V. Runkana. Simulation of nanoparticle synthesis in an aerosol flame reactor using a coupled flame dynamicsmonodisperse population balance model. *Journal of Aerosol Science*, 43(1):1 – 13, 2012. ISSN 0021-8502. doi: 10.1016/j.jaerosci.2011.08.007. URL `http://www.sciencedirect.com/science/article/pii/S0021850211001492`.

[20] F. Cavallo Marincola, T. Ma, and A. M. Kempf. Large eddy simulations of the darmstadt turbulent stratified flame series. *Proceedings of the Combustion Institute*, 34(1): 1307 – 1315, 2013. ISSN 1540-7489. doi: 10.1016/j.proci.2012.08.001. URL `http://www.sciencedirect.com/science/article/pii/S1540748912003720`.

[21] I. Celik, Z. Cehreli, and I. Yavuz. Index of resolution quality for large eddy simulations. *Journal of Fluids Engineering*, 127(5):949–958, 2005.

[22] K.-Y. Chan, J. Ding, J. Ren, S. Cheng, and K. Y. Tsang. Supported mixed metal nanoparticles as electrocatalysts in low temperature fuel cells. *Journal of Materials Chemistry*, 14 (4):505–516, 2004.

[23] F. Charlette, C. Meneveau, and D. Veynante. A power-law flame wrinkling model for les of premixed turbulent combustion part i- non-dynamic formulation and initial tests. *Combustion and Flame*, 131:159–180, 2002.

[24] D.-H. Chen and X.-R. He. Synthesis of nickel ferrite nanoparticles by sol-gel method. *Materials Research Bulletin*, 36(78):1369 – 1377, 2001. ISSN 0025-5408. doi: 10.1016/s0025-5408(01)00620-1. URL `http://www.sciencedirect.com/science/article/pii/S0025540801006201`.

[25] M. Chrigui, J. Gounder, A. Sadiki, A. R. Masri, and J. Janicka. Partially premixed reacting acetone spray using les and fgm tabulated chemistry. *Combustion and Flame*, 159(8):2718–2741, 2012.

[26] M. Chrigui, A. R. Masri, A. Sadiki, and J. Janicka. Large eddy simulation of a polydisperse ethanol spray flame. *Flow, Turbulence and Combustion*, 90(4):813–832, 2013. ISSN 1386-6184. doi: 10.1007/s10494-013-9449-9.

[27] O. Colin, F. Ducros, D. Veynante, and T. J. Poinsot. A thickened flame model for large eddy simulations of turbulent premixed combustion. *Physics of Fluids*, 12(7):1843–1863, 2000.

[28] A. W. Cook and J. J. Riley. A subgrid model for equilibrium chemistry in turbulent flows. *Physics of Fluids*, 6(8):2868–2870, 1994.

[29] R. Courant, K. Friedrichs, and H. Lewy. Über die partiellen {D}ifferenzengleichungen der mathematischen {P}hysik. *Mathematische Annalen*, 100(1):32–74, 1928. ISSN 1432-1807. doi: 10.1007/bf01448839.

[30] M.-C. Daniel and D. Astruc. Gold nanoparticles: assembly, supramolecular chemistry, quantum-size-related properties, and applications toward biology, catalysis, and nanotechnology. *Chemical reviews*, 104(1):293–346, 2004.

[31] S. Das and S. C. Garrick. The effects of turbulence on nanoparticle growth in turbulent reacting jets. *Physics of Fluids*, 22(10):103303, 2010. doi: 10.1063/1.3486203. URL `http://scitation.aip.org/content/aip/journal/pof2/22/10/10.1063/1.3486203`.

[32] S. De and S. H. Kim. Large eddy simulation of dilute reacting sprays: Droplet evaporation and scalar mixing. *Combustion and Flame*, 160(10):2048 – 2066, 2013. ISSN 0010-2180. doi: 10.1016/j.combustflame.2013.04.024. URL `http://www.sciencedirect.com/science/article/pii/S0010218013001685`.

[33] L. Deng, A. M. Kempf, O. Hasemann, O. P. Korobeinichev, and I. Wlokas. Investigation of the sampling nozzle effect on laminar flat flames. *Combustion and Flame*, 162:1737–1747, 2015.

[34] S. Dolgaev, A. Simakin, V. Voronov, G. Shafeev, and F. Bozon-Verduraz. Nanoparticles produced by laser ablation of solids in liquid environment. *Applied surface science*, 186(1): 546–551, 2002.

[35] P. Domingo, L. Vervisch, and J. Réveillon. Dns analysis of partially premixed combustion in spray and gaseous turbulent flame-bases stabilized in hot air. *Combustion and Flame*, 140(3):172 – 195, 2005. ISSN 0010-2180. doi: 10.1016/j.combustflame.2004.11.006. URL `http://www.sciencedirect.com/science/article/pii/S0010218004002342`.

[36] T. Dreier, O. Feroughi, A. Langer, and C. Schulz. Spatially-resolved measurements of gas-phase temperature and sio concentration in a low-pressure nanoparticle synthesis reactor using laser-induced fluorescence. In *Imaging and Applied Optics 2014*, page LM1D.2. Optical Society of America, 2014. doi: 10.1364/lacsea.2014.lm1d.2. URL `http://www.osapublishing.org/abstract.cfm?URI=LACSEA-2014-LM1D.2`.

[37] L. Durand and W. Polifke. Implementation of the thickened flame model for large eddy simulation of turbulent premixed combustion in a commercial solver. *ASME Turbo Expo*, pages 869–878, 2007.

[38] S. H. Ehrman, M. I. Aquino-Class, and M. R. Zachariah. Effect of temperature and vapor-phase encapsulation on particle growth and morphology. *Journal of materials research*, 14 (04):1664–1671, 1999.

[39] S. R. Engel, A. F. Koegler, Y. Gao, D. Kilian, M. Voigt, T. Seeger, W. Peukert, and A. Leipertz. Gas phase temperature measurements in the liquid and particle regime of a flame spray pyrolysis process using o2-based pure rotational coherent anti-stokes raman scattering. *Appl. Opt.*, 51(25):6063–6075, Sep 2012. doi: 10.1364/ao.51.006063. URL `http://ao.osa.org/abstract.cfm?URI=ao-51-25-6063`.

[40] R. Fan, D. L. Marchisio, and R. O. Fox. Application of the direct quadrature method of moments to polydisperse gas-solid fluidized beds. *Powder Technology*, 139:7–20, 2004.

[41] A. Favre. Turbulence: Spacetime statistical properties and behavior in supersonic flows. *Physics of Fluids (1958-1988)*, 26(10):2851–2863, 1983. doi: 10.1063/1.864049. URL http://scitation.aip.org/content/aip/journal/pof1/26/10/10.1063/1.864049.

[42] O. M. Feroughi, L. Deng, S. Kluge, T. Dreier, H. Wiggers, I. Wlokas, and C. Schulz. Experimental and numerical study of a hmdso-seeded premixed laminar low-pressure flame for sio2 nanoparticle synthesis. *Proceedings of the Combustion Institute*, pages –, 2016. ISSN 1540-7489. doi: 10.1016/j.proci.2016.07.131. URL http://www.sciencedirect.com/science/article/pii/S154074891630390X.

[43] J. Floyd, A. M. Kempf, A. Kronenburg, and R. H. Ram. A simple model for the filtered density function for passive scalar combustion LES. *Combust. Theory Mod.*, 13(4):559–588, 2009. doi: 10.1080/13647830802632200. URL http://www.tandfonline.com/doi/abs/10.1080/13647830802632200.

[44] R. O. Fox. Optimal moment sets for multivariate direct quadrature method of moments. *IECR*, 48:9686–9896, 2009.

[45] B. M. Franchetti, F. Cavallo Marincola, S. Navarro-Martinez, and A. M. Kempf. Large eddy simulation of a pulverised coal jet flame. *Proceedings of the Combustion Institute*, 34(2):2419 – 2426, 2013. ISSN 1540-7489. doi: 10.1016/j.proci.2012.07.056. URL http://www.sciencedirect.com/science/article/pii/S1540748912003483.

[46] M. Frenklach. Dynamics of discrete distribution for smoluchowski coagulation model. *Journal of Colloid and Interface Science*, 108(1):237 – 242, 1985. ISSN 0021-9797. doi: 10.1016/0021-9797(85)90256-5. URL http://www.sciencedirect.com/science/article/pii/0021979785902565.

[47] M. Frenklach and S. J. Harris. Aerosol dynamics modeling using the method of moments. *Journal of Colloid and Interface Science*, 118(1):252 – 261, 1987. ISSN 0021-9797. doi: 10.1016/0021-9797(87)90454-1. URL http://www.sciencedirect.com/science/article/pii/0021979787904541.

[48] M. Frenklach and A. Kazakov. Reduced reaction sets based on grimech1.2. http://www.me.berkeley.edu/drm/, 2000.

[49] S. K. Friedlander. *Smoke, Dust and Haze. Fundamentals of Aerosol Dynamics*. Oxford University Press, Inc., 2000.

[50] N. A. Fuchs. *The mechanics of aerosols*. 1964.

[51] C. Fureby. A fractal flame-wrinkling large eddy simulation model for premixed turbulent combustion. *Proceedings of the Combustion Institute*, 30(1):593 – 601, 2005. ISSN 1540-7489. doi: 10.1016/j.proci.2004.08.068. URL http://www.sciencedirect.com/science/article/pii/S0082078404001316.

[52] H.-W. Ge and E. Gutheil. Probability density function (pdf) simulation of turbulent spray flows. *Atomization and sprays*, 16(5), 2006.

[53] F. Gelbard, Y. Tambour, and J. H. Seinfeld. Sectional representations for simulating aerosol dynamics. *Journal of Colloid and Interface Science*, 76(2):541–556, 1980.

[54] M. Germano, U. Piomelli, P. Moin, and W. H. Cabot. A dynamic subgrid-scale eddy viscosity model. *Physics of Fluids A*, 3(7):1760–1765, 1991.

[55] M. Goodson and M. Kraft. An efficient stochastic algorithm for simulating nano-particle dynamics. *Journal of Computational Physics*, 183(1):210–232, 2002.

[56] D. G. Goodwin. Cantera. http://code.google.com/p/cantera, 2009.

[57] J. D. Gounder, A. Kourmatzis, and A. R. Masri. Turbulent piloted dilute spray flames: Flow fields and droplet dynamics. *Combustion and Flame*, 159(11):3372 – 3397, 2012. ISSN 0010-2180. doi: 10.1016/j.combustflame.2012.07.014. URL `http://www.sciencedirect.com/science/article/pii/S0010218012002271`.

[58] S. Grimm, M. Schultz, S. Barth, and R. Muller. Flame pyrolysis – a preparation route for ultrafine pure γ-fe2o3 powders and the control of their particle size and properties. *Journal of Materials Science*, 32(4):1083–1092, 1997. ISSN 1573-4803. doi: 10.1023/a:1018598927041.

[59] A. J. Gröhn, B. Buesser, J. K. Jokiniemi, and S. E. Pratsinis. Design of turbulent flame aerosol reactors by mixing-limited fluid dynamics. *Industrial & Engineering Chemistry Reasearch*, 50(6):3159–3168, 2011.

[60] A. J. Gröhn, S. E. Pratsinis, and K. Wegner. Fluid-particle dynamics during combustion spray aerosol synthesis of zro2. *Chemical Engineering Journal*, 191:491–502, 2012.

[61] A. J. Gröhn, S. E. Pratsinis, A. Sánchez-Ferrer, R. Mezzenga, and K. Wegner. *Industrial & Engineering Chemistry Research*, 53(26):10734–10742, 2014.

[62] D. Guo, G. Xie, and J. Luo. Mechanical properties of nanoparticles: basics and applications. *Journal of Physics D: Applied Physics*, 47(1):013001, 2014. URL `http://stacks.iop.org/0022-3727/47/i=1/a=013001`.

[63] E. Gutheil and W. A. Sirignano. Counterflow spray combustion modeling with detailed transport and detailed chemistry. *Combustion and Flame*, 113(12):92 – 105, 1998. ISSN 0010-2180. doi: 10.1016/s0010-2180(97)00192-2. URL `http://www.sciencedirect.com/science/article/pii/S0010218097001922`.

[64] S. Hardt, H. Grimm, I. Wlokas, H. Wiggers, A. M. Kempf, and C. Schulz. Iron-oxide nanoparticle synthesis from liquid spray flames under variable pressure conditions. June 2012.

[65] C. Hasse and N. Peters. A two mixture fraction flamelet model applied to split injections in a di diesel engine. *Proceedings of the Combustion Institute*, 30(2):2755–2762, 2005.

[66] C. Heye, V. Raman, and A. R. Masri. Les/probability density function approach for the simulation of an ethanol spray flame. *Proceedings of the Combustion Institute*, 34 (1):1633 – 1641, 2013. ISSN 1540-7489. doi: 10.1016/j.proci.2012.06.107. URL `http://www.sciencedirect.com/science/article/pii/S1540748912002155`.

[67] M. Ihme, L. Shunn, and J. Zhang. Regularization of reaction progress variable for application to flamelet-based combustion models. *Journal of Computational Physics*, 231 (23):7715 – 7721, 2012. ISSN 0021-9991. doi: 10.1016/j.jcp.2012.06.029. URL `http://www.sciencedirect.com/science/article/pii/S0021999112003440`.

[68] H. D. Jang. Generation of silica nanoparticles from tetraethylorthosilicate (teos) vapor in a diffusion flame. *Aerosol Science and Technology*, 30(5):477–488, 1999. doi: 10.1080/027868299304516.

[69] J. Janicka and A. Sadiki. Large eddy simulation of turbulent combustion systems. In *Proc. Combust. Inst.*, volume 30, pages 537–547, 2005. imp-import.

[70] C. Janzen, J. Knipping, B. Rellinghaus, and P. Roth. Formation of silica-embedded iron-oxide nanoparticles in low-pressure flames. *Journal of Nanoparticle Research*, 5(5-6):589–596, 2003. ISSN 1388-0764. doi: 10.1023/b%3anano.0000006109.37251.fd.

[71] P. Jenny, D. Roekaerts, and N. Beishuizen. Modeling of turbulent dilute spray combustion. *Progress in Energy and Combustion Science*, 38(6):846 – 887, 2012. ISSN 0360-1285. doi: 10.1016/j.pecs.2012.07.001. URL `http://www.sciencedirect.com/science/article/pii/S0360128512000445`.

[72] J. I. Jeong and M. Choi. A sectional method for the analysis of growth of polydisperse non-spherical particles undergoing coagulation and coalescence. *Journal of Aerosol Science*, 32 (5):565–582, 2001.

[73] J. I. Jeong and M. Choi. A simple bimodal model for the evolution of non-spherical particles undergoing nucleation, coagulation and coalescence. *Journal of Aerosol Science*, 34(8):965 – 976, 2003. ISSN 0021-8502. doi: 10.1016/s0021-8502(03)00067-3. URL `http://www.sciencedirect.com/science/article/pii/S0021850203000673`.

[74] W. P. Jones and B. E. Launder. The prediction of laminarization with a two-equation model of turbulence. *International Journal of Heat and Mass Transfer*, 15(2):301 – 314, 1972. ISSN 0017-9310. doi: 10.1016/0017-9310(72)90076-2. URL `http://www.sciencedirect.com/science/article/pii/0017931072900762`.

[75] W. P. Jones, S. Lyra, and S. Navarro-Martinez. Large eddy simulation of a swirl stabilized spray flame. *Proceedings of the Combustion Institute*, 33(2):2153 – 2160, 2011. ISSN 1540-7489. doi: 10.1016/j.proci.2010.07.032. URL `http://www.sciencedirect.com/science/article/pii/S1540748910002956`.

[76] H. K. Kammler, L. Mädler, and S. E. Pratsinis. Flame synthesis of nanoparticles. *Chemical engineering & technology*, 24(6):583–596, 2001.

[77] H. K. Kammler, R. Mueller, O. Senn, and S. E. Pratsinis. Synthesis of silica-carbon particles in a turbulent h2-air flame aerosol reactor. *AIChE journal*, 47(7):1533–1543, 2001.

[78] C. M. Kaul, V. Raman, E. Knudsen, E. S. Richardson, and J. H. Chen. Large eddy simulation of a lifted ethylene flame using a dynamic nonequilibrium model for subfilter scalar variance and dissipation rate. *Proceedings of the Combustion Institute*, 34 (1):1289 – 1297, 2013. ISSN 1540-7489. doi: 10.1016/j.proci.2012.06.079. URL `http://www.sciencedirect.com/science/article/pii/S1540748912001873`.

[79] R. J. Kee, F. M. Rupley, and J. A. Miller. The chemkin thermodynamic data base. *Technical Report SAND87-8215, Sandia National Laboratories*, 1, 1990.

[80] K. L. Kelly, E. Coronado, L. L. Zhao, and G. C. Schatz. The optical properties of metal nanoparticles: the influence of size, shape, and dielectric environment. *The Journal of Physical Chemistry B*, 107(3):668–677, 2003.

[81] A. M. Kempf. *Large-Eddy Simulation of Non-Premixed Turbulent Flames*. PhD thesis, Darmstadt University of Technology, Germany, 2003.

[82] A. M. Kempf, B. Geurts, and J. C. Oefelein. Error analysis of large-eddy simulation of the turbulent non-premixed sydney bluff-body flame. *Combust. Flame*, 158:2408–2419, 2011. URL `http://www.sciencedirect.com/science/article/pii/S0010218011001271`.

[83] A. M. Kempf, S. Wysocki, and M. Pettit. An efficient, parallel low-storage implementation of Klein's turbulence generator for LES and DNS. *Computers and Fluids*, 60:58–60, 2012.

ISSN 0045-7930. doi: 10.1016/j.compfluid.2012.02.027. URL http://www.sciencedirect.com/science/article/pii/S0045793012000825?v=s5.

[84] D. Kilian, S. Engel, B. Borsdorf, Y. Gao, A. F. Kögler, S. Kobler, T. Seeger, S. Will, A. Leipertz, and W. Peukert. Spatially resolved flame zone classification of a flame spray nanoparticle synthesis process by combining different optical techniques. *Journal of Aerosol Science*, 69:82 – 97, 2014. ISSN 0021-8502. doi: 10.1016/j.jaerosci.2013.12.002. URL http://www.sciencedirect.com/science/article/pii/S0021850213002401.

[85] Y. P. Kim and J. H. Seinfeld. Simulation of multicomponent aerosol condensation by the moving sectional method. *Journal of Colloid and Interface Science*, 135(1):185 – 199, 1990. ISSN 0021-9797. doi: 10.1016/0021-9797(90)90299-4. URL http://www.sciencedirect.com/science/article/pii/0021979790902994.

[86] W. D. Kingery. Introduction to ceramics. 1960.

[87] M. Klein, A. Sadiki, and J. Janicka. A digital filter based generation of inflow data for spatially developing direct numerical or large eddy simulations. *Journal of Computational Physics*, 186:652–665, 2003.

[88] A. Y. Klimenko and R. W. Bilger. Conditional moment closure for turbulent combustion. *Progress in energy and combustion science*, 25(6):595–687, 1999.

[89] J. Knipping, H. Wiggers, B. Rellinghaus, P. Roth, D. Konjhodzic, and C. Meier. Synthesis of high purity silicon nanoparticles in a low pressure microwave reactor. *Journal of nanoscience and nanotechnology*, 4(8):1039–1044, 2004.

[90] A. N. Kolmogorov. The local structure of turbulence in incompressible viscous fluid for very large reynolds numbers. In *Dokl. Akad. Nauk SSSR*, volume 30, pages 301–305. JSTOR, 1941.

[91] S.-C. Kong and R. D. Reitz. Application of detailed chemistry and cfd for predicting direct injection hcci engine combustion and emissions. *Proceedings of the Combustion Institute*, 29(1):663–669, 2002.

[92] S.-C. Kong, Y. Sun, and R. D. Rietz. Modeling diesel spray flame liftoff, sooting tendency, and nox emissions using detailed chemistry with phenomenological soot model. *Journal of Engineering for Gas Turbines and Power*, 129(1):245–251, 2007.

[93] A. Kowalik. *Modellierung und Simulation der Synthese von Eisen-Nanopartikeln in Gasphasenreaktoren*. PhD thesis, University of Duisburg-Essen, 2007.

[94] F. E. Kruis, H. Fissan, and A. Peled. Synthesis of nanoparticles in the gas phase for electronic, optical and magnetic applicationsa review. *Journal of Aerosol Science*, 29(56): 511 – 535, 1998. ISSN 0021-8502. doi: 10.1016/s0021-8502(97)10032-5. URL http://www.sciencedirect.com/science/article/pii/S0021850297100325.

[95] G. Kuenne, A. Ketelheun, and J. Janicka. Les modeling of premixed combustion using a thickened flame approach coupled with fgm tabulated chemistry. *Combustion and Flame*, 158(9):1750 – 1767, 2011. ISSN 0010-2180. doi: 10.1016/j.combustflame.2011.01.005. URL http://www.sciencedirect.com/science/article/pii/S0010218011000204.

[96] G. Kuenne, F. Seffrin, F. Fuest, T. Stahler, A. Ketelheun, D. Geyer, J. Janicka, and A. Dreizler. Experimental and numerical analysis of a lean premixed stratified burner using 1d raman/rayleigh scattering and large eddy simulation. *Combustion and Flame*, 159 (8):2669 – 2689, 2012. ISSN 0010-2180. doi: 10.1016/j.combustflame.2012.02.010. URL http://www.sciencedirect.com/science/article/pii/S0010218012000594.

[97] S. Kumar and D. Ramkrishna. On the solution of population balance equations by discretizationiii. nucleation, growth and aggregation of particles. *Chemical Engineering Science*, 52(24):4659–4679, 1997.

[98] K. A. Kusters, S. E. Pratsinis, B. Scarlett, and F. E. Kruis. A simple model for the evolution of the characteristics of aggregate particles undergoing coagulation and sintering. *Aerosol science and technology*, 19(4):514–526, 1993.

[99] F. S. Lai, J. Pich, G. M. Hidy, and S. K. Friedlander. The self-preserving particle size distribution for brownian coagulation in the free-molecule regime. *Journal of Colloid and Interface Science*, 39(2):395 – 405, 1972. ISSN 0021-9797. doi: 10.1016/0021-9797(72)90034-3. URL `http://www.sciencedirect.com/science/article/pii/0021979772900343`.

[100] J. D. Landgrebe and S. E. Pratsinis. Gas-phase manufacture of particulates: interplay of chemical reaction and aerosol coagulation in the free-molecular regime. *Industrial & Engineering Chemistry Research*, 28(10):1474–1481, 1989. doi: 10.1021/ie00094a007.

[101] G. Lecocq, S. Richard, O. Colin, and L. Vervisch. Gradient and counter-gradient modeling in premixed flames: Theoretical study and application to the les of a lean premixed turbulent swirl-burner. *Combustion Science and Technology*, 182(4-6):465–479, 2010. doi: 10.1080/00102200903462920.

[102] T. Lederlin and H. Pitsch. Large-eddy simulation of an evaporating and reacting spray. *Center for Turbulence Research, Annual Research Briefs*, pages 479–490, 2008.

[103] G. Ledoux, J. Gong, F. Huisken, O. Guillois, and C. Reynaud. Photoluminescence of size-separated silicon nanocrystals: Confirmation of quantum confinement. *Applied Physics Letters*, 80(25):4834–4836, 2002.

[104] S.-A. Lee, K.-W. Park, J.-H. Choi, B.-K. Kwon, and Y.-E. Sung. Nanoparticle synthesis and electrocatalytic activity of pt alloys for direct methanol fuel cells. *Journal of the Electrochemical Society*, 149(10):A1299–A1304, 2002.

[105] D. Li, W. Y. Teoh, C. Selomulya, R. C. Woodward, P. Munroe, and R. Amal. Insight into microstructural and magnetic properties of flame-made γ-fe 2 o 3 nanoparticles. *Journal of Materials Chemistry*, 17(46):4876–4884, 2007.

[106] D. K. Lilly. A proposed modification of the {G}ermano subgridscale closure method. *Physics of Fluids A*, 4(3):633–635, 1992. doi: 10.1063/1.858280. URL `http://scitation.aip.org/content/aip/journal/pofa/4/3/10.1063/1.858280`.

[107] H.-F. Lin, S.-C. Liao, and S.-W. Hung. The dc thermal plasma synthesis of zno nanoparticles for visible-light photocatalyst. *Journal of photochemistry and photobiology A: Chemistry*, 174(1):82–87, 2005.

[108] S. Lindsay. *Introduction to nanoscience*. OUP Oxford, 2009.

[109] J. Loeffler, S. Das, and S. C. Garrick. Large eddy simulation of titanium dioxide nanoparticle formation and growth in turbulent jets. *Aerosol Science and Technology*, 45(5):616–628, 2011. doi: 10.1080/02786826.2010.551147.

[110] J. Loeffler, S. Das, and S. C. Garrick. Large eddy simulation of titanium dioxide nanoparticle formation and growth in turbulent jets. *Aerosol Science and Technology*, 45(5):616–628, 2011. doi: 10.1080/02786826.2010.551147.

[111] T. Ma, Y. Gao, A. M. Kempf, and N. Chakraborty. Validation and implementation of algebraic les modelling of scalar dissipation rate for reaction rate closure in turbulent premixed combustion. *Combustion and Flame*, 161(12):3134 – 3153, 2014. ISSN 0010-2180. doi: 10.1016/j.combustflame.2014.05.023. URL http://www.sciencedirect.com/science/article/pii/S0010218014001643.

[112] U. Maas and S. B. Pope. Simplifying chemical kinetics: Intrinsic low-dimensional manifolds in composition space. *Combustion and Flame*, 88(34):239 – 264, 1992. ISSN 0010-2180. doi: 10.1016/0010-2180(92)90034-m. URL http://www.sciencedirect.com/science/article/pii/001021809290034M.

[113] L. Mädler, H. K. Kammler, S. E. Pratsinis, and R. Mueller. Controlled synthesis of nanostructured particles by flame spray pyrolysis. *Journal of Aerosol Science*, 33(2):369–389, 2002.

[114] L. Mädler, W. J. Stark, and S. E. Pratsinis. Flame-made ceria nanoparticles. *Journal of Materials Research*, 17:1356–1362, 2002. ISSN 2044-5326. doi: 10.1557/jmr.2002.0202. URL http://journals.cambridge.org/article_S088429140006739X.

[115] B. Magnussen and B. Hjertager. On mathematical modeling of turbulent combustion with special emphasis on soot formation and combustion. *Proc. Combust. Inst.*, 16(1):719–729, Jan 1977. doi: 10.1016/s0082-0784(77)80366-4.

[116] D. L. Marchisio and R. O. Fox. Solution of population balance equations using the direct quadrature method of moments. *Journal Aerosol Science*, 36:43–73, 2005.

[117] D. L. Marchisio and R. O. Fox. *Computational models for polydisperse particulate and multiphase systems*. Cambridge University Press, 2013.

[118] N. M. Marinov. A detailed chemical kinetic model for high temperature ethanol oxidation. *International Journal of Chemical Kinetics*, 31(3):183–220, 1999. ISSN 1097-4601. doi: 10.1002/(sici)1097-4601(1999)31:3⟨183::aid-kin3⟩3.0.co;2-x.

[119] F. R. Menter. Two-equation eddy-viscosity turbulence models for engineering applications. *AIAA J.*, 32(8):1598–1605, 1994.

[120] R. S. Miller, K. Harstad, and J. Bellan. Evaluation of equilibrium and non-equilibrium evaporation models for many-droplet gas-liquid flow simulations. *International Journal of Multiphase Flow*, 24(6):1025 – 1055, 1998. ISSN 0301-9322. doi: 10.1016/s0301-9322(98)00028-7. URL http://www.sciencedirect.com/science/article/pii/S0301932298000287.

[121] S. E. Miller and S. C. Garrick. Nanoparticle coagulation in a planar jet. *Aerosol science and technology*, 38(1):79–89, 2004.

[122] S. Modem, S. C. Garrick, M. R. Zachariah, and K. E. J. Lehtinen. Direct numerical simulation of nanoparticle coagulation in a temporal mixing layer. *Proceedings of the Combustion Institute*, 29(1):1071 – 1077, 2002. ISSN 1540-7489. doi: 10.1016/s1540-7489(02)80135-3. URL http://www.sciencedirect.com/science/article/pii/S1540748902801353.

[123] P. Moin and S. V. Apte. Large-eddy simulation of realistic gas turbine combustors. *AIAA journal*, 44(4):698–708, 2006.

[124] P. Moin, K. Squires, W. Cabot, and S. Lee. A dynamic subgridscale model for compressible turbulence and scalar transport. *Physics of Fluids A*, 3(11):2746–2757, 1991. doi: 10.1063/1.858164. URL http://scitation.aip.org/content/aip/journal/pofa/3/11/10.1063/1.858164.

[125] Y. Mu, H. Liang, J. Hu, L. Jiang, and L. Wan. Controllable pt nanoparticle deposition on carbon nanotubes as an anode catalyst for direct methanol fuel cells. *The Journal of Physical Chemistry B*, 109(47):22212–22216, 2005.

[126] M. E. Mueller and H. Pitsch. Large eddy simulation subfilter modeling of soot-turbulence interactions. *Physics of Fluids (1994-present)*, 23(11):115104, 2011.

[127] M. E. Mueller and H. Pitsch. Les model for sooting turbulent nonpremixed flames. *Combustion and Flame*, 159(6):2166–2180, 2012.

[128] M. E. Mueller and H. Pitsch. Large eddy simulation of soot evolution in an aircraft combustor. *Physics of Fluids*, 25(11):110812, 2013. doi: 10.1063/1.4819347. URL http://scitation.aip.org/content/aip/journal/pof2/25/11/10.1063/1.4819347.

[129] R. Mueller, L. Mädler, and S. E. Pratsinis. Nanoparticle synthesis at high production rates by flame spray pyrolysis. *Chemical Engineering Science*, 58(10):1969–1976, 2003.

[130] R. Mueller, H. K. Kammler, S. E. Pratsinis, A. Vital, G. Beaucage, and P. Burtscher. Non-agglomerated dry silica nanoparticles. *Powder Technology*, 140(1):40–48, 2004.

[131] S. P. R. Muppala, N. K. Aluri, F. Dinkelacker, and A. Leipertz. Development of an algebraic reaction rate closure for the numerical calculation of turbulent premixed methane, ethylene, and propane/air flames for pressures up to 1.0 mpa. *Combustion and Flame*, 140(4):257 – 266, 2005. ISSN 0010-2180. doi: 10.1016/j.combustflame.2004.11.005. URL http://www.sciencedirect.com/science/article/pii/S0010218004002329.

[132] A. Neophytou and E. Mastorakos. Simulations of laminar flame propagation in droplet mists. *Combustion and Flame*, 156(8):1627 – 1640, 2009. ISSN 0010-2180. doi: 10.1016/j.combustflame.2009.02.014. URL http://www.sciencedirect.com/science/article/pii/S0010218009001199.

[133] F. Nicoud, H. B. Toda, O. Cabrit, S. Bose, and J. Lee. Using singular values to build a subgrid-scale model for large eddy simulations. *Physics of Fluids*, 23(8):085106, 2011. doi: 10.1063/1.3623274. URL http://link.aip.org/link/?PHF/23/085106/1.

[134] Y.-S. Niu, L. Vervisch, and P. D. Tao. An optimization-based approach to detailed chemistry tabulation: Automated progress variable definition. *Combustion and Flame*, 160(4):776 – 785, 2013. ISSN 0010-2180. doi: 10.1016/j.combustflame.2012.11.015. URL http://www.sciencedirect.com/science/article/pii/S0010218012003562.

[135] C. Olbricht, O. T. Stein, J. Janicka, J. A. van Oijen, S. Wysocki, and A. M. Kempf. LES of lifted flames in a gas turbine model combustor using top-hat filtered PFGM chemistry. *Fuel*, 96:100–107, 2012. ISSN 0016-2361. doi: 10.1016/j.fuel.2012.01.018. URL http://www.sciencedirect.com/science/article/pii/S0016236112000300.

[136] H. Olguin and E. Gutheil. Influence of evaporation on spray flamelet structures. *Combustion and Flame*, 161(4):987 – 996, 2014. ISSN 0010-2180. doi: 10.1016/j.combustflame.2013.10.010. URL http://www.sciencedirect.com/science/article/pii/S0010218013003842.

[137] C. Olm, T. Varga, É. Valkó, S. Hartl, C. Hasse, and T. Turányi. Development of an ethanol combustion mechanism based on a hierarchical optimization approach. *International Journal of Chemical Kinetics*, 48(8):423–441, 2016. ISSN 1097-4601. doi: 10.1002/kin.20998.

[138] M. L. Ostraat, J. W. De Blauwe, M. L. Green, L. D. Bell, H. A. Atwater, and R. C. Flagan. Ultraclean two-stage aerosol reactor for production of oxide-passivated silicon nanoparticles for novel memory devices. *Journal of The Electrochemical Society*, 148(5):G265–G270, 2001.

[139] S. Panda and S. E. Pratsinis. Modeling the synthesis of aluminum particles by evaporation-condensation in an aerosol flow reactor. *Nanostructured Materials*, 5(78):755 – 767, 1995. ISSN 0965-9773. doi: 10.1016/0965-9773(95)00292-m. URL http://www.sciencedirect.com/science/article/pii/096597739500292M.

[140] Q. A. Pankhurst, J. Connolly, S. Jones, and J. Dobson. Applications of magnetic nanoparticles in biomedicine. *Journal of physics D: Applied physics*, 36(13):R167, 2003.

[141] C. Pera, J. Réveillon, L. Vervisch, and P. Domingo. Modeling subgrid scale mixture fraction variance in {LES} of evaporating spray. *Combustion and Flame*, 146(4):635 – 648, 2006. ISSN 0010-2180. doi: 10.1016/j.combustflame.2006.07.003. URL http://www.sciencedirect.com/science/article/pii/S0010218006001623.

[142] E. Pérez-Tijerina, M. G. Pinilla, S. Mejia-Rosales, U. Ortiz-Méndez, A. Torres, and M. José-Yacamán. Highly size-controlled synthesis of au/pd nanoparticles by inert-gas condensation. *Faraday discussions*, 138:353–362, 2008.

[143] N. Peters. Laminar diffusion flamelet models in non-premixed turbulent combustion. *Progress in Energy and Combustion Science*, 10(3):319 – 339, 1984. ISSN 0360-1285. doi: 10.1016/0360-1285(84)90114-x. URL http://www.sciencedirect.com/science/article/pii/036012858490114X.

[144] N. Peters. *Turbulent Combustion*. Cambridge University Press, 2000.

[145] M. Pettit, B. Coriton, A. Gomez, and A. M. Kempf. Large-eddy simulation and experiments on non-premixed highly turbulent opposed jet flows. *Proc. Combust.Inst.*, 33:1391–1399, 2011.

[146] C. D. Pierce. *Progress-variable approach for large-eddy simulation of turbulent combustion*. PhD thesis, Stanford University, 2001.

[147] C. D. Pierce and P. Moin. A dynamic model for subgrid-scale variance and dissipation rate of a conserved scalar. *Physics of Fluids*, 10:3041, 1998.

[148] C. D. Pierce and P. Moin. Progress-variable approach for large-eddy simulation of non-premixed turbulent combustion. *Journal of Fluid Mechanics*, 504:73–97, 2004. ISSN 1469-7645. doi: 10.1017/s0022112004008213. URL http://journals.cambridge.org/article_S0022112004008213.

[149] U. Piomelli and J. Liu. Large-eddy simulation of rotating channel flows using a localized dynamic model. *Physics of Fluids*, 7(4):839–848, 1995. doi: 10.1063/1.868607. URL http://link.aip.org/link/?PHF/7/839/1.

[150] H. Pitsch. Large-eddy simulation of turbulent combustion. *Annu. Rev. Fluid Mech.*, 38: 453–482, 2006. imp-import.

[151] T. J. Poinsot and D. Veynante. *Theoretical and Numerical Combustion*. Aquaprint, Bordeaux, France, 3rd edition, 2012.

[152] S. B. Pope. *Turbulent Flows*. Cambridge University Press, 2000. imp-import.

[153] L. A. Porter, H. C. Choi, J. Schmeltzer, A. E. Ribbe, L. C. Elliott, and J. M. Buriak. Electroless nanoparticle film deposition compatible with photolithography, microcontact printing, and dip-pen nanolithography patterning technologies. *Nano Letters*, 2(12):1369–1372, 2002.

[154] S. E. Pratsinis. Flame aerosol synthesis of ceramic powders. *Progress in Energy and Combustion Science*, 24(3):197 – 219, 1998. ISSN 0360-1285. doi: 10.1016/s0360-1285(97)00028-2. URL http://www.sciencedirect.com/science/article/pii/S0360128597000282.

[155] S. E. Pratsinis, W. Zhu, and S. Vemury. The role of gas mixing in flame synthesis of titania powders. *Powder Technology*, 86(1):87 – 93, 1996. ISSN 0032-5910. doi: 10.1016/0032-5910(95)03041-7. URL http://www.sciencedirect.com/science/article/pii/0032591095030417.

[156] F. Proch. *Highly-resolved numerical simulation of turbulent premixed and stratified combustion under adiabatic and non-adiabatic conditions with tabulated chemistry*. PhD thesis, University of Duisburg-Essen, Nov. 2016.

[157] F. Proch and A. M. Kempf. Numerical analysis of the cambridge stratified flame series using artificial thickened flame les with tabulated premixed flame chemistry. *Combustion and Flame*, 161(10):2627 – 2646, 2014. ISSN 0010-2180. doi: 10.1016/j.combustflame.2014.04.010. URL http://www.sciencedirect.com/science/article/pii/S0010218014001126.

[158] F. Proch, M. W. A. Pettit, T. Ma, M. Rieth, and A. M. Kempf. *Direct and Large-Eddy Simulation IX*, chapter Investigations on the Effect of Different Subgrid Models on the Quality of LES Results, pages 141–147. Springer International Publishing, Cham, 2015. ISBN 978-3-319-14448-1. doi: 10.1007/978-3-319-14448-1_19.

[159] M. Ranz and R. Marshall, W. Evaporation from drops: Part i. *Chemical Engineering Progress*, 48:141–146, 1952.

[160] O. Reynolds. An experimental investigation of the circumstances which determine whether the motion of water shall be direct or sinuous, and of the law of resistance in parallel channels. *Proceedings of the royal society of London*, 35(224-226):84–99, 1883.

[161] O. Reynolds. On the dynamical theory of incompressible viscous fluids and the determination of the criterion. *Proceedings of the Royal Society of London*, 56(336-339):40–45, 1894.

[162] M. Rieth, F. Proch, O. T. Stein, M. W. A. Pettit, and A. M. Kempf. Comparison of the Sigma and Smagorinsky LES models for grid generated turbulence and a channel flow. *Computers and Fluids*, 99(0):172 – 181, 2014. ISSN 0045-7930. doi: 10.1016/j.compfluid.2014.04.018. URL http://www.sciencedirect.com/science/article/pii/S004579301400156X.

[163] A. Rittler, F. Proch, and A. M. Kempf. Les of the sydney piloted spray burner. *Proceedings of the European Combustion Meeting*, 6, 2013.

[164] A. Rittler, F. Proch, and A. M. Kempf. {LES} of the sydney piloted spray flame series with the {PFGM}/{ATF} approach and different sub-filter models. *Combustion and Flame*, 162 (4):1575 – 1598, 2015. ISSN 0010-2180. doi: 10.1016/j.combustflame.2014.11.025. URL http://www.sciencedirect.com/science/article/pii/S0010218014003794.

[165] A. Rittler, L. Deng, I. Wlokas, and A. M. Kempf. Large eddy simulations of nanoparticle synthesis from flame spray pyrolysis. *Proceedings of the Combustion Institute*, 36, 2016.

[166] A. Rittler, I. Wlokas, and A. M. Kempf. Large eddy simulation of iron-oxide nanoparticle synthesis from spray flame pyrolysis in a pilot scale reactor. 2017.

[167] P. Roth. Particle synthesis in flames. *Proceedings of the combustion institute*, 31(2):1773–1788, 2007.

[168] O. V. Salata. Applications of nanoparticles in biology and medicine. *Journal of nanobiotechnology*, 2(1):3, 2004.

[169] L. Schiller and A. Z. Naumann. Über die grundlegenden Berechnungen bei der Schwerkraftaufbereitung. *Zeitschr. Verein dt. Ing.*, 77:318–320, 1933.

[170] R. Schmechel, M. Kennedy, H. Von Seggern, H. Winkler, M. Kolbe, R. Fischer, L. Xaomao, A. Benker, M. Winterer, and H. Hahn. Luminescence properties of nanocrystalline y2o3: Eu3+ in different host materials. *Journal of Applied Physics*, 89(3):1679–1686, 2001.

[171] F. G. Schmitt. About boussinesq's turbulent viscosity hypothesis: historical remarks and a direct evaluation of its validity. *Comptes Rendus Mécanique*, 335(9-10):617–627, 2007.

[172] C. Schneider, A. Dreizler, J. Janicka, and E. Hassel. Flow field measurements of stable and locally extinguishing hydrocarbon-fuelled jet flames. *Combustion and Flame*, 135(1): 185–190, 2003.

[173] J. M. Senoner, M. Sanjosé, T. Lederlin, F. Jaegle, M. García, E. Riber, B. Cuenot, L. Gicquel, H. Pitsch, and T. J. Poinsot. Eulerian and lagrangian large-eddy simulations of an evaporating two-phase flow. *C. R. Mecanique*, 337:458–468, 2009.

[174] T. Seto, A. Hirota, T. Fujimoto, M. Shimada, and K. Okuyama. Sintering of polydisperse nanometer-sized agglomerates. *Aerosol Science and Technology*, 27(3):422–438, 1997. doi: 10.1080/02786829708965482.

[175] T.-H. Shih, W. W. Liou, A. Shabbir, Z. Yang, and J. Zhu. A new k-ϵ eddy viscosity model for high reynolds number turbulent flows. *Computers & Fluids*, 24(3):227–238, 1995.

[176] J. S. Smagorinsky. General circulation experiments with the primitive equations, 1, the basic experiment. *Monthly Weather Review*, 91(1):99–164, 1963.

[177] G. P. Smith, D. M. Golden, M. Frenklach, N. W. Moriarty, B. Eiteneer, M. Goldenberg, C. T. Bowman, R. K. Hanson, S. Song, W. C. Gardiner, Jr., V. V. Lissianski, and Z. Qin. http://www.me.berkeley.edu/gri_mech, 2000.

[178] P. SPALART and S. ALLMARAS. *A one-equation turbulence model for aerodynamic flows*. Aerospace Sciences Meetings. American Institute of Aeronautics and Astronautics, 1992. doi: 10.2514/6.1992-439. doi:10.2514/6.1992-439.

[179] D. B. Spalding. Mixing and chemical reaction in steady confined turbulent flames. *Symposium (International) on Combustion*, 13(1):649–657, 1971. doi: 10.1016/s0082-0784(71)80067-x.

[180] P. T. Spicer, O. Chaoul, S. Tsantilis, and S. E. Pratsinis. Titania formation by ticl 4 gas phase oxidation, surface growth and coagulation. *Journal of Aerosol Science*, 33(1):17–34, 2002.

[181] O. T. Stein. *Large Eddy Simulation of Combustion in Swirling and Opposed Jet Flows*. PhD thesis, Imperial College London, 2009.

[182] F. Stellacci, C. A. Bauer, T. Meyer-Friedrichsen, W. Wenseleers, V. Alain, S. M. Kuebler, S. J. Pond, Y. Zhang, S. R. Marder, and J. W. Perry. Laser and electron-beam induced growth of nanoparticles for 2d and 3d metal patterning. *Advanced Materials*, 14(3):194, 2002.

[183] R. Strobel and S. E. Pratsinis. Direct synthesis of maghemite, magnetite and wustite nanoparticles by flame spray pyrolysis. *Advanced Powder Technology*, 20(2):190 – 194, 2009. ISSN 0921-8831. doi: 10.1016/j.apt.2008.08.002. URL `http://www.sciencedirect.com/science/article/pii/S0921883108000289`.

[184] Y. Sung, V. Raman, and R. O. Fox. Multiscale modeling of tio2 nanoparticle production in flame reactors: Effect of chemical mechanism. *Ind. Eng. Chem.*, 49(21):10663–10673, 2010. URL `http://dx.doi.org/10.1021/ie100560h`.

[185] Y. Sung, V. Raman, and R. O. Fox. Large-eddy-simulation-based multiscale modeling of tio2 nanoparticle synthesis in a turbulent flame reactor using detailed nucleation chemistry. *Chemical Engineering Science*, 66:4370–4381, 2011.

[186] Y. Sung, V. Raman, H. Koo, M. Mehta, and R. O. Fox. Large-eddy simulation modeling of turbulent flame synthesis of titania nanoparticles using a bivariate particle description. *AIChE Journal*, 60(2):459–472, 2014. ISSN 1547-5905. doi: 10.1002/aic.14279.

[187] W. Sutherland. Lii. the viscosity of gases and molecular force. *Philosophical Magazine Series 5*, 36(223):507–531, 1893. doi: 10.1080/14786449308620508.

[188] P. K. Sweby. High resolution schemes using flux limiters for hyperbolic conservation laws. *SIAM journal on numerical analysis*, 21(5):995–1011, 1984.

[189] M. T. Swihart. Vapor-phase synthesis of nanoparticles. *Current Opinion in Colloid & Interface Science*, 8(1):127 – 133, 2003. ISSN 1359-0294. doi: 10.1016/s1359-0294(03)00007-4. URL `http://www.sciencedirect.com/science/article/pii/S1359029403000074`.

[190] N. S. Tabrizi, M. Ullmann, V. Vons, U. Lafont, and A. Schmidt-Ott. Generation of nanoparticles by spark discharge. *Journal of Nanoparticle Research*, 11(2):315–332, 2009.

[191] W. Y. Teoh, R. Amal, and L. Mädler. Flame spray pyrolysis: an enabling technology for nanoparticles design and fabrication. *Nanoscale*, 2(8):1324–1347, 2010.

[192] J. Tillou, J. Michel, C. Angelberger, C. Bekdemir, and D. Veynante. Large-eddy simulation of diesel spray combustion with exhaust gas recirculation. *Oil Gas Sci Technol*, 2013.

[193] S. Tsantilis. *Population balance modeling of synthesis of nanoparticles in aerosol flame reactors*, volume 39. Springer Berlin Heidelberg, 2004. ISBN 978-3-540-21180-8. doi: 10.1007/978-3-642-18756-8_19.

[194] S. Tsantilis, H. Briesen, and S. E. Pratsinis. Sintering time for silica particle growth. *Aerosol Science and Technology*, 34(3):237–246, 2001. doi: 10.1080/02786820119149. URL `http://www.tandfonline.com/doi/abs/10.1080/02786820119149`.

[195] A. Tyliszczak, D. E. Cavaliere, and E. Mastorakos. Les/cmc of blow-off in a liquid fueled swirl burner. *Flow, Turbulence and Combustion*, 92(1-2):237–267, 2014.

[196] S. Ukai, A. Kronenburg, and O. T. Stein. Les-cmc of a dilute acetone spray flame. *Proceedings of the Combustion Institute*, 34(1):1643–1650, 2013.

[197] S. Ukai, A. Kronenburg, and O. T. Stein. Simulation of dilute acetone spray flames with les-cmc using two conditional moments. *Flow, turbulence and combustion*, 93(3):405–423, 2014.

[198] S. Ukai, A. Kronenburg, and O. T. Stein. Large eddy simulation of dilute acetone spray flames using cmc coupled with tabulated chemistry. *Proceedings of the Combustion Institute*, 35(2):1667–1674, 2015.

[199] G. D. Ulrich. Theory of particle formation and growth in oxide synthesis flames. *Combustion Science and Technology*, 4(1):47–57, 1971. doi: 10.1080/00102207108952471.

[200] F. Urban Iii, A. Hosseini-Tehrani, P. Griffiths, A. Khabari, Y.-W. Kim, and I. Petrov. Nanophase films deposited from a high-rate, nanoparticle beam. *Journal of Vacuum Science & Technology B*, 20(3):995–999, 2002.

[201] J. A. van Oijen and L. P. H. de Goey. Modelling of premixed laminar flames using flamelet-generated manifolds. *Combust. Sci. Technol.*, 161(1):113–137, 2000. doi: 10.1080/00102200008935814.

[202] J. A. van Oijen, F. A. Lammers, and L. P. H. de Goey. Modeling of complex premixed burner systems by using flamelet-generated manifolds. *Combustion and Flame*, 127(3): 2124 – 2134, 2001. ISSN 0010-2180. doi: 10.1016/s0010-2180(01)00316-9. URL `http://www.sciencedirect.com/science/article/pii/S0010218001003169`.

[203] J. A. van Oijen, R. J. M. Bastiaans, and L. P. H. de Goey. Low-dimensional manifolds in direct numerical simulations of premixed turbulent flames. *Proc. Combust. Inst.*, 31(1): 1377–1384, 2007. ISSN 1540-7489. doi: 10.1016/j.proci.2006.07.076. URL `http://www.sciencedirect.com/science/article/pii/S1540748906000939`.

[204] S. Vemury and S. E. Pratsinis. Dopants in flame synthesis of titania. *Journal of the American Ceramic Society*, 78(11):2984–2992, 1995.

[205] S. Vemury and S. E. Pratsinis. Self-preserving size distributions of agglomerates. *Journal of Aerosol Science*, 26(2):175 – 185, 1995. ISSN 0021-8502. doi: 10.1016/0021-8502(94)00103-6. URL `http://www.sciencedirect.com/science/article/pii/0021850294001036`.

[206] H. K. Versteeg and W. Malalasekera. *An Introduction to Computational Fluid Dynamics - The Finite Volume Method*. Pearson Prentice Hall, 2007.

[207] A. W. Vreman, B. A. Albrecht, J. A. van Oijen, L. P. H. de Goey, and R. J. M. Bastiaans. Premixed and nonpremixed generated manifolds in large-eddy simulation of sandia flame d and f. *Combustion and Flame*, 153(3):394 – 416, 2008. ISSN 0010-2180. doi: 10.1016/j.combustflame.2008.01.009. URL `http://www.sciencedirect.com/science/article/pii/S0010218008000667`.

[208] G. Wang and S. C. Garrick. Modeling and simulation of titania formation and growth in temporal mixing layers. *Journal of Aerosol Science*, 37(4):431 – 451, 2006. ISSN 0021-8502. doi: 10.1016/j.jaerosci.2005.04.007. URL `http://www.sciencedirect.com/science/article/pii/S0021850205000819`.

[209] G. Wang, M. Boileau, and D. Veynante. Implementation of a dynamic thickened flame model for large eddy simulations of turbulent premixed combustion. *Combustion and Flame*, 158 (11):2199 – 2213, 2011. ISSN 0010-2180. doi: 10.1016/j.combustflame.2011.04.008. URL `http://www.sciencedirect.com/science/article/pii/S0010218011001131`.

[210] K. Wegner and S. E. Pratsinis. Scale-up of nanoparticle synthesis in diffusion flame reactors. *Chemical Engineering Science*, 58(20):4581 – 4589, 2003. ISSN 0009-2509. doi: 10.1016/j.ces.2003.07.010. URL `//www.sciencedirect.com/science/article/pii/S0009250903003725`.

[211] K. Wegner and S. E. Pratsinis. Gas-phase synthesis of nanoparticles: scale-up and design of flame reactors. *Powder Technology*, 150(2):117 – 122, 2005. ISSN 0032-5910. doi: 10.1016/j.powtec.2004.11.022. URL `//www.sciencedirect.com/science/article/pii/S0032591004004905`. Scale-Up in Particle Processing.

[212] K. Wegner, W. J. Stark, and S. E. Pratsinis. Flame-nozzle synthesis of nanoparticles with closely controlled size, morphology and crystallinity. *Materials Letters*, 55(5):318–321, 2002.

[213] C. Weise. *Towards the modelling of a spray flame process for nanoparticle synthesis.* PhD thesis, University of Duisburg-Essen, Nov. 2015.

[214] C. Weise, J. Menser, S. A. Kaiser, A. M. Kempf, and I. Wlokas. Numerical investigation of the process steps in a spray flame reactor for nanoparticle synthesis. *Proceedings of the Combustion Institute*, 35(2):2259 – 2266, 2015. ISSN 1540-7489. doi: 10.1016/j.proci.2014.05.037. URL http://www.sciencedirect.com/science/article/pii/S1540748914000406.

[215] H. G. Weller, G. Tabor, A. D. Gosman, and C. Fureby. Application of a flame-wrinkling les combustion model to a turbulent mixing layer. *Proceedings of the Combustion Institute*, 27(1):899–907, 1998.

[216] D. C. Wilcox. Reassessment of the scale-determining equation for advanced turbulence models. *AIAA journal*, 26(11):1299–1310, 1988.

[217] D. C. Wilcox et al. *Turbulence modeling for CFD*, volume 2. DCW industries La Canada, CA, 1998.

[218] C. R. Wilke. A viscosity equation for gas mixtures. *Journal of Chemical Physics*, 18(4):517–519, 1950.

[219] J. H. Williamson. Low-storage runge-kutta schemes. *Journal of Computational Physics*, 35 (1):48–56, 1980.

[220] I. Wlokas, A. Faccinetto, B. Tribalet, C. Schulz, and A. M. Kempf. Mechanism of iron oxide formation from iron pentacarbonyl-doped low-pressure hydrogen/oxygen flames. *Int. J. Chem. Kinet.*, 45(8):487–498, 2013.

[221] Y. Xiong and S. E. Pratsinis. Gas phase production of particles in reactive turbulent flows. *Journal of Aerosol Science*, 22(5):637 – 655, 1991. ISSN 0021-8502. doi: 10.1016/0021-8502(91)90017-c. URL //www.sciencedirect.com/science/article/pii/002185029190017C.

[222] Y. Xiong and S. E. Pratsinis. Formation of agglomerate particles by coagulation and sinteringpart i. a two-dimensional solution of the population balance equation. *Journal of Aerosol Science*, 24(3):283–300, 1993.

[223] Y. Xiong, M. K. Akhtar, and S. E. Pratsinis. Formation of agglomerate particles by coagulation and sinteringpart ii. the evolution of the morphology of aerosol-made titania, silica and silica-doped titania powders. *Journal of Aerosol Science*, 24(3):301–313, 1993.

[224] V. Yakhot, S. Orszag, S. Thangam, T. Gatski, and C. Speziale. Development of turbulence models for shear flows by a double expansion technique. *Physics of Fluids A: Fluid Dynamics (1989-1993)*, 4(7):1510–1520, 1992.

[225] C. L. Yeh, S. H. Yeh, and H. K. Ma. Flame synthesis of titania particles from titanium tetraisopropoxide in premixed flames. *Powder Technology*, 145(1):1 – 9, 2004. ISSN 0032-5910. doi: 10.1016/j.powtec.2004.04.042. URL //www.sciencedirect.com/science/article/pii/S0032591004002190.

[226] G. Zhou. *Numerical simulations of physical discontinuities in single and multi-fluid flows for arbitrary Mach numbers.* PhD thesis, Chalmers University of Technology, Goteborg, Sweden, 1995.